Opportunities for the direct manipulation of a phase-driven Andreev spin qubit

Yoan Fauvel

To cite this version:

Yoan Fauvel. Opportunities for the direct manipulation of a phase-driven Andreev spin qubit. Condensed Matter [cond-mat]. Université Grenoble Alpes [2020-..], 2024. English. NNT : 2024GRALY013 . tel-04673032

HAL Id: tel-04673032
https://theses.hal.science/tel-04673032v1

Submitted on 19 Aug 2024

THÈSE

Pour obtenir le grade de

DOCTEUR DE L'UNIVERSITÉ GRENOBLE ALPES

École doctorale : PHYS - Physique
Spécialité : Physique de la Matière Condensée et du Rayonnement
Unité de recherche : PHotonique, ELectronique et Ingéniérie QuantiqueS

Opportunités de manipulation directe d'un qubit de spin d'Andreev piloté en phase

Opportunities for the direct manipulation of a phase-driven Andreev spin qubit

Présentée par :

Yoan FAUVEL

Direction de thèse :

Julia MEYER PROFESSEURE DES UNIVERSITES, UNIVERSITE GRENOBLE ALPES	Directrice de thèse
Manuel HOUZET DIRECTEUR DE RECHERCHE, CEA CENTRE DE GRENOBLE	Co-directeur de thèse

Rapporteurs :

MARCELO GOFFMAN
DIRECTEUR DE RECHERCHE, CEA CENTRE DE PARIS-SACLAY
ELSA PRADA
CHARGEE DE RECHERCHE, INSTITUTO DE CIENCIA DE MATERIALES

Thèse soutenue publiquement le **9 avril 2024**, devant le jury composé de :

SERGE FLORENS, DIRECTEUR DE RECHERCHE, CNRS DELEGATION ALPES	Président
MARCELO GOFFMAN, DIRECTEUR DE RECHERCHE, CEA CENTRE DE PARIS-SACLAY	Rapporteur
ELSA PRADA, CHARGEE DE RECHERCHE, INSTITUTO DE CIENCIA DE MATERIALES	Rapporteure
CLEMENS WINKELMANN, MAITRE DE CONFERENCES HDR, GRENOBLE INP	Examinateur

Abstract

The research presented in this thesis delves into a theoretical exploration of Andreev bound states (ABS) hosted in Josephson junctions with spin-orbit coupling (SOC). ABS are fermionic bound states that appear at the junction between two superconducting electrodes forming a Josephson junction. These bound states are at the core of the microscopic description of the Josephson effect and provide an explanation for the transfer of Cooper pairs from one superconducting electrode to the other. Crucially, when the superconducting phase difference between the two electrodes is non-zero, a supercurrent can flow in the junction, depending on the occupancy of the ABS. The presence of this supercurrent facilitates the coupling between a microwave resonator and a junction due to its sensibility to the electromagnetic field. This coupling then allows for the detection and manipulation of ABS.

Furthermore, in the presence of SOC along with a superconducting phase bias, the spin degeneracy of ABS can be lifted. Therefore such a junction provides a unique opportunity to realize a special kind of spin qubit known as Andreev spin qubit (ASQ). The qubit operation can be performed via an AC modulation of an electrostatic gate or magnetic flux, thanks to the sensitivity of the ABS to the electric potential or the phase difference, respectively. So far, the coherent manipulation of such qubits has been realized in gate-driven experiments as well as in flux-driven experiments with the use of additional Andreev levels. However, the direct transition between the two ABS forming the ASQ has remained out of reach in flux-driven experiments.

In this thesis, we investigate two distinct types of Josephson junctions with SOC with the aim of estimating the amplitude of the matrix elements of the current operator between two ABS forming an ASQ. These elements characterize the coupling strength between the qubit and an external flux drive, indicating which transitions between ABS are within reach.

Our first project focuses on a superconductor-normal-superconductor junction where the normal region consists of a nanowire with Rashba SOC. As a minimal model, we consider a generic scatterer located along the nanowire. Unless this scatterer possesses additional spatial (mirror) symmetries, it is responsible for inducing spin-flip transmission probability. Using the scattering formalism, we derive the energy spectrum of ABS and assess how SOC influences the spin-splitting between opposite spin states. We then obtain analytical expressions for the matrix elements of the current operator. Notably, our study reveals that SOC allows one to have finite elements between opposite spin states.

In a second project, the system we study consists of a superconductor - double quantum dots - superconductor junction. A quantum dot consists of a tiny region defined by electrostatic gates or impurities. Due to its small size, Coulomb repulsion can be significant. In the simplest case of a quantum

dot with a single level, even in the presence of SOC in the coupling between the dot and the leads, spin degeneracy of ABS is still preserved. However, recent experiments showed that additional levels allow to lift the spin degeneracy. Here, we introduce a second quantum dot which provides an additional level and offers more control on each level. By using an effective model, we identify the minimal ingredients that are necessary to lift the spin degeneracy. Our results reveal that this splitting is achievable through spin-dependent couplings with the leads and is reduced by the Coulomb repulsion. Additionally, the presence of a finite coupling between the two dots, combined with SOC in the couplings with the leads, allows one to have finite matrix elements of the current operator between opposite spin states, which we obtain numerically.

In short, we present in this thesis two platforms for the realization of phase-driven ASQ.

Résumé

Les recherches présentées dans cette thèse portent sur l'exploration théorique des états liés d'Andreev (ABS) dans des jonctions Josephson avec couplage spin-orbite (SOC). Les ABS sont des états liés apparaissent à la jonction entre deux électrodes supraconductrices formant une jonction Josephson. Ils sont au cœur de la description microscopique de l'effet Josephson expliquant le transfert des paires de Cooper d'une électrode à l'autre. Lorsque la différence de phase supraconductrice entre les deux électrodes est non nulle, un supercourant peut circuler dans la jonction, en fonction de l'occupation des ABS. Grâce à ce supercourant, un résonateur micro-ondes peut être facilement couplé à la jonction due à sa sensibilité au champ électromagnétique. Ce couplage permet de détecter et de manipuler les ABS.

En outre, en présence de SOC et d'une différence de phase supraconductrice, la dégénérescence de spin des ABS peut être levée. Une telle jonction offre une occasion unique de réaliser un type de qubit de spin connu sous le nom de qubit de spin d'Andreev (ASQ). La manipulation du qubit peut être réalisée par une modulation en courant AC d'une grille électrostatique ou d'un flux magnétique, grâce à la sensibilité des ABS au potentiel électrique ou à la différence de phase, respectivement. Jusqu'à présent, leur manipulation a été réalisée dans des expériences pilotées par grilles et dans des expériences pilotées par flux grâce à l'utilisation d'ABS supplémentaires. Cependant, la transition directe entre deux ABS formant un ASQ est restée hors de portée dans les expériences pilotées par flux.

Dans cette thèse, nous étudions deux types de jonctions Josephson avec SOC dans le but d'estimer l'amplitude des éléments de matrice de l'opérateur courant entre deux ABS formant un ASQ. Ces éléments caractérisent la force de couplage entre le qubit et un flux externe, indiquant quelles transitions entre ABS sont accessibles.

Notre projet initial porte sur une jonction supraconducteur-normal-supraconducteur où, la région normale consiste en un nanofil avec effet Rashba. Comme modèle minimal, nous considérons une impureté générique située le long du nanofil. À moins que cette impureté présente des symétries spatiales additionnelles, elle permet d'induire une probabilité de transmission retournant le spin. En utilisant le formalisme des matrices de diffusion, nous dérivons le spectre en énergie des ABS et évaluons l'influence du SOC sur la séparation en spin entre états de spin opposés. Nous obtenons ensuite des expressions analytiques pour les éléments de matrice de l'opérateur courant. Notre étude révèle que le SOC permet d'avoir des éléments finis entre états de spin opposés.

Dans un second projet, nous étudions est une jonction supraconducteur - points quantiques - supraconducteur. Un point quantique (QD) consiste en une minuscule région définie par des grilles électrostatiques ou des impuretés. En raison de sa taille, la répulsion Coulombienne peut être significative.

Dans le cas le plus simple d'un seul QD, malgré la présence de SOC dans le couplage entre le QD et les électrodes, la dégénérescence de spin est préservée. Cependant, de récentes expériences montrent que la présence d'autres niveaux permet de lever la dégénérescence de spin. Ici, nous introduisons un second QD, fournissant un niveau supplémentaire et offrant plus de contrôle sur chaque niveau. Avec un modèle effectif, nous identifions les ingrédients minimaux pour lever la dégénérescence de spin. Nos résultats montrent que la séparation en spin est permise grâce au SOC dans les couplages avec les électrodes (tunnel) et est réduite par la force de la répulsion Coulombienne. De plus, la présence d'un couplage entre les deux QD, avec le SOC dans les couplages tunnel, permet d'obtenir des éléments de matrice finis entre états de spin opposés, que nous avons obtenu numériquement.

En bref, nous présentons dans cette thèse deux plateformes pour la réalisation d'ASQ pilotées en phase.

Acknowledgements/Remerciements

Maintenant arrivé, après ces trois années et quelques mois, au terme de ma thèse, il me tient à cœur d'exprimer mes remerciements pour toutes les personnes m'ayant permis d'en arriver là. Ces trois années ont été très riches pour moi, que ce soit en défi ou en émotions, mais elles ont également été d'une grande richesse intellectuelle.

Dans un premier temps, je tiens évidemment à remercier mes encadrants Julia et Manuel pour m'avoir permis de faire cette thèse. Vous m'avez entre autres appris à être plus critique envers mon travail et par la même occasion à être plus rigoureux. Je n'ai aucun doute quant au fait que ces qualités me serviront toujours. J'espère que mes piètres qualités de rédacteur ne vous auront pas trop démoralisé. Merci de m'avoir guidé pendant la thèse et de m'avoir encouragé à pousser les recherches que j'ai pu réaliser.

Mes remerciements vont également aux membres du Groupe Théorie. En particulier, j'aimerais remercier mes colocs de bureaux Baptiste, Anthony, Thomas et Romy. Baptiste et Anthony, vous m'avez beaucoup aidé à m'intégrer au labo durant ma première année malgré les périodes de confinement. Travailler avec vous dans le même bureau aura été vraiment enrichissant et stimulant. Toutes nos discussions sur nos projets respectifs ont toujours été inspirantes et enrichissantes pour moi. Les moments passés ensemble pendant notre temps libre, les barbecues chez Anthony, les séances d'escalade et bien d'autres m'auront permis de garder le moral et de surmonter les difficultés de la thèse. Cette thèse sans vous n'aurait certainement pas été la même. Je souhaite le meilleur aux nouveaux doctorants et aux permanents du groupe pour la suite.

J'ai aussi rencontré de nombreux amis pendant ma thèse. Ainsi, je tenais à vous remercier Estelle, Guillaume, Maxime, Thibaud, Seddik, Théo et tous les autres avec qui j'ai pu passer de précieux moments au labo mais aussi à Cargèse et à Aussois.

Je me dois de vous remercier Haude, Marie et Timothée. Haude, merci de m'avoir initié à l'escalade, j'y suis potentiellement devenu légèrement accroc maintenant. Sans toi, je n'aurai également peut-être pas découvert la Roue du Temps et je serai vraiment passé à côté de quelque chose. Marie, Timothée, je vous ai rencontré d'une manière bien étrange au karaoké des Doctoriales. Mais quelle rencontre ! Je n'ai passé que de bons moments avec vous, même si ce n'est probablement pas l'avis de ma cheville qui s'est retrouvé immobilisée de nombreuse fois depuis que je vous connais. Finalement, je voudrais également adresser mes remerciements à tous mes amis qui ont toujours été présents pendant mes études.

Et évidemment, le meilleur pour la fin, ma famille. Je ne saurai suffisamment vous remercier pour tout ce que vous m'apporter et pour votre support inconditionnel. Merci à mes deux soeurs Sandy et Lilou, pour le temps qu'elles ont passé avec moi, leur écoute et leur soutien. Et pour finir, merci à mes parents sans qui je n'aurai tout simplement pas fait ces études. Vous m'avez permis de développer ma curiosité et mon amour pour les sciences. Merci également pour tout votre soutien. Cela n'aura pas toujours été facile, mais merci à vous tous d'être présents pour moi.

Contents

Introduction

In the fascinating field of quantum computing, several technologies have the ambition to transform the computing landscape as we know it. To do so, physicists came up with the idea of developing systems that use the properties of quantum mechanics to store information, called qubits. Thus, where classical bits can only take the values 0 or 1, the qubits, thanks to their quantum properties, can be placed in a superposition state of 0 and 1 at the same time. A quantum computer operating with multiple qubits can therefore have a greater computing power than a classical computer operating with the same number of classical bits. At the heart of this endeavor lies the world of condensed matter, where the properties of quantum mechanics manifest themselves at macroscopic scale. Condensed matter physics explores the physics of collections of particles, such as atoms or electrons, as they interact with each other and arrange themselves in various ways. The unique feature of condensed matter comes from the emergent properties that arise from the interaction of these collections of particles, which are absent at the level of individual particles. In the context of quantum computing, condensed matter systems, such as superconductors and semiconductors, provide an ideal platform for building quantum circuits and harnessing the power of quantum mechanics to perform computations. In addition, these systems benefit from already existing fabrication techniques like thin-film deposition and lithography, which can provide a foundation for manufacturing qubits with similar processes. Another advantage of these systems is their potential integration with classical electronics.

One of the key milestones that quantum computing must reach to fulfill its promise is so-called quantum supremacy, which means that a programmable quantum system would be able to solve a problem that is unsolvable by a classical computer. In this quest, a team of Google recently claimed to have achieved quantum supremacy [1]. The system they used to achieve this result is a quantum computer composed of 53 working qubits. Despite this claim, the use of quantum computers to revolutionize computing is still a long way off. In fact, current quantum computers are still subject to a large number of errors and are limited in the number of qubits they can implement. These two problems limit the maximum performance and fidelity of current quantum computers. It is therefore necessary to develop new systems that allow the realization of qubits that are less sensitive to noise and/or easier to realize/integrate.

Superconductors and semiconductors are among the most studied materials for this purpose. These two platforms each have amazing properties. Superconductors are known for their ability to carry current without dissipation thanks to the pairing of electrons in what is called a Cooper pair. This phase of matter is also characterized by a complex order parameter called the superconducting gap, which defines the energy range in which electrons form Cooper pairs. As for semiconductors, they have a low density of charge carriers compared to metals, so their chemical potential can be manipulated by field effect. In addition, some semiconductor materials exhibit strong spin-orbit coupling, i.e., coupling between the spin degree of freedom and the motion of the particles that carry the spin.

The more common qubits realized by superconducting circuits are based on Josephson tunnel junctions. These junctions consist of a thin layer of an insulating material separating two superconducting reservoirs. The charge and the phase being conjugate variables in a superconductor, modifying one also change the other. Therefore, in Josephson junctions, when there is a finite superconducting phase difference between the two superconductors, a coherent transfer of Cooper pairs across the insulator can take place, such that it gives rise to a non-dissipative current even at zero voltage. This phenomenon is known as the Josephson effect [2]. In addition, it is known since the 1960s that in a Josephson junction subject to a current bias with finite capacitance, this phase difference acts as a particle moving in a tilted washboard potential with a mass given by the capacitance of the junction [3]. In 1985, it was experimentally demonstrated that the phase difference obeys the rules of quantum mechanics through energy level quantization by John M. Martinis, Michel H. Devoret, and John Clarke [4]. They showed that in such junction, irradiating the latter with microwaves at appropriate frequency, i.e. a frequency matching the energy difference between two energy levels, that the escape rate of the particle from the energy well is changed. Since the escape rate of this particle changes with its energy, their experiment highlighted the presence of quantized quasi-levels (see Fig. 0.1). The fact that this phase difference follows the rules of quantum mechanics has since been used to design various superconducting qubits [5], most notably the transmons [6] used by Google to claim quantum supremacy. These are realized by a circuit in which two superconducting islands coupled through two Josephson junctions in parallel forming a closed loop (a system known as a superconducting quantum interference device, or SQUID for short).

On the other hand, semiconductor qubits are implemented using quantum dots, which are tiny regions in semiconductor materials defined by electrostatic gates or impurities. These quantum dots serve as electron boxes, with dimensions typically in the tens of nanometers, where electrons are confined. The energies in quantum dots are discrete, and it is now possible to trap a single electron in them [7]. In semiconductor materials with strong spin-orbit coupling, it is possible to use the spin degree of freedom of this electron as a basis for semiconductor spin qubit realization [8–10].

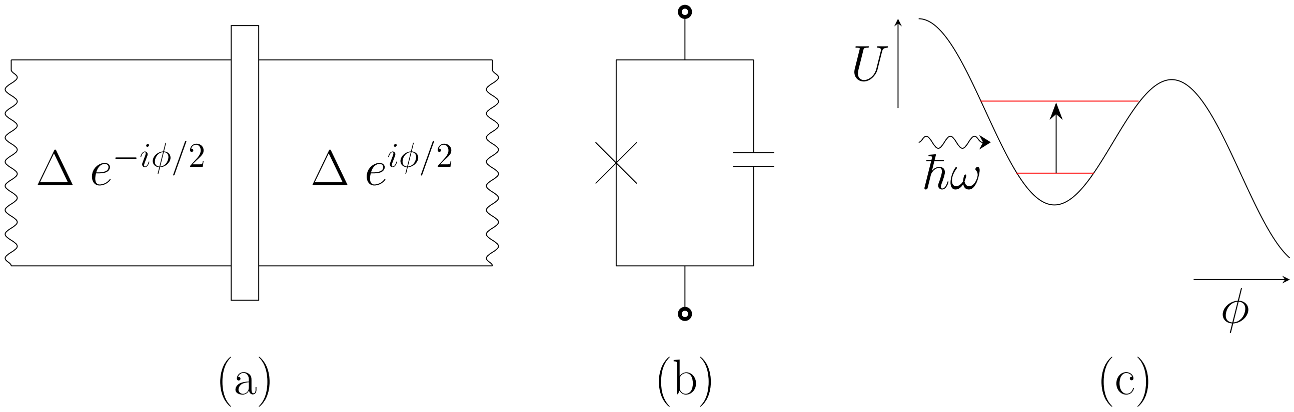

Figure 0.1: Schematic of a phase biased Josephson junction (panel (a)), circuit diagram of a circuit with a Josephson junction and a capacitance (panel (b)), and the quantized energy level of the tilted washboard potential in red highlighted by the experiment of Martinis, Devoret and Clarke in [4] (panel (c)). Irradiating the junction causes a particle to make a transition into an excited state changing its escape rate from the well.

A good qubit should possess long coherence times and high fidelity, maintaining its quantum state superposition accurately. It should be readable, allowing for accurate measurements. Interactions between qubits, control, low error rates, and robustness to noise and environmental factors are critical for reliable quantum computing. Meeting these requirements is essential for building efficient and practical quantum computing systems. Although semiconductor spin qubits as the one realized with silicon or with nitrogen-vacancy centers in diamond [11, 12] offer a relatively long coherence time exceeding μs and a size allowing for a high integration density, they lack the ability to realize and control the interaction between multiple spin qubits over long distances, which limits the increase in the number of qubits coupled together [13–16]. The difficulty in coupling multiple semiconductor spin qubits over long distances stems from the low spin magnetic moment of electrons. Also, the coherence time of these qubits is sensitive to the nuclear spin of the material used for their fabrication, as well as charge noise. In contrast, superconducting qubits offer a larger coupling, but are limited by their short coherence time [17–20]. These qubits exploit the Josephson effect, which makes them well suited for integration into electrical circuits. However, their coherence time is sensitive to variations in the electromagnetic environment around them. These fluctuations can induce decoherence, which prevents the qubits to maintain their quantum state over time. In general, superconducting qubits rely on the ratio between the Josephson energy and the capacitive energy. Hence, they are sensitive to charge noise and to flux noise. The two platforms appear to complement each other. Therefore, it is natural to want to find a way to combine their advantages.

One way to do this is to use Josephson junctions containing semiconductors. Although most superconducting qubits consist of tunnel junctions, it is possible to replace the thin insulating layer between the two superconductors with another material, such as a metal or a semiconductor. In those cases, we call the normal region a weak link in order to distinguish it from tunnel junctions. Regardless of the nature of this material, the property of supercurrent to be a periodic function of the superconducting phase difference remains [21, 22]. This reflects the fact that an arbitrary number of Cooper pairs are transferred coherently across the junction. A part of the current flowing in the junction originates from the contribution of the continuum of state above the superconducting gap, i.e., the energy range in which electrons pair up to form Cooper pairs. The other part of it comes from subgap states. A quasiparticle in the weak link cannot penetrate the superconducting electrodes if its energy is below the superconducting gap. At the interface between the two materials an incoming quasiparticle can be reflected "normally" as at any interface. But another phenomenon can occur. When an electron arrives at the interface, it can be reflected as a hole moving in the opposite direction in the normal region. In this way, a Cooper pair is transferred to the superconducting electrode. This particular phenomenon is called Andreev reflection [23]. In a Josephson junction, this hole can then undergo Andreev reflection at the other electrode and be converted back into an electron (see Fig. 0.2) and lead to a destruction of a Cooper pair in the electrode. This cycle allows Cooper pairs to transfer from one superconducting electrode to the other, creating a supercurrent across the junction. In the weak link, interference between the electron and the hole leads to the formation of bound states with quantized energies. They are referred to as the Andreev bound states (ABS) [23–26]. Being mainly localized in the weak link, these bound states inherit the electronic properties of this junction region. Since their theoretical description, Andreev bound states have been observed with spectroscopy experiments in various systems such as atomic contacts [27, 28], carbon nanotubes [29], and semiconductor nanowires [30, 31].

In tunnel junctions, which have many conduction channels of small transmission probability, the supercurrent arises from the collective behavior of ABS. Each of these states represents a degree of freedom that can be populated by electronic excitations, the Bogoliubons. However, due to their vast number and close energy proximity, manipulating them individually is impractical. In fact, each ABS detaches from the gap with a binding energy $\epsilon_{Bi} = \frac{\Delta\tau_i}{2}\sin^2\frac{\phi}{2}$ in the case of a short junction, i.e., when the length of the non-superconducting region is small compared to the characteristic size of a Cooper pair ξ, where

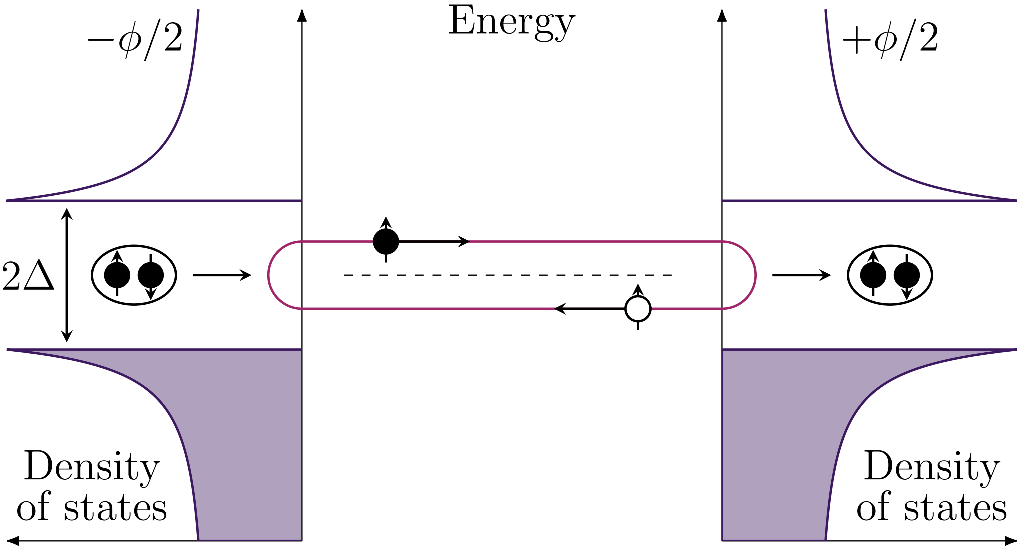

Figure 0.2: Schematic representation of an Andreev bound state between two superconducting reservoirs. The right moving electron in the normal region represented by a black dot is converted into a left moving hole represented by an empty dot due to Andreev reflection at the right superconducting interface. The reflected hole is converted into an electron at the other interface. This process allows for the transmission of a Cooper pair from the left to the right superconductor.

Δ is the superconducting gap, ϕ the phase difference and τ_i is the transmission probability of channel i. As one can see, if τ_i is small, then each ABS hardly detaches from the gap and disperses little with the phase. The current flowing in the junction is related to the energy by the relation $I = \frac{2e}{\hbar}\partial E/\partial\phi$, each ABS contributes to the total current giving rise to the Josephson effect. Nevertheless, in certain structures, a limited number of conduction channels with good transmission probability can be achieved, resulting in a set of well-separated Andreev levels. In this case, ABS may disperse more deeply into the superconducting gap and exhibit much more dispersion with the phase (see Fig. 0.3). Therefore, in a Josephson junction with high transmission conduction channels, each ABS may carry more current than an ABS of a tunnel junction. Using this current to couple the Josephson junction capacitively or inductively to a microwave resonator allows to detect and manipulate the quantum state of the junction. Experimentally, it is feasible to measure the resonant frequency of a specific resonator. When this resonator is coupled to a junction, it is observed that the quantum state of the junction impacts the resonant frequency. Furthermore, by applying a resonant signal that matches the energy gap between two states, it becomes possible to induce transitions between these states. For a resonator which is inductively coupled to the junction, this signal can be a microwave pulse sent through the resonator which will produce a phase fluctuation over the junction. We will refer to those as phase driven transitions. Another possibility is to drive the transitions by sending a microwave pulse on electrostatic gates placed below the normal region of the junction. We will therefore refer to these as gate driven transitions. Consequently, by measuring changes in the resonance frequency of the resonator and stimulating various potential transitions, it becomes feasible to reconstruct the excitation spectrum of the junction. These techniques serve as the foundation for circuit quantum electrodynamic experiments (cQED) [32] which were originally developed for readout and control of superconducting qubits.

In the junction ground state, all energy levels below the Fermi level are occupied by quasiparticles. Due to the spin degeneracy, the ground state of the junction is therefore populated by an even number of quasiparticles. Since the ground state is occupied by an even number of quasiparticles, the configuration in which this parity is maintained is called the even-parity sector. If the junction is driven out of equilibrium, transitions between different ABS can occur. For instance, a quasiparticle occupying one of the levels below the Fermi level can be promoted to a positive energy level. This transition is called a pair transition, as it results of a quasiparticle occupying the positive energy level and leaving the original level unoccupied (see left panel of Fig. 0.3). Another type of transition can be possible when a quasiparticle occupies a positive-energy ABS. If the junction has other ABSs, which is possible if the junction is of finite length, it can be excited or desexcited to one of them. This is called a single-particle transition (see left and middle panel of Fig. 0.3). An additional quasiparticle can also be trapped in an ABS. We often refer to this phenomenon as quasiparticle poisoning [33]. In this case, the junction is occupied by an odd number of quasiparticles. Therefore, this configuration is referred to as the odd parity sector.

Hybrid junctions composed of materials exhibiting strong spin-orbit coupling have garnered significant attention in recent years. This attention is particularly focused on the exploration of topological superconductivity and the investigation of non-abelian Andreev states known as Majorana zero modes [34–36]. The latter would benefit from topological protection which relies on non-local properties and are less sensitive to local variations or noise. These would make it possible to create qubits with very low noise sensitivity. With this type of qubit, a quantum computer with a low error rate would be possible. However, their experimental observation faces a number of challenges. Another utilization of the spin of a trapped quasiparticle, such that the junction resides in the odd parity sector, was proposed in 2003 as a support for quantum information called an Andreev spin qubit (ASQ) [37]. The first problem facing the realization of this type of qubit is the need to be in the odd parity sector. To be in this parity sector, a quasiparticle needs to be trapped within an Andreev level as explained above. The lifetime of this trapped quasiparticle can exceed the μs [33], thus limiting the maximum operating time of an ASQ. The other issue is that, to realize an ASQ, we need to lift the spin degeneracy of ABS. However, the theory describing ABS in a 1D system with spin-orbit coupling does not predict the lifting of the spin degeneracy without the use of a strong Zeeman field [38, 39], which can be detrimental to superconductivity. In fact, it is necessary to consider higher dimensional systems to achieve this effect. In this case, for a weak link of finite length with spin-orbit coupling and a finite phase difference due to a weak magnetic field breaking time reversal symmetry, it becomes possible to lift spin degeneracy even without the use of a Zeeman field [40–42]. Without spin degeneracy, new transitions are accessible. Thus, in addition to spin-conserving transitions, spin-flipping single-particle transitions become possible (see right panel of Fig. 0.3). These transitions have been used in cQED experiments on junctions made with InAs nanowires, highlighting the spin structure of Andreev bound states in this type of structure [43–45]. Ultimately, these experiments have paved the way for the realization of an ASQ.

The first realization of an ASQ was made in 2021 by the team of Michel Devoret [47]. In their experiment, they used a Josephson junction with an InAs nanowire coupled to a resonator. Their junction, which exhibits multiple doublets of ABS, due to the finite length of the weak link, allowed them to manipulate the spin of a trapped quasiparticle using two different doublets. Thus, by performing two phase-driven transitions, one conserving the spin and the other reversing it, they realized an ASQ. The second realization of an ASQ was made one year later [48]. Here, the authors used a more complex system made of a transmon coupled to an InAs/Al Josephson junction. With the use of electrostatic gates, they defined a quantum dot in the InAs region. The advantage of defining a quantum dot resides in the possibility to tune the Coulomb repulsion strength on the dot. Hence, with the appropriate tuning of the gates, it becomes possible to favor a ground state with an odd number of electrons occupying the dot. In addition, they used a fixed external magnetic field in order to increase the energy splitting between opposite spin states, allowing for an easier manipulation of the qubit. In this configuration, they were able to directly manipulate the spin states of the doublet ground state via electric dipole spin resonance by sending a microwave pulse into one of the gates. This technique refers to the fact that an oscillating electric field can

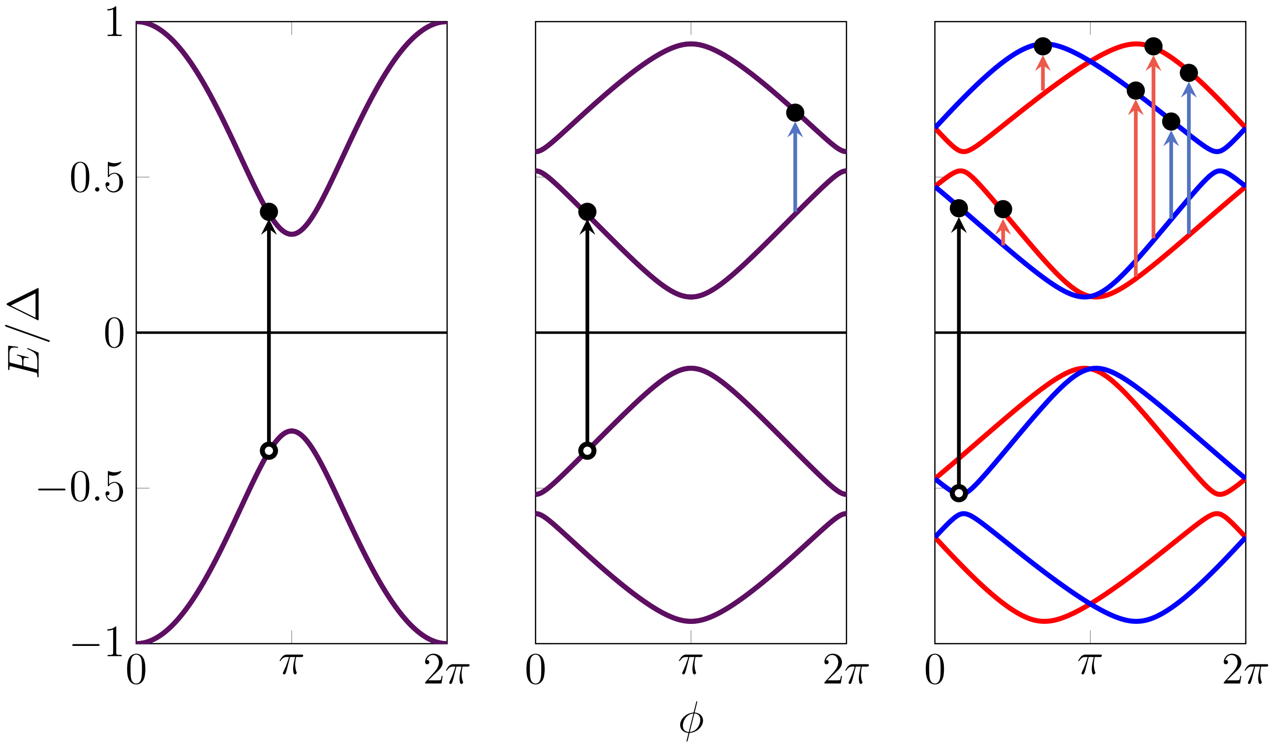

Figure 0.3: ABS energy spectrum for different Josephson junctions. The left panel corresponds to the spectrum of a short junction such as an atomic contact Josephson junction. The middle panel corresponds to the scenario of a finite length Josephson junction. The right panel is for a finite length junction with spin-orbit coupling. In right panel, red curves correspond to pseudo-spin up states whereas blue curves correspond to pseudo-spin down states (see discussion in [46]). Black arrows show pair transitions between the ground state and one excited state. Light blue arrows show spin conserving single particle transitions, whereas light red arrows show spin-flip single particle transitions. Occupied states above Fermi level are represented by black dots whereas unoccupied states below Fermi level by empty dots.

be coupled to the spin of an electron thanks to spin-orbit coupling. This coupling between field and spin then allows to control the dynamics of the latter. In both experiments, they reach coherence time on the order of tens of nanoseconds. This short coherence time seems to be limited by the nuclear environment, i.e., the nuclear spin of InAs, a problem that is already known for the realization of semiconductors spin qubits. Thus, as pointed out in [48], the coherence time could be increased with the use of nuclear-spin-free semiconductors. Although the spin structure of this type of junction has been demonstrated, as well as the realization of ASQ, the observation and manipulation of the spin within the lowest energy doublet , which constitutes the qubit's basis, have not yet been achieved in phase-driven experiments. This transition has only been observed in gate-driven experiments. However, it should also be possible to drive this transition with the phase.

It is in this context that this thesis is inscribed. If the intra-doublet transition has not yet been used in phase-driven experiments, this is partly due to the fact that it was considered impossible. The quantity that determines whether this transition is possible is the current operator. Thus, the non-diagonal matrix elements of this operator are directly related to the transitions accessible in cQED experiments. Without a magnetic field, the non-diagonal elements between the two spin states within the lowest energy doublet were predicted to be zero. However, they can be made non-zero by spin-flip scattering processes. These processes can occur when a potential presents an asymmetry in the transverse direction of the normal region. This potential may be the result of a potential applied by a gate, or it may be due to the presence of impurities [45, 47]. Therefore, in this thesis, we have studied spin-split ABS and the effect of spin-flip processes on their energy spectrum and associated current operator matrix elements. In addition to indicating whether a transition is possible or not, the off diagonal elements are also related to the magnitude of the frequency shift and resonance linewidth in microwave spectroscopy experiments, as well as the Rabi oscillation for a driven transition [49–51]. We have first studied a Josephson junction with a Rashba nanowire and an asymmetrical potential. By modeling the asymmetric potential by a delta barrier potential, we have shown how spin-flip transmission through the barrier acts on the energy spectrum and allows to have finite off-diagonal matrix elements of the current operator between opposite spin states. We have also studied a Josephson junction whose normal region consists of two coupled quantum dots, which present the advantage of allowing to control the parity of the ground state. In this system, the combination of a coupling between the dots and a spin-dependent coupling between the dots and the superconducting electrodes also allows, in the odd parity sector, to obtain a spin-degeneracy-free energy spectrum and finite matrix elements for the current operator between opposite spin states (see Fig. 0.4).

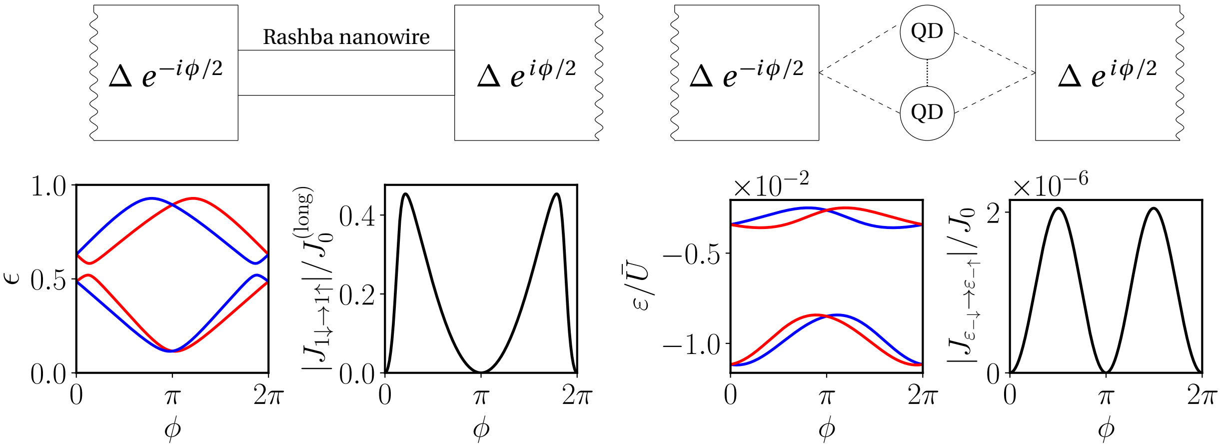

(a)

(b)

Figure 0.4: Energy spectrum and some matrix elements of the current operator for each with the corresponding junction shown above. In the panel (a), the energy spectrum is normalized by the superconducting gap. In the panel (b), the energy spectrum shown is the one of the two lowest energy doublets of the dots normalized by the mean of the Coulomb repulsion strength of each dot. On both panel red lines correspond to spin up states and blue lines to spin down states. Due to SOC, the spin degeneracy of these states is lifted for phases different from $\phi = n\pi$ with $n \in \mathbb{N}$. For each panel, the matrix element of the current operator for the intra-doublet transition within the lowest energy doublet is shown in black. For both junctions, the magnitude of this matrix element is maximal when the splitting between the two spin states of the doublet is also maximal. These two junctions are studied in Chap. 2 and Chap. 3.

This thesis is organized as follows.

In chapter 1, we will present the required physics basis for understanding the work presented here. We start by presenting the BCS theory which describes superconducting materials. We then discuss the Josephson effect, Andreev reflection and Andreev bound states, which are the key ingredients for the realization of Andreev spin qubit. Finally, we study two Josephson junction systems for the remainder of this manuscript. The first one is the superconductor - normal - superconductor (S-N-S) Josephson junction and the second one is the superconductor - quantum dot - superconductor (S-QD-S).

In chapter 2, we study ABS in a Josephson junction with a Rashba nanowire. We first show what are the important ingredients in order to obtain a spin-splitting of ABS, as well as the key mechanism in order to manipulate the spin in flux-driven experiments. Next, we present analytical and numerical results of the relevant quantities, i.e., the energy spectrum and the current operator matrix elements of this kind of junction.

In chapter 3, we present another Josephson junction circuit made with two coupled quantum dots. We begin by presenting why a single quantum dot junction is insufficient to lift the spin degeneracy. We then proceed with the study of the energy spectrum in such junctions. By using an effective model, we finally determine the minimal set of ingredients in order to lift the spin degeneracy, and, to have finite matrix elements of the current operator between opposite spin states which we obtained numerically.

We finally conclude and provide perspectives.

CHAPTER 1

Superconductivity, Josephson effect and Andreev bound states

Contents

In this chapter, we present important physical theories that are necessary for the understanding of this thesis. Superconductivity being present in all the devices being studied in this thesis, we will start by discussing the theory of Bardeen, Cooper and Schrieffer (BCS theory) in Sec. 1.1 which describes the microscopic mechanism of superconductivity [52]. We will also present the mean field approximation and Bogoliubov-de Gennes (BdG) Hamiltonian in Sec. 1.1.2, which allows one to find the eigenenergies and eigenstates of a superconductor. To derive those results, we follow the books of Tinkham [53], Asano [54], and the notes of Carsten Timm [55]. Then, since this manuscript is mainly focused on the study of ABS, the other sections will be dedicated to it. The energy spectrum and current operator matrix elements of ABS being dependent on the scattering in the normal region, we will introduce the scattering formalism in Sec. 1.2. Finally, we will study the energy spectrum of ABS in S-N-S junctions in Sec. 1.3 and of S-QD-S junctions in Sec. 1.4.

1.1 BCS theory and Bogoliubov-de Gennes Hamiltonian

Superconductivity is a state of matter in which electrons form pairs due to an effective attractive potential between them. In this manuscript, we will only study devices with conventional superconductors called BCS superconductors. This name comes from the initials of Bardeen, Cooper and Schrieffer, who established a microscopic theory to describe them [52]. In this section, we will therefore present the BCS theory and then use the mean field approximation leading to the BdG Hamiltonian, which allows one to obtain the eigenenergies and eigenstates of a superconductor.

1.1.1 BCS theory

The BCS theory describes superconductors in which the pairs are formed between two electrons on the Fermi surface with opposite spins and momenta thanks to a weak attractive interaction between them. The idea that even a weak attraction can bind pairs of electrons was presented by Cooper in 1956 [56]. He showed that the Fermi sea is unstable against the formation of at least one bound pair, regardless of how weak the attractive interaction is if it exists. In superconductors, the Coulomb interaction between electrons is still present but, is being dominated by the attractive one. This interaction is mediated by the phonons of the crystal. To understand how this phonon-mediated interaction leads to the formation of the so-called Cooper pairs, we can use a simple picture. At very low temperatures, the ions forming the crystal lattice are almost immobile (no vibrations around their equilibrium position). So when an electron moves in this crystal, it attracts the surrounding ions. Due to the stiffness of this lattice, after the electron has passed, the lattice remains locally deformed, creating an attractive potential for another electron as shown in Fig. 1.1. The result is a non-zero correlation between these two electrons. In this way, we can explain why electrons form pairs thanks to this non-instantaneous attractive potential. The idea that the electron-lattice interaction is important to explain superconductivity was first suggested by Fröhlich in 1950 [57]. This suggestion was confirmed experimentally by the discovery of the isotope effect, i.e., the dependence of the critical temperature T_c and critical magnetic field H_c on the mass of isotopes of the same element [58, 59].

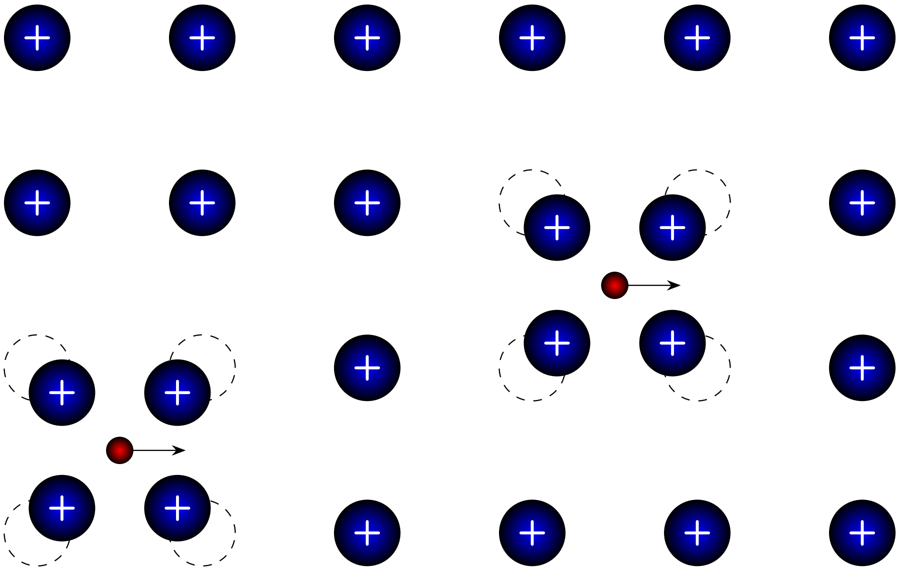

Figure 1.1: Schematic representation of the lattice deformation due to the passage of electrons.

An accurate description of this phenomenon involves quantum mechanics. We can write the Hamiltonian which describes a superconductor as $H = H_0 + H_I$, where H_0 describes the free electrons within a periodic lattice potential and H_I the interaction between them when the lattice is deformed, giving rise to the attractive interaction. In second quantization, we write H_0 as

$$H_0 = \sum_{\alpha} \int \mathrm{d}\boldsymbol{r} \Psi^{\dagger}_{\alpha}(\boldsymbol{r}) \left[-\frac{\hbar^2 \nabla^2}{2m} - E_F \right] \Psi_{\alpha}(\boldsymbol{r}), \tag{1.1}$$

where α stands for the spin degree of freedom of the electron and Ψ_{α} is its associated field operator. E_F is the Fermi energy, representing the energy of the highest energy occupied electron state at zero temperature. m is the effective mass of electrons which takes into account the interactions of electrons with the periodic lattice. The interaction Hamiltonian H_I can be written as

$$H_I = \frac{1}{2} \sum_{\alpha\beta} \int \mathrm{d}\boldsymbol{r} \int \mathrm{d}\boldsymbol{r}' \Psi^{\dagger}_{\alpha}(\boldsymbol{r}) \Psi^{\dagger}_{\beta}(\boldsymbol{r}') V(\boldsymbol{r} - \boldsymbol{r}') \Psi_{\beta}(\boldsymbol{r}') \Psi_{\alpha}(\boldsymbol{r}), \tag{1.2}$$

where V is the effective nonlocal interaction potential, which combines the effect of the Coulomb interaction as well as the interaction arising from the deformation of the lattice. Since electrons are fermions, their associated field operators follow the anticommutation relations

$$\left\{ \Psi_{\alpha}(\boldsymbol{r}), \Psi^{\dagger}_{\beta}(\boldsymbol{r}') \right\} = \delta_{\alpha,\beta} \delta(\boldsymbol{r} - \boldsymbol{r}'), \tag{1.3}$$

$$\left\{ \Psi_{\alpha}(\boldsymbol{r}), \Psi_{\beta}(\boldsymbol{r}') \right\} = 0. \tag{1.4}$$

To diagonalize the single-particle Hamiltonian H_0, we can go to momentum space using the Fourier transformation which leads to

$$\Psi_{\alpha}(\boldsymbol{r}) = \frac{1}{\sqrt{\mathscr{V}_{\mathrm{vol}}}} \sum_{\boldsymbol{k}} c_{\boldsymbol{k},\alpha} e^{i\boldsymbol{k}.\boldsymbol{r}}, \tag{1.5}$$

where $\mathscr{V}_{\mathrm{vol}}$ is the volume of the solid. The normalization condition and completeness of the basis requires

$$\frac{1}{\mathscr{V}_{\mathrm{vol}}} \int \mathrm{d}\boldsymbol{r}\, e^{i(\boldsymbol{k}-\boldsymbol{k}').\boldsymbol{r}} = \delta_{\boldsymbol{k},\boldsymbol{k}'}, \tag{1.6}$$

$$\frac{1}{\mathscr{V}_{\mathrm{vol}}} \sum_{\boldsymbol{k}} e^{i\boldsymbol{k}.(\boldsymbol{r}-\boldsymbol{r}')} = \frac{1}{(2\pi)^d} \int \mathrm{d}\boldsymbol{k}\, e^{i\boldsymbol{k}.(\boldsymbol{r}-\boldsymbol{r}')} = \delta(\boldsymbol{r} - \boldsymbol{r}'), \tag{1.7}$$

with d the spatial dimension of the solid. Using these relations, we can find the anticommutation relations for the fermionic operators in momentum space

$$\left\{ c_{\boldsymbol{k},\alpha}, c^{\dagger}_{\boldsymbol{k}',\beta} \right\} = \delta_{\alpha,\beta} \delta_{\boldsymbol{k},\boldsymbol{k}'}, \tag{1.8}$$

$$\left\{ c_{\boldsymbol{k},\alpha}, c_{\boldsymbol{k}',\beta} \right\} = 0. \tag{1.9}$$

We now need to apply the Fourier transformation to the single-particle and the interaction Hamiltonian. For the single-particle Hamiltonian, it leads to

$$H_0 = \sum_{\alpha} \sum_{\boldsymbol{k}} \xi_{\boldsymbol{k}} c^{\dagger}_{\boldsymbol{k},\alpha} c_{\boldsymbol{k},\alpha}, \tag{1.10}$$

where

$$\xi_{\boldsymbol{k}} = \frac{\hbar^2 \boldsymbol{k}^2}{2m} - E_F \tag{1.11}$$

describes the kinetic energy of an electron relative to the Fermi level. For the interaction Hamiltonian, we first need to introduce the Fourier transform of the interaction potential. It reads,

$$V(\boldsymbol{r}) = \frac{1}{\mathscr{V}_{\text{vol}}} \sum_{\boldsymbol{q}} V_{\boldsymbol{q}} e^{i\boldsymbol{q}.\boldsymbol{r}}. \tag{1.12}$$

Using the previous relations, we can now write the total Hamiltonian in the momentum space as

$$H = \sum_{\alpha} \sum_{\boldsymbol{k}} \xi_{\boldsymbol{k}} c^{\dagger}_{\boldsymbol{k},\alpha} c_{\boldsymbol{k},\alpha} + \frac{1}{2\mathscr{V}_{\text{vol}}} \sum_{\alpha,\beta} \sum_{\boldsymbol{k}_1,\boldsymbol{k}_2,\boldsymbol{q}} c^{\dagger}_{\boldsymbol{k}_1+\boldsymbol{q},\alpha} c^{\dagger}_{\boldsymbol{k}_2-\boldsymbol{q},\beta} V_{\boldsymbol{q}} c_{\boldsymbol{k}_2,\beta} c_{\boldsymbol{k}_1,\alpha}. \tag{1.13}$$

The second term of this Hamiltonian describes the interaction between the two electrons. These two electrons come with momentum $\boldsymbol{k}_1$ and $\boldsymbol{k}_2$, they undergo the effective interaction which results in a transfer of momentum $\boldsymbol{q}$ from one electron to the other such that their momenta become $\boldsymbol{k}_1 + \boldsymbol{q}$ and $\boldsymbol{k}_2 - \boldsymbol{q}$. As we said at the beginning of this section, the pairing occurs between electrons of opposite spins and momenta. We will impose another condition in order to simplify the interaction. The main property that is required is that the interaction is attractive. Even though the effective interaction in the Hamiltonian does not contain information about its source, we assume here that this attractive interaction results from the electron-phonon interaction. Therefore, we can assume that in this case, the interaction is attractive for frequencies below the Debye frequency, which is the typical phonon frequency. The conditions we impose are the following,

- The attraction is between two electrons of opposite spins $\beta = -\alpha$ and opposite momenta $\boldsymbol{k}_2 = -\boldsymbol{k}_1$.
- The two electrons have energies in an energy window near the Fermi level E_F and delimited by the Debye energy $\hbar\omega_D$.
- In this energy window, the interaction is attractive and independent of momenta, therefore, $V_{\boldsymbol{q}} = -V$ with V a positive constant.

This last condition implies that from here we make the approximation that the potential is local in the real space. With all of these conditions satisfied, we can finally write the BCS Hamiltonian which reads

$$H_{\text{BCS}} = \sum_{\alpha} \sum_{\boldsymbol{k}} \xi_{\boldsymbol{k}} c^{\dagger}_{\boldsymbol{k},\alpha} c_{\boldsymbol{k},\alpha} - \frac{V}{\mathscr{V}_{\text{vol}}} \sum_{\boldsymbol{k},\boldsymbol{k}'} c^{\dagger}_{-\boldsymbol{k}',\downarrow} c^{\dagger}_{\boldsymbol{k}',\uparrow} c_{\boldsymbol{k},\uparrow} c_{-\boldsymbol{k},\downarrow} \Theta(\hbar\omega_D - |\xi_{\boldsymbol{k}}|) \Theta(\hbar\omega_D - |\xi_{\boldsymbol{k}'}|), \tag{1.14}$$

where $\Theta(x)$ is the Heaviside function defined such that

$$\Theta(x) = \begin{cases} 0 & x < 0, \\ 1 & x > 0 \end{cases}. \tag{1.15}$$

The idea of Bardeen, Cooper and Schrieffer was that due to the attractive interaction, the ground state of the system is modified. They proposed the ansatz that, in this ground state, the states $|\boldsymbol{k},\uparrow\rangle$ and $|-\boldsymbol{k},\downarrow\rangle$ form so-called Cooper pairs. The resulting ground state is therefore a superposition of states built up of such pairs. In particular, they proposed that either the states $|\boldsymbol{k},\uparrow\rangle$ and $|-\boldsymbol{k},\downarrow\rangle$ are occupied or empty allowing to write the wavefunction in the form

$$|\Psi\rangle_{\text{BCS}} = \prod_{k} \left(u_{\boldsymbol{k}} + v_{\boldsymbol{k}} c^{\dagger}_{\boldsymbol{k},\uparrow} c^{\dagger}_{-\boldsymbol{k},\downarrow} \right) |0\rangle, \tag{1.16}$$

where $|0\rangle$ is the vacuum state without any electrons and $u_{\boldsymbol{k}}$, $v_{\boldsymbol{k}}$ are complex coefficients verifying $|u_{\boldsymbol{k}}|^2 + |v_{\boldsymbol{k}}|^2 = 1$. Such a ground state is peculiar since it is a superposition of states with a different number of electrons, meaning that the number of electrons can fluctuate. A consequence of this is that expressions with an unequal number of electronic creation or destruction operators can have non-vanishing expectation values. This property will be of use in the next section in order to diagonalize the BCS Hamiltonian.

1.1.2 Mean field approximation and BdG Hamiltonian

The interaction term in the BCS Hamiltonian (1.14) is quartic and cannot be diagonalized. It is therefore necessary to simplify it in order to obtain the eigenenergies and eigenstates. To do so, we can use the mean field approximation. This approximation assumes that the fluctuations of the electronic creation and destruction operators around their mean values are small. We thus introduce the average of these operators as

$$\Delta e^{i\varphi} \equiv \frac{V}{\mathscr{V}_{\text{vol}}} \sum_{\boldsymbol{k}} \left\langle c_{\boldsymbol{k},\uparrow} c_{-\boldsymbol{k},\downarrow} \right\rangle \Theta(\hbar\omega_D - |\xi_{\boldsymbol{k}}|), \tag{1.17}$$

where $\Delta e^{i\varphi}$ is referred to as the pair potential or superconducting order parameter, with $\Delta > 0$. This order parameter can only be non-zero if the mean value $\left\langle c_{\boldsymbol{k},\uparrow} c_{-\boldsymbol{k},\downarrow} \right\rangle$ is non-zero, which is the case with the ground state proposed by Bardeen, Cooper, and Schrieffer. This pair potential describes the Cooper pairs and is antisymmetric under permutation of the two spins. One can relate this pair potential to the typical size of a Cooper pair, ξ_{BCS} through the relation

$$\xi_{\text{BCS}} = \frac{\hbar v_F}{\pi \Delta} \tag{1.18}$$

where v_F is the Fermi velocity. This length scale is particularly useful for describing the temperature dependence of the superconducting phase transition characterized by the divergence of ξ_{BCS}. We can now start to rewrite the BCS Hamiltonian using the average values of the operators. For that, we write

$$c_{\boldsymbol{k},\uparrow} c_{-\boldsymbol{k},\downarrow} = \left\langle c_{\boldsymbol{k},\uparrow} c_{-\boldsymbol{k},\downarrow} \right\rangle + \left[c_{\boldsymbol{k},\uparrow} c_{-\boldsymbol{k},\downarrow} - \left\langle c_{\boldsymbol{k},\uparrow} c_{-\boldsymbol{k},\downarrow} \right\rangle \right], \tag{1.19}$$

$$c^\dagger_{-\boldsymbol{k},\downarrow} c^\dagger_{\boldsymbol{k},\uparrow} = \left\langle c^\dagger_{-\boldsymbol{k},\downarrow} c^\dagger_{\boldsymbol{k},\uparrow} \right\rangle + \left[c^\dagger_{-\boldsymbol{k},\downarrow} c^\dagger_{\boldsymbol{k},\uparrow} - \left\langle c^\dagger_{-\boldsymbol{k},\downarrow} c^\dagger_{\boldsymbol{k},\uparrow} \right\rangle \right]. \tag{1.20}$$

The terms $\left\langle c^\dagger_{-\boldsymbol{k},\downarrow} c^\dagger_{\boldsymbol{k},\uparrow} \right\rangle$ can be obtained by taking the hermitian conjugate of Eq. (1.17). Under this form, it allows one to identify the first terms as the average values of the operators, and the second terms as the fluctuations around these average values. By keeping only the first order term in fluctuations, we obtain for the interacting part of the BCS Hamiltonian

$$\tilde{\sum_{\boldsymbol{k},\boldsymbol{k}'}} c^\dagger_{-\boldsymbol{k}',\downarrow} c^\dagger_{\boldsymbol{k}',\uparrow} c_{\boldsymbol{k},\uparrow} c_{-\boldsymbol{k},\downarrow} \approx -\frac{\mathscr{V}_{\text{vol}}\Delta^2}{V^2} + \frac{\mathscr{V}_{\text{vol}}}{V} \tilde{\sum_{\boldsymbol{k}}} \left[\Delta e^{-i\varphi} c_{\boldsymbol{k},\uparrow} c_{-\boldsymbol{k},\downarrow} + \Delta e^{i\varphi} c^\dagger_{-\boldsymbol{k},\downarrow} c^\dagger_{\boldsymbol{k},\uparrow} \right], \tag{1.21}$$

where we have introduced the notation

$$\tilde{\sum_{\boldsymbol{k}}} = \sum_{\boldsymbol{k}} \Theta(\hbar\omega_D - |\xi_{\boldsymbol{k}}|). \tag{1.22}$$

The mean field Hamiltonian is thus given as

$$H_{\text{MF}} = \sum_{\alpha} \sum_{\boldsymbol{k}} \xi_{\boldsymbol{k}} c^\dagger_{\boldsymbol{k},\alpha} c_{\boldsymbol{k},\alpha} - \frac{\mathscr{V}_{\text{vol}}}{V} \tilde{\sum_{\boldsymbol{k}}} \left[\Delta e^{-i\varphi} c_{\boldsymbol{k},\uparrow} c_{-\boldsymbol{k},\downarrow} + \Delta e^{i\varphi} c^\dagger_{-\boldsymbol{k},\downarrow} c^\dagger_{\boldsymbol{k},\uparrow} \right] + \frac{\mathscr{V}_{\text{vol}}\Delta^2}{V^2}. \tag{1.23}$$

In the latter, we will drop the notation $\tilde{\sum}$ in order to simplify a bit the notations, but one has to keep in mind the energy window restriction such when needed in order to obtain a finite result. By introducing the Nambu spinor,

$$C_{\boldsymbol{k}} \equiv \begin{pmatrix} c_{\boldsymbol{k},\uparrow} \\ c^\dagger_{-\boldsymbol{k},\downarrow} \end{pmatrix}, \tag{1.24}$$

we write the mean field Hamiltonian in the form

$$\begin{aligned} H_{\mathrm{MF}} &= \sum_{\boldsymbol{k}} C_{\boldsymbol{k}}^{\dagger} \begin{pmatrix} \xi_{\boldsymbol{k}} & \Delta e^{i\varphi} \\ \Delta e^{-i\varphi} & -\xi_{-\boldsymbol{k}} \end{pmatrix} C_{\boldsymbol{k}} + \xi_{\boldsymbol{k}} + \frac{\mathscr{V}_{\mathrm{vol}}\Delta^2}{V^2}, \\ &= \sum_{\boldsymbol{k}} C_{\boldsymbol{k}}^{\dagger} H_{\mathrm{BdG}} C_{\boldsymbol{k}} + \xi_{\boldsymbol{k}} + \frac{\mathscr{V}_{\mathrm{vol}}\Delta^2}{V^2}, \end{aligned} \tag{1.25}$$

where we introduced the Bogoliubov-de Gennes Hamiltonian H_{BdG} [60]

$$H_{\mathrm{BdG}} = \begin{pmatrix} \xi_{\boldsymbol{k}} & \Delta e^{i\varphi} \\ \Delta e^{-i\varphi} & -\xi_{-\boldsymbol{k}} \end{pmatrix}. \tag{1.26}$$

The eigenvalues of this Hamiltonian allow us to obtain the eigenenergies up to a constant offset energy. Note that here we have $\xi_{-\boldsymbol{k}} = \xi_{\boldsymbol{k}}$ because we consider here a parabolic dispersion. The two eigenvalues $\pm E_{\boldsymbol{k}}$ are given as

$$E_{\boldsymbol{k}} = \sqrt{\xi_{\boldsymbol{k}}^2 + \Delta^2}. \tag{1.27}$$

We can see from this equation that the energy dispersion is gapped by 2Δ. For this reason, Δ is called the superconducting gap (see Fig.1.2). The associated eigenvectors are

$$\psi_{\boldsymbol{k},+} = \begin{pmatrix} u_{\boldsymbol{k}} e^{i\frac{\varphi}{2}} \\ v_{\boldsymbol{k}} e^{-i\frac{\varphi}{2}} \end{pmatrix}, \qquad \psi_{\boldsymbol{k},-} = \begin{pmatrix} -v_{\boldsymbol{k}} e^{i\frac{\varphi}{2}} \\ u_{\boldsymbol{k}} e^{-i\frac{\varphi}{2}} \end{pmatrix}, \tag{1.28}$$

where $\psi_{\boldsymbol{k},+}$ is associated with $E_{\boldsymbol{k}}$ and $\psi_{\boldsymbol{k},-}$ with $-E_{\boldsymbol{k}}$. The components of the two eigenvectors are given as

$$u_{\boldsymbol{k}} = \sqrt{\frac{1+\xi_{\boldsymbol{k}}/E_{\boldsymbol{k}}}{2}}, \qquad v_{\boldsymbol{k}} = \sqrt{\frac{1-\xi_{\boldsymbol{k}}/E_{\boldsymbol{k}}}{2}}. \tag{1.29}$$

Those coefficients verify $u_{\boldsymbol{k}}^2 + v_{\boldsymbol{k}}^2 = 1$, which allows one to verify the normalization condition of the two wavefunctions $|\psi_{\boldsymbol{k},+}|^2 = |\psi_{\boldsymbol{k},-}|^2 = 1$. In fact, one can show that these two coefficients correspond to the ones of the BCS ground state of Eq. (1.16). The Bogoliubov-de Gennes Hamiltonian also presents another property called particle-hole symmetry. This symmetry indicates that for every state ψ with energy $E_{\boldsymbol{k}}$, it exists an accompanying state $\mathcal{P}\psi$ with energy $-E_{\boldsymbol{k}}$, with $\mathcal{P}$ the particle-hole symmetry operator. We can easily see this with the states $\psi_{\boldsymbol{k},+}$ and $\psi_{\boldsymbol{k},-}$. These two states have opposite energies and are related through

$$\psi_{\boldsymbol{k},-} = -i\tau_y \mathcal{C}\psi_{\boldsymbol{k},+} = \mathcal{P}\psi_{\boldsymbol{k},+}, \tag{1.30}$$

where τ_y is the Pauli matrix in Nambu space and $\mathcal{C}$, the complex conjugation operator. This symmetry implies that the Bogoliubov-de Gennes Hamiltonian verifies

$$\mathcal{P} H_{\mathrm{BdG}} \mathcal{P}^{-1} = -H_{\mathrm{BdG}}. \tag{1.31}$$

We now introduce new operators using the Bogoliubov transformations [61, 62]

$$\gamma_{\boldsymbol{k},\sigma} = u_{\boldsymbol{k}} c_{\boldsymbol{k},\sigma} e^{-i\frac{\varphi}{2}} + \sigma v_{\boldsymbol{k}} c_{-\boldsymbol{k},-\sigma}^{\dagger} e^{i\frac{\varphi}{2}}, \tag{1.32}$$

such that we can write the mean field Hamiltonian in a diagonal form

$$H_{\mathrm{MF}} = \sum_{\boldsymbol{k}} \begin{pmatrix} \gamma_{\boldsymbol{k},\uparrow}^{\dagger} & \gamma_{-\boldsymbol{k},\downarrow} \end{pmatrix} \begin{pmatrix} E_{\boldsymbol{k}} & 0 \\ 0 & -E_{\boldsymbol{k}} \end{pmatrix} \begin{pmatrix} \gamma_{\boldsymbol{k},\uparrow} \\ \gamma_{-\boldsymbol{k},\downarrow}^{\dagger} \end{pmatrix} + \xi_{\boldsymbol{k}} + \frac{\mathscr{V}_{\mathrm{vol}}\Delta^2}{V^2}. \tag{1.33}$$

The quasiparticle created by those new operators is a superposition of the creation of an electron with amplitude u and the destruction of another with amplitude v. Since it involves the destruction of one electron, we often refer to those quasi-particles as a superposition of an electron and a hole. We named those quasiparticles as bogoliubons in reference to the Bogoliubov transformation used to write them. We can check that those operators follow the anticommutation rules for fermions

$$\left\{\gamma_{\boldsymbol{k},\sigma}, \gamma_{\boldsymbol{k}',\sigma'}\right\} = 0, \tag{1.34}$$

$$\left\{\gamma_{\boldsymbol{k},\sigma}, \gamma_{\boldsymbol{k}',\sigma'\dagger}\right\} = \delta_{\sigma,\sigma'}\delta_{\boldsymbol{k},\boldsymbol{k}'}. \tag{1.35}$$

The superconducting ground state is defined as follows,

$$\gamma_{\boldsymbol{k},\sigma}\left|0\right\rangle = 0, \tag{1.36}$$

such that the creation of a bogoliubon corresponds to an elementary excitation in a BCS superconductor. Now, we will determine the value of the pair potential Δ. We can find it in a self-consistent way. First, using its definition in Eq. (1.17), we can write it using the Bogoliubov transformation as

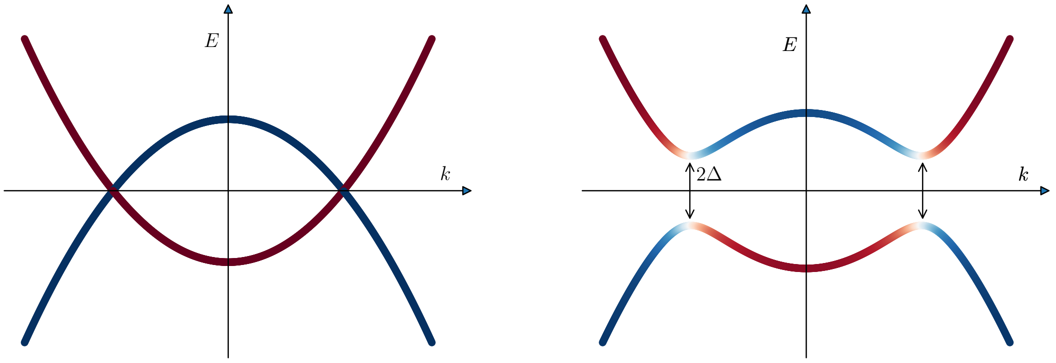

Figure 1.2: Bands structure for obtained with H_{BdG}. In panel (a), we consider a parabolic dispersion in the normal state, i.e. $\Delta = 0$. In this case, the band in red is for electrons while the one in blue is for holes. In panel (b), the pairing leads to a finite coupling between the two bands which results in a gap between them. The finite coupling implies a mixing between the electron and hole character of quasiparticles. Hence, a more reddish color indicates a larger electron amplitude while a more blue-tinted color indicates a larger hole amplitude.

$$\Delta e^{i\varphi} = \frac{V}{\mathscr{V}_{\mathrm{vol}}}\sum_{\boldsymbol{k}} u_{\boldsymbol{k}} v_{\boldsymbol{k}} e^{i\varphi}(1-2f(E_{\boldsymbol{k}})) = \frac{V}{\mathscr{V}_{\mathrm{vol}}}\sum_{\boldsymbol{k}} \frac{\Delta e^{i\varphi}}{2E_{\boldsymbol{k}}}\tanh\left(\frac{E_{\boldsymbol{k}}}{2k_B T}\right), \tag{1.37}$$

where we used the relations

$$\left\langle \gamma^{\dagger}_{\boldsymbol{k},\sigma}\gamma_{\boldsymbol{k}',\sigma'}\right\rangle = f(E_{\boldsymbol{k}})\delta_{\boldsymbol{k},\boldsymbol{k}'}\delta_{\sigma,\sigma'}, \qquad \left\langle \gamma_{\boldsymbol{k},\sigma}\gamma_{\boldsymbol{k}',\sigma'}\right\rangle = 0, \tag{1.38}$$

with $f(E) = (1+\exp[E/(k_B T)])^{-1}$, the Fermi distribution function. The amplitude of Δ is obtained by solving the gap equation (1.37). In order to do this calculation, we introduce the density of states per volume and per spin

$$\nu(\xi) = \frac{1}{\mathscr{V}_{\mathrm{vol}}}\sum_{\boldsymbol{k}}\delta(\xi - \xi_{\boldsymbol{k}}). \tag{1.39}$$

Transforming the sum of (1.37) into an integral, we obtain

$$1 = V \int_0^{\hbar\omega_D} \mathrm{d}\xi \frac{\nu(\xi)}{\sqrt{\xi^2+\Delta^2}} \tanh\left(\frac{\sqrt{\xi^2+\Delta^2}}{2k_B T}\right). \tag{1.40}$$

At zero temperature, we can approximate this integral as

$$1 \approx V\nu_0 \ln(2\hbar\omega_D/\Delta_0), \tag{1.41}$$

where ν_0 is the density of states at the Fermi level per unit volume and spin in the normal state and Δ_0, the pair potential at zero temperature, is given as

$$\Delta_0 = 2\hbar\omega_D e^{-1/(V n_0)}. \tag{1.42}$$

We can also determine the critical temperature T_c, i.e., the temperature at which the transition between the normal and the superconducting state occurs. For that, we can take the limit $\Delta \to 0$ in the gap equation. It leads to

$$1 = V\nu_0 \ln\left(\frac{2\hbar\omega_D\gamma_0}{\pi k_B T_c}\right), \tag{1.43}$$

where we considered $\hbar\omega_D \gg T_c$ and used the Euler constant $\ln(\gamma_0) \approx 0.577$. Thus, we obtain

$$T_c = \frac{\gamma_0}{\pi k_B}\Delta_0 \tag{1.44}$$

The general temperature dependence of the gap is shown in Fig. 1.3. Finally, we can look at the density of states in superconductors. This density of states is given as

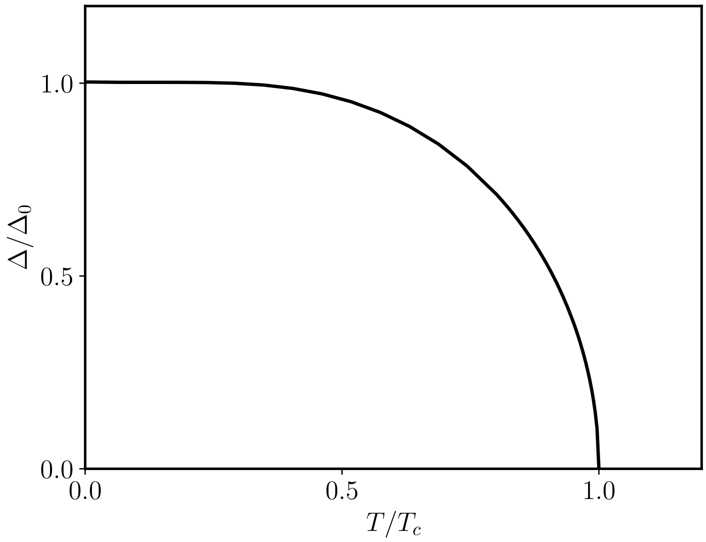

Figure 1.3: Temperature dependence of the superconducting gap.

$$\nu_S(E) = \frac{dN}{dE}. \tag{1.45}$$

The subscripts "S" stands for superconducting and N is the total number of states with energy less than E. We find,

$$\begin{aligned}\nu_S(E) &= \frac{dN}{d\xi}\frac{d\xi}{dE},\\ &= \nu_0\frac{d}{dE}\sqrt{E^2-\Delta^2},\\ &= \nu_0\frac{E}{\sqrt{E^2-\Delta^2}}\end{aligned} \tag{1.46}$$

So, we can summarize

$$\nu_S(E) = \begin{cases} 0 & \text{for } 0 \le |E| < \Delta,\\ \nu_0\frac{|E|}{\sqrt{E^2-\Delta^2}} & \text{for } |E| \ge \Delta. \end{cases} \tag{1.47}$$

Notable features are the gap in the density of states, i.e., no states below the superconducting gap, and divergences at $|E| = \Delta$ (see Fig. 1.4). In the limit $\Delta \to 0$, we obtain $\nu_S(E) = \nu_0$.

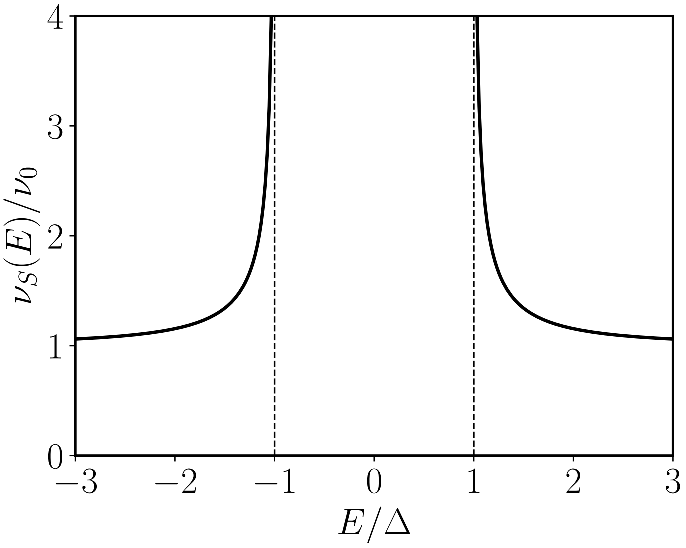

Figure 1.4: Density of states of a BCS superconductor.

1.2 Scattering formalism

In this thesis, we are mainly interested in the study of Josephson junctions and their transport properties. A good way to describe these properties is provided by the scattering formalism. In particular, as we will see later in Sec. 1.3, it is useful for describing the normal region of a Josephson junction, which is where scattering takes place. In this section, we will therefore present this formalism. We will start with the example of the scattering at a Dirac-δ potential. This kind of potential is often used to model impurities or the interface between two materials. Then, we will introduce the scattering matrices, which generalize the concept of reflection and transmission of incoming particles. We will continue by presenting the transfer matrix and how it allows one to determine the scattering matrix of a system with different sources of scattering. To illustrate how practical it is, we will use two examples, a system with free propagation and one or two Dirac-δ potentials.

1.2.1 Scattering due to a Dirac-delta potential

To introduce the scattering formalism, we start with the Dirac-delta potential. In this thesis, we will use it to model impurities, local potentials or interfaces between materials. In this example, we will treat the 1D delta potential. We can write this potential as $V(x) = V\delta(x)$. Therefore, the Schrödinger equation with such potential reads

$$-\frac{\hbar^2}{2m}\psi''(x) + V\delta(x)\psi(x) = E\psi(x), \tag{1.48}$$

where $\psi''(x)$ denotes the second derivative of $\psi(x)$ with respect to x. For $x \neq 0$, the solution of the Schrödinger equation is trivial, and we can write the wave functions as plane waves

$$\psi(x) = \begin{cases} \psi_L(x) = A_L e^{ikx} + B_L e^{-ikx} & \text{for } x < 0, \\ \psi_R(x) = A_R e^{ikx} + B_R e^{-ikx} & \text{for } x > 0, \end{cases} \tag{1.49}$$

with $k = \sqrt{2mE}/\hbar$. The continuity of the wave function implies

$$\psi_L(0) = \psi_R(0) \equiv \psi(0), \tag{1.50}$$

leading to

$$A_L + B_L = A_R + B_R. \tag{1.51}$$

However, due to the delta function, the derivatives are not continuous at $x = 0$. One way to deal with this problem is to integrate the Schrödinger equation around $x = 0$. Doing so allows one to obtain the difference between the derivatives of the two wavefunctions. We obtain

$$\psi'_R(0) - \psi'_L(0) = -\frac{2mV}{\hbar^2}\psi(0), \tag{1.52}$$

which leads to

$$A_R - B_R + B_L - A_L = -2i\frac{mV}{\hbar^2 k}(A_R + B_R). \tag{1.53}$$

For positive energies, the free moving particles may be scattered at the delta potential as illustrated in Fig. 1.5. In this example, we will consider an incoming particle from the left side of the delta potential. This incoming particle can be either reflected on the potential with a probability amplitude r or transmitted to the right side of it with a probability amplitude t. With those assumptions, we can simplify the previous equations by setting $A_L = 1$, $B_L = r$, $A_R = t$ and $B_R = 0$. Using eqs. (1.50) and (1.52), we obtain the following relation

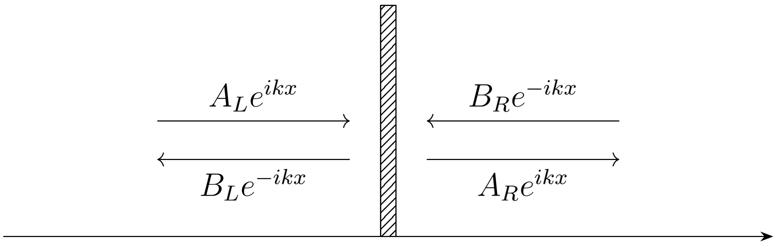

Figure 1.5: Scattering from a delta potential.

$$r = -i\frac{mV/(\hbar^2 k)}{1 + imV/(\hbar^2 k)} = -i\frac{V/(\hbar v)}{1 + iV/(\hbar v)}, \tag{1.54}$$

$$t = \frac{1}{1 + imV/(\hbar^2 k)} = \frac{1}{1 + iV/(\hbar v)}, \tag{1.55}$$

where we introduce $v = \hbar k/m$, the velocity of the particle. It is easy to check that $R+T=1$, where $R=|r|^2$ and $T=|t|^2$. In the limit $V/(\hbar v)\to 0$, one can see that $T\to 1$ and $R\to 0$ such that the particle moves freely from left to right. On the other hand, in the limit $V/(\hbar v)\to\infty$ we have the opposite, $R\to 1$ and $T\to 0$.

In the case of an incoming particle coming from the right, we would have found the same results. The cases of an incoming particle coming from the left or from the right can be reunited together into a more general theory which is the scattering matrix formalism.

1.2.2 Scattering and transfer matrix

Here, we will derive the scattering and transfer matrix formalism for 1D systems. More details can be found in the book of Markoš and Soukoulis [63]. In a system with a localized potential such as the delta potential of the previous example, or a square potential, we can always treat the scattering problem of left/right incoming particles (or both). The idea is to separate the space into three different regions. One of these regions is described by a scattering matrix. The two others being on the left and right of this scattering region, in which no potential is present. In these two regions, we can write the wavefunctions as in Eq. (1.49) where here $\psi_{L/R}(x)$ denotes the wavefunction at the left/right side of the scattering region. In the central scattering region, the wavefunction is unknown unless we know the specific form of the potential. What we want to obtain are the scattering amplitudes, which indicate the probability of an incoming state to be either reflected or transmitted in terms of the amplitude of the incoming state through the scattering region. Therefore, we can write this problem as a matrix equation.

$$\begin{pmatrix} B_L \\ A_R \end{pmatrix} = \mathcal{S}\begin{pmatrix} A_L \\ B_R \end{pmatrix} = \begin{pmatrix} \mathcal{S}_{11} & \mathcal{S}_{12} \\ \mathcal{S}_{21} & \mathcal{S}_{22} \end{pmatrix}\begin{pmatrix} A_L \\ B_R \end{pmatrix}, \tag{1.56}$$

where the $\mathcal{S}$ matrix is called the scattering matrix. Since this matrix relates the amplitude of incoming states to the amplitude of the outgoing states, we can write it in a shortened way as

$$\psi_{\text{out}} = \mathcal{S}\psi_{\text{in}}. \tag{1.57}$$

Under this form, we can associate the coefficient of the scattering matrix to the scattering amplitudes. It can be written as

$$\mathcal{S} = \begin{pmatrix} r & t' \\ t & r' \end{pmatrix}, \tag{1.58}$$

where r and r' describe the reflection of a state coming from the left/right, t the transmission from right to left and t' the transmission from left to right. Due to the conservation of the probability current, the scattering matrix $\mathcal{S}$ must be unitary. The probability current density J of the wave function is defined as

$$J = -i\frac{\hbar}{2m}\left(\psi^*(x)\partial_x\psi(x) - \psi(x)\partial_x\psi^*(x)\right) \tag{1.59}$$

Therefore, the probability current density to the left and right side of the scattering region is

$$J_L = \frac{\hbar k}{m}\left(|A_L|^2 - |B_L|^2\right), \tag{1.60}$$

$$J_R = \frac{\hbar k}{m}\left(|A_R|^2 - |B_R|^2\right). \tag{1.61}$$

The conservation of the probability current implies $J_L = J_R$. Hence, we can write

$$\begin{aligned} & |B_L|^2 + |A_R|^2 = |A_L|^2 + |B_R|^2 \\ \Leftrightarrow\quad & \psi_{\text{out}}^\dagger\psi_{\text{out}} = \psi_{\text{in}}^\dagger\psi_{\text{in}} \\ \Leftrightarrow\quad & \psi_{\text{in}}^\dagger\mathcal{S}^\dagger\mathcal{S}\psi_{\text{in}} = \psi_{\text{in}}^\dagger\psi_{\text{in}} \\ \Rightarrow\quad & \mathcal{S}^\dagger\mathcal{S} = \mathcal{S}\mathcal{S}^\dagger = \mathbb{1} \end{aligned} \tag{1.62}$$

This property implies that we can also describe the incoming state using the scattering matrix. This can be written as

$$\psi_{\text{in}} = \mathcal{S}^\dagger \psi_{\text{out}}. \tag{1.63}$$

By using the unitarity we obtain the following relation for the scattering coefficients

$$|t| = |t'|, \tag{1.64}$$

$$|r| = |r'|, \tag{1.65}$$

$$r = -r'^* \frac{t}{t'^*} = -r'^* \frac{t'}{t^*} \tag{1.66}$$

For the rest of this section, we redefine the scattering coefficients up to a global phase corresponding to the average of the phase of t and t' that we denote as ϕ_t and $\phi_{t'}$ leading to $t' = t^*$ and $r' = -r^*$ such that

$$\mathcal{S} = e^{i\theta} \begin{pmatrix} r & t^* \\ t & -r^* \end{pmatrix}, \qquad \theta = \frac{\phi_t + \phi_{t'}}{2}. \tag{1.67}$$

In the case of our previous example, the delta potential yields

$$\mathcal{S}_0 = \frac{1}{1 + iV/(\hbar v)} \begin{pmatrix} -iV/(\hbar v) & 1 \\ 1 & -iV/(\hbar v) \end{pmatrix}, \tag{1.68}$$

such that we can write

$$\theta = -\arctan \beta, \tag{1.69}$$

$$r = -i\beta/\sqrt{1+\beta^2}, \tag{1.70}$$

$$t = 1/\sqrt{1+\beta^2}, \tag{1.71}$$

$$\beta = V/(\hbar v). \tag{1.72}$$

So far, we've seen that with the scattering matrix, we can express the amplitude of the outgoing states in terms of the incoming states. Another possibility is to express the states that are on the right side of the scattering region in terms of the states that are on the left side of it. This is the purpose of the transfer matrix, which we will call $\mathcal{M}$. This can be written as

$$\begin{pmatrix} A_R \\ B_R \end{pmatrix} = \mathcal{M} \begin{pmatrix} A_L \\ B_L \end{pmatrix} = \begin{pmatrix} \mathcal{M}_{11} & \mathcal{M}_{12} \\ \mathcal{M}_{21} & \mathcal{M}_{22} \end{pmatrix} \begin{pmatrix} A_L \\ B_L \end{pmatrix}, \tag{1.73}$$

that we can reduce to

$$\psi_R = \mathcal{M} \psi_L, \tag{1.74}$$

with $\psi_{R/L} = (A_{R/L}, B_{R/L})^T$. Solving the scattering matrix equation for A_R and B_R in terms of A_L and B_L allows expressing the transfer matrix coefficients in terms of the scattering matrix ones

$$\mathcal{M} = -\frac{1}{\mathcal{S}_{12}} \begin{pmatrix} \text{Det}\,\mathcal{S} & -\mathcal{S}_{22} \\ \mathcal{S}_{11} & -1 \end{pmatrix}. \tag{1.75}$$

As this matrix also involves the amplitude of the incoming and outgoing states, we can express the scattering matrix coefficients in terms of the transfer matrix ones

$$\mathcal{S} = \frac{1}{\mathcal{M}_{22}} \begin{pmatrix} -\mathcal{M}_{21} & 1 \\ \text{Det}\,\mathcal{M} & \mathcal{M}_{12} \end{pmatrix}. \tag{1.76}$$

The benefit of using the transfer matrix is that, for a system with multiple sources of scattering, we can define a transfer matrix for each of these sources. The total transfer matrix which describes all the scattering regions will be given by the product of the transfer matrices associated to each scattering source. As an example, we can consider a system with two scattering sources. We can write this using the transfer matrix as

$$\psi_R = \mathcal{M}\psi_L = \mathcal{M}_2\mathcal{M}_{1\to 2}\mathcal{M}_1\psi_L, \tag{1.77}$$

where $\mathcal{M}_{1,2}$ corresponds to the transfer matrix of the first and second scattering sources while $\mathcal{M}_{1\to 2}$ is the transfer matrix that describes the propagation between the two scattering sources. Two concrete examples will be given in the next part of this section.

1.2.3 Free propagation and delta potential

In this part, we will present how we can use the transfer matrix in order to obtain the scattering matrix for a system with different sources of scattering. We will make use of two examples which we will use later to describe the scattering in Josephson junctions. The first example consists of a system in which the scattering region of interest is composed of a delta potential placed at a position x_0. On both sides of this potential, the particle moves freely, i.e., there is no potential. We consider that this region is of length d. This example is exactly the same as the one at the beginning of this section. But here, we include a region of free propagation as a part of the scattering region (see Fig.1.6) so that the wavefunction at the left and right sides of this region can be written as

$$\psi_L(x) = A_L e^{ikx} + B_L e^{-ikx}, \tag{1.78}$$

$$\psi_R(x) = A_R e^{ik(x-d)} + B_R e^{-ik(x-d)}. \tag{1.79}$$

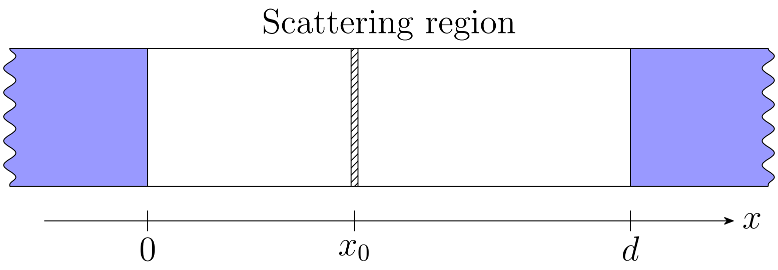

Figure 1.6: Schematic representation of the system considered in the first example. In blue are the two regions between which we want to describe the scattering. The delta potential is represented by the dashed area at x_0.

The transfer matrix of this system can be written as

$$\begin{aligned}\mathcal{M} = \mathcal{M}_R\mathcal{M}_0\mathcal{M}_L &= \begin{pmatrix} e^{ik(d-x_0)} & 0 \\ 0 & e^{-ik(d-x_0)} \end{pmatrix} \begin{pmatrix} (|r|^2 t^{-1} + t^*)e^{i\theta} & -r^* t^{-1} \\ -r t^{-1} & t^{-1}e^{-i\theta} \end{pmatrix} \begin{pmatrix} e^{ikx_0} & 0 \\ 0 & e^{-ikx_0} \end{pmatrix}, \\ &= \begin{pmatrix} -(|r|^2 t^{-1} + t^*)e^{i\theta+ikd} & r^* t^{-1} e^{-ik(2x_0-d)} \\ r t^{-1} e^{ik(2x_0-d)} & t^{-1} e^{-i\theta-ikd} \end{pmatrix}.\end{aligned} \tag{1.80}$$

From this transfer matrix, we obtain the following scattering matrix for the whole scattering region

$$\mathcal{S} = e^{i\theta+ikd}\begin{pmatrix} r e^{ik(2x_0-d)} & t \\ t^* & -r^* e^{-ik(2x_0-d)} \end{pmatrix} \tag{1.81}$$

This result is coherent with what we can expect. An incoming particle that is transmitted will gain a phase e^{ikd} due to its propagation. And, an incoming particle that is reflected will gain a phase which depends on which side of the potential the incoming particle is.

The last example that we will present is a system composed of two delta potentials, separated by a region of length d where no potential is present. We will consider the case where the two delta potentials can be different, such that we denote the scattering coefficients of the scattering matrix of the left and right sides with the subscripts L and, R respectively. Following the same procedure as before, we obtain

$$\mathcal{M} = \begin{pmatrix} (|r_R|^2 t_R^{-1} + t_R^*)e^{i\theta_R} & -r_R^* t_R^{-1} \\ -r_R t_R^{-1} & t_R^{-1} e^{-i\theta_R} \end{pmatrix} \begin{pmatrix} e^{ikd} & 0 \\ 0 & e^{-ikd} \end{pmatrix} \begin{pmatrix} (|r_L|^2 t_L^{-1} + t_L^*)e^{i\theta_L} & -r_L^* t_L^{-1} \\ -r_L t_L^{-1} & t_L^{-1} e^{-i\theta_L} \end{pmatrix} \tag{1.82}$$

The scattering matrix obtained for this system from the transfer matrix can again be written in the form

$$\mathcal{S} = e^{i\tilde{\theta}} \begin{pmatrix} \tilde{r} & \tilde{t} \\ \tilde{t}^* & -\tilde{r}^* \end{pmatrix}, \tag{1.83}$$

where its coefficients read

$$\tilde{t} = t_R t_L / \left|1 + r_R r_L^* e^{i(\theta_R+\theta_L+2kd)}\right|, \tag{1.84}$$

$$\tilde{r} = \left(r_L e^{-i\theta_R - ikd} + r_R e^{i\theta_L + ikd}\right) / \left|1 + r_R r_L^* e^{i(\theta_R+\theta_L+2kd)}\right|, \tag{1.85}$$

$$\tilde{\theta} = \theta_R + \theta_L + kd - \arctan\left(\frac{\mathrm{Im}\left[1 + r_R r_L^* e^{i(\theta_R+\theta_L+2kd)}\right]}{\mathrm{Re}\left[1 + r_R r_L^* e^{i(\theta_R+\theta_L+2kd)}\right]}\right). \tag{1.86}$$

We can see that the denominator of $\tilde{t}$ and $\tilde{r}$ involves the reflection amplitude of both delta potentials. To understand this, we can picture the path that an incoming particle from the left can take. At the first potential, this particle is either transmitted or reflected. If it is transmitted, it will freely propagate until it arrives at the second delta potential. Here again, it can be either transmitted or reflected. In the scenario where the particle is reflected, the same thing happens on the left side. In fact, once the particle is being transmitted in the region between the two potentials, it can be reflected a multiple number of times until it comes out of the scattering region (see Fig. 1.7). This can be written in the form of a power series of the reflection amplitude as

$$\tilde{t} = t_R \left[1 - r_R r_L^* e^{i(\theta_R+\theta_L+2kd)} + \left(-r_R r_L^* e^{i(\theta_R+\theta_L+2kd)}\right)^2 + \ldots\right] t_L e^{ikd} = \frac{t_R t_L e^{ikd}}{1 + r_R r_L^* e^{i(\theta_R+\theta_L+2kd)}}. \tag{1.87}$$

The same happens for the reflection amplitude. To obtain the form of Eq. (1.83), we then rewrite the scattering amplitudes. If the two delta potential are the same, the scattering coefficients simplify into

$$\tilde{t} = t^2 / \left|1 + |r|^2 e^{2i(\theta+kd)}\right|, \tag{1.88}$$

$$\tilde{r} = 2r\cos(\theta + kd) / \left|1 + |r|^2 e^{2i(\theta+kd)}\right|, \tag{1.89}$$

$$\tilde{\theta} = 2\theta + kd - \arctan\left(\frac{\mathrm{Im}\left[1 + |r|^2 e^{2i(\theta+kd)}\right]}{\mathrm{Re}\left[1 + |r|^2 e^{2i(\theta+kd)}\right]}\right). \tag{1.90}$$

In this case, we can see that if $kd = (2n+1)\frac{\pi}{2} - \theta$, with $n \in \mathbb{Z}$, the reflection amplitude vanishes. These peaks of transmission are called transmission resonances or Fabry-Pérot resonances (see Fig. 1.8). In the limit $\beta = V/(\hbar v) \to \infty$, the term $\theta \to -\pi/2$. Thus, the condition for the resonance becomes $kd = n\pi$.

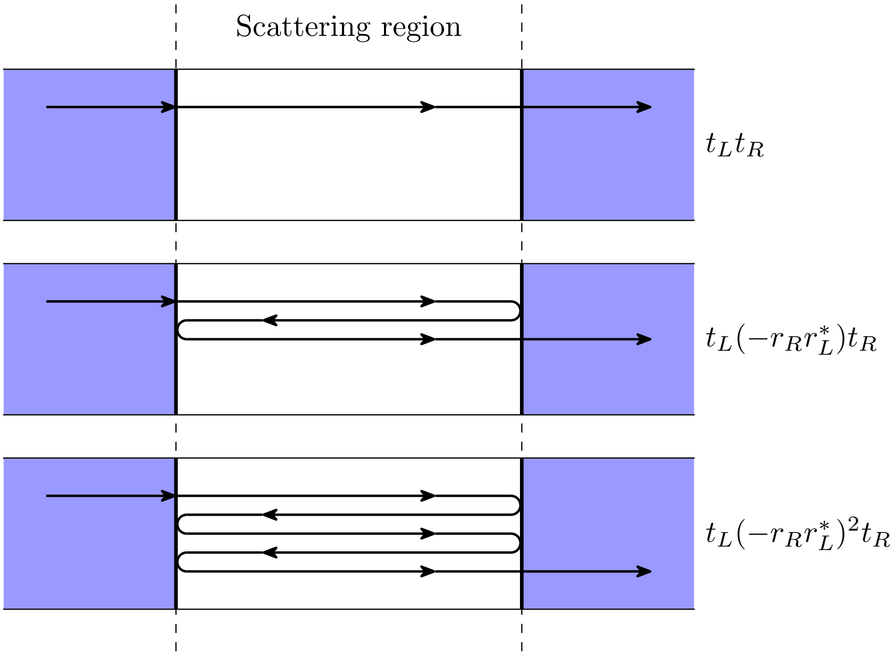

Figure 1.7: Illustration of the system with the two delta potentials. The left and right regions are separated by the scattering region. An incoming particle from the left, depicted here with the arrow, can be reflected multiple times before being transmitted to the right side of the scattering region.

k being related to the wavelength of the incoming state through $\lambda = 2\pi/k$, we can write the condition as $d = n\lambda/2$. If this condition is verified, this means that all the transmitted waves are in phase, such that we observe constructive interferences, whereas the reflected waves are in phase opposition leading to destructive interferences. In fact, in this case, the problem is analogous to a particle in a box where the wavelength of the wavefunction must be $\lambda = 2nd$. Due to the reflection phase shift, which depends on the height of the potential, the positions of the resonance peaks are shifted depending on the applied potential.

1.2.3.1 Resonant level with the doublet delta potentials

In the previous section, we discussed the general properties of a scattering region with two delta potentials. Also, we made the analogy with a particle in a box which has discrete energy levels when we are in the limit $\beta \to \infty$. We saw that the transmission was maximal when the energy of the incident particle matched one of these discrete energy levels. We may focus on a single resonant level (the one closest to E_F), that we will denote as E_r. Also, we won't require both potentials to be identical. Assuming that the scattering region separates two normal leads with parabolic dispersion, we have for an incident electron

$$k = k_F\sqrt{1+E/\mu}, \tag{1.91}$$

where μ is the electrochemical potential (equivalent to the Fermi energy at zero temperature) and $k_F = \sqrt{2m\mu}/\hbar$. In the limit $\mu \gg E$, we may linearize this expression such that

$$k = k_F + \frac{E}{\hbar v_F}. \tag{1.92}$$

The maximum of transmission is still given by the constructive interference condition, i.e.

$$\varphi_{\mathrm{tot}} + \frac{Ed}{\hbar v_F} = (2n+1)\frac{\pi}{2}, \tag{1.93}$$

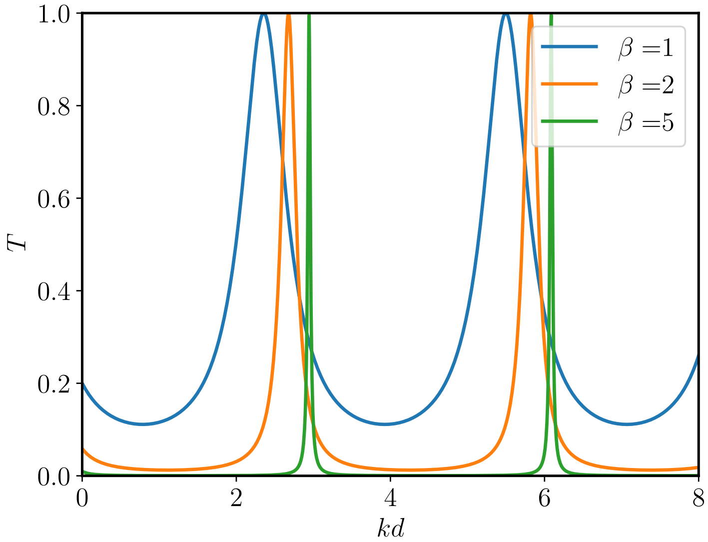

Figure 1.8: Transmission T of the scattering region as function of kd with various strengths of the delta potentials $\beta = V/(\hbar v)$. We observe resonances when $kd = (2n+1)\frac{\pi}{2} - \theta$ with $\theta = -\arctan\beta$.

where we define $\varphi_{\text{tot}} = \theta + k_F d$. Let's expand the transmission coefficient around the resonance condition $E \to E_r$

$$\begin{aligned}\tilde{t}(E) &= \frac{t_R t_L}{\sqrt{\left(1+\sqrt{R_R R_L}\right)^2 - 4\sqrt{R_R R_L}\sin^2\left(\varphi_{\text{tot}} + Ed/(\hbar v_F)\right)}}, \\ &= \frac{t_R t_L}{\sqrt{\left(1+\sqrt{R_R R_L}\right)^2 - 4\sqrt{R_R R_L}\sin^2((2n+1)\pi/2 + (E-E_r)d/(\hbar v_F))}}, \\ &= \frac{t_R t_L}{\sqrt{\left(1-\sqrt{R_R R_L}\right)^2 + 4\sqrt{R_R R_L}((E-E_r)d/(\hbar v_F))^2}}.\end{aligned} \tag{1.94}$$

The resonant level E_r is well-defined only when t_L, $t_R \ll 1$. Thus, at the lowest order we obtain

$$\tilde{t}(E) = \frac{t_R t_L}{\sqrt{(T_L + T_R)^2/4 + 4((E-E_r)d/(\hbar v_F))^2}}. \tag{1.95}$$

Introducing the coupling rates of the level into the leads $\Gamma_j = T_j \hbar v_F/(2d)$ we can write

$$\tilde{t}(E) = \frac{\sqrt{\Gamma_R \Gamma_L}\, e^{i(\phi_{tR}+\phi_{tL})}}{\sqrt{((\Gamma_R + \Gamma_L)/2)^2 + (E-E_r)^2}}, \tag{1.96}$$

which corresponds to the Breit-Wigner formula [64]. We can see that the transmission coefficient has a Lorentzian shape of energy width $\Gamma_L + \Gamma_R$ and amplitude $4\Gamma_L\Gamma_R/(\Gamma_L + \Gamma_R)^2$

In fact, this model is well suited to describe a junction containing a quantum dot. A quantum dot can be modeled as a small region of space defined by electrostatic gates or impurities. Due to its small size, electrons in a quantum dot have discrete energy levels. Hence, the double potential model describes well the coupling between the dots and the leads. Therefore, according to this model, when the energy of electrons from the leads does not match one of the quantum dot's levels, it makes it difficult to tunnel into the quantum dot. In contrast, when one of its levels is in resonance, electrons can easily tunnel from the electrodes into the dot.

1.3 Josephson effect and ABS

As we said in the introduction, a Josephson junction consists of a weak link separating two superconducting electrodes. Those junctions are characterized by a dissipationless current which arises from the superconducting phase difference between the two electrodes. The Josephson relations which capture the essential physics of Josephson junctions are [2, 53, 65]

$$I(\varphi) = \frac{2e}{\hbar}\frac{\partial E_J(\varphi)}{\partial \varphi}, \qquad \frac{\mathrm{d}\varphi}{\mathrm{d}t} = \frac{2eV}{\hbar}, \tag{1.97}$$

where φ corresponds to the phase difference between the two electrodes, $E_J(\varphi)$ is the junction energy and V is the voltage bias. The transfer of Cooper pairs from one electrode to the other constitutes a part of this current and is allowed by the formation of ABS in the weak link which disperses with the phase difference. In junctions shorter than the coherence length, $\xi = \hbar v_F/(\Delta)$, the system energy is fixed by occupation of the ABS. Hereafter, we will introduce the scattering reflection mechanism that permits the formation of those bound states. Properties of Josephson junctions being dependent on the energy, we will derive the energy spectrum of ABS for a typical junction using the scattering matrix formalism, where the weak link is a non-superconducting metal, we refer to this system as a S-N-S junction. Finally, we will present one way to treat the case of a weak link separated from the superconducting electrodes by strong electrostatic gates, which allows defining the weak link as a quantum dot.

1.3.1 Andreev reflection

Andreev reflections appear at the interface between a normal non-superconducting material and a superconductor. This scattering process corresponds to the situation where an incident electron is being reflected as a hole in the normal region, while a Cooper is formed in the superconductor. This scattering process is illustrated in Fig. 1.9. To capture this process, we first need to describe the spatially-inhomogeneous problem since we have a superconducting and a normal material. This can be done from the mean field Hamiltonian we introduced in Sec. 1.1.2 that, this time, we will write in real space.

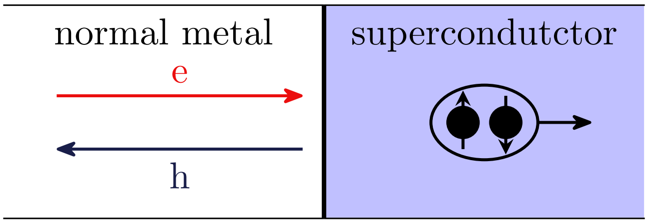

Figure 1.9: Andreev reflection at a normal metal - superconductor interface. An incoming electron from the normal metal is being reflected as a hole at the interface. This process results in the formation of a Cooper pair in the superconductor. The outgoing charge comprising the hole and the Cooper pair is equal to the one of the incoming electron.

This Hamiltonian reads

$$H_{\mathrm{MF}} = \int \mathrm{d}\boldsymbol{r} \sum_{\sigma} \psi^{\dagger}_{\sigma}(\boldsymbol{r}) H_0(\boldsymbol{r}) \psi_{\sigma}(\boldsymbol{r}) + \int \mathrm{d}\boldsymbol{r} \left(\psi^{\dagger}_{\uparrow}(\boldsymbol{r}) \Delta(\boldsymbol{r}) e^{i\varphi} \psi^{\dagger}_{\downarrow}(\boldsymbol{r}) + \mathrm{h.c.} \right), \tag{1.98}$$

$$= \int \mathrm{d}\boldsymbol{r} \begin{pmatrix} \psi^{\dagger}_{\uparrow}(\boldsymbol{r}) & \psi_{\downarrow}(\boldsymbol{r}) \end{pmatrix} H_{\mathrm{BdG}}(\boldsymbol{r}) \begin{pmatrix} \psi_{\uparrow}(\boldsymbol{r}) \\ \psi^{\dagger}_{\downarrow}(\boldsymbol{r}) \end{pmatrix},$$

$$H_{\mathrm{BdG}}(\boldsymbol{r}) = \begin{pmatrix} H_0(\boldsymbol{r}) & \Delta(\boldsymbol{r}) \\ \Delta^*(\boldsymbol{r}) & -H_0(\boldsymbol{r}) \end{pmatrix}, \tag{1.99}$$

$$H_0(\boldsymbol{r}) = -\frac{\hbar^2 \nabla^2}{2m} - \mu. \tag{1.100}$$

A Bogoliubov transformation can be used to solve the problem such that

$$\psi_{\uparrow}(\boldsymbol{r}) = \sum_{\nu} (u^*_{\nu}(\boldsymbol{r}) \gamma_{\nu\uparrow} - v_{\nu}(\boldsymbol{r}) \gamma^{\dagger}_{-\nu\downarrow}), \tag{1.101}$$

$$\psi^{\dagger}_{\downarrow}(\boldsymbol{r}) = \sum_{\nu} (u_{\nu}(\boldsymbol{r}) \gamma^{\dagger}_{-\nu\downarrow} + v^*_{\nu}(\boldsymbol{r}) \gamma_{\nu\uparrow}), \tag{1.102}$$

where the exact form of $u_\nu(\boldsymbol{r})$ and $v_\nu(\boldsymbol{r})$ depends on $\xi(\boldsymbol{r})$. The index ν labels the different eigenstates of the BdG Hamiltonian such that

$$H_{\mathrm{BdG}}(\boldsymbol{r}) \begin{pmatrix} u_{\nu}(\boldsymbol{r}) \\ v_{\nu}(\boldsymbol{r}) \end{pmatrix} = E_{\nu} \begin{pmatrix} u_{\nu}(\boldsymbol{r}) \\ v_{\nu}(\boldsymbol{r}) \end{pmatrix}. \tag{1.103}$$

Here again, we can see that $H_{\mathrm{BdG}}(\boldsymbol{r})$ has particle-hole symmetry such that $\mathcal{P} H_{\mathrm{BdG}}(\boldsymbol{r}) \mathcal{P}^{-1} = -H_{\mathrm{BdG}}(\boldsymbol{r})$ with $\mathcal{P} = -i\tau_y \mathcal{C}$. This symmetry implies that for a state of energy E it exist another state of energy $-E$.

To capture the Andreev reflection process, we will use the BdG Hamiltonian of Eq. (1.99). Here, we will consider a one dimensional infinite lead which is described by the following equation in real space

$$\begin{pmatrix} H_0(x) & \Delta(x) \\ \Delta^*(x) & -H_0(x) \end{pmatrix} \begin{pmatrix} u(x) \\ v(x) \end{pmatrix} = E \begin{pmatrix} u(x) \\ v(x) \end{pmatrix}, \tag{1.104}$$

where the normal Hamiltonian is

$$H_0(x) = -\frac{\hbar^2}{2m} \frac{\mathrm{d}^2}{\mathrm{d}x^2} - \mu. \tag{1.105}$$

The superconducting gap $\Delta(x)$ verifies $\Delta(x) = \Delta e^{i\varphi} \Theta(x)$, with $\Theta(x)$ the Heaviside function and φ the phase of the superconducting order parameter. This Hamiltonian describes a normal region with parabolic dispersion in the region $x < 0$ and a superconducting region for $x > 0$. In the superconducting region, this Hamiltonian is equivalent to Eq. (1.26) but written in the real space instead of the momentum space. To obtain the amplitude associated to Andreev reflection, we will follow the same procedure as in the previous section for reflection and transmission coefficients. Therefore, we need to solve the Schrödinger equation in both regions. In the normal region, we have to solve

$$\pm \left(-\frac{\hbar^2}{2m} \frac{\mathrm{d}^2}{\mathrm{d}x^2} - \mu \right) \eta_{\pm}(x) = E \eta_{\pm}(x). \tag{1.106}$$

The solutions of those equations are

$$\eta_{\pm}(x) = a_{\pm} e^{ik_{\pm}x} + b_{\pm} e^{-ik_{\pm}x}, \tag{1.107}$$

where $a_\pm$ and $b_\pm$ are constants. The values of $k_\pm$ are given as

$$k_\pm = \frac{1}{\hbar}\sqrt{2m(\mu \pm E)} = k_F\sqrt{1 \pm \frac{E}{\mu}}, \tag{1.108}$$

with $k_F = \sqrt{2m\mu}/\hbar$. The + solution corresponds to an electron which belongs to the energy branch $\xi = \hbar^2 k^2/(2m)$, whereas the − solution corresponds to a hole and belongs to the branch $-\xi$. From the group velocity $v = \partial\xi/(\hbar\partial k)$, we find that, for $k > 0$, the group velocity of electrons is positive and the one of holes is negative in the x-direction. Thus, the terms a_+ and b_- describe right-moving particles, while the terms b_+ and a_- describe left-moving particles. The full wavefunction in the normal region can be written as a superposition of the electron and hole wavefunction

$$\psi_N(x) = \begin{pmatrix}1\\0\end{pmatrix}\frac{\eta_+(x)}{\sqrt{v_{k+}}} + \begin{pmatrix}0\\1\end{pmatrix}\frac{\eta_-(x)}{\sqrt{v_{k-}}}, \tag{1.109}$$

with $v_\pm = \hbar k_\pm/m$.

In the superconducting region, we have to solve the BdG equation

$$\begin{pmatrix} -\frac{\hbar^2}{2m}\frac{\mathrm{d}^2}{\mathrm{d}x^2} - \mu & \Delta e^{i\varphi} \\ \Delta e^{-i\varphi} & \frac{\hbar^2}{2m}\frac{\mathrm{d}^2}{\mathrm{d}x^2} + \mu \end{pmatrix}\begin{pmatrix}u(x)\\v(x)\end{pmatrix} = E\begin{pmatrix}u(x)\\v(x)\end{pmatrix}, \tag{1.110}$$

where $u(x)$ and $v(x)$ describe electron and hole like quasiparticles respectively. The superconducting gap being constant in the superconductor, we can assume plane wave solutions $\sim e^{iqx}$. The possible values of q are found by solving the eigenvalues problem. We obtain four different solutions $q = q_\pm$ and $q = -q_\pm$ with $q_\pm$ given as

$$q_\pm = \frac{1}{\hbar}\sqrt{2m\left(\mu \pm \sqrt{E^2-\Delta^2}\right)} = k_F\sqrt{1 \pm \frac{\sqrt{E^2-\Delta^2}}{\mu}}. \tag{1.111}$$

The + solution describes quasi electrons while the − solutions describe quasi holes which respectively belong to the branch $\pm E_k$ with $E = \sqrt{\xi^2+\Delta^2}$. The wavefunction in the superconducting region can therefore be written as

$$\psi_S(x) = \frac{1}{\sqrt{v_{q+}}}\begin{pmatrix}ue^{i\varphi/2}\\ve^{-i\varphi/2}\end{pmatrix}\left[c_1e^{iq_+x} + c_2e^{-iq_+x}\right] + \frac{1}{\sqrt{v_{q-}}}\begin{pmatrix}ve^{i\varphi/2}\\ue^{-i\varphi/2}\end{pmatrix}\left[d_1e^{iq_-x} + d_2e^{-iq_-x}\right], \tag{1.112}$$

where u and v are given in Eq. (1.29) and

$$v_{q\pm} = \frac{\hbar q_\pm}{m}\frac{\xi}{E}, \tag{1.113}$$

with $\xi = \mathrm{sign}(E)\sqrt{E^2-\Delta^2}$.

As one can see, we have normalized the wavefunctions $\psi_N(x)$ by $\sqrt{v_{k\pm}}$ and $\psi_S(x)$ by $\sqrt{v_{q\pm}}$. In the following, we will want to describe the normal-superconductor interface with a scattering matrix. This normalization ensures that the current is conserved, so we can use these states as a basis for this scattering matrix. The resulting scattering problem can be written as

$$\begin{pmatrix}b_+\\a_-\\c_1\\d_2\end{pmatrix} = \mathcal{S}_{NS}\begin{pmatrix}a_+\\b_-\\c_2\\d_1\end{pmatrix}, \qquad \mathcal{S}_{NS} = \begin{pmatrix} r_{nn}^{ee} & r_{nn}^{eh} & t_{ns}^{ee} & t_{ns}^{eh} \\ r_{nn}^{he} & r_{nn}^{hh} & t_{ns}^{he} & t_{ns}^{hh} \\ t_{sn}^{ee} & t_{sn}^{eh} & r_{ss}^{ee} & r_{ss}^{eh} \\ t_{sn}^{he} & t_{sn}^{hh} & r_{ss}^{he} & r_{ss}^{hh} \end{pmatrix}, \tag{1.114}$$

where the lower indices ij of the scattering coefficients indicate that the incoming state is from the region j and the outgoing state is from the region i. On the other hand, the upper indices kl indicate the quasi electron / quasi hole nature of the incoming state (indice l) and outgoing state (indice k). For example, t_{ns}^{eh} describes the transmission of a quasi hole from the superconductor to a quasi electron in the normal region. Defining $\psi_{\text{out}} = \begin{pmatrix} b_+, & a_-, & c_1, & d_2 \end{pmatrix}^T$ and $\psi_{\text{in}} = \begin{pmatrix} a_+, & b_-, & c_2, & d_1 \end{pmatrix}^T$, we can easily see that, imposing $J_N = J_S$, where $J_{N/S} = \frac{\hbar}{m} \operatorname{Im}\left[\psi_{N/S}^\dagger(x)\partial_x \tau_z \psi_{N/S}(x)\right]$ is the current obtained in the normal / superconducting region and τ_z the Pauli matrix in the Nambu space, leads to $\psi_{\text{out}}^\dagger \psi_{\text{out}} = \psi_{\text{in}}^\dagger \psi_{\text{in}}$, ensuring that $\mathcal{S}_{NS}^\dagger \mathcal{S}_{NS} = \mathbb{1}_4$.

As in Sec. 1.2, the scattering coefficients can be obtained by matching the wavefunctions and their first derivative at $x = 0$. This yields

$$\psi_N(0) = \psi_S(0), \tag{1.115}$$

$$\psi_N'(0) = \psi_S'(0). \tag{1.116}$$

From here, we assume $|E|, \Delta \ll \mu$ such that we at the lowest order in k_F, we have $k_\pm \approx q_\pm \approx k_F$ [24, 66]. For a quasiparticle coming from the normal metal, we can put $c_2 = d_1 = 0$ whereas for a quasiparticle coming from the superconductor, we can put $a_+ = b_- = 0$. We obtain the following scattering coefficients [54]

$$\begin{aligned} &r_{ss}^{eh} = -\alpha, \qquad r_{ss}^{he} = -\alpha, \qquad r_{nn}^{eh} = \alpha e^{i\varphi}, \qquad r_{nn}^{he} = \alpha e^{-i\varphi} \\ &t_{sn}^{hh} = t_{NS} e^{i\varphi/2}, \qquad t_{sn}^{ee} = t_{NS} e^{-i\varphi/2}, \qquad t_{ns}^{ee} = t_{NS} e^{i\varphi/2}, \qquad t_{ns}^{hh} = t_{NS} e^{-i\varphi/2}, \end{aligned} \tag{1.117}$$

with

$$\alpha = \frac{E}{\Delta} - \operatorname{sign}(E)\sqrt{\frac{E^2}{\Delta^2} - 1}, \qquad t_{NS} = \sqrt{\frac{2E}{E + \sqrt{E^2 - \Delta^2}}}\sqrt{\operatorname{Re}\left[\frac{\sqrt{E^2 - \Delta^2}}{E}\right]}, \tag{1.118}$$

and the other scattering coefficients are zero. As one can see, for $|E| < \Delta$, one part of the wavefunction in the superconductor is evanescent and the other explodes when x increases. Thus, in this case, we necessarily have $c_2 = d_1 = 0$. The evanescent part of the wavefunction indicates that the transport channels are evanescent, which is why we have $t_{NS} = 0$. The only remaining process is the Andreev reflection in the normal region. In the following, we will denote $r_{nn}^{he} = r_{A,e}(E, \varphi)$ and $r_{nn}^{eh} = r_{A,h}(E, \varphi) = r_{A,e}(E, -\varphi)$ as they correspond to Andreev reflection for an electron reflected into a hole and a hole reflected into an electron in the normal region. Also, from now on, we will only consider particles with energy $|E| < \Delta \ll \mu$ such that

$$\alpha = \frac{E}{\Delta} - i\sqrt{1 - \frac{E^2}{\Delta^2}} = \exp\left[-i \arccos\frac{E}{\Delta}\right]. \tag{1.119}$$

The value of the modulus of r_A is plotted in Fig. 1.10.

1.3.2 ABS in a "zero-length" junction

In a Josephson junction, Andreev reflection on both normal-superconductor interfaces can lead to the formation of bound states known as Andreev bound states. Those bound states are therefore a superposition of an electron and a hole. In this section, we will derive the energy spectrum of ABS in a junction with perfect transmission. In order to obtain this energy spectrum, we will first consider that the normal region is of length d. We will consider a right moving electron starting from $x = 0$ in the normal region that is being reflected as a hole at the right interface, i.e., at $x = d$. The wavefunction in the normal region can thus be written as

$$\psi_N(x) = N\left[\begin{pmatrix} 1 \\ 0 \end{pmatrix} e^{i\left(k_F + \frac{E}{\hbar v_F}\right)x} + \begin{pmatrix} 0 \\ \alpha e^{-i\varphi_R + i(k_F + \frac{E}{\hbar v_F})d} \end{pmatrix} e^{i\left(k_F - \frac{E}{\hbar v_F}\right)(x-d)}\right], \tag{1.120}$$

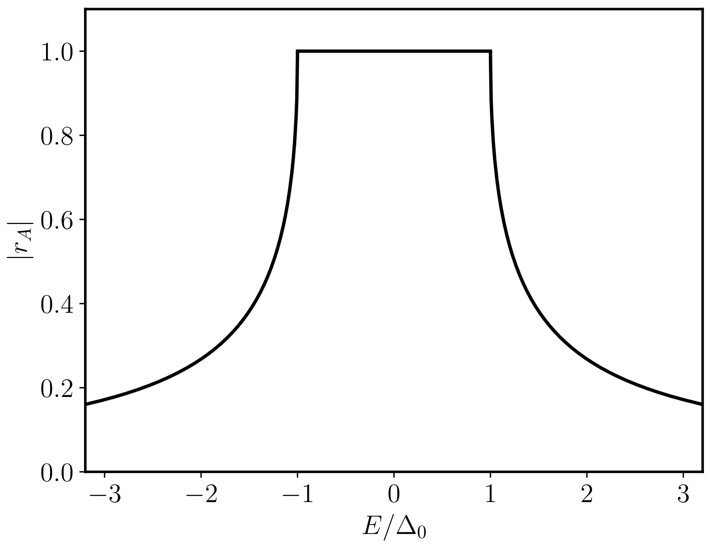

Figure 1.10: Modulus of the Andreev reflection coefficient

with N being the normalization coefficient. We can note that here, we have an additional phase factor of $e^{i\frac{Ed}{\hbar v_F}}$ for the Andreev reflection amplitude. This phase comes from the free propagation of the electron in the normal region. After the first Andreev reflection on the right interface, the reflected hole will, in turn, freely propagate in the normal region until it arrives at the left interface. The reflected hole, in turn, undergoes an Andreev reflection. The resulting electron has therefore an amplitude given as

$$A\alpha e^{-i(k_F-\frac{E}{\hbar v_F})d+i\varphi_L},$$

where $A=\alpha e^{-i\varphi_R+i(k_F+\frac{E}{\hbar v_F})d}$ is the amplitude of the reflected hole. The reflected electron has the same amplitude as the initial one but with an additional phase of $\alpha^2 e^{2i\frac{Ed}{\hbar v_F}-i\phi}$, with $\phi=\varphi_R-\varphi_L$. A bound state appears if there is constructive interference between the initial electron and the reflected one. This condition can be written as

$$\alpha^2 e^{2i\frac{Ed}{\hbar v_F}-i\phi}=1. \tag{1.121}$$

The same study can be made for a left moving electron in the normal region, which leads to the following condition for constructive interference and therefore, for the formation of a bound state [23, 24]

$$\alpha^2 e^{2i\frac{Ed}{\hbar v_F}+i\phi}=1. \tag{1.122}$$

These two conditions simply follow from the Bohr-Sommerfeld quantization rule, which implies that a bound state corresponds to a closed quasi-particle trajectory with a total phase accumulated during one cycle equal to a multiple of 2π. We can use these expressions to determine the energy spectrum of these bound states. It leads to

$$2\frac{Ed}{\hbar v_F}\pm\phi-2\arccos\frac{E}{\Delta}=2q\pi, \tag{1.123}$$

with $q\in\mathbb{Z}$. In the zero-length limit, i.e., $d\to 0$ (the case of finite length will be treated in Sec. 1.3.3), we can neglect the first term which allows us to write

$$E_\pm=\pm\Delta\cos\frac{\phi}{2}\text{sign}\left[\sin\frac{\phi}{2}\right]. \tag{1.124}$$

As expected by the particle-hole symmetry of the Bogoliubov-de Gennes Hamiltonian, we obtain two states with opposite energy. The term sign $\left[\sin\frac{\phi}{2}\right]$ comes from the domain in which arccos(x) is defined. The energy of these bound states cross perfectly at the Fermi energy at $\phi = \pi \bmod 2\pi$, and, are in contact with the continuum for $\phi = 0 \bmod 2\pi$ as shown in Fig. 1.11. The energy spectrum being 2π periodic, we will restrain ourselves to the interval $\phi \in [0, 2\pi]$ in the following.

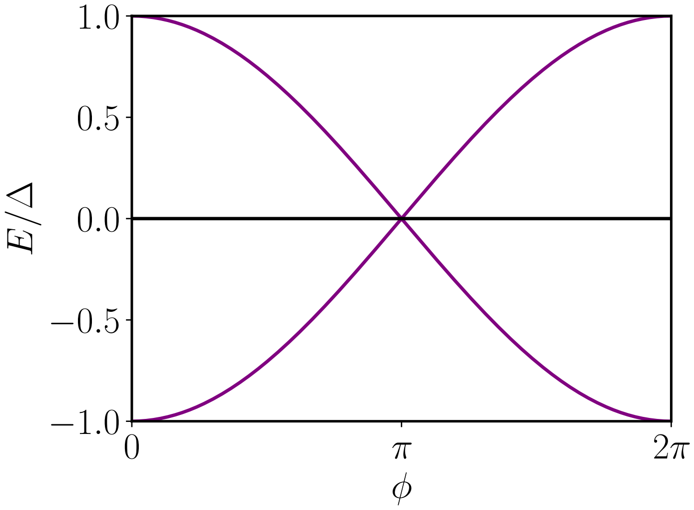

Figure 1.11: Energy spectrum of ABS hosted in a "zero-length" junction.

1.3.2.1 Effect of backscattering

In reality, some disorder will be present in the junction, leading to the scattering of electrons and holes. Therefore, we need to take into account the scattering when calculating the energy spectrum. To do so, we will use the scattering formalism in order to describe the scattering processes in the normal region. Here, we will consider that there is finite backscattering in the normal region and that the length of this region is negligible such that we can model it with a delta potential. The scattering matrix that describes this potential for electrons is the same as in Eq. (1.67)

$$\mathcal{S}_e = e^{i\theta}\begin{pmatrix} r & t \\ t & -r^* \end{pmatrix}. \tag{1.125}$$

At the interfaces, the outgoing electron states will undergo Andreev reflection and therefore reflected as holes. The question is, how can we describe the scattering of holes in the normal region? We still can define ingoing and outgoing states for holes, so we still can use the scattering matrix formalism such that we can write

$$\psi^h_{\text{out}} = \mathcal{S}_h(E)\psi^h_{\text{in}}. \tag{1.126}$$

But, we have to determine what is $\mathcal{S}_h(E)$, the scattering matrix for holes. First of all, the Hamiltonian which describes holes is the opposite of the one which describes electrons. Hence, electrons and holes should be described by similar scattering matrices but with opposite energy dependence. Next, the basis in which we have written the Hamiltonian for holes is the time reversal symmetric of the basis in which we have written the Hamiltonian for electrons (see Appendix A for more details on TRS). Thus, we can write

$$\Theta\psi^e_{\text{out}}(-E) = \mathcal{S}_h(E)\Theta\psi^e_{\text{in}}(-E), \tag{1.127}$$

where Θ is the TRS operator and where we have written the energy dependence explicitly. From this relation, we can easily see that

$$\mathcal{S}_h(E)=\Theta\mathcal{S}_e(-E)\Theta^\dagger. \tag{1.128}$$

Here, we do not consider the spin of particles such that this operator is $\Theta=\mathcal{C}$, where $\mathcal{C}$ denotes complex conjugation. So, in our case, we have

$$\mathcal{S}_h(E)=\mathcal{S}_e^*(-E)=\mathcal{S}_e^*. \tag{1.129}$$

We can now construct a scattering matrix which links outgoing electrons to incoming holes. The reflected hole on the right interface has an amplitude given as $\alpha(E)e^{-i\varphi_R}$, whereas, the ones on the left interface have an amplitude given as $\alpha(E)e^{-i\varphi_L}$. We can therefore link the incoming holes to the outgoing electrons with the matrix

$$\psi^h_{\text{in}}=\alpha(E)r_A(\varphi_L,\varphi_R)\psi^e_{\text{out}}=\alpha(E)\begin{pmatrix}e^{-i\varphi_L} & 0\\ 0 & e^{-i\varphi_R}\end{pmatrix}\psi^e_{\text{out}}. \tag{1.130}$$

To link the Andreev reflected electrons to the outgoing holes, the procedure is the same. It leads to

$$\psi^e_{\text{in}}=\alpha(E)r_A(-\varphi_L,-\varphi_R)\psi^h_{\text{out}}=\alpha(E)\begin{pmatrix}e^{i\varphi_L} & 0\\ 0 & e^{i\varphi_R}\end{pmatrix}\psi^h_{\text{out}}. \tag{1.131}$$

We can combine these equations to obtain

$$\psi^e_{\text{in}}=\alpha^2(E)r_A(-\varphi_L,-\varphi_R)\mathcal{S}_e^*r_A(\varphi_L,\varphi_R)\mathcal{S}_e\psi^e_{\text{in}}\equiv\alpha^2(E)M(\phi)\psi^e_{\text{in}} \tag{1.132}$$

Written in this form allows one to see explicitly that this combination of scattering matrices describes a bound state. An important remark is that here, $M(\phi)$ is to be distinguished from a transfer matrix that we denoted as $\mathcal{M}$ in Sec. 1.2.2. $M(\phi)$ is a product of scattering matrices and so verifies the relation $M^\dagger M=\mathbb{1}$. Also, note that here again only the phase difference matters which is why we did write only a ϕ dependence in $M(\phi)$. Equation (1.132) implies [25]

$$\text{Det}\left[\mathbb{1}-\alpha^2(E)M(\phi)\right]=0. \tag{1.133}$$

Doing the matrix product, we obtain for $M(\phi)$

$$M(\phi)=\begin{pmatrix}R+Te^{-i\phi} & 2i\sqrt{RT}\sin\frac{\phi}{2}e^{-i\frac{\phi}{2}-i\phi_r}\\ 2i\sqrt{RT}\sin\frac{\phi}{2}e^{i\frac{\phi}{2}+i\phi_r} & R+Te^{i\phi}\end{pmatrix}, \tag{1.134}$$

where θ_r is the phase of the reflection coefficient and, we recall that $R=|r|^2$ and $T=|t|^2$. The eigenvalues and eigenvectors of this matrix are found by diagonalizing it. The rotation matrix that diagonalizes it, is

$$W=e^{-i\frac{\delta}{2}\sigma_z}e^{-i\frac{\gamma}{2}\sigma_y}, \tag{1.135}$$

where $\sigma_{y,z}$ are the Pauli matrices and

$$\delta=\theta_r+\frac{\phi}{2},\qquad \gamma=\arctan\frac{-\sqrt{R}}{\sqrt{T}\cos\frac{\phi}{2}}, \tag{1.136}$$

such that,

$$W^\dagger M(\phi)W=\left(R+T\cos\phi\right)\mathbb{1}-2i\,\text{sign}\left(\cos\frac{\phi}{2}\right)\sqrt{T}\sin\frac{\phi}{2}\sqrt{R+T\cos^2\frac{\phi}{2}}\sigma_z=e^{-2i\chi(\phi)\sigma_z}, \tag{1.137}$$

with

$$\chi(\phi)=\arccos\left(\operatorname{sign}\left(\cos\frac{\phi}{2}\right)\sqrt{R+T\cos^2\frac{\phi}{2}}\right). \tag{1.138}$$

The condition for obtaining a bound state can therefore be written as

$$\pm\chi(\phi)-\arccos\frac{E}{\Delta}=q\pi, \tag{1.139}$$

This is very similar to what we obtained for the perfectly transmitted junction, but here instead of a phase factor of $\phi/2$, we have $\chi(\phi)$ due to finite backscattering. This equation leads to,

$$E_\pm=\pm\Delta\sqrt{R+T\cos^2\frac{\phi}{2}}\operatorname{sign}\left(\cos\frac{\phi}{2}\right)=\pm\Delta\sqrt{1-T\sin^2\frac{\phi}{2}}\operatorname{sign}\left(\cos\frac{\phi}{2}\right). \tag{1.140}$$

As expected, in the limit $T\to 1$, we recover the energy spectrum of the perfectly transmitted junction, i.e., $E_\pm=\pm\Delta\cos\phi/2$.

The main effect of adding backscattering is that a gap of $2\Delta\sqrt{R}$ opened at $\phi=\pi$, which results from the mixing of left and right moving particles, as represented in Fig. 1.12. The energy spectrum in this case is represented in Fig. 1.13.

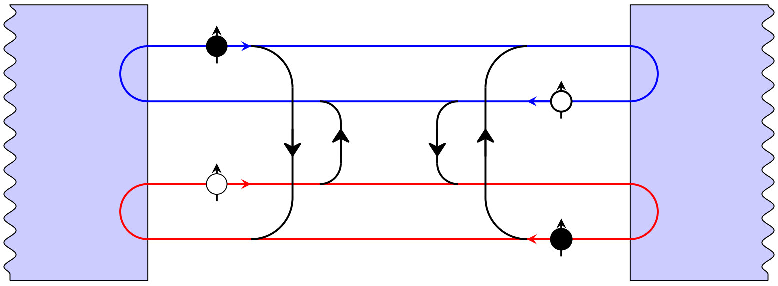

Figure 1.12: Representation of the scattering processes that give rise to the ABS. Due to the finite backscattering, a mixing occurs between the left and right moving particles.

1.3.3 Effect of finite length

Until now, we have neglected the length of the junction. However, as we can see in Eq. (1.123), the length of the junction induced a phase proportional to the energy of ABS. The drawback is that even in the simplest case of perfect transmission, this equation is a transcendental equation, so it is in principle impossible to find an analytical solution to it. However, we can find approximate solutions in certain limits.

1.3.3.1 Short-length limit

The first limit that we can look at is the short length limit, $d/\xi\ll 1$. We introduce the notations $\lambda=d/\xi=\Delta L/(\hbar v_F)$, and $\epsilon=E/\Delta\in[-1,1]$, such that we need to solve

$$\lambda\epsilon+\rho\frac{\phi}{2}-\arccos\epsilon-q\pi=0, \tag{1.141}$$

with $\rho=\pm1$. We can rewrite this equation under the form

$$\epsilon=\cos\left(\lambda\epsilon+\rho\frac{\phi}{2}-q\pi\right)\operatorname{sign}\left[\sin\left(\lambda\epsilon+\rho\frac{\phi}{2}-q\pi\right)\right]. \tag{1.142}$$

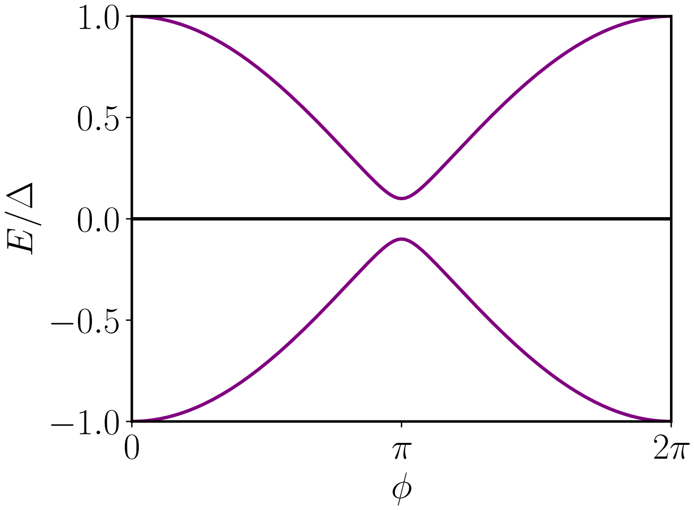

Figure 1.13: Energy spectrum of ABS in a "zero-length" junction in the presence of backscattering at $T = 0.99$.

In the following, we will forget about the sign term, but one has to keep in mind that it restricts the values for which we have solutions for the energies. In particular, we take $q = 0$ and restrain ourselves to the study of $\epsilon > 0$ since we know that particle-hole symmetry implies that for a state at energy ϵ, it exists a state at energy $-\epsilon$. Also, we restrain ourselves to the phase interval $\phi \in [0, 2\lambda\epsilon]$ such that we can write

$$|\epsilon| = \left|\cos\left(\lambda\epsilon + \rho\frac{\phi}{2}\right)\right|. \tag{1.143}$$

In the short length limit, we have $\lambda \ll 1$. Therefore, we can develop this equation up to the second order in λ. It leads to

$$|\epsilon| = \left|\left(1 - \frac{1}{2}\lambda^2\epsilon^2\right)\cos\left(\rho\frac{\phi}{2}\right) - \lambda\epsilon\sin\left(\rho\frac{\phi}{2}\right)\right|. \tag{1.144}$$

By solving this equation, we find the following expression for the energy at the second order in λ

$$|\epsilon_\rho| = \left|\cos\frac{\phi}{2} - \rho\frac{1}{2}\lambda\sin\phi + \frac{1}{4}\lambda^2\cos\frac{\phi}{2}\left(1 - 3\cos\phi\right)\right|. \tag{1.145}$$

We can see that the effect of length is to bring out a new ABS as shown in Fig. 1.14. However, where the first level extends over the entire phase range, i.e., from $\phi = 0$ to $\phi = 2\pi$, this new level quickly joins the continuum of states when $|\epsilon| = 1$. We can develop Eq. (1.145) around $\phi \to 0$ in order to find when this new state joins the continuum. We find

$$|\epsilon_\rho| \approx 1 - \frac{\lambda^2}{2} - \rho\frac{\lambda}{2}\phi - \frac{1}{8}\phi^2. \tag{1.146}$$

This equation allows us to see that the maximal allowed value for ϕ for the solution with $\rho = -1$ is $\phi_{\max} = 2\lambda$, and that the two states crossed each other at $\phi_c = 0$ with an energy given as $\epsilon_c = 1 - \lambda^2/2$.

We can make the analogy with a potential well to understand the effect of the length. In a potential well, the number of bound states is dictated by the height and the width of this potential, such that, the number of states increases with them. In some way, the normal region of a Josephson junction is a potential well with height fixed by the value of the superconducting gap. Therefore, the number of ABS hosted

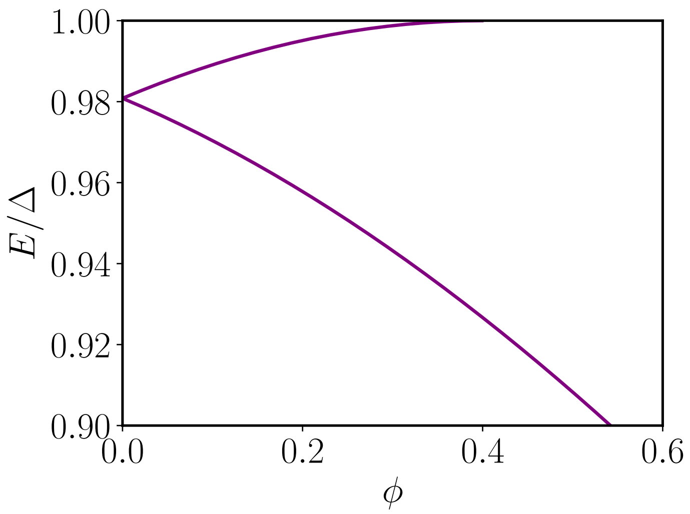

Figure 1.14: Energy spectrum of ABS for a short length junction. Due to the finite length of the junction, an additional level appears but quickly joins the continuum in the short length limit. In this case, we took $\lambda = 0.2$.

in the junction depends on the length of the normal region. In fact, the number of states is determined by the minimal and maximal value of q in Eq. (1.141). Each new ABS is gradually detached from the continuum. Thus, for positive energy, and for $0 < \phi < 2\pi$, we take $\epsilon = 1$ in Eq. (1.141) which gives the maximum allowed value for q. We find $q_{\max} = [(\lambda + \rho\phi/2)/\pi]$. For negative energy, we just have to take $\epsilon = -1$ leading to $q_{\min} = -1 - [(\lambda - \rho\phi/2)/\pi]$. In $q_{\max}$ and $q_{\min}$, $[x]$ refers to the integer part of x.

As for the zero length limit, we can try to include the effect of backscattering. As we can see in Fig. 1.15, adding backscattering leads to the opening of a gap between the two levels at $\phi = \phi_c$. We will model the scattering in the normal region as a combination of free propagation and of scattering on a delta potential placed at $x = x_0$. The matrix which describes the scattering of electrons is the same as Eq. (1.80), which reads

$$\mathcal{S}_e(E) = e^{i\theta + ikd} \begin{pmatrix} r e^{ikd\tilde{x}_0} & t \\ t^* & -r^* e^{-ikd\tilde{x}_0} \end{pmatrix}, \tag{1.147}$$

with $\tilde{x}_0 = 2x_0/d - 1$ and $k = k_F + E/(\hbar v_F)$. Adding the effect of finite length results in an additional global phase factor as well as a phase for the reflection, which both depend on the energy. To obtain the transcendental equation for the energy spectrum, the procedure is the same as for the “zero-length” junction case. This equation takes the form

$$\lambda\epsilon \pm \arccos\sqrt{\frac{1 + T\cos\phi + R\cos(2\lambda\epsilon\tilde{x}_0)}{2}} - \arccos\epsilon - n\pi = 0. \tag{1.148}$$

In order to characterize the gap which opened due to the finite value of R, we will treat R perturbatively and place ourselves at $\phi = 0$ where the crossing occurs at perfect transmission. At this phase, the energy of the lowest energy state is $\epsilon = \epsilon_c - \delta$ with $\epsilon_c = 1 - \lambda^2/2$ the energy at which the two states crossed at perfect transmission. At first order in $\sqrt{R}$, for the lowest energy state, Eq. (1.148) becomes

$$\lambda(\epsilon_c - \delta) + \sqrt{R}|\sin(\lambda(\epsilon_c - \delta)\tilde{x}_0)| - \arccos(\epsilon_c - \delta) = 0. \tag{1.149}$$

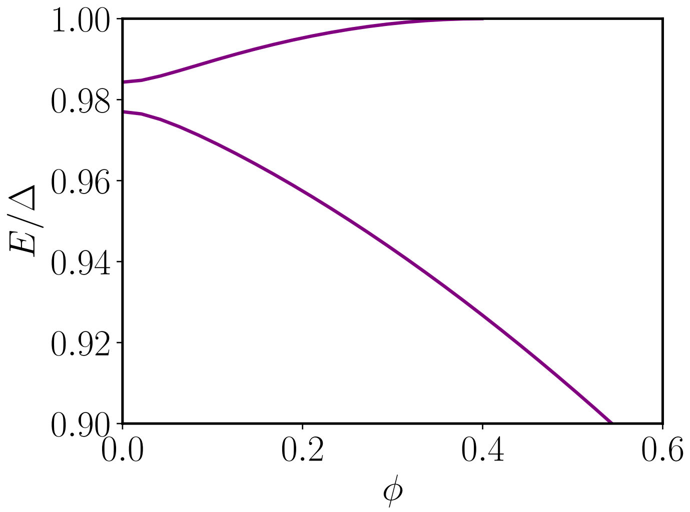

Figure 1.15: Finite backscattering leads to the opening of a gap at $\phi = 0$ between the two states. Here, we model the scattering with a single delta potential placed at position x_0. We took $\lambda = 0.2$, $T = 0.99$ and $x_0 = d$.

By Assuming $\lambda, \delta \ll 1$, we develop this equation at the second order in λ and first order in δ, we obtain the following expression for δ

$$\delta = \sqrt{R}\lambda^2 |\tilde{x}_0|. \tag{1.150}$$

As we see, with this model, the gap depends on the position of the delta potential in the normal region and can even lead to a closing of this gap when the potential is placed at the middle of the normal region even though there is finite backscattering. Indeed, when the potential is at this particular position, the phase acquired from the propagation in the normal region is the same for the reflected and transmitted particles. Thus, at $\phi = 0$, the only phase acquired by particles which form the ABS is the phase acquired through propagation. This phase being the same for reflected and transmitted particles, the resulting ABS have the same energy at $\phi = 0$. The resulting energies of the two states can be obtained by finding the eigenvalues of the matrix

$$\begin{pmatrix} \epsilon_+ & \delta \\ \delta & \epsilon_- \end{pmatrix}, \tag{1.151}$$

where $\epsilon_\pm$ correspond to the state with a positive / negative slope with the phase (see Eq. (1.146)). The eigenvalues of this matrix are

$$\epsilon_{>/<} = \frac{1}{2}\left[\epsilon_+ + \epsilon_- \pm \sqrt{(\epsilon_+ - \epsilon_-)^2 + 4\delta^2}\right], \tag{1.152}$$

where $\epsilon_>$ correspond to the state with the highest energy and $\epsilon_<$ to the state of lowest energy. A complementary view on the structure of Andreev levels in the vicinity of zero phase is discussed in Ref. [67]

1.3.3.2 Low energy limit and long length junction

The other limit that we can look at is the low energy limit $\epsilon \ll 1$. Hence, we can develop Eq. (1.141) at the first order in ϵ, which leads to

$$(1+\lambda)\epsilon + \rho\frac{\phi}{2} - (2q+1)\pi = 0. \tag{1.153}$$

With this form, it is easy to find the energy spectrum

$$\epsilon_{q,\rho} = \frac{1}{2}\frac{(2q+1)\pi - \rho\phi}{1+\lambda}. \tag{1.154}$$

This expression for the energy works for arbitrary length junction. Nevertheless, where for a short junction this expression works for phases close to π, we can see that, for high values of λ, i.e., for a long length junction, we can use this expression for phases in the range $\phi \in [0, 2\pi]$ for the lowest values of q. For the remainder of this section, we will only look at positive energies since we know that for each positive energy solution, there is a negative energy one. In addition, we restrict ourselves to the interval $[0, \pi]$, since the spectrum is symmetric with respect to π. As for the short junction, we can see that the different states cross each other at different phases (see Fig. 1.16). Between two states with the same values for q, we can see that the energy level with a positive slope and the one with a negative slope cross each other at $\phi_c = 0$ with an energy $\epsilon_c \approx (2q+1)\pi/(2\lambda)$. The other crossings are between states ϵ_q and ϵ_{q+1} with opposite slope. One can easily see that the crossings occur at $\phi = \pi$ at the energy $\epsilon_c \approx (q+1)\pi/\lambda$.

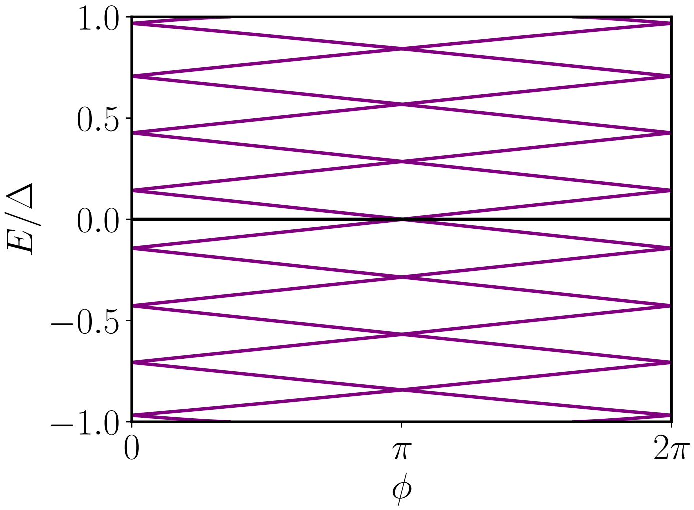

Figure 1.16: Energy spectrum of ABS in the long length limit. We took $\lambda = 10$.

Here again, we can see in Fig. 1.17, that adding finite backscattering leads to the opening of gaps at those crossings. With the same calculation as for the short length junction, assuming $\sqrt{R}, \lambda\delta, \epsilon_c \ll 1$ and $\lambda \gg 1$, we can develop Eq. (1.148) around ϕ_c, at the lowest order in $\sqrt{R}$ and δ which allows us to find the value of δ for the different crossings. Thus, for the crossing between states with the same value of q, we find a gap δ given as

$$\delta_{0,q} \approx \sqrt{R}\left|\sin\left((2q+1)\pi\frac{\tilde{x}_0}{2}\right)\right|/\lambda, \tag{1.155}$$

whereas for the states q and $q+1$, we find

$$\delta_{\pi,q} \approx \sqrt{R}|\cos\left((q+1)\pi\tilde{x}_0\right)|/\lambda. \tag{1.156}$$

The modification of the energies around the phases at which those gaps open is again given by Eq. (1.152). As for the short length limit, we can see that depending on the position of the delta potential the gaps between different ABS can be closed even if we have finite backscattering [68, 69].

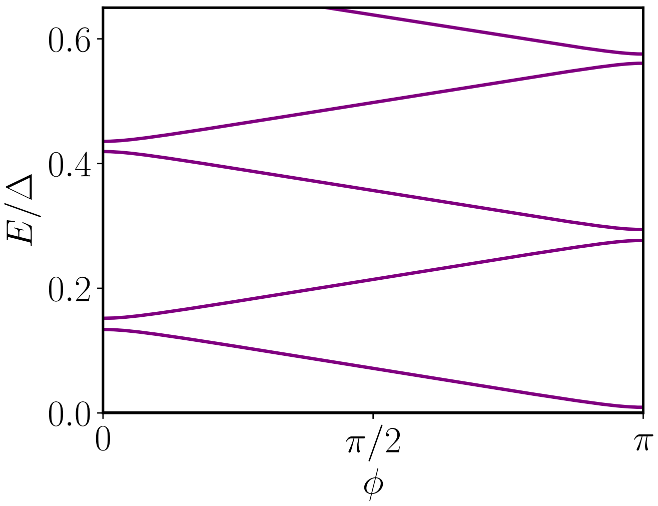

Figure 1.17: Gaps opening in the energy spectrum of ABS in the long length limit with finite backscattering. Here, we took $\lambda = 10$, $T = 0.99$ and $x_0 = d$.

1.3.3.3 Particular case of the double delta potential

As we have seen in the scattering formalism section (see Sec. 1.2), a scattering region with two delta potentials separated by a region of a given length can present peaks of transmission even at high potential. In addition, we discussed in Sec. 1.2.3.1 why this model is well suited for describing junctions containing a quantum dot. Therefore, we will here look at the effect of this kind of scattering on the energy spectrum of ABS. We will first discuss the general properties of the energy spectrum of ABS with this model, then focus on a resonant level. As for the single delta potential, we have already done the calculation of the scattering matrix for electrons. This matrix reads

$$\mathcal{S}_e(E) = e^{i\tilde{\theta}(E)} \begin{pmatrix} \tilde{r}(E) & \tilde{t}(E) \\ \tilde{t}(E) & -\tilde{r}^*(E) \end{pmatrix}, \tag{1.157}$$

where $\tilde{t}(E)$, $\tilde{r}(E)$ and $\tilde{\theta}(E)$ are given by Eq. eq. (1.84), Eq. (1.85), and Eq. (1.86) respectively. Also, we introduced the quantity

$$2\varphi_{\text{tot}} = 2k_F d - \arctan\beta_R - \arctan\beta_L, \tag{1.158}$$

with $\beta_{R/L} = V_{R/L}/(\hbar v_F)$ where $V_{R/L}$ the height of the right/left delta potential respectively and

$$|K(E)|^2 = (1-\sqrt{R_L R_R})^2 + 4\sqrt{R_R R_L}\cos^2\left(\varphi_{\text{tot}} + \lambda\epsilon\right). \tag{1.159}$$

We will consider this scattering region as the normal region of the Josephson junction, such that the delta potentials represent non-perfect interfaces between the superconducting electrode and a normal region of perfect transmission.

The transcendental equation which allows one to determine the energy spectrum can be obtained with the same procedure as for the single delta potential model. It leads to

$$\frac{\tilde{\theta}(E)-\tilde{\theta}(-E)}{2} \pm \arccos\sqrt{\frac{1+\mathrm{Re}[\tilde{t}*(-\epsilon)\tilde{t}(\epsilon)e^{-i\phi}]+\mathrm{Re}[\tilde{r}*(-\epsilon)\tilde{r}(\epsilon)]}{2}} - \arccos\epsilon - q\pi = 0. \tag{1.160}$$

Neglecting the effect of length, we can write the energy in the same form as for the single delta potential

$$\epsilon = \pm\sqrt{\tilde{R} + \tilde{T}\cos^2\frac{\phi}{2}}, \tag{1.161}$$

with $\tilde{R} = |\tilde{r}|^2$ and $\tilde{T} = |\tilde{t}|^2$. When we consider a non zero-length junction, we can as before find limiting regimes to obtain an approximate expression for the energy spectrum. Far from the resonance condition, the single potential and double potential yield a very similar energy spectrum. This is because, in this case, the reflection and transmission coefficients for the double delta potential model are simply rescaled compared to the single delta potential model. Here, we mainly want to characterize the energy spectrum when the resonnance condition is satisfied, i.e., when $V_R = V_L$ and $\tilde{T}(E) = \tilde{T}(-E) = 1$ even when $V_{R/L} \neq 0$.

This energy dependence in the resonance condition implies that the energy spectrum of ABS in a finite length junction can present features of a junction with perfect transmission only for peculiar values of ϵ and ϕ. The main feature of a junction with perfect transmission is the crossing between positive and negative energy ABS at $\phi = \pi$. This crossing happens at energy $\epsilon_c = 0$ such that the condition for resonance is given by $\varphi_{\text{tot}} = (2n+1)\pi/2$ with $n \in \mathbb{Z}$. In fact, other gaps can be closed even when we are not at resonance [70, 71]. This can happen when,

$$\arccos\sqrt{\frac{1 + \text{Re}[\tilde{t}*(-\epsilon)\tilde{t}(\epsilon)e^{-i\phi}] + \text{Re}[\tilde{r}*(-\epsilon)\tilde{r}(\epsilon)]}{2}} = (q_1 - q_2)\frac{\pi}{2}, \tag{1.162}$$

such that the states with the same or different values q and opposite ρ have the same energy. In both case, this is possible when $|K(E)| = |K(-E)|$ and when $\phi = n\pi$ and does not necessarily implies $\tilde{T}(E) = \tilde{T}(-E) = 1$. If $q_1 = q_2$, then the gap at $\phi = 0$ is close when $\varphi_{\text{tot}} = n\pi$. For $q_1 = q_2 + 1$, then, it is the gap at $\phi = \pi$ which is close when $\varphi_{\text{tot}} = (2n+1)\pi/2$. Different cases are shown in Fig. 1.18

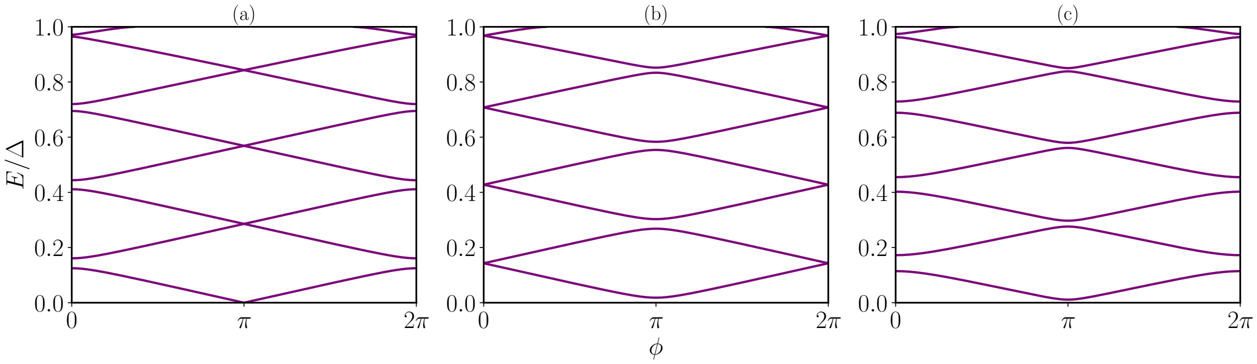

Figure 1.18: Energy spectrum of ABS in the long length limit $\lambda = 10$ with the two delta potential model. On the panel (a) and (b), we set $T_R = T_L = 0.99$. In the panel (a), we set $\varphi_{\text{tot}} = \pi/2$ such that all the gaps at $\phi = \pi$ are closed due to the resonance conditions being satisfied. In panel (b), we have $\varphi_{\text{tot}} = \pi$, which results in the closing of the gaps at $\phi = 0$. Finally, in panel (c), we set $T_L \neq T_R$ and $\varphi_{\text{tot}} = \pi$. In this last situation, the resonance condition is not satisfied and therefore, all the gaps are opened.

1.3.4 Resonant level

We have previously discussed the energy spectrum of ABS for a model with two delta potentials. As pointed out in Sec. 1.2.3.1 this model is well suited to describe a junction with a quantum dot. In the following, we will discuss Josephson junctions where the normal region is a quantum dot that we will model as a single energy level which can be doubly occupied. Therefore, we will here focus on a single resonant level E_r. In addition, we will neglect Coulomb repulsion on the dot. This will allow us to obtain the energy spectrum of ABS in a superconductor - quantum dot - superconductor (S-QD-S) junction. In Sec. 1.2.3.1, we already derived the transmission coefficient in Eq. (1.96) for such scenario. The equation that determines the energy of ABS is still given by Eq. (1.160). Multiplying this equation by a factor 2, rearranging the terms and using the cos function, we obtain

$$\left(1-2\frac{E^2}{\Delta^2}\right)\cos\left(\tilde{\theta}(E)-\tilde{\theta}(-E)\right)+2\frac{E}{\Delta}\sqrt{1-\frac{E^2}{\Delta^2}}\sin\left(\tilde{\theta}(E)-\tilde{\theta}(-E)\right)-\mathrm{Re}[\tilde{t}^*(-\epsilon)\tilde{t}(\epsilon)e^{-i\phi}]-\mathrm{Re}[\tilde{r}^*(-\epsilon)\tilde{r}(\epsilon)]=0, \tag{1.163}$$

Plugin $2\varphi_{\mathrm{tot}}=(2n+1)\pi-E_r d/(\hbar v_F)$, $R_j=1-2d\Gamma_j/(\hbar v_F)$ and developing at the second order in Γ_j and the lowest order in d, leads to [72]

$$0=\left(\Delta^2-E^2\right)\left(E^2-E_r^2-\Gamma^2/4\right)+E^2\Gamma\sqrt{\Delta^2-E^2}+\Delta^2\Gamma_R\Gamma_L\sin^2\frac{\phi}{2}, \tag{1.164}$$

with $\Gamma=\Gamma_L+\Gamma_R$. If we suppose E small compared to other energies and keep only the terms at second order in E, we can solve this equation. We obtain

$$E=\pm\Delta_{\mathrm{eff}}\sqrt{1-\tau_{\mathrm{eff}}\sin^2\frac{\phi}{2}}, \tag{1.165}$$

with

$$\Delta_{\mathrm{eff}}=\sqrt{\frac{\Delta^2}{1+\frac{4\Delta^2+\Delta\Gamma}{4E_r^2+\Gamma^2}}}, \qquad \tau_{\mathrm{eff}}=\frac{4\Gamma_L\Gamma_R}{4E_r^2+\Gamma^2}, \tag{1.166}$$

which has the same form as the expression for the energy spectrum of a zero-length junction, but, with an effective gap Δ_{eff} and an effective transparency τ_{eff}. In the limit of a large coupling with the leads $\Gamma_j=T_j\hbar v_F/(2d)\gg 1$, the effective gap tends to $\Delta_{\mathrm{eff}}\to\Delta$. We can also note that the effective transparency is given by $\tilde{T}(E_r)$. Γ_j describing the coupling between the normal region and the superconducting leads, it makes sense that the effective gap Δ_{eff} shrinks as Γ gets smaller since the normal region gets less coupled to the superconductors. The energy spectrum obtained with Eq. (1.164) is shown in Fig. 1.19 for different limits. As we can see, the energy spectrum is very well described by Eq. (1.165) in all of these limits.

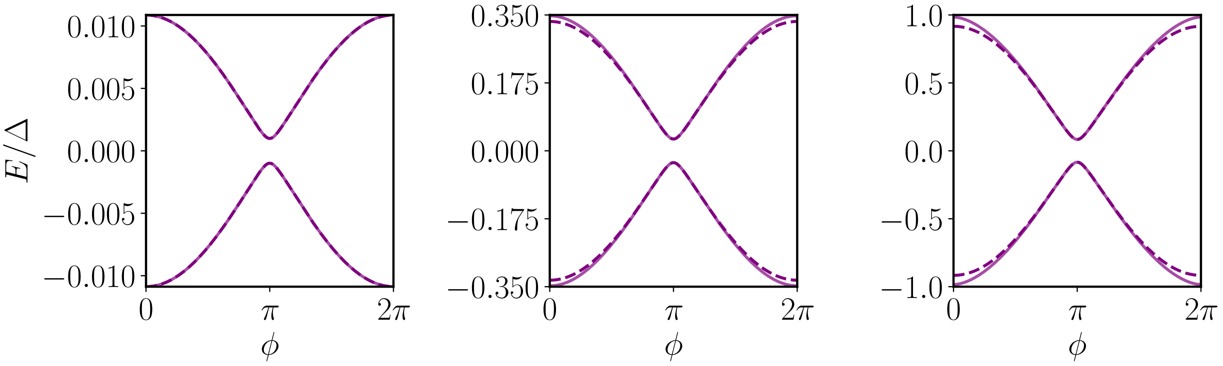

Figure 1.19: Energy spectrum for resonant level in different limits obtained with Eq. (1.164) and Eq. (1.165) represented in full and dashed lines respectively. For all the panels, we have $\Gamma_R/\Gamma_L = 1.2$ and $E_r = 0$, such that the effective transmission τ_{eff} is the same for all panels. To the left, we are in the limit $\Gamma/\Delta \ll 1$ such that the effective gap is given as $\Delta_{\text{eff}} \approx \Gamma/2$. In the middle panel, we have $\Gamma = \Delta$, therefore the effective gap is given as $\Delta_{\text{eff}} \approx \Delta/3$. Finally, on the right panel, we are in the limit $\Gamma/\Delta \gg 1$, which leads to $\Delta_{\text{eff}} \approx \Delta$. As one can see, the maximal value of E/Δ is different in each panel as it is limited by Δ_{eff}.

1.4 The S-QD-S junction

In this section, we will study in more detail the S-QD-S junction. As we said earlier, this kind of junction can be seen as a limit case of the S-N-S Josephson junction, where we model the normal region by two potentials separating a small normal region from the superconducting electrodes. But, before discussing the S-QD-S junction, we will discuss the simpler case of a normal metal-quantum dot-normal metal (N-QD-N) junction.

The particularity of this system is that the number of electrons on a quantum dot can be experimentally controlled by a gate electrode. This gate, which is capacitively coupled to the dot, allows the manipulation of its electrochemical potential and thus the shifting of energy levels relative to the Fermi level. By adjusting this gate so that one of the dot's levels is in resonance, electrons readily tunnel from the electrodes to the dot. In the previous section, we did not consider Coulomb repulsion. However, due to the limited size of the dot, Coulomb repulsion can be significant. The consequence of this is that adding an electron means overcoming the Coulomb repulsion from the other electrons in the dot. Hence, this additional energy cost makes it less probable for electrons to be added to the dot. Consequently, at low temperatures, the Coulomb interaction suppresses the conductance except at the so-called charge degeneracy points. We refer to this phenomenon as Coulomb blockade [73–75]. At these points of charge degeneracy, the states with n and $n \pm 1$ electrons on the dot have the same energy. This allows electrons to hop on off the dots without having to overcome a barrier. This leads to the apparition of a periodic peak pattern in the conduction, which is accessible experimentally. This pattern, known as Coulomb diamonds is represented in Fig. 1.20 for a single-layer graphene quantum dot from [76]. This figure shows the differential conductance as a function of the bias voltage V_{bias} versus the gate voltage V_{PG}. The effect of V_{PG} is simply to shift the energy levels of the dot. We can see the characteristic diamond shape.

Since the number of electrons on the dot can be manipulated, it means that the total spin S on the dot can also be manipulated. It turns out that each level of the quantum dot can be doubly occupied. Thus, when the number of electrons occupying the last occupied level of the dot is even, the total spin on the dot is zero while, when there is an odd number of electrons the total is $S = 1/2$. In the latter case,

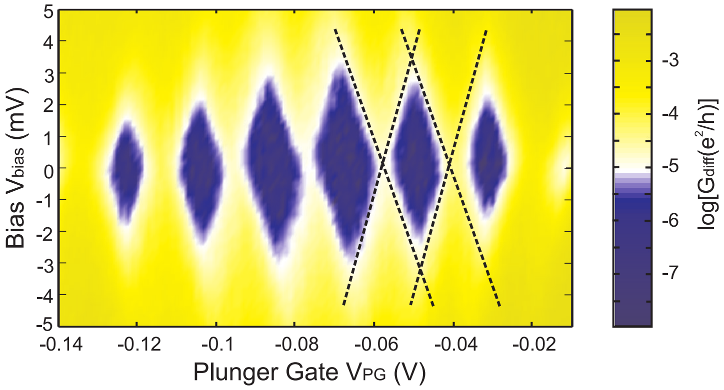

Figure 1.20: Differential conductance of a single-layer graphene quantum dot connected to a source and a drain obtained by C. Stampfer et al. in [76].

this localized spin can be seen as a magnetic impurity surrounded by a Fermi sea, a role played by the two normal electrodes. This is precisely the situation in which the so-called Kondo effect can be observed [77]. In this case, adding a second electron will cost an on-site Coulomb energy. If this energy is superior to the Fermi energy of the normal electrodes $\mu_{R/L}$ then, an electron cannot tunnel into the dot. Moreover, if the on-site energy of the dot ε_d is smaller than the Fermi energy of the leads, the electron on the dot cannot tunnel off the dot. This is what we depicted earlier when we talked about Coulomb blockade. However, even if first order tunneling leads to a high energy state, higher order processes in which an intermediate state is of high energy are allowed provided the system returns back to a low energy state at the end. We are interested in virtual tunneling events that effectively flip the spin on the dot (see Fig. 1.21). A succession of these spin-flip processes will effectively screen the local spin on the dot such that the electrons in the normal leads and on the dot together form a spin-singlet state. This correlated state gives rise to the Kondo effect. In a quantum dot, this effect leads to an increase of the density of states near the Fermi energy resulting in an increase of the differential conductance at zero bias when the dot is occupied by an odd number of electrons. In contrast, the Kondo effect leads to an increase of resistivity in the case of a magnetic impurity in a bulk metal. In this scenario, the impurity constitutes a scattering center for the freely moving electrons. Replacing the normal electrodes by superconducting electrodes such that we now have an S-QD-S junction leads to more complex behavior and different physics. For instance, an interesting interplay between the physics of the Kondo effect and superconductivity can take place. In the S-QD-S, the characteristic energy of the conduction bands is set by the superconducting gap Δ. Thus, the ground state of this kind of junction results from a competition between the Kondo effect and superconductivity.

In general, quantum dots can host several levels which can be coupled between each other due to multiple interactions such as Coulomb or spin-spin interactions. When in a junction, each level in the dot can be coupled to the electrodes, with a coupling that is level dependent. Due to these multiple interactions and couplings, an exact modeling of a dot coupled to an electrode is impossible. However, if the device exhibits relatively large level spacing, we can simplify the description of the dot by keeping only the electronic level closest to the Fermi energy. This approximation may be justified as the occupation of the level closest to the Fermi energy is most likely to change. A simple Hamiltonian which describes this kind of quantum dot coupled to two superconducting electrodes is the Anderson model,

$$H = \sum_{a=L,R} H_a + H_D + \sum_{a=L,R} H_{T,a}, \tag{1.167}$$

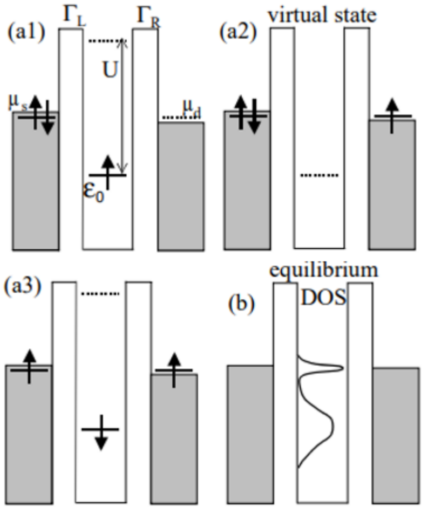

Figure 1.21: Schematic representation of virtual processes leading to a spin flip of the spin on the dot from [78]. In (a1), the state won't change from first order tunneling processes as it would cost the Coulomb energy to add an electron on the dot. However, higher order processes allow to transfer the electron of the dot to the right electrode (panel (a2)) such that the system is in a virtual high energy state. Then, an electron from the left electrode will tunnel to the quantum dot leaving the system in a low energy state with a spin-flip of the spin in the quantum dot (panel (a3)). The Kondo effect results in an increase of the density of state (DOS) around the Fermi energy as depicted in panel (b).

with

$$H_a = \sum_{\boldsymbol{k},\sigma} \xi_{\boldsymbol{k},a} c^\dagger_{\boldsymbol{k},\sigma,a} c_{\boldsymbol{k},\sigma,a} + \sum_{\boldsymbol{k}} \left(\Delta_a c^\dagger_{\boldsymbol{k},\uparrow,a} c^\dagger_{\boldsymbol{k},\downarrow,a} + \text{h.c.} \right), \tag{1.168}$$

$$H_D = \sum_{\sigma} \varepsilon_d d^\dagger_\sigma d_\sigma + U n_\uparrow n_\downarrow, \tag{1.169}$$

$$H_{T,a} = \sum_{\boldsymbol{k},\sigma} (t_a d^\dagger_\sigma c_{\boldsymbol{k},\sigma,a} + \text{h.c.}). \tag{1.170}$$

In those equations, d_σ is the annihilation operator of an electron of spin σ on the dot, $c_{\boldsymbol{k},\sigma,a}$ the one of an electron with spin σ, momentum $\boldsymbol{k}$ on the superconducting electrode $a = L, R$ which stands for the left or right electrode. The operator $n_\sigma = d^\dagger_\sigma d_\sigma$ is the number operator. $\xi_{\boldsymbol{k},a}$ is the energy of an electron of momentum $\boldsymbol{k}$, spin σ in the electrode i and Δ_i the superconducting gap of this electrode. ε_d is the on-site energy of the dot and U, the strength of the Coulomb interaction. The couplings between the dot and the electrodes a are set by t_a, with t_a real.

In the atomic limit, i.e., when the dot is decoupled from the leads, we can see that depending on the values of ε_d and U, a certain number of electrons on the dot will be preferential from an energy point of view. U corresponding to the Coulomb interaction, we know it is a positive value. Thus, we can see that for $\varepsilon_d \geq 0$, the state with 0 particles will be preferred as a ground state for the dot. In the case $\varepsilon_d < 0$, if $U > -\varepsilon_d$, the state with one electron on the dot will be preferred, whereas, if $U < -\varepsilon_d$, it is the state with two electrons on the dot that will be preferred. To simplify the discussion of the S-QD-S junction, we will make the following assumptions:

- The leads are described by conventional BCS superconductors with the same gap amplitude $\Delta_a = \Delta e^{i\varphi_a}$.

- We assume that we have the same constant normal-state density of state ν_S in the superconductors.
- We assume an $\boldsymbol{k}$ - independent tunneling amplitude t_a, i.e., the electrons always tunnel from the same position in the leads.

An exact theoretical description of a quantum dot coupled to superconducting leads is only possible when the Coulomb interaction is fully neglected. In the beginning, a non-superconducting version of this Hamiltonian was used to describe the Kondo effect [79] we discussed earlier. Experimentally, the Coulomb interaction U, the gap Δ and the hybridization $\Gamma_a = \pi \nu_S t_a^2$ energies are typically all of the same order of magnitude, which represents a challenge for analytical techniques [80, 81]. As a result, this model Hamiltonian has been studied using various analytical approaches, such as perturbative expansions in the Coulomb interaction [82] or in the tunnel coupling [83]. However, these techniques are unable to describe entirely the physics of a quantum dot coupled to superconducting electrodes. Non-perturbative calculations, like numerical simulations based on the numerical renormalization group (NRG) [84–87] or quantum Monte Carlo methods [88], have also been developed to address this problem. However, these non-perturbative methods are computationally expensive, as they require resources and time. This limitation can restrict the size of the system or the timescale that can be realistically simulated. Nevertheless, we can try to give at least a qualitative description of these kinds of junctions. Therefore, we will consider here what is called the "atomic limit". In this limit, we consider the superconducting gap as being the dominant characteristic energy of the system, such that $\Delta \to \infty$. It might then be tempting to project the total Hamiltonian into the low energy sector, i.e., in the subspace describing the quantum dot. Unfortunately, this would simply describe an isolated quantum dot and would not capture the physic induced by the coupling between the dot and the electrodes. In order to go around this problem, we will use the Schrieffer-Wolff transformation, which allows us capturing this coupling even in the low energy sector.

1.4.1 Schrieffer-Wolff transformation

The Schrieffer-Wolff transformation is a version of degenerate perturbation theory in which the low energy Hamiltonian is obtained from the exact one by a unitary transformation decoupling the low and high energy sectors. This transformation was initially proposed by Schrieffer and Wolff as the name suggests, with the aim of describing the Kondo effect in the single impurity Anderson model (SIAM) [89, 90]. Our model is a superconducting version of this model where the dot plays the role of the impurity and the tunnel couplings between the dot and the superconducting leads play the role of a perturbation coupling the low and high energy sector, i.e., the dot and the superconducting leads. The Hamiltonian of this model can be written in a general way as,

$$H_{\text{SIAM}} = H = H_L + H_H + \lambda V = H_0 + \lambda V, \tag{1.171}$$

where the subscripts L and H denote the low and high energy sectors and V is the coupling between the two sectors. We define the projectors onto the high and low energy subspace as $P_H = \sum_{|\Phi_H\rangle} |\Phi_H\rangle \langle \Phi_H|$ and $P_L = \sum_{|\Phi_L\rangle} |\Phi_L\rangle \langle \Phi_L|$. To capture the coupling between the two sectors when looking at the low energy excitations of the system, Schrieffer and Wolff proposed to perform a well-chosen unitary transformation of the Hamiltonian before projecting onto the low energy sector. By defining this transformation as $U = e^{\lambda S}$, such that $S = -S^\dagger$, with the requirement of eliminating the linear term in λ, we obtain the Hamiltonian

$$\tilde{H} = U H U^\dagger. \tag{1.172}$$

By using a series expansion, we can write

$$\tilde{H} = H + \lambda[S,H] + \frac{\lambda^2}{2}[S,[S,H]] + \cdots + \frac{\lambda^n}{n!}[S,H]_n + \cdots. \tag{1.173}$$

Eliminating the linear term in λ implies $[S,H_0]=-V$. Using this conditions leads to the following expression for the transformed Hamiltonian

$$\tilde{H}=H_0+\sum_{n=1}^{\infty}\frac{n\lambda^{n+1}}{(n+1)!}[S,V]_n\,. \tag{1.174}$$

Now, the question is how to appropriately choose S. First, we can write all the terms in the form

$$H_0=P_LHP_L+P_HHP_H=\begin{pmatrix}H_L & 0\\ 0 & H_H\end{pmatrix}, \tag{1.175}$$

$$V=P_LHP_H+P_HHP_L=\begin{pmatrix}0 & \mathcal{V}^\dagger\\ \mathcal{V} & 0\end{pmatrix}, \tag{1.176}$$

$$S=\begin{pmatrix}0 & -\mathcal{S}^\dagger\\ \mathcal{S} & 0\end{pmatrix}. \tag{1.177}$$

Finally, using the condition $[H_0,S]=V$, we obtain

$$S=\sum_{|\Phi_L\rangle|\Phi_H\rangle}|\Phi_H\rangle\frac{\langle\Phi_H|\,V\,|\Phi_L\rangle}{\langle\Phi_H|\,H_H\,|\Phi_H\rangle-\langle\Phi_L|\,H_L\,|\Phi_L\rangle}\langle\Phi_L|-\text{h.c.}. \tag{1.178}$$

To construct a low energy effective Hamiltonian, one has to project $\tilde{H}$ onto the low energy sector, i.e.

$$H_{\text{eff}}=P_L\tilde{H}P_L. \tag{1.179}$$

Due to the off-diagonal structure of S, one can see that only the even orders in V of $\tilde{H}$ will contribute to the modification of the initial low energy Hamiltonian H_L.

1.4.2 Effective Hamiltonian and energy spectrum of the S-QD-S junction

Now that we have all the tools we need, we can construct the effective low energy Hamiltonian, which describes the S-QD-S junction. Using the previous notation, we have

$$\lambda V=\sum_{a=L,R}H_{T,a}. \tag{1.180}$$

The high energy sector is constituted by states with quasiparticle excitations in the superconducting leads, while the low energy sector by states without quasiparticles in the leads. First, we diagonalize the superconducting Hamiltonian using the Bogoliubov-de Gennes transformation

$$c_{\boldsymbol{k},\sigma,a}=e^{i\varphi_a/2}(u_{\boldsymbol{k}}\gamma_{\boldsymbol{k},\sigma,a}-\sigma v_{\boldsymbol{k}}\gamma^\dagger_{-\boldsymbol{k},-\sigma,a}). \tag{1.181}$$

Thus, we can write the superconducting Hamiltonian and the tunnel Hamiltonian as

$$H_a=\sum_{\boldsymbol{k},\sigma}E_{\boldsymbol{k},a}\gamma^\dagger_{\boldsymbol{k},\sigma,a}\gamma_{\boldsymbol{k},\sigma,a}, \tag{1.182}$$

$$H_{T,a}=t\sum_{\boldsymbol{k},\sigma}\left[\gamma^\dagger_{\boldsymbol{k},\sigma,a}\left(u_{\boldsymbol{k}}e^{-i\varphi_a/2}d_\sigma-\sigma v_{\boldsymbol{k}}e^{i\varphi_a/2}d^\dagger_{-\sigma}\right)+\text{h.c.}\right]. \tag{1.183}$$

Now, we perform the Schrieffer-Wolff transformation at the lowest order in $[S,H_{T,a}]$ and project onto the low energy sector,

$$H_{\text{eff}}=H_D+\frac{1}{2}P_L\left[S,\sum_{a=L,R}H_{T,a}\right]P_L, \tag{1.184}$$

which at the lowest order in $1/H_a$ such that the terms $1/(H_a - H_D) \approx 1/H_a$ gives

$$H_{\text{eff}} = H_D - \frac{1}{2}\sum_{a=L,R}\sum_{|\Phi_H\rangle,|\Phi_L\rangle,\left|\Phi'_L\right\rangle} |\Phi_L\rangle \left(\frac{\langle\Phi_L| H_{T,a} |\Phi_H\rangle \langle\Phi_H| H_{T,a} \left|\Phi'_L\right\rangle}{\langle\Phi_H| H |\Phi_H\rangle - \langle\Phi_L| H |\Phi_L\rangle} + \frac{\langle\Phi_L| H_{T,a} |\Phi_H\rangle \langle\Phi_H| H_{T,a} \left|\Phi'_L\right\rangle}{\langle\Phi_H| H |\Phi_H\rangle - \left\langle\Phi'_L\right| H \left|\Phi'_L\right\rangle} \right) \left\langle\Phi'_L\right|, \tag{1.185}$$

$$= H_D - \sum_{a=L,R}\sum_{|\Phi_H\rangle,|\Phi_L\rangle,\left|\Phi'_L\right\rangle} |\Phi_L\rangle \langle\Phi_L| H_{T,a} |\Phi_H\rangle \langle\Phi_H| \frac{1}{H} |\Phi_H\rangle \langle\Phi_H| H_{T,i} \left|\Phi'_L\right\rangle \left\langle\Phi'_L\right|, \tag{1.186}$$

$$= H_D - \sum_{a=L,R} t_a^2 \left[\sum_{\boldsymbol{k},\sigma} \left(\frac{u_{\boldsymbol{k}}^2 - v_{\boldsymbol{k}}^2}{E_{\boldsymbol{k},a}} \right) d_\sigma^\dagger d_\sigma - \sum_{\boldsymbol{k},\sigma} \sigma \left(\frac{u_{\boldsymbol{k}} v_{\boldsymbol{k}}}{E_{\boldsymbol{k},a}} e^{i\varphi_a} d_\sigma^\dagger d_{-\sigma}^\dagger + \text{h.c.} \right) \right] + \text{cste}, \tag{1.187}$$

where $|\Phi_H\rangle$ denotes high energy states and $|\Phi_L\rangle$ and $\left|\Phi'_L\right\rangle$ denote low energy states. The second term in the first line corresponds to the effective coupling between the dot and the electrodes. It can be understood as follows. We start from a low energy state, described by H_D (no quasiparticles in the superconducting leads). Due to the coupling between the dot and the leads, this low energy state couples to the high energy sector, which results in a virtual high energy state corresponding to the $\langle\Phi_H| H_{T,a} \left|\Phi'_L\right\rangle$ term. Then, because this state is high in energy and the system can go back to the low energy sector thanks to the coupling, this virtual high energy state goes back to a low energy state, which corresponds to the term $\langle\Phi_L| H_{T,a} |\Phi_H\rangle$ term. This process is represented in Fig. 1.22.

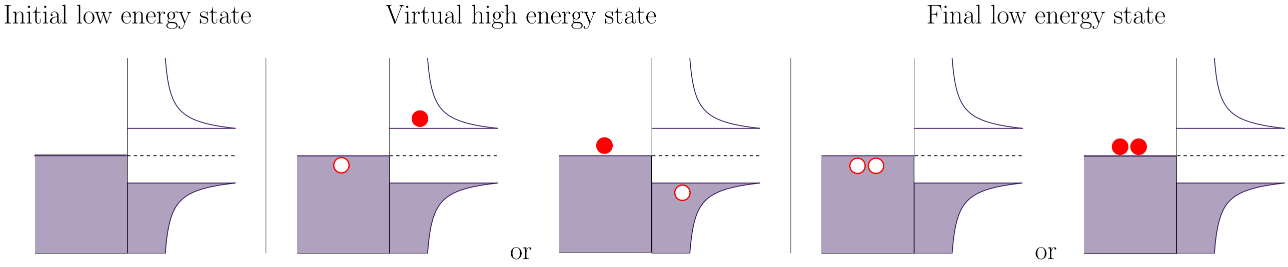

Figure 1.22: Schematic representation of the physics described by Eq. (1.186) for a normal metal coupled to a superconductor. For a quantum dot, the situation is a bit different, since there is no continuum of states but discrete energy levels.

In Eq. (1.187), the first term is odd in $\boldsymbol{k}$ and so vanishes when summing over $\boldsymbol{k}$. For the second term, we can write

$$\sum_{\boldsymbol{k}} \frac{u_{\boldsymbol{k}} v_{\boldsymbol{k}}}{E_{\boldsymbol{k}}} = \frac{\nu_S}{2} \int \mathrm{d}\xi \frac{\Delta}{\xi^2 + \Delta^2} = \frac{\pi \nu_S}{2}. \tag{1.188}$$

Finally, we obtain the following effective Hamiltonian

$$\begin{aligned} H_{\text{eff}} &= \sum_\sigma \varepsilon_d d_\sigma^\dagger d_\sigma + U n_\uparrow n_\downarrow + \pi \nu_S \sum_{a=L,R} t_a^2 \left(e^{i\varphi_a} d_\uparrow^\dagger d_\downarrow^\dagger + \text{h.c.} \right), \\ &= \sum_\sigma \varepsilon_d d_\sigma^\dagger d_\sigma + U n_\uparrow n_\downarrow + \left(\Gamma_\phi d_\uparrow^\dagger d_\downarrow^\dagger e^{i\frac{\varphi_R + \varphi_L}{2}} + \text{h.c.} \right), \end{aligned} \tag{1.189}$$

with

$$\Gamma_\phi = \Gamma \cos\frac{\phi}{2} + i\delta\Gamma \sin\frac{\phi}{2}, \tag{1.190}$$

$$\Gamma = \Gamma_R + \Gamma_L, \qquad \delta\Gamma = \Gamma_R - \Gamma_L, \tag{1.191}$$

As one can see in Eq. (1.189), this Hamiltonian is very similar to the one describing a superconductor. This is called the proximity effect. The tunnel coupling between the dot and the superconducting leads gives rise to BCS-like correlations on the dot, leading to the induction of superconductivity in the latter. The physical interpretation of this Hamiltonian is quite simple. For finite value of the superconducting gap Δ, the quantum dot is coupled to the Cooper pairs inside the gap as well as the quasiparticle excitations. In the atomic limit $\Delta \to \infty$, the dot is no longer coupled to the quasiparticles, but it is still coupled to the Cooper pairs. Thus, the proximity effect survives with a local pairing which depends on the hybridization Γ_ϕ between the dots and the superconducting leads.

The Hilbert space associated with Eq. (1.189) is spanned by the states $\{|0\rangle, |\uparrow\rangle, |\downarrow\rangle, |\uparrow\downarrow\rangle\}$. The eigenstates of this Hamiltonian are a superposition of these four states. Two of the eigenstates are simple. Those two states are $|\uparrow\rangle$ and $|\downarrow\rangle$ with an energy of ε_d. The last two eigenstates are given by a superposition of $|0\rangle$ and $|\uparrow\downarrow\rangle$ which reads

$$|+\rangle = u_d e^{i\phi_\Gamma} |\uparrow\downarrow\rangle + v_d e^{-i\phi_\Gamma} |0\rangle, \tag{1.192}$$

$$|-\rangle = -v_d e^{i\phi_\Gamma} |\uparrow\downarrow\rangle + u_d e^{-i\phi_\Gamma} |0\rangle, \tag{1.193}$$

with eigenenergies

$$\varepsilon_\pm = \varepsilon_d + \frac{U}{2} \pm \sqrt{\left(\varepsilon_d + \frac{U}{2}\right)^2 + |\Gamma_\phi|^2} \equiv \xi_d \pm \sqrt{\xi_d^2 + |\Gamma_\phi|^2}, \tag{1.194}$$

where the coefficients of the eigenstates are given as

$$u_d = \frac{1}{\sqrt{2}} \sqrt{1 + \frac{\xi_d}{\xi_d^2 + |\Gamma_\phi|^2}}, \qquad v_d = \frac{1}{\sqrt{2}} \sqrt{1 - \frac{\xi_d}{\xi_d^2 + |\Gamma_\phi|^2}}, \tag{1.195}$$

and

$$\phi_\Gamma = \arctan\left(\frac{\delta\Gamma}{\Gamma} \tan\frac{\phi}{2}\right) + \frac{\varphi_R + \varphi_L}{2}. \tag{1.196}$$

By introducing the quantities

$$\tau = \frac{4\Gamma_L \Gamma_R}{\xi_d^2 + \Gamma^2}, \qquad \Delta_{\text{eff}} = \sqrt{\xi_d^2 + \Gamma^2}, \tag{1.197}$$

we can rewrite the eigenenergies as,

$$\varepsilon_\pm = \xi_d \pm \Delta_{\text{eff}} \sqrt{1 - \tau \sin^2\frac{\phi}{2}} \tag{1.198}$$

which is very similar to the equation of the ABS energy spectrum of a zero-length junction. Note that the effective gap Δ_{eff} and τ introduced in Eq. (1.197) are very similar to the ones obtained in Eq. (1.166) when taking the limit $\Delta \to \infty$. The only difference is a factor 2 in the definition of Γ_j. Here, we can also characterize the parity of the ground state. The eigenstates of Eq. (1.189) can be classified into two groups: states with an odd number of particles occupying the dot, corresponding to the spin-doublet states $|\uparrow\rangle$ and $|\downarrow\rangle$, and states with an even number of particles occupying the dot, corresponding to the states $|+\rangle$ and $|-\rangle$. The latter states are superpositions of $|0\rangle$ and $|\uparrow\downarrow\rangle$, corresponding to spin-singlet states. Examining the spin-singlet states, we observe that ε_+ is always larger than ε_-. Consequently, the effective Hamiltonian has two potential ground states: either the spin-singlet state $|-\rangle$, or, the spin-doublet states $\{|\uparrow\rangle, |\downarrow\rangle\}$. The transition between these two parity sectors occurs for

$$\varepsilon_d = \varepsilon_d + \frac{U}{2} - \sqrt{\left(\varepsilon_d + \frac{U}{2}\right)^2 + |\Gamma_\phi|^2}, \tag{1.199}$$

$$\Leftrightarrow \xi_d^2 + |\Gamma_\phi|^2 = \frac{U^2}{4}. \tag{1.200}$$

The phase diagram representing the parity of the ground state of the effective Hamiltonian is shown in Fig. 1.23.

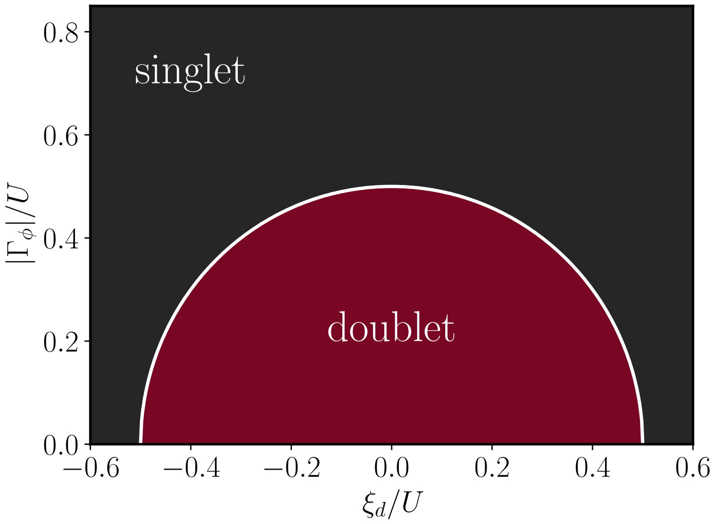

Figure 1.23: Phase diagram of a single quantum dot junction coupled to superconducting electrodes with Coulomb interaction U, energy level ξ_d and hybridization Γ_ϕ at $\phi = 0$ in the superconducting atomic limit. The white line corresponds to the transitions between the singlet and doublet sector.

One can notice that taking $U = 0$ in Eq. (1.199) does not reproduce the energy spectrum we obtained in Sec. 1.3.4. This is because what we are describing here are the superconducting states of the quantum dot due to its coupling with the superconducting leads and not ABS. ABS being discrete subgap states, they result in peaks in the density of states of the dot indicating at which energies an electron may enter or leave the latter. Therefore, this corresponds to transitions between states with n and $n \pm 1$ electrons. Hence, we can interpret these peaks in the DOS as transitions between the superconducting states of the quantum dot we just described. In the superconducting atomic limit, the energy scale of the states of the dot is necessarily lower than the superconducting gap, so transitions between the superconducting state of the dot will indeed result in sub-gap peaks in the DOS. As the states $|\pm\rangle$ are superpositions of an empty and doubly occupied dot, the transition from the doublet states $|\sigma\rangle$ needs to be a coherent addition of an electron and a hole such that the final singlet state can be understood within the Andreev reflection picture. Thus, our effective Hamiltonian in Eq. (1.189) describes the energies of ABS as transitions energies from the doublet states to the singlet states and the resulting energy spectrum of ABS is given as [91, 92]

$$E = \pm(\varepsilon_\pm - \varepsilon_d) = \pm\left(\frac{U}{2} \pm \Delta_{\text{eff}}\sqrt{1 - \tau \sin^2\frac{\phi}{2}}\right), \tag{1.201}$$

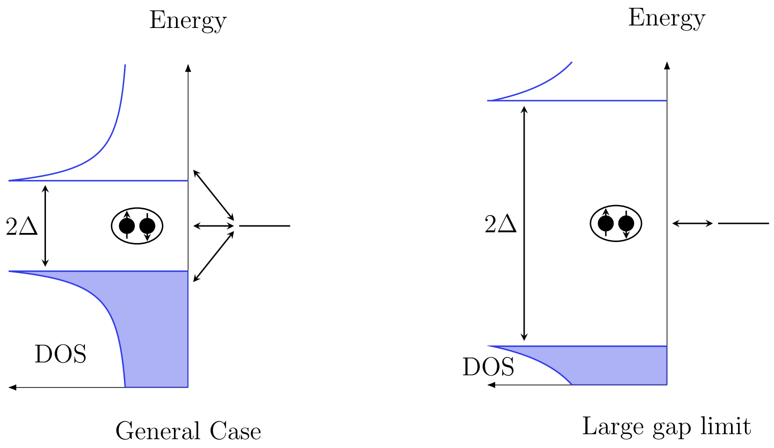

Figure 1.24: Schematic representation of the effect of the superconducting atomic limit. In the general case, the quantum dot is coupled to the continuum of states and to the Cooper pairs. However, when the gap becomes large, the dot is only coupled to the Cooper pairs.

which allows us to recover the energy spectrum we obtained in Eq. (1.165) as we take $U = 0$.

Unfortunately, the effective Hamiltonian presented in Eq. (1.189) is not sufficient to describe all aspects of the system's physics. Firstly, it only accounts for doublet states stabilized by the Coulomb interaction or spin-singlet states resulting from the proximity effect. However, when the Coulomb interaction is significantly stronger compared to other energies, the electron's spin occupying the dot level can be screened through the Kondo effect, leading to a spin-singlet ground state. But here, by taking the superconducting atomic limit $\Delta \to \infty$, we have thrown away the contribution of the continuum of states, such that the dot is only coupled to the Cooper pairs as depicted in Fig. 1.24. But, as pointed out at the beginning of this section, the Kondo effect results from a coupling between the spin on the dot and the conduction states. Hence, it cannot be described by the limit we took.
Despite these limitations, the effective model still provides a qualitative description of the system that suffices for our purposes in the following sections of this thesis.

1.5 Conclusion

In this chapter, we have introduced the necessary tools essential for comprehending this thesis. We explored the BCS theory, which describes the properties of superconductivity and how these properties give rise to Andreev bound states (ABS) in Josephson junctions. Utilizing the scattering matrix formalism, we derived the energy spectrum of ABS and examined these bound states in detail.

Moving forward to the next chapter, our focus will be on the impact of spin-orbit coupling (SOC) on the energy spectrum of ABS and how it can lift the spin degeneracy of these states. We will also study how to access this energy spectrum experimentally, and how we can manipulate the spin of one of these bound states to use it as a basis for realizing an Andreev spin qubits.

CHAPTER 2

Spin-split ABS in Rashba nanowire Josephson junction

Contents

For the moment, we have seen in the previous chapter that ABS are formed due to Andreev reflections at the interfaces of the normal region with the superconducting electrodes. However, in the junctions we studied in this chapter, ABS present a spin degeneracy which prevents us from distinguishing the spin state of a single state, and, therefore does not allow one to realize a spin qubit thanks to them. But, thankfully, it is not the end of the story. In fact, it is possible to lift the spin degeneracy of ABS. A first obvious solution is to use a Zeeman field. However, a magnetic field can be detrimental to superconductivity, so this is not the solution we are going for. In Sec. 1.3, we saw that the energy spectrum of ABS depends on the phase acquired by quasiparticles as they travel through the normal region. In particular, this phase depends on the Fermi velocities of the quasiparticles. Therefore, another way to lift the spin degeneracy is to have spin-dependent Fermi velocities. This can be achieved thanks to spin-orbit coupling (SOC). The effect of SOC on the energy spectrum of ABS and the resulting current in the junction has long been the subject of numerous studies [93, 94], but, it is only recently that the spin-splitting of ABS has been experimentally observed [43–45, 95]. To realize an ASQ when the junction is subject to quasiparticle poisoning [33], i.e. when a non-equilibrium quasiparticle is trapped within an ABS, then remains the question of the spin manipulation. Initially, S. Park and A. Levy Yeyati proposed to use a magnetic field to manipulate the spin of the ABS forming the ASQ [42]. Nonetheless, spectroscopy realized in [43] indicates that the spin degree of freedom of ABS can be relevant even in the absence of a magnetic field. Therefore, the main objective of our work will be to demonstrate how it is possible to obtain finite matrix elements of the current operator between opposite spin states in flux-driven experiments, thanks to spin-flip transmission probability.

In this chapter, we will start in Sec. 2.1 with a short presentation on the effect of SOC in solids. Then, in Sec. 2.2 we will show how SOC in quasi-1D systems can lead to the lifting of the spin degeneracy of ABS, and study the scattering in such system. Next, we will study the ABS energy spectrum in this kind of system. We will continue in Sec. 2.3 with a discussion on how to probe ABS in experiments. In particular, we will show that to determine which transitions are accessible in flux-driven experiments, we have to calculate the matrix elements of the current operator associated with ABS. Finally, in Sec. 2.4, we will discuss our primary findings, highlighting that the spin-flip transmission probability enables the existence of finite matrix elements between opposite spin states, as we detailed in our paper [46].

2.1 Some words on spin-orbit coupling (SOC)

Spin-orbit coupling is a relativistic effect which results from the interaction of the spin of a particle with its motion. This effect manifests itself for example in the shift of an electron's atomic energy levels. This shift originates from the magnetic field produced by the nuclei felt by the electron in its rest frame. The magnetic field felt by the electron is given as

$$\boldsymbol{B}_{\text{SOC}} = \frac{\boldsymbol{p} \times \boldsymbol{E}_{\text{nuc}}}{mc^2}, \tag{2.1}$$

where $\boldsymbol{p}$ is the electron momentum, $\boldsymbol{E}_{\text{nuc}}$ the electric field produced by the nucleus, m the mass of the electron and finally c the speed of light. The effect of this magnetic field on the electron can be described with a Zeeman Hamiltonian

$$H_{\text{SOC}} = \frac{g\mu_B}{2}\boldsymbol{B}_{\text{SOC}} \cdot \boldsymbol{\sigma} = \frac{g\mu_B}{2mc^2}(\boldsymbol{p} \times \boldsymbol{E}_{\text{nuc}}) \cdot \boldsymbol{\sigma}, \tag{2.2}$$

where $\boldsymbol{\sigma}$ is a vector containing the Pauli matrices $\sigma_{x,y,z}$, g is the g-factor for electron spin and μ_B is the Bohr magneton. Note that the Thomas energy due to the precession of the electron should be taken into account to properly describe the interaction energy such that g should be replaced by $(g-1)$ [96].

However, in a solid, an electron can be free to move through a crystal instead of being bound to a nucleus. The crystal being charge neutral, there is in general no net electric field in a solid. However, if the crystal presents an inversion asymmetry, then an electric field may arise. If this asymmetry is intrinsic to the material, we talk about bulk inversion asymmetry and it results in a Dresselhaus kind of SOC [97]. This asymmetry can also result from an external potential such as boundary effects, contacts with other materials or simply applied via electrostatic gates, we talk about Rashba SOC. In this thesis we will focus on the Rashba interaction. For instance, we can consider an electric field pointed in the z direction. The resulting Hamiltonian that describes this effect is known as the Rashba Hamiltonian, which reads

$$H_R = \frac{g\mu_B}{2mc^2}(\boldsymbol{p} \times E\hat{z}) \cdot \boldsymbol{\sigma} = \frac{\alpha_R}{\hbar}\hat{z} \cdot (\boldsymbol{\sigma} \times \boldsymbol{p}), \tag{2.3}$$

where $\hat{z}$ is the unit vector in the z direction and α_R gives the coupling strength. In the next section, we will look at the effect of such SOC on ABS.

2.1.1 In a 1D system

Our objective is to obtain spin-dependent velocities, and, a 1D system allows to have well separated ABS. Therefore, we will look at the effect of the Rashba interaction in a 1D system such as a wire along the x direction (similar to the one represented in Fig. 2.1 neglecting its size in the transverse direction). We still consider an electric field pointing in the z direction such that the Rashba Hamiltonian for this system reads

$$\begin{aligned} H &= \frac{\hbar^2 k_x^2}{2m} - \alpha_R \sigma_y k_x - \mu, \\ &= \frac{1}{2m}(\hbar k_x - m\alpha_R \sigma_y/\hbar)^2 - \frac{m\alpha_R^2}{2\hbar^2} - \mu. \end{aligned} \tag{2.4}$$

We can see here, that for a 1D system, the only effect of the Rashba interaction is to shift the position of both spin energy bands by $\pm m\alpha_R/\hbar^2$. We denote the momenta at which those bands crossed the Fermi level k_{F1} and k_{F2}, with $k_{F2} - k_{F1} = 2m\alpha_R/\hbar^2$. The splitting between the two dispersion bands, unfortunately, is not enough to obtain spin-dependent velocities at the Fermi level. We can verify this by computing these velocities v_1 and v_2

$$v_1 = \frac{1}{\hbar}\frac{\mathrm{d}E}{\mathrm{d}k_x}\bigg|_{k_x = k_{F1}} = \frac{\hbar k_{F1}}{m} - \frac{\alpha_R}{\hbar}, \tag{2.5}$$

$$v_2 = \frac{1}{\hbar}\frac{\mathrm{d}E}{\mathrm{d}k_x}\bigg|_{k_x = k_{F2}} = \frac{\hbar k_{F2}}{m} + \frac{\alpha_R}{\hbar}. \tag{2.6}$$

By using $k_{F1} - k_{F2} = 2m\alpha_R/\hbar$, we can easily see that $v_1 = v_2$. Do note that a tight-binding model resulting in cosine dispersion relations yields the same consequence for the velocities as shown in [50].

2.1.2 Quasi-1D system

The 1D system is not enough to split the spin degeneracy. Thus, we need to look at a higher dimensions system. Here, we will consider a 3D system that can be considered as a quasi-1D system. An example of such a system is shown in Fig. 2.1, where the system is elongated along one axis, with dimensions significantly smaller in the transverse directions. It has been shown that in this kind of system, Rashba interaction significantly affects the band structure [98]. As we are studying a quasi-1D system, we want to describe it with an effective 1D Hamiltonian. For this section, we will follow the derivation made in [42]. We will consider that a harmonic confinement potential is applied in the y and z directions that we can write as

$$H_c = \frac{1}{2} m\omega_0^2 (y^2 + z^2). \tag{2.7}$$

We can define an effective diameter $W = 2\sqrt{\hbar/(m\omega_0)}$ of the system. Note that instead of a harmonic con-

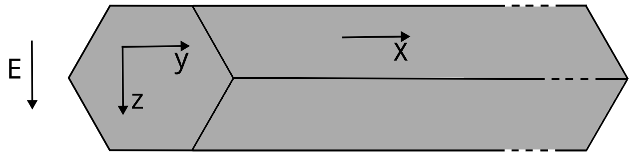

Figure 2.1: Schematic representation of a long nanowire aligned in the x direction. The electric field $\boldsymbol{E}$ pointed in the z direction results in a Rashba interaction.

finement potential, we could have chosen a hard-wall confinement potential. Quasi-1D systems are often made from cylindrical nanowires or 2D electron gases heterostructures. Hence, the appropriate choice of confinement potential depends on the system we want to model. But, as detailed in [42], the following results are independent of such geometric differences.

The full Hamiltonian reads,

$$H = \frac{p_x^2 + p_y^2 + p_z^2}{2m} + \frac{\alpha_R}{\hbar}(\sigma_x p_y - \sigma_y p_x) + \frac{1}{2} m \omega_0^2 (y^2 + z^2) - \mu. \tag{2.8}$$

As one can see, a part of this Hamiltonian describes a 2D harmonic oscillator. In order to define a 1D effective Hamiltonian, we need to integrate out the y and z coordinates. The eigenvalues of the Hamiltonian which describe the 2D harmonic oscillator are

$$E_{n_y,n_z} = \hbar\omega_0(n_y + n_z + 1) = \frac{4\hbar^2}{mW^2}(n_y + n_z + 1), \tag{2.9}$$

where n_y, $n_z \in \mathbb{N}$. We already know that the term $-\alpha_R \sigma_y p_x/\hbar$ leads to a k_x shift of the bands depending on the spin values in the y direction. Hence, we can write the eigenstates $\phi_{n_y,n_z,\sigma}(y,z)$ (with $\sigma = \uparrow, \downarrow$) for the lowest eigenvalues $\hbar\omega_0$ and $2\hbar\omega_0$ in the eigenbasis of σ_y of the 2D harmonic oscillator Hamiltonian as

$$\phi_{0,0,\sigma}(y,z) = \frac{2}{\sqrt{\pi}W} e^{-2(y^2+z^2)/W^2} \Omega_\sigma, \tag{2.10}$$

$$\phi_{1,0,\sigma}(y,z) = 2\sqrt{2} y \phi_{0,0,\sigma}(y,z), \tag{2.11}$$

$$\phi_{0,1,\sigma}(y,z) = 2\sqrt{2} z \phi_{0,0,\sigma}(y,z), \tag{2.12}$$

with $\Omega_{\uparrow,\downarrow} = (1, \pm i)^T/\sqrt{2}$, the eigenstates of σ_y. By integrating the y and z coordinates, we can see that it leads to a finite coupling η between the state $\phi_{0,0,\sigma}(y,z)$ and $\phi_{1,0,\sigma}(y,z)$ through the spin-orbit interaction

$$\begin{aligned}\eta &= \iint \mathrm{d}y\mathrm{d}z \phi^\dagger_{1,0,\uparrow}(y,z) \frac{\alpha_R}{\hbar} \sigma_x p_y \phi_{0,0,\downarrow}(y,z), \\ &= \frac{\sqrt{2}\alpha_R}{W}.\end{aligned} \tag{2.13}$$

Due to the symmetry of the eigenstates, $\phi_{0,1,\sigma}(y,z)$ does not couple to $\phi_{0,0,\sigma}(y,z)$ through the spin-orbit interaction

$$\iint \mathrm{d}y\mathrm{d}z \phi^\dagger_{0,1,\sigma}(y,z) \frac{\alpha_R}{\hbar} \sigma_x p_y \phi_{0,0,-\sigma}(y,z) = 0, \tag{2.14}$$

such that we can project the full Hamiltonian in the basis spanned by the relevant states $\{\phi_{0,0,\uparrow}, \phi_{0,0,\downarrow}, \phi_{1,0,\uparrow}, \phi_{1,0,\downarrow}\}$. Here, we made the choice to project the full Hamiltonian in the lowest energy states. This choice is relevant if the chemical potential only crosses these subbands. In particular, we will see that, to lift the spin degeneracy, it is enough that it crosses only the lowest subbands. The effective 1D Hamiltonian we obtain is

$$H_{1\mathrm{D}} = \frac{p_x^2}{2m} + E_+ + E_- \Sigma_z - \frac{\alpha_R}{\hbar} p_x \tilde{\sigma}_z + \eta \tilde{\sigma}_y \Sigma_y - \mu, \tag{2.15}$$

where $E_\pm = (E_{0,0} \pm E_{1,0})/2$, the Pauli matrices $\tilde{\sigma}_{y,z}$ act in the basis $\{\Omega_\uparrow, \Omega_\downarrow\}$, whereas the Pauli matrices $\Sigma_{y,z}$ act in the subspace of the transverse degree of freedom $\{\phi_{0,0,\sigma}, \phi_{1,0,\sigma}\}$. In the regime $E < E_{1,0}$, only the lowest subbands is occupied with an energy E given as

$$E = \frac{\hbar^2 k_x^2}{2m} + E_+ - \sqrt{(E_- \mp \alpha_R k_x)^2 + \eta^2} - \mu. \tag{2.16}$$

We can see that putting $\eta = 0$ allows one to recover the dispersion for a 1D system of Eq. (2.4) shifted by $E_{0,0}$. The higher subband has the same dispersion relation but shifted by $E_{1,0}$. If $\eta = 0$, then, the two subbands cross each other at degeneracy points and lead to the same velocity for each spin as for the pure 1D system. However, if $\eta \neq 0$, then a gap opens up between the subbands and the spin velocities we obtain at the Fermi level are (see Fig. 2.2)

$$v_1 = \frac{\hbar k_{F1}}{m} + \frac{\alpha_R (E_- - \alpha_R k_{F1})}{\hbar\sqrt{(E_- - \alpha_R k_{F1})^2 + \eta^2}}, \tag{2.17}$$

$$v_2 = \frac{\hbar k_{F2}}{m} - \frac{\alpha_R (E_- + \alpha_R k_{F2})}{\hbar\sqrt{(E_- + \alpha_R k_{F2})^2 + \eta^2}}. \tag{2.18}$$

The eigenstates of electrons moving to the right and left $\psi_{R/L,j=1,2}$ with velocities v_j are related through

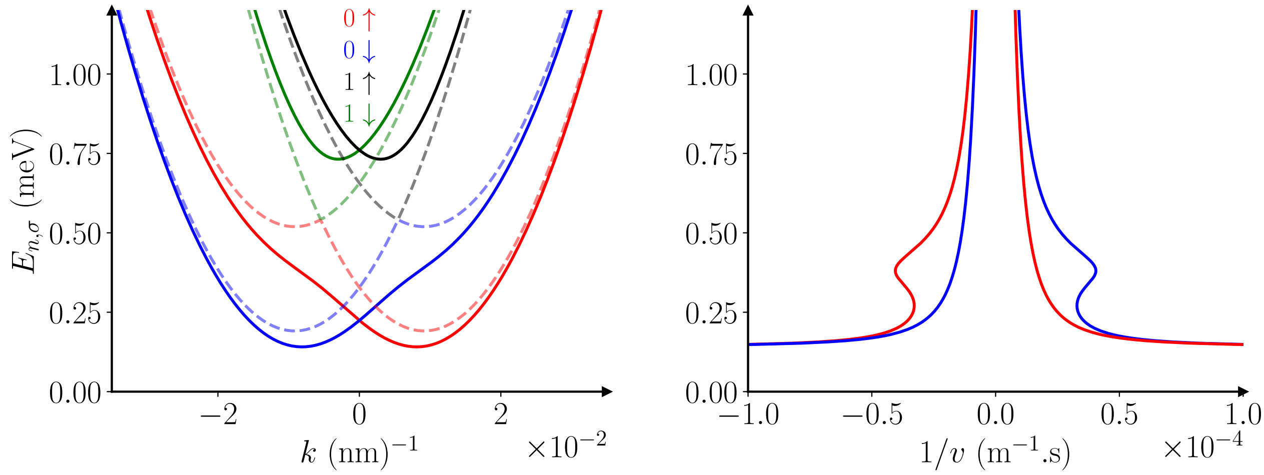

Figure 2.2: Dispersion relation of the quasi-1D system with Rashba SOC on the left panel. The coupling term η between the subbands results in a gap opening between the first and second energy subbands. On the right panel is energy as a function of the inverse of the velocities for the lowest subbands. On this panel, red/blue lines are associated with the corresponding subband in the dispersion on the left. As one can see, the mixing between the subbands results in spin-dependent velocities, with a maximal difference between the two velocities at the hybridization points. The parameters are $\alpha_R = 30$ meV nm, $W = 200$ nm and $m = 0.023 m_e$ with m_e the mass of the electron.

time reversal symmetry (TRS) and can be written as

$$\psi_{R,1} = \mathscr{T}\psi_{L,1} = \frac{e^{ik_{F1}x}}{\sqrt{|v_1|}}\left(-\sin\frac{\theta_1}{2}, 0, 0, \cos\frac{\theta_1}{2}\right)^T, \tag{2.19}$$

$$\psi_{R,2} = -\mathscr{T}\psi_{L,2} = \frac{e^{ik_{F2}x}}{\sqrt{|v_2|}}\left(0, -\sin\frac{\theta_2}{2}, \cos\frac{\theta_2}{2}, 0\right)^T, \tag{2.20}$$

with $\mathscr{T} = i\tilde{\sigma}_y \Sigma_0 \mathcal{C}$ the time reversal operator, and,

$$\theta_1 = \arctan\frac{-\eta}{E_- - \alpha_R k_{F1}}, \tag{2.21}$$

$$\theta_2 = \arctan\frac{\eta}{E_- + \alpha_R k_{F2}}. \tag{2.22}$$

Another consequence of the hybridization between the different subbands is that the spin is no longer a good quantum number anymore and we should talk about pseudo-spin from now on. In the following, we will refer to these states with a shortened notation for simplicity. We will denote them as R_1, L_1, R_2 and L_2.

As we can see, considering a finite size system in the transverse direction to the propagation is enough to obtain spin-dependent velocities, and, therefore, should lead to the lifting of the spin degeneracy of ABS as we will see in the next section.

2.2 Energy spectrum of spin-split Andreev bound states

In this section, we will derive the energy spectrum of ABS hosted in Josephson junctions with a quasi-1D normal region in which the particles have a spin-dependent velocity. We will consider the most general scattering potential which respects TRS, allowing to have spin-dependent scattering coefficients as well as scattering processes which couple opposite spin textures. We will show that the SOC leads to a lifting of the spin degeneracy. In addition, we will study the effect of the spin-flip processes on this energy spectrum. To do so, we will consider the limit $\lambda = \Delta L/(\hbar v) \ll 1$ and $\epsilon = E/\Delta \ll 1$ for a one barrier model as in Chap. 1. Additionally, we will briefly study the energy spectrum with a model involving a scattering potential at each normal-superconductor interface.

Let's begin by introducing the effective 1D Hamiltonian of the system. We consider a normal region of length d coupled to superconductors on either side. The superconductors induce a pair potential with amplitude

$$\Delta(x) = \Delta[\theta(-x) + \theta(x-d)], \tag{2.23}$$

where θ is the Heaviside step function, and the phase $\phi(x)$ is equal to $-\phi/2$ and $\phi/2$ in the left and right superconductor, respectively. The normal part of the junction consists of a quasi-one dimensional nanowire with Rashba spin-orbit coupling. As detailed in the previous section, in such systems the lowest subband of transverse quantization splits into two pseudo-spin bands with different Fermi momenta k_{Fj} and different Fermi velocities v_j, where $j = 1,2$, depending on the propagation direction. An example is shown in Fig. 2.3. In the following, we will linearize these pseudo-spin bands around the Fermi level μ. The corresponding Hamiltonian H_0 takes the form

$$H_0 = \begin{pmatrix} H_1 & 0 \\ 0 & H_2 \end{pmatrix}, \qquad H_j = \hbar v_j \left[(-1)^j i\partial_x \sigma_z - k_{Fj}\right], \tag{2.24}$$

in the basis $\psi = (R_1, L_1, L_2, R_2)^T$. Furthermore, σ_z is the Pauli matrix that acts in the right/left subspace. Note that R_1 and L_2 (R_2 and L_1) belong to the same pseudo-spin band. The Hamiltonian respects time reversal symmetry (TRS), i.e., $\Theta H_0 \Theta^{-1} = H_0$ with the time reversal operator

$$\Theta = \begin{pmatrix} i\sigma_y \mathcal{C} & 0 \\ 0 & i\sigma_y \mathcal{C} \end{pmatrix}. \tag{2.25}$$

Thus, the states R_j and L_j form a Kramers pair.

We impose that the scattering in this system also respects TRS. Hence, the most general form allowed for a scattering potential which respects this symmetry is

$$H_b = \begin{pmatrix} U_1(x) & U_3(x) \\ U_3^\dagger(x) & U_2(x) \end{pmatrix}, \tag{2.26}$$

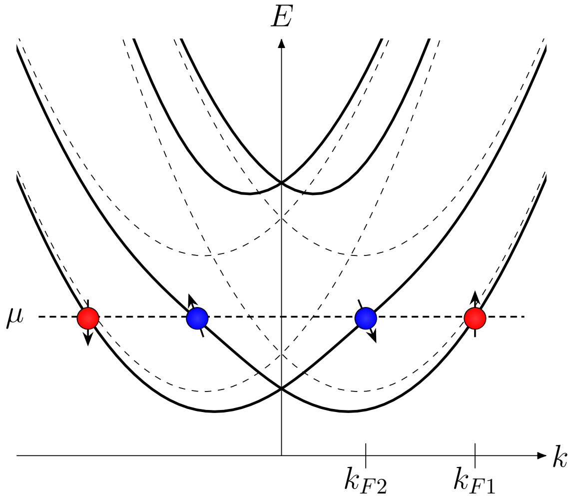

Figure 2.3: Electron band structure of the nanowire. The dotted lines correspond to the case without coupling between the transverse subbands. The two Kramers pairs are represented by different colors. Note that the coupling between the transverse subbands leads to a tilt between the respective spin quantization axes of the two pairs.

where the potentials $U_{1,2}$ are restrained to be proportional to the identity $U_{1,2} = u_{1,2}\mathbb{1}$ with $u_{1,2}$ real as TRS forbids backscattering within a Kramers pair. By contrast, U_3 takes the form

$$U_3 = u_0\mathbb{1} + i\boldsymbol{u}\cdot\boldsymbol{\sigma}, \tag{2.27}$$

with $u_{0,x,y,z}$ real. The diagonal terms of the block U_3 couple counter-propagating states within the same pseudo-spin band, whereas the off-diagonal terms of the block U_3 couple co-propagating states in opposite pseudo-spin bands. The latter are present if the scattering potential possesses an asymmetry in the transverse direction. Symmetry arguments that prove this statement are present in the supplementary material of Ref. [45, 47]. Here, we will present a short argument making it easy to understand why this coupling is possible. As we saw previously, the SOC couples the transverse subbands of opposite spin. Then, if a potential allows coupling the transverse subbands with the same spin, it can lead to a coupling between opposite spins of the lowest subband. Using the symmetry of the eigenstates of the 2D harmonic oscillator, we can restrain the symmetry of the potential such that it allows one to couple different subbands with the same spin. The eigenstate associated with the lowest energy is even in y, while, the eigenstate associated to the second-lowest energy is odd in y. Thus, when projecting to the subspace spanned by $\left\{\phi_{0,0,\uparrow}, \phi_{0,0,\downarrow}, \phi_{1,0,\uparrow}, \phi_{1,0,\downarrow}\right\}$, a potential presenting an asymmetry in the y direction will lead to a finite coupling between the state $\phi_{0,0,\sigma}$ and $\phi_{1,0,\sigma}$.

As done in [42], we consider that the spinor part of Eqs. (2.19) and (2.20) does not change significantly for subgap energies $|E| < \Delta$. Hence, we can consider θ_j as being fixed, such that $\theta_j(k_{xj}) = \theta_j(k_{Fj})$. This approximation can be justified if the subband separation is very large compared to the superconducting gap, i.e., $2|E_-| = 2\hbar^2/(mW^2) \gg \Delta$. Finally, we assume that SOC is unchanged under the superconductor. The 1D Bogoliubov-de Gennes Hamiltonian, which describes the system reads

$$H_{\text{BdG}} = (H_0 + H_b)\tau_z + \Delta(x)\left[\cos\phi(x)\tau_x - \sin\phi(x)\tau_y\right], \tag{2.28}$$

where $\tau_{x,y,z}$ are Pauli matrices in particle-hole (Nambu) space, and we chose the basis $\Psi = (\psi, \Theta\psi)^T$. The particle-hole symmetry operator in this basis is given by $\mathcal{P} = -i\tau_y\Theta$ such that $\mathcal{P}H_{\text{BdG}}\mathcal{P}^{-1} = -H_{\text{BdG}}$.

The Hamiltonian (2.28) will allow us to characterize the Andreev bound states that form in the normal region at subgap energies $|E| < \Delta$. To derive the ABS energy spectrum, we want to use the scattering formalism. So first, we need to determine the scattering matrix which describes the scattering of electrons on the scattering potential described by H_b

2.2.1 Scattering in the normal region

We will now study the different scattering processes that can take place in the normal region of the junction. To describe the scattering of electrons on the scattering potential described by H_b, we will use the scattering formalism. The resulting scattering matrix $\mathcal{S}_e$, relates the incoming states $\Psi_{e,\text{in}} = \left(R^{\text{in}}_{1,e}, R^{\text{in}}_{2,e}, L^{\text{in}}_{2,e}, L^{\text{in}}_{1,e}\right)^T$ and the outgoing states $\Psi_{e,\text{out}} = \left(L^{\text{out}}_{2,e}, L^{\text{out}}_{1,e}, R^{\text{out}}_{1,e}, R^{\text{out}}_{2,e}\right)^T$ (see Fig. 2.4). With this choice, TRS imposes

$$\Theta\mathcal{S}_e^{\dagger}\Theta^{-1} = \mathcal{S}_e, \tag{2.29}$$

with the same Θ as given in Eq. (2.25). The most general form of $\mathcal{S}_e$ then reads [99]

$$\mathcal{S}_e(E) = e^{i\xi(E)}\begin{pmatrix} r(E) & 0 & -t^*(E) & -s^*(E) \\ 0 & r(E) & -s & t(E) \\ t(E) & s^*(E) & r^*(E) & 0 \\ s(E) & -t^*(E) & 0 & r^*(E) \end{pmatrix}. \tag{2.30}$$

Here, r and t are pseudo-spin conserving reflection and transmission coefficients, while s describes spin-flip transmission. As pointed out before, TRS forbids spin-flip reflection.

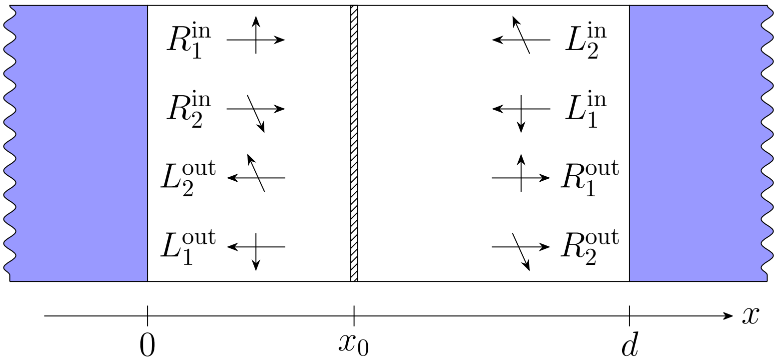

Figure 2.4: Schematic of the scattering problem. The incoming and outgoing states are taken at both superconducting/normal interfaces. In this scheme, we consider that a barrier is present at position x_0, such that the incoming and outgoing states freely propagate in the junction area of length d and are being scattered at this barrier.

To obtain the expression of these coefficients, we will consider a specific model with a single short-range scattering potential at a position $x = 0$, i.e., in Eq. (2.26), we choose $U_j(x) = U_j\delta(x)$. To link the scattering coefficients to the scattering potential, we will consider a spin up incoming electron from the left side of the barrier. The resulting wavefunctions on both side of the potential are

$$\psi_{\text{left}}(x) = \left(\frac{e^{ik_1x}}{\sqrt{v_1}}, 0, \frac{re^{-ik_2x}}{\sqrt{v_2}}, 0\right), \tag{2.31}$$

$$\psi_{\text{right}}(x) = \left(\frac{te^{ik_1x}}{\sqrt{v_1}}, 0, 0, \frac{se^{ik_2x}}{\sqrt{v_2}}\right), \tag{2.32}$$

where we have normalized each component by a factor $1/\sqrt{v_i}$ such that the current is conserved, ensuring that we can use these states as a basis for the scattering matrix, as we did when deriving the scattering matrix for a normal-superconductor interface in Sec. 1.3.1. To obtain the scattering coefficients, we integrate the Schrödinger equation around $x=0$ as in Sec. 1.2

$$\int_{0^-}^{0^+} \mathrm{d}x H_0 \psi(x) + \int_{0^-}^{0^+} \mathrm{d}x H_b \psi(x) = \int_{0^-}^{0^+} \mathrm{d}x E \psi(x). \tag{2.33}$$

By using half-sum regularization, it leads to

$$0 = \int_{0^-}^{0^+} \mathrm{d}x H_0 \psi(x) + \frac{1}{2} H_b \left(\psi_{\mathrm{right}}(0^+) + \psi_{\mathrm{left}}(0^-) \right). \tag{2.34}$$

After integrating the first term, we have to solve the following system

$$-2i\hbar\sqrt{v_1}(t-1) + u_1(1+t)/\sqrt{v_1} + (u_0 + i u_z) r/\sqrt{v_2} + i(u_x - i u_y) s/\sqrt{v_2} = 0, \tag{2.35}$$

$$(u_0 - i u_z) s + i(u_x + i u_y) r = 0, \tag{2.36}$$

$$-2i\hbar\sqrt{v_2} r + u_2 r/\sqrt{v_2} + (u_0 - i u_z)(1+t)/\sqrt{v_1} = 0 \tag{2.37}$$

$$-2i\hbar\sqrt{v_2} s + u_2 s/\sqrt{v_2} - i(u_x + i u_y)(1+t)/\sqrt{v_1} = 0. \tag{2.38}$$

By introducing the quantity $\tilde{u}_j = u_j - 2i\hbar v_j$ for $j = 1, 2$, $u_r = u_0 + i u_z$ and $u_s = u_x + i u_y$, we can rewrite this system as

$$\tilde{u}_1 t + \tilde{u}_1^* + \sqrt{\frac{v_1}{v_2}} (u_r r + i u_s^* s) = 0, \tag{2.39}$$

$$(u_r^* s + i u_s r) = 0, \tag{2.40}$$

$$\tilde{u}_2 r + \sqrt{\frac{v_2}{v_1}} u_r^* (1+t) = 0, \tag{2.41}$$

$$\tilde{u}_2 s - i u_s \sqrt{\frac{v_2}{v_1}} (1+t) = 0. \tag{2.42}$$

We obtain the following expression for the scattering coefficients that we defined up to a global phase factor θ as

$$r = \frac{4 u_r^* \hbar \sqrt{v_1 v_2}}{\left| |u_r|^2 + |u_s|^2 - \tilde{u}_1 \tilde{u}_2 \right|}, \tag{2.43}$$

$$t = -i \frac{|u_r|^2 + |u_s|^2 - \tilde{u}_1^* \tilde{u}_2}{\left| |u_r|^2 + |u_s|^2 - \tilde{u}_1 \tilde{u}_2 \right|}, \tag{2.44}$$

$$s = -i \frac{4 u_s \hbar \sqrt{v_1 v_2}}{\left| |u_r|^2 + |u_s|^2 - \tilde{u}_1 \tilde{u}_2 \right|}, \tag{2.45}$$

$$\theta = -\frac{\pi}{2} - \arg\left[|u_r|^2 + |u_s|^2 - \tilde{u}_1 \tilde{u}_2 \right]. \tag{2.46}$$

As an example, we will model the scattering region by a delta potential in the x direction placed at a position $0 < x_0 < d$. We will assume that this potential does not depend on the z coordinates. However, we will consider that this potential presents an asymmetry in the y direction. We can write this potential as [45]

$$V(x, y) = \delta(x - x_0) \left[V_s(y) + V_{AS}(y) \right], \qquad V_{S,AS}(y) = \frac{V(y) \pm V(-y)}{2}. \tag{2.47}$$

Mapping this potential onto the subspace spanned by $\{\phi_{0,0,\uparrow},\, \phi_{0,0,\downarrow},\, \phi_{1,0,\uparrow},\, \phi_{1,0,\downarrow}\}$ leads to

$$\iint \mathrm{d}y\,\mathrm{d}z\,\phi^\dagger_{0,0,\sigma}(y,z)V_S(y)\phi_{0,0,\sigma'}(y,z) = V_{S1}\delta_{\sigma,\sigma'}, \tag{2.48}$$

$$\iint \mathrm{d}y\,\mathrm{d}z\,\phi^\dagger_{1,0,\sigma}(y,z)V_S(y)\phi_{1,0,\sigma'}(y,z) = V_{S2}\delta_{\sigma,\sigma'}, \tag{2.49}$$

$$\iint \mathrm{d}y\,\mathrm{d}z\,\phi^\dagger_{0,0,\sigma}(y,z)V_{AS}(y)\phi_{1,0,\sigma'}(y,z) = V_A\delta_{\sigma,\sigma'}, \tag{2.50}$$

whereas all other matrix elements are zero and where we used the symmetry of the wavefunction and of the potential. We will not look at a peculiar form of $V(y)$. The only thing that is important, here, is that it has an asymmetry in the y direction such that we obtain a finite coupling V_A between the subbands. Thanks to this coupling, when we project onto the subspace spanned by $\{R_1,\, L_1,\, L_2,\, R_2\}$, i.e., the states corresponding to the lowest subbands, we obtain the following scattering potential

$$H_{b,V} = \delta(x - x_0)\begin{pmatrix} U_{1,V} & U_{3,V} \\ U^\dagger_{3,V} & U_{2,V} \end{pmatrix}, \tag{2.51}$$

where the label V is here to avoid confusion with the general derivation we made above. The potentials $U_{1/2,V}$ are proportional to the identity, $U_{1/2,V} = u_{1/2,V}\mathbb{1}$, with $u_{1/2,V}$ given as

$$u_{1/2,V} = V_{S1}\sin^2\frac{\theta_{1/2}}{2} + V_{S2}\cos^2\frac{\theta_{1/2}}{2}, \tag{2.52}$$

where $\theta_{1/2}$ are given in Eqs. (2.21) and (2.22). And, $U_{3,V}$ takes the form

$$U_{3,V} = u_{0,V} + i\,u_{y,V}\sigma_y \tag{2.53}$$

with $u_{r/s,V}$ real and given as

$$u_{r,V} = -V_{S1}\sin\frac{\theta_1}{2}\sin\frac{\theta_2}{2} + V_{S2}\cos\frac{\theta_1}{2}\cos\frac{\theta_2}{2}, \tag{2.54}$$

$$u_{s,V} = -V_A\sin\frac{\theta_1+\theta_2}{2} \tag{2.55}$$

As one can see in Eq. Eq. (2.45), the spin-flip term is proportional to $u_{s,V}$ which originates from the asymmetry of the potential in the transverse direction. A particularity of this simple model is that, for $\eta = 0$, we have $\theta_2 = -\theta_1 = \pi$, and, therefore, it leads to $u_{s,V} = 0$, such that co-propagating states with opposite spin will not be coupled through this kind of scattering potential Also, it is to be noted that, according to Eq. (2.43), it is possible to have zero-backscattering if $u_{r,V} = 0$, i.e., if the potential is completely asymmetric in the transverse direction. Later in this manuscript, we will be interested in the limit $1 - |t|^2 \ll 1$. With this simple model, this limit can be obtained in a system with small SOC $(\theta_1 + \theta_2) \ll 1$ and a mostly asymmetric potential.

In the following, we will continue with the general form of H_b which respects TRS, given in Eq. (2.26). What we also need to obtain is the scattering matrix for holes in the normal region. As in Sec. 1.3.2.1, holes are described by $H_h = -\Theta H_e \Theta^{-1}$, so we can define the incoming and outgoing states for holes as $\Psi_{h,\mathrm{in}}(E) = \Theta\Psi_{e,\mathrm{in}}(-E)$ and $\Psi_{h,\mathrm{out}}(E) = \Theta\Psi_{e,\mathrm{out}}(-E)$. Thus, the scattering matrix for holes is given as

$$\mathcal{S}_h(E) = \Theta\mathcal{S}_e(-E)\Theta^{-1} = \mathcal{S}^\dagger_e(-E). \tag{2.56}$$

An ABS will form in the junction when $\Psi_{e,\mathrm{in}} = \alpha^2(E) r_A(-\phi)\mathcal{S}_h(E) r_A(\phi)\mathcal{S}_e(E)\Psi_{e,\mathrm{in}}$ where $r_A(\phi)$ takes the usual form given in Sec. 1.3.2.1. Hence, we define $M(E,\phi) = r_A(-\phi)\mathcal{S}_h(E) r_A(\phi)\mathcal{S}_e(E)$, such that the discrete energy spectrum of ABS is given by the roots of the secular equation given in Eq. (1.133). Therefore, one can directly calculate the roots of Eq. (1.133) in this basis, or, we can first diagonalize $M(E,\,\phi)$ such that we have an ABS when one of the eigenvalues is equal to $(\alpha^*(E))^2$. The benefit of the second approach is that we will have access to the eigenvectors of $M(E,\,\phi)$ which will be of great use in the remainder of this manuscript. The diagonalization of $M(E,\,\phi)$ is done in Appendix B.

2.2.2 Energy spectrum

Now that we have obtained the eigenvalues of $M(E,\phi)$ in Appendix B, we can easily find the roots of Eq. (1.133). The solutions can be cast in the form

$$\frac{\xi(E)-\xi(-E)}{2}+\rho\chi_\sigma(E,\phi)-\arccos\frac{E}{\Delta}-q\pi=0, \tag{2.57}$$

with $q\in\mathbb{Z}$, $\sigma,\rho=\pm1$ and

$$\chi_\sigma(E,\phi)=\arccos\sqrt{\frac{1+\tau(E)\cos\big(\phi-\sigma\omega(E)\big)+\mathrm{Re}[r^*(-E)r(E)]}{2}}, \tag{2.58}$$

$$\tau(E)=\sqrt{\left(|t(E)|^2+|s(E)|^2\right)\left(|t(-E)|^2+|s(-E)|^2\right)}, \tag{2.59}$$

$$\omega(E)=\mathrm{sign}(E)\arccos\left(\frac{\mathrm{Re}[t^*(-E)t(E)+s^*(-E)s(E)]}{\tau(E)}\right). \tag{2.60}$$

Note that particle-hole symmetry implies that for a state with energy E, it exists a state with energy $-E$. This reflects in the energy solutions of Eq. (2.57) which obey $E_{q,\rho,\sigma}=-E_{-(q+1),-\rho,-\sigma}$. In the following, we will thus concentrate on energies $E>0$ only. Furthermore, TRS implies $\mathcal{T}H_{\mathrm{BdG}}(\phi)\mathcal{T}^{-1}=H_{\mathrm{BdG}}(-\phi)$ with $\mathcal{T}=\tau_0\Theta$. In addtion, the energy spectrum is 2π periodic, such that we have $E_{q,\rho,\sigma}(2\pi-\phi)=E_{q,\rho,-\sigma}(\phi)$. Thus, it will be sufficient to consider phases $0\le\phi\le\pi$. The maximum number of ABS is set by the maximum value that q can take. This value is obtained by setting $E=\Delta$ in Eq. (2.57), leading to

$$q_{\mathrm{max}}=\left[\frac{1}{\pi}\left(\frac{\xi(\Delta)-\xi(-\Delta)}{2}+\rho\chi_\sigma(\Delta,\phi)\right)\right], \tag{2.61}$$

where $[x]$ stands for the integer part of x. In the absence of backscattering, $\tau(E)=1$ and Eq. (2.58) reduces to

$$\chi_\sigma(E,\phi)=(\phi-\sigma\omega(E))/2.$$

In this form, one can see explicitly that the spin-splitting originates from $\omega(E)$. One notices further that $\omega(E)=0$, if the scattering coefficients are energy-independent. Note that σ corresponds to the pseudo-spin of right-moving electrons involved in the ABS at $T=1$ and when $v_1>v_2$. In the following, we will continue to call the states $\sigma=1$ spin up and $\sigma=-1$ spin down, even though the pseudo-spin of the ABS is not well defined at $T\neq1$.

In the following, most of our results will be obtained for a specific model with a single short-range scattering potential at a position x_0 along the nanowire. We will therefore start by discussing the energy spectrum of ABS for this model. A discussion of a model with a barrier at each interface between the nanowire and the superconducting leads forming the junction can be found in Appendix C.

In the case of a single scattering potential, the scattering coefficients take the following form:

$$r(E)=re^{i\bar{k}d\tilde{x}_0},\quad t(E)=te^{\frac{1}{2}i\delta kd},\quad s(E)=se^{\frac{1}{2}i\delta kd\tilde{x}_0}, \tag{2.62}$$

and $\xi(E)=\bar{k}d+\theta$ which we obtained from the results presented in Sec. 1.2.2. Here, $\tilde{x}_0=2x_0/d-1$ and $\bar{k}=(k_1+k_2)/2$, $\delta_k=k_1-k_2$ with $k_j=k_{Fj}+E/(\hbar v_j)$. Equation (2.57) can be solved numerically in all parameter regimes, whereas analytical solutions are possible only in limiting cases. For this particular model, Eqs. (2.57), (2.58), (2.59) and (2.60) can be written as

$$\bar{\lambda}\epsilon+\rho\chi_\sigma(\epsilon,\phi)-\arccos\epsilon-q\pi=0, \tag{2.63}$$

with

$$\chi_\sigma(\epsilon,\phi) = \arccos\sqrt{R\cos^2(\bar{\lambda}\epsilon\tilde{x}_0) + \tau\cos^2\left(\frac{\phi-\sigma\omega}{2}\right)}, \tag{2.64}$$

$$\omega = \mathrm{sign}(\epsilon)\arccos\left[\frac{T\cos(\delta\lambda\epsilon) + S\cos(\delta\lambda\epsilon\tilde{x}_0)}{\tau}\right], \tag{2.65}$$

$$\tau = T + S, \tag{2.66}$$

where $T = |t|^2$, $S = |s|^2$, $R = |r|^2$ and $\epsilon = E/\Delta$. A sample spectrum obtained numerically is shown in Fig. 2.5. By putting $s = 0$ in Eq. (2.65) allows one to recover the results present in the literature for spin-split ABS [42, 43]. As can be seen, the spin degeneracy is lifted except for phases multiple of π, which effectively preserves TRS and, hence, Kramers degeneracy. Otherwise, the states group into doublets of opposite spin, which we labeled by an index $m \in \mathbb{N}^*$ that increases with energy. Specifically, the doublets with odd m contain the states $((m-1)/2, +, \sigma)$, whereas the doublets with even m contain the states $(m/2-1, -, \sigma)$. The energies within a doublet will then be denoted $E_{m\sigma}$.

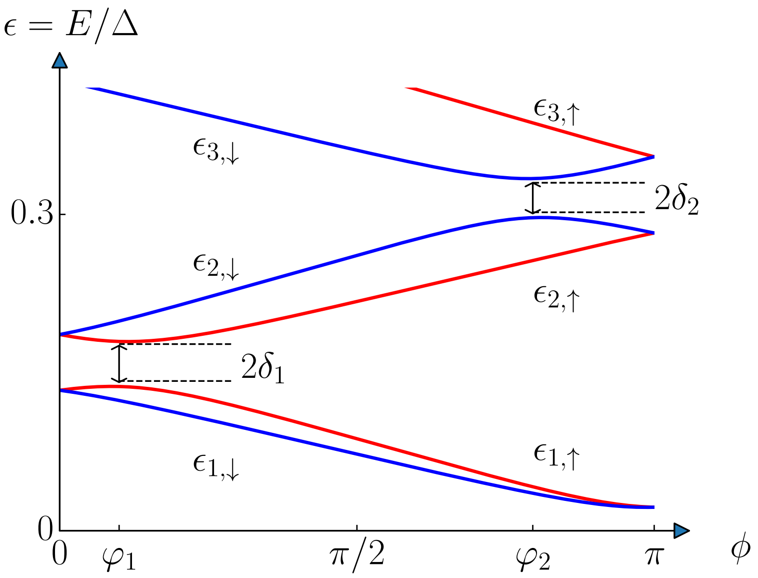

Figure 2.5: Energy spectrum of ABS for a model with a single scattering center in the junction, shown up to an energy $\bar{E} \ll \Delta$. Here, $T = 0.95$, $S = 0$, $\lambda_1 = 8$, $\lambda_2 = 10$, and $\tilde{x}_0 = 0.9$. Red lines correspond to spin up states, while blue lines correspond to spin down states. We denote the gap between doublet m and $m+1$ at phase φ_m as δ_m.

We will now characterize the energy spectrum more precisely thanks to analytical results obtained for the same regime we discussed in Sec. 1.3.

2.2.2.1 Zero and short length limit

The simplest form is obtained in the zero-length limit $d \to 0$ where the scattering coefficients do not depend on energy. In that case, the spin-orbit coupling plays no role since there is no propagation in the normal region, and, one recovers the well-knwon result of a single spin-degenerate ABS with energy [40]

$$\epsilon^{(0)}_{1\sigma}(\phi) = \epsilon_0 \equiv \sqrt{1-(T+S)\sin^2\frac{\phi}{2}}, \tag{2.67}$$

It is interesting to note that, in this limit, only the total transmission $T+S$ matters [40, 100].

Spin-split Andreev levels are obtained once one takes into account a finite length of the junction as illustrated in Fig. 2.5. To better understand the effect of the different parameters on this splitting, we start by taking the finite length of the junction into account perturbatively. Namely, we compute the corrections to ϵ_0 to first order in $\lambda_j = \Delta d/(\hbar v_j)$, which yields

$$\epsilon_{1\sigma} = \epsilon_0 + \delta\epsilon_{\text{shift}} + \sigma\delta\epsilon_{\text{split}}, \tag{2.68}$$

with

$$\delta\epsilon_{\text{shift}} = -\bar{\lambda}\epsilon_0\sqrt{1-\epsilon_0^2}, \tag{2.69}$$

$$\delta\epsilon_{\text{split}} = \frac{1}{2}|\delta\lambda|\sqrt{1-\epsilon_0^2}\sqrt{T+S\tilde{x}_0^2}\cos\frac{\phi}{2}, \tag{2.70}$$

where $\bar{\lambda} = (\lambda_1+\lambda_2)/2$ and $\delta\lambda = \lambda_1 - \lambda_2$. Here, $\delta\epsilon_{\text{shift}}$ describes a shift of both eigenvalues, whereas $\delta\epsilon_{\text{split}}$ describes the spin splitting. Furthermore, we recover the $\sin\phi$-dependence of the splitting predicted pertubatively in SOC in Refs. [37, 40]. Finally, we note that the splitting depends separately on the spin-conserving transmission T and the spin-flip transmission S. At $R=0$ and $S \ll T$ up to small corrections $\propto S$, the result simplifies to

$$\epsilon_{1\sigma} = \cos\frac{\phi}{2} - \frac{1}{2}\left(\bar{\lambda} - \frac{1}{2}\sigma|\delta\lambda|\right)\sin\phi. \tag{2.71}$$

In contrast, in the limit, $T \ll S$, it yields

$$\epsilon_{1\sigma} = \cos\frac{\phi}{2} - \frac{1}{2}\left(\bar{\lambda} - \frac{1}{2}\sigma|\tilde{x}_0\delta\lambda|\right)\sin\phi. \tag{2.72}$$

In this particular case, one can easily see that for $\tilde{x}_0 = 0$, there is no lifting of the spin degeneracy. In fact, this result is more general than the case of perfect transmission ($R=0$). For $T=0$, we have $\omega(E)=0$ for $\tilde{x}_0=0$, such that there is no spin-splitting of ABS. This can be easily understood with a simple picture. We know that the splitting originates from the propagation of particles in the normal region. These particles will acquire a given phase depending on their spin polarization. However, if there is no possibility of spin-conserving transmission through the scattering potential, but only spin-flip transmission, the transmitted particles will acquire the propagation phases of both spin polarizations. In the particular limit of $\tilde{x}_0=0$, the scattering potential is placed at the middle of the nanowire such that, the particles of each spin polarization will acquire the same phase from their propagation in this normal region.

The approximation for Eq. (2.68) is valid for phases not too close to zero. As detailed in Sec. 1.3.3 and as can be observed in Fig. 2.5, additional Andreev levels may appear in a finite length junction. From Eq. (2.57), setting $T=1$ and $\epsilon=1$, one can see that, for a short length junction, the additional states quickly join the continuum at $\phi = 2\lambda_j$. Taking into account corrections up to second order in λ_j as in Sec. 1.3.3, one finds a crossing between the doublets $m=1$ and $m=2$ that takes place at $\varphi_1 \approx |\delta\lambda|$ [67] (see Fig. 2.6).

2.2.2.2 Low energy limit and long length junction

In arbitrary length junctions, a simple expression for the low-energy spectrum, $\epsilon \ll 1$, can be obtained at $R=0$ as done in Sec. 1.3.3 and $S \ll T$, namely

$$\epsilon_{m\sigma} = \frac{f_m(\phi)}{2(1+\bar{\lambda})+(-1)^m\sigma|\delta\lambda|}, \tag{2.73}$$

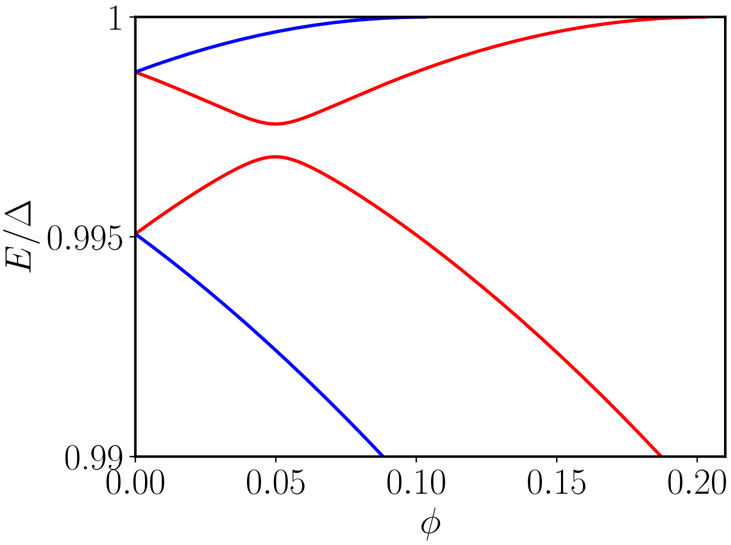

Figure 2.6: Energy spectrum obtained for a short length junction. The parameters are $T = 0.95$, $S = 0$, $R = 0.05$, $\tilde{x}_0 = 0.3$, $\lambda_1 = 2\lambda_2 = 0.1$. As pointed out in the main text, we can see that an avoided crossing is present at $\varphi_1 \approx |\delta\lambda|$, and that the additional states quickly joins the continuum at $\phi = 2\lambda_j$.

while in the limit $T \ll S$, we have

$$\epsilon_{m\sigma} = \frac{f_m(\phi)}{2(1+\bar{\lambda})+(-1)^m\sigma|\tilde{x}_0\delta\lambda|}, \tag{2.74}$$

with

$$f_m(\phi) = \begin{cases} m\pi - \phi, & m \ \text{ odd}, \\ \\ (m-1)\pi + \phi, & m \ \text{ even}. \end{cases} \tag{2.75}$$

In the short junction limit, $\bar{\lambda}, \delta\lambda \ll 1$, Eqs. (2.73) and (2.74) coincide with Eqs. (2.71) and (2.72) respectively for ϕ near π when the condition $\epsilon \ll 1$ is verified. In the following, we will continue with the case $S \ll T$. Time-reversal invariance at phases $\phi = 0, \pi$ imposes level crossings at these phases. Namely, $\epsilon_{2m,\sigma} = \epsilon_{2m-1,-\sigma}$ at $\phi = 0$, whereas $\epsilon_{2m,\sigma} = \epsilon_{2m+1,-\sigma}$ at $\phi = \pi$. In the long junction limit $\bar{\lambda} \gg 1$, and assuming $\delta\lambda \ll \bar{\lambda}$, Eq. (2.73) can be written at the first order in $|\delta\lambda|/\bar{\lambda}$ as

$$\epsilon_{m\sigma} \approx \frac{f_m(\phi)}{2\bar{\lambda}}\left(1-(-1)^m\sigma\frac{|\delta\lambda|}{2\bar{\lambda}}\right). \tag{2.76}$$

The phases at which different levels cross each other can be found by looking at $\epsilon_{m\sigma} = \epsilon_{m'\sigma'}$. The crossings between same spin-states of doublets m and $m+1$ occur at phases

$$\varphi_m = \begin{cases} \pi m \frac{|\delta\lambda|}{2\bar{\lambda}} & m \ \text{ odd}, \\ \\ \pi - \pi m \frac{|\delta\lambda|}{2\bar{\lambda}}, & m \ \text{ even}. \end{cases} \tag{2.77}$$

Note that for m odd, the crossing is between spin up states whereas for m even, the crossing is between spin down states. These crossings are not protected by TRS and are lifted at finite R as we will see in the following. The resulting spectrum resembles the one shown in Fig. 2.5 at phases $\varphi_m < \phi < \varphi_{m+1}$ for m

odd and $\varphi_{m-1} < \phi < \varphi_m$ for m even. The energy gaps δ_m which open for finite R, in units of Δ, at the anti-crossings can be obtained by calculating the energy perturbatively in R at the phases $\phi_c = \varphi_m$ using with the help of Eq. (2.57) (the procedure is the same as the one detailed in Sec. 1.3.3). We find

$$\delta_m = \frac{\sqrt{R}}{\bar{\lambda}} \begin{cases} \left|\sin\left(\pi m \frac{\tilde{x}_0}{2}\right)\right| & m \text{ odd}, \\ \\ \left|\cos\left(\pi m \frac{\tilde{x}_0}{2}\right)\right|, & m \text{ even}. \end{cases} \tag{2.78}$$

Note that these gaps close at particular values of $\tilde{x}_0$. This happens when the reflected and transmitted part of the wavefunction acquire the same phase through propagation in the normal region. The energies of the two states involved in the anti-crossing are then given as

$$\epsilon_m^{>/<} = \frac{1}{2}\left(\epsilon_m^+ + \epsilon_m^- \pm \sqrt{(\epsilon_m^+ - \epsilon_m^-)^2 + 4\delta_m^2}\right), \tag{2.79}$$

where $\epsilon_m^\pm$ corresponds to the energy level with positive/negative slope as a function of ϕ. For m odd,

$$\epsilon_m^\pm = \frac{\pi m \pm \phi}{2\bar{\lambda}}\left(1 \mp \frac{|\delta\lambda|}{2\bar{\lambda}}\right), \tag{2.80}$$

whereas for m even,

$$\epsilon_m^\pm = \frac{\pi(m \mp 1) \pm \phi}{2\bar{\lambda}}\left(1 \pm \frac{|\delta\lambda|}{2\bar{\lambda}}\right). \tag{2.81}$$

Note that $\epsilon_m^- - \epsilon_m^+ = (\varphi_m - \phi)/\bar{\lambda}$ for all m.

The doublet $m = 1$ requires special attention. At $T = 1$, it crosses with the negative energy states at phase $\phi = \pi$, leading to a four-fold degeneracy at the Fermi level. Finite back-scattering opens up a gap (while preserving the two-fold degeneracy imposed by TRS). Using the same method as outlined above, we find that the positive energy states are shifted to $\delta_\pi = \sqrt{R}/\bar{\lambda}$.

Until now, we have mainly studied the energy spectrum of ABS. We have shown how SOC can lift the spin degeneracy of ABS. Also, we saw that spin-flip transmission allows one to couple opposite spin sectors resulting in a modification of the energy splitting between opposite spin states when considering one scattering potential in the junction. In the next sections, we will assess how ABS can be probed. We will give a particular interest to circuit quantum electrodynamics (cQED) experiments, which are the types of experiments now performed for the detection and manipulation of ABS. We will show that, the current operator associated with ABS is a quantity of interest to determine which transitions between ABS are accessible in these experiments. Thus, we will turn to the evaluation of the matrix elements of this operator for a model with one scattering potential.

2.3 How to probe and manipulate ABS

The majority of this manuscript has, for the moment, been devoted to the study of spin-split ABS in order to use them as a basis for the realization of ASQs. However, although theory tells us that it is possible to lift the spin degeneracy of ABS, it needs to be verified experimentally. This section will thus be dedicated to the detection of ABS. We begin with a brief discussion of tunnel spectroscopy experiments which provided the first direct evidence of the existence of ABS. Next, we will discuss the basic idea behind circuit quantum electrodynamics (cQED), which corresponds to the types of experiments now performed for the detection and manipulation of ABS. In particular, we'll show that the current operator associated with ABS is the quantity that allows us to determine the accessible transitions between ABS in these experiments.

2.3.1 Tunnel spectroscopy

Initially, ABS in Josephson junctions were detected in tunnel spectroscopy experiments. The principle of these experiments was to use a tunnel probe to measure the differential conductance of a junction. Due to the presence of ABS in the normal region of the junction which are discrete subgap states, the density of states (DOS) of this region will present discrete peaks for energies below the superconducting gap. The differential conductance being related to the DOS, the latter shows both a spatial and a phase dependence [101]. Hence, by measuring the differential conductance, it is possible to obtain the DOS and directly compare the energy spectrum predicted by theory with the experimental result. To do so, one can use a tunnel probe placed near the normal region of the junction. By applying a bias voltage V to the tunnel probe, a current will flow in the latter when there is an accessible state at energy eV. This current can be expressed as

$$I_{\mathrm{TP}} \propto \int \mathrm{d}\varepsilon\,(n_{\mathrm{TP}}(\varepsilon - eV) - n_{\mathrm{WL}}(\varepsilon))\,\rho_{\mathrm{TP}}(\varepsilon - eV)\rho_{\mathrm{WL}}(\varepsilon), \tag{2.82}$$

where the labels TP and WL stand for tunnel probe and weak link, n_i are the Fermi-Dirac distributions and ρ_i the DOS, V is the bias voltage applied to the tunnel probe. The corresponding differential conductance is obtained by taking the derivative of I_{TP} with respect to V, which yields

$$\frac{\partial I_{\mathrm{TP}}}{\partial V} \propto \int \mathrm{d}\varepsilon \left[n'_{\mathrm{TP}}(\varepsilon - eV)\rho_{\mathrm{TP}}(\varepsilon - eV) + (n_{\mathrm{WL}}(\varepsilon) - n_{\mathrm{TP}}(\varepsilon - eV))\rho'_{\mathrm{TP}}(\varepsilon - eV)\right]\rho_{\mathrm{WL}}(\varepsilon), \tag{2.83}$$

where the prime denotes the derivative with respect to V. In the simplest case, we can assume that the DOS of the tunnel probe is independent of the bias voltage V. In this case, we can easily see that the differential conductance is directly proportional to DOS. This is a reasonable approximation when considering a normal probe, but for instance, it will fail for a superconducting probe as its DOS is gapped. Therefore, in this case, additional work is required to extract the DOS from the differential conductance as done in [29] where a superconducting tunnel probed was use.

This type of experiment has allowed to demonstrate the presence of ABS in S-N-S and S-QD-S junctions [29, 101–104] as shown in Fig. 2.7.

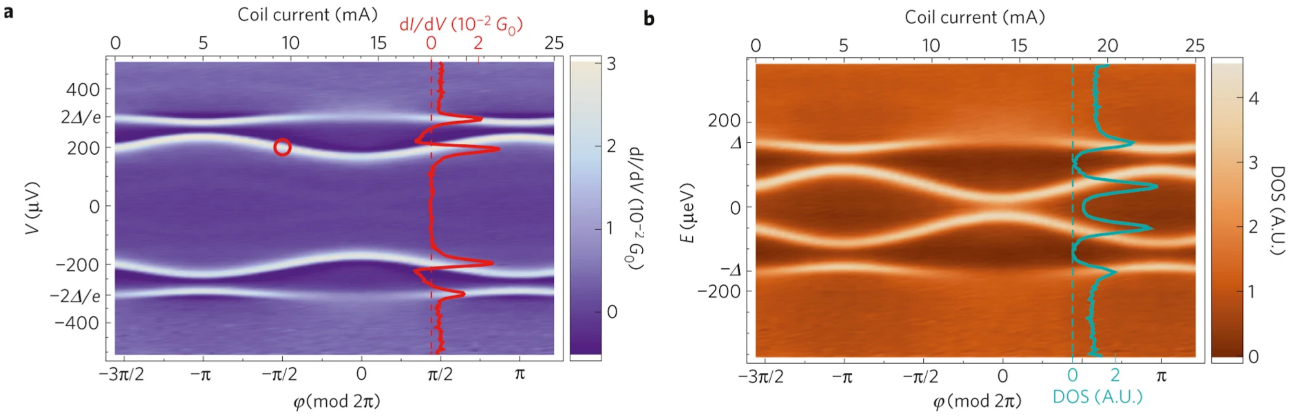

Figure 2.7: Differential conductance and corresponding density of states (DOS) obtained in [29] for a carbon nanotube Josephson junction. The tunnel probe used was superconducting, which explains the difference between the two figures. In this case, the DOS can be obtained by an appropriate deconvolution of the measured differential conductance. The sharp resonances are the signature of the ABS in the nanotube. The periodicity of the pattern shows the sensitivity of ABS to the superconductive phase difference denoted here as φ.

2.3.2 Using cQED to probe ABS

More recently, the use of cQED to detect ABS has become more widespread. In particular, this experimental technique has been of great use for the experimental characterization of spin-split ABS and for the realization of an ASQ [43–45, 47, 48, 50, 95]. Originally developed for readout and control of superconducting qubits, cQED involves coupling a microwave resonator to a quantum circuit of interest [32, 105]. These resonators are typically made of superconducting materials, ensuring minimal energy dissipation. Basically, they can be described as LC resonators. In this section, we will present the basic idea behind cQED. We will start by discussing a system with a resonator coupled to a quantum circuit. We will show that in such systems, the resonance frequency of the resonator depends on the quantum state occupied by the quantum circuit. We will see that, in phase-driven experiments, this shift is linked to the current operator. Finally, we will show that the current operator associated with ABS allows one to determine which transitions between ABS are accessible within flux-driven experiments.

The basic principle of cQED is as follows. At first glance, the direct determination of the quantum state of our target system may seem complex. However, determining the resonance frequency of a resonator is easier. Thus, if coupling our system of interest to a resonator allows us to modify the resonant frequency of the latter as a function of the quantum state of the system, we can determine the quantum state that our system occupies. Let's start by writing down the Hamiltonian of this kind of system. First, we can describe the resonator with the following Hamiltonian

$$\hat{H}_r = \hbar\omega_r \left(a^\dagger a + \frac{1}{2}\right), \tag{2.84}$$

where ω_r corresponds to the resonant frequency of the resonator and a ($a^\dagger$) to the photon annihilation (creation) operator. From now on, we will follow the derivation made in [106]. We will consider a general quantum circuit described by the Hamiltonian $\hat{H}_{\text{qc}}(x)$, which depends on a dimensionless control parameter x, contingent on the coupling scheme with the resonator. The latter can either be inductive or capacitive, as shown in Fig. 2.8. Thus, x can correspond to a flux through a loop or an excess charge on a capacitor. We will denote $|n\rangle$ the eigenstates of $\hat{H}_r$, with n being the number of photons in the resonator, and, $|\Phi_i(x)\rangle$ the eigenstates of $\hat{H}_{\text{qc}}(x)$ such that $\hat{H}_{\text{qc}}(x)|\Phi_i(x)\rangle = E_i\,|\Phi_i(x)\rangle$. When coupling the resonator to the quantum circuit, a flux or charge fluctuation in the resonator leads to $x \to x_0 + \hat{x}_r$, with x_0 the phase through the loop containing the quantum circuit or the number of charge in the latter and, $\hat{x}_r = \lambda(sa + s^* a^\dagger)$ where λ is a coupling constant that depends on the coupling scheme and $s = 1$ ($-i$) for flux (charge) fluctuations. The coupling constant λ is given by the product of the geometric coupling ratio and of the zero point fluctuations of the phase or the charge (see Ref. [50, 106–108]). For a capacitive coupling, one obtains

$$\lambda = \frac{C_M}{C_R}\sqrt{\frac{R_Q}{4\pi Z_R}}, \tag{2.85}$$

whereas for an inductive coupling, one obtains

$$\lambda = \frac{\mathcal{M}}{L_R}\sqrt{\frac{\pi Z_R}{R_Q}}, \tag{2.86}$$

where $Z_R = \sqrt{L_R/C_R}$, $R_Q = h/4e^2$ is the resistance quantum, C_R and L_R are the capacitance and the inductance of the resonator respectively, $\mathcal{M}$ is the mutual inductance of the resonator and the quantum circuit, and, C_M the coupling capacitance. A derivation of these couplings is given in [50], see section 4.2.1 therein.

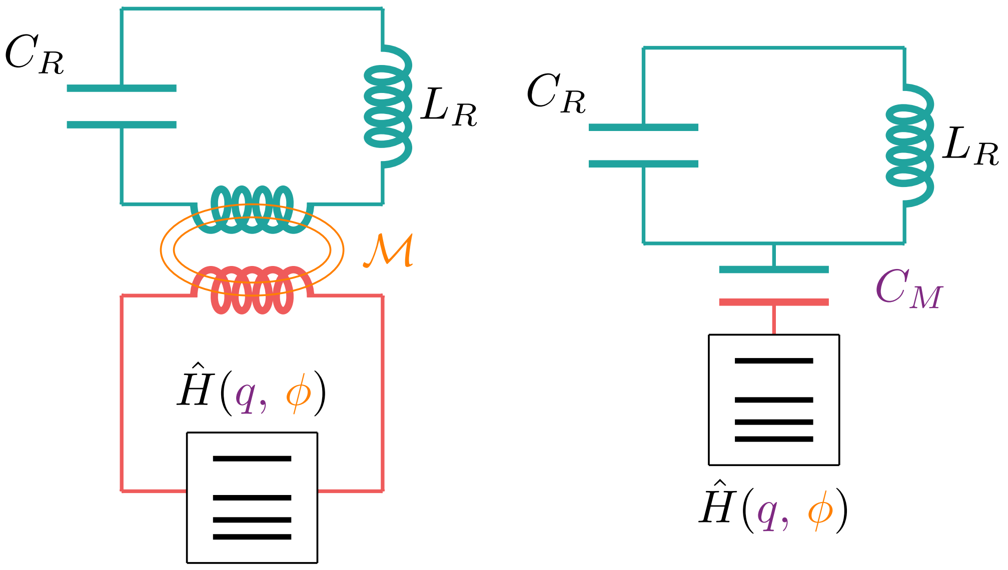

(a) (b)

Figure 2.8: Resonator-quantum circuit coupling schemes. The resonator is a LC circuit represented in cyan. The quantum circuit is described by $\hat{H}(q,\phi)$ and is represented by the black box containing discrete energy levels (thick black lines). In red is represented the circuit which allows one to link the resonator to the quantum circuit. In panel (a) is represented an inductive coupling through a mutual inductance $\mathcal{M}$, while, in panel (b) is represented a capacitive coupling through a capacitance C_M.

Designing the system such that $\lambda \ll 1$ (which can be done by keeping the geometric coupling ratio small for example), we can obtain the full Hamiltonian of the system by expanding $\hat{H}_{\mathrm{qc}}(x_0+\hat{x}_r)$ up to second order in $\hat{x}_r$ which yields

$$\hat{H} = \hbar\omega_r\left(a^\dagger a + \frac{1}{2}\right) + \hat{H}_{\mathrm{qc}}(x_0) + \lambda\hat{H}'_{\mathrm{qc}}(x_0)(sa + s^* a^\dagger) + \lambda^2\hat{H}''_{\mathrm{qc}}(x_0)\left(a^\dagger a + \frac{1}{2}\right), \tag{2.87}$$

where the prime stands for the derivative with respect to x. The terms $\lambda^2 a^{(\dagger)2}$ lead to corrections of order λ^4 and have therefore been neglected. When the term proportional to $\hat{H}''_{\mathrm{qc}}(x_0)$ can be neglected, this Hamiltonian is known as the Jaynes-Cummings Hamiltonian when $\hat{H}_{\mathrm{qc}}$ describes a two levels system [32, 109, 110]. To determine the correction to the energies of this Hamiltonian, we introduce the basis set $\{|\Phi_i n\rangle = |\Phi_i\rangle \otimes |n\rangle\}$, where we have not written the x dependencies for simplicity. We can see that the first order correction yields zero since it involves states with different numbers of photons. Therefore, the lowest order correction to the energies is given by the second order correction which is why developing $\hat{H}$ up to second order in λ earlier is necessary. Assuming that the $|\Phi_i\rangle$ are non-degenerate, the second order correction can be written as $\delta E_{i,n} = \delta E^{(1)}_{i,n} + \delta E^{(2)}_{i,n}$ with

$$\begin{aligned}\delta E^{(1)}_{i,n} &= \lambda^2 \sum_{j\neq i, n'\neq n} \frac{\left|\left\langle \Phi_j n' \right| \hat{H}'_{\text{qc}}(s a + s^* a^\dagger) |\Phi_i n\rangle\right|^2}{E_i - E_j + \hbar\omega_r (n - n')} \\ &= \lambda^2 \sum_{j\neq i} \left|\left\langle \Phi_j \right| \hat{H}'_{\text{qc}} |\Phi_i\rangle\right|^2 \left(\frac{n+1}{E_i - E_j - \hbar\omega_r} + \frac{n}{E_i - E_j + \hbar\omega_r}\right),\end{aligned} \tag{2.88}$$

$$\delta E^{(2)}_{i,n} = \lambda^2 \langle \Phi_i n | \hat{H}''_{\text{qc}}(a^\dagger a + 1/2) |\Phi_i n\rangle = \lambda^2 \langle \Phi_i | \hat{H}''_{\text{qc}} |\Phi_i\rangle (n + 1/2). \tag{2.89}$$

Thus, we need to compute $\langle \Phi_i | \hat{H}''_{\text{qc}} |\Phi_i\rangle$. To do so, we can use the Hellmann-Feynman theorem, which establishes that $E'_i = \langle \Phi_i | \hat{H}'_{\text{qc}} |\Phi_i\rangle$. Taking the derivative of this last expression, we obtain,

$$E''_i = \langle \Phi_i | \hat{H}''_{\text{qc}} |\Phi_i\rangle + \left\langle \Phi'_i \right| \hat{H}'_{\text{qc}} |\Phi_i\rangle + \langle \Phi_i | \hat{H}'_{\text{qc}} \left|\Phi'_i\right\rangle, \tag{2.90}$$

which involves $\left|\Phi'_i\right\rangle$ terms. Using $\hat{H}_{\text{qc}} |\Phi_i\rangle = E_i |\Phi_i\rangle$, we can write $\left|\Phi'_i\right\rangle = -(E_i - \hat{H}_{\text{qc}})^{-1}(E_i - \hat{H}_{\text{qc}})' |\Phi_i\rangle$. Thus, we write

$$\langle \Phi_i | \hat{H}'_{\text{qc}} \left|\Phi'_i\right\rangle = -\langle \Phi_i | \hat{H}'_{\text{qc}} (E_i - \hat{H}_{\text{qc}})^{-1} (E_i - \hat{H}_{\text{qc}})' |\Phi_i\rangle. \tag{2.91}$$

Now, using the identity relation $\sum_j \left|\Phi_j\right\rangle \left\langle \Phi_j\right| = 1$, we have

$$\begin{aligned}\langle \Phi_i | \hat{H}'_{\text{qc}} \left|\Phi'_i\right\rangle &= -\langle \Phi_i | \hat{H}'_{\text{qc}} (E_i - \hat{H}_{\text{qc}})^{-1} \left(\sum_j \left|\Phi_j\right\rangle \left\langle \Phi_j\right|\right) (E_i - \hat{H}_{\text{qc}})' |\Phi_i\rangle \\ &= \sum_{j\neq i} \frac{\left|\langle \Phi_i | \hat{H}'_{\text{qc}} \left|\Phi_j\right\rangle\right|^2}{E_j - E_i}.\end{aligned} \tag{2.92}$$

The term $\left\langle \Phi'_i \right| \hat{H}'_{\text{qc}} |\Phi_i\rangle$ can be computed the same way. At the end, we find a correction to the energy given by

$$\delta E_{i,n} = \lambda^2 \left[E''_i (n + 1/2) + \sum_{j\neq i} \left|\langle \Phi_i | \hat{H}'_{\text{qc}} \left|\Phi_j\right\rangle\right|^2 \left(\frac{2n+1}{E_j - E_i} + \frac{n+1}{E_i - E_j - \hbar\omega_r} + \frac{n}{E_i - E_j + \hbar\omega_r}\right)\right] \tag{2.93}$$

By factorizing the right part of this equation by $(n + 1/2)$, we can rewrite this equation as

$$\delta E_{i,n} = \hbar\delta\omega^{(i)}_r (n + 1/2) - \lambda^2 \sum_{j\neq i} \left|\langle \Phi_i | \hat{H}'_{\text{qc}} \left|\Phi_j\right\rangle\right|^2 \left(\frac{1}{E_j - E_i + \hbar\omega_r} - \frac{1}{E_j - E_i - \hbar\omega_r}\right), \tag{2.94}$$

where $\delta\omega^{(i)}_r$ corresponds to the frequency shift of the resonator when the state $|\Phi_i\rangle$ is occupied. Using Eq. (2.93) and Eq. (2.94), we obtain the following expression for the frequency shift [45, 106]

$$\frac{\hbar\delta\omega^{(i)}_r}{\lambda^2} = E''_i + \sum_{j\neq i} \left|\langle \Phi_i | \hat{H}'_{\text{qc}} \left|\Phi_j\right\rangle\right|^2 \left(\frac{2}{E_j - E_i} - \frac{1}{E_j - E_i + \hbar\omega_r} - \frac{1}{E_j - E_i - \hbar\omega_r}\right). \tag{2.95}$$

This equation holds far from resonance, i.e., when $E_j - E_i$ differs from $\hbar\omega_r$ by much more than the coupling energy, i.e., we need to have $\lambda^2 \left|\langle \Phi_i | \hat{H}'_{\text{qc}} \left|\Phi_j\right\rangle\right| \ll \left|E_j - E_i \mp \hbar\omega_r\right|$ otherwise, the perturbation theory cannot be legitimely used. We now introduce the notation $\omega_{ij} = (E_j - E_i)/\hbar$ to shorten the equations.

In the limit $\delta\omega_r^{(i)} \ll \omega_{ij}$, known as the adiabatic regime, one can easily see that the frequency shift is given by $\hbar\delta\omega_r^{(i)} = \lambda^2 E_i''$. This result can be interpreted as a renormalization of the capacitance / inductance of the resonator by the one of the quantum circuit. When the terms coming from H_{qc}'' can be neglected, i.e., when $\omega_r \sim \omega_{ij}$, one recovers the dispersive shift that can be derived from the Jaynes-Cummings Hamiltonian yielding

$$\delta\omega_r^{(i)} = -\frac{\lambda^2}{\hbar^2}\sum_{j\neq i}\left|\langle\Phi_i|\hat{H}_{\mathrm{qc}}'\left|\Phi_j\right\rangle\right|^2\left(\frac{1}{\omega_{ij}+\omega_r}+\frac{1}{\omega_{ij}-\omega_r}\right), \tag{2.96}$$

In our case, we are interested in flux driven experiments, where the coupling with the resonator induces phase fluctuations across the weak link. The control parameter corresponding to the phase, we need to calculate the derivative of the weak link Hamiltonian $\hat{H}_{\mathrm{wl}}$ with respect to the phase, which can be written as

$$\hat{H}_{\mathrm{wl}}' = \frac{\partial \hat{H}_{\mathrm{wl}}}{\partial\phi} = \frac{\Phi_0}{2\pi}\hat{J}, \tag{2.97}$$

where $\hat{H}_{\mathrm{wl}}$ is the Hamiltonian that describes the weak link which corresponds to our quantum circuit, $\hat{J}$ is the current operator and $\Phi_0 = h/2e$ is the superconducting flux quantum. Until now, we have looked at the frequency shift of the resonator for a given occupied state. However, the quantum state of the weak link is a many-body state, i.e., a state where multiple ABS may be occupied. For example, we can start with the ground state that we will denote $\left|g\right\rangle$. This state is obtained by filling all ABS with negative energy. The resulting frequency shift will therefore be the sum of the frequency shifts for each occupied state, which can be written as

$$\delta\omega_r^{|g\rangle} = \frac{1}{2}\sum_{i<0,\sigma}\delta\omega_r^{(i,\sigma)}, \tag{2.98}$$

where we denote the many-body state with bracket notation whereas we denote a single state i with spin σ with parentheses. The factor 1/2 results from the particle-hole redundancy of the BdG-Hamiltonian. Once the frequency shift of the ground state is known, one can determine the shift associated to any state $|\Psi\rangle$ by creating the appropriate electron-like $\gamma_{i,\sigma}^{\dagger}\left|g\right\rangle$ (with $i>0$) or hole-like $\gamma_{i,\sigma}\left|g\right\rangle$ (with $i<0$) excitation from the ground state, where $\gamma_{i,\sigma}^{(\dagger)}$ stand for the Bogoliubov quasiparticle annihilation (creation). Hence, the resulting shift of the resonator's frequency for a state $|\Psi\rangle$ is given by (see [45, 50])

$$\delta\omega_r^{|\Psi\rangle} = \delta\omega_r^{|g\rangle} + \sum_{i>0,\sigma}\left[n_{i,\sigma}\delta\omega_r^{(i,\sigma)} - (1-n_{-i,\sigma})\delta\omega_r^{(-i,\sigma)}\right], \tag{2.99}$$

where $n_{i,\sigma} = 0, 1$ is the occupancy of the state i, σ.

So far, we have looked at the frequency shift for a system with no drive applied. But, to manipulate the qubit, one further need to drive transitions between ABS. When a drive is applied, the story is a bit different. What can be done, is to first send a microwave signal at appropriate frequency in order to realize a superposition of two states. During the application of this signal, the probability of measuring one of the two states oscillates. These oscillations are the so-called Rabi oscillations. The excitation spectrum can be obtained by sending two microwave pulses. One is here to drive the transitions between states. The second microwave pulse at frequency ω_r allows one to measure the state of the system, the resulting frequency shift of the transition between the two states can be written as [45, 50]

$$\delta\omega_r^{|i\rangle\to|j\rangle} = \delta p_{|j\rangle}\left(\delta\omega_r^{|j\rangle} - \delta\omega_r^{|i\rangle}\right), \tag{2.100}$$

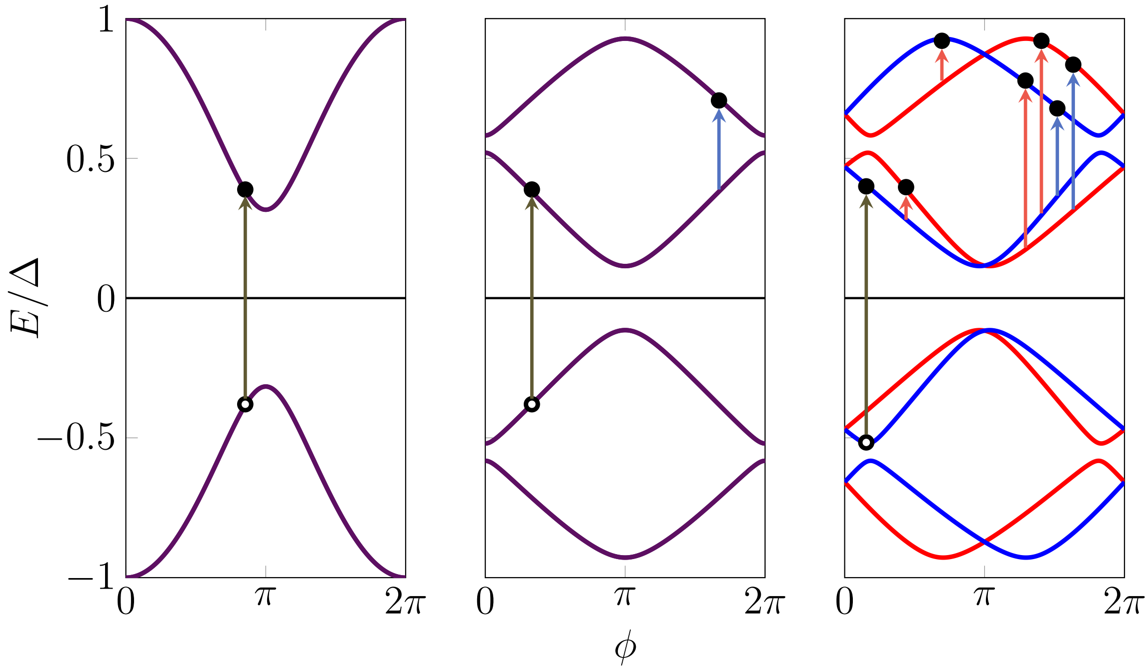

Figure 2.9: Possible transitions between ABS for different Josephson junctions. Left panel corresponds to the spectrum of an atomic contact Josephson junction. Middle panel corresponds to the scenario of a finite length Josephson junction. Right panel is for a finite length junction with spin-orbit coupling. In the right panel, blue curves correspond to spin up states whereas red curves correspond to spin down states. In the left and middle panels, since ABS are spin degenerate the color is the average between spin up and spin down colors. Dark green arrow show pair transitions between the ground state and one excited state. Blue arrows show spin conserving single particle transitions, whereas pink arrows show spin-flip single particle transitions. Occupied states are represented by black dots whereas unoccupied states by empty dots.

where $\delta p_{|j\rangle}$ stands for the population change in the state $|j\rangle$ due to the microwave drive. This change in population is linked to the driving of the system. The driving can be modeled by adding the following term to the Hamiltonian [45]

$$\hat{A}(t) = \frac{1}{2} \sum_{i\sigma<j\sigma'} \left(A_{i\sigma,j\sigma'} \gamma^{\dagger}_{i\sigma} \gamma_{j\sigma'} e^{i\omega_d t} + \text{h.c.} \right), \tag{2.101}$$

where ω_d is the drive frequency [45]. In the case of flux-driving, it turns out that $A_{i\sigma,j\sigma'} \propto \langle \Phi_{i\sigma} | \hat{H}'_{\text{wl}} | \Phi_{j\sigma'} \rangle$. The possible transitions between ABS are shown on Fig. 2.9. As presented in the introduction of this manuscript, there are two kinds of possible transitions between ABS. The first kind of possible transitions are called pair transitions. They involve the breaking of a Cooper pair as it results of an quasiparticle occupying one of the negative energy level being promoted to a positive energy level, leaving its original level empty. The other kind of possible transitions are called single particle transition. They involve the transition of a quasiparticle occupying a positive energy level to another one. These are the ones we are most interested in for the realization of an ASQ.

Thanks to the knowledge acquired in this section, we can see that calculating the current operator is essential both for assessing the feasibility of transitions between different states in a flux-driven experiment and for observing the spin-split energy spectrum of ABS. Therefore, in the next section, we will evaluate the different matrix elements of the current operator.

2.4 Current operator

We now turn to the evaluation of the matrix elements of the current operator for a one scattering potential model. Namely, we are interested in transitions between Andreev levels when a microwave drive is applied to the junction. In particular, we will restrain ourselves to the odd parity sector, since we are interested in the spin-flip transition between excited levels. As we saw previously, the microwave drive leads to a variation of the phase difference ϕ across the junction. The coupling of the junction to the microwave drive is in this case described by the current operator

$$\hat{J} = \frac{2\pi}{\Phi_0}\frac{\partial H_{\text{BdG}}}{\partial \phi}, \tag{2.102}$$

with $\Phi_0 = h/2e$ is the superconducting flux quantum and, the off-diagonal elements of $\hat{J}$ in the basis of Andreev levels determine which transitions can be induced.

Using a gauge transformation $H_{\text{BdG}} \to \tilde{H}_{\text{BdG}} = e^{-i\phi g(x)\tau_z/2} H_{\text{BdG}} e^{i\phi g(x)\tau_z/2}$, Eq. (2.28) can be brought into the form

$$\tilde{H}_{\text{BdG}} = H_e\tau_z + \frac{\hbar}{2}\phi\frac{\partial g(x)}{\partial x}\begin{pmatrix} v_1\sigma_z & 0 \\ 0 & -v_2\sigma_z \end{pmatrix}\tau_0 + \Delta(x)\tau_x, \tag{2.103}$$

where $g(x)$ describes the phase profile along the x direction with $g(d) = -g(0) = 1/2$. Therefore, the current operator may be written as

$$\hat{J} = \frac{\hbar\pi}{\Phi_0}\frac{\partial g(x)}{\partial x}\begin{pmatrix} v_1\sigma_z & 0 \\ 0 & -v_2\sigma_z \end{pmatrix}. \tag{2.104}$$

The elements of the current operator are given by

$$J_{nn'} = \int \mathrm{d}x \Psi_n^\dagger(x)\hat{J}\Psi_{n'}^\dagger(x), \tag{2.105}$$

where $\Psi_n(x)$ is the wavefunction of the Andreev level n associated with the spectrum obtained in Sec. 2.2.2 and $n = (m,\sigma)$ is a composite index. For the diagonal elements, the expression simplifies to $J_{nn} = \frac{e}{\hbar}\partial_\phi E_n$ as expected from the Feynman-Hellmann theorem. Time-reversal symmetry relates states at phases ϕ and $2\pi - \phi$. In particular, $\mathcal{T}\Psi_{m\sigma}(2\pi-\phi) = \Psi_{m-\sigma}(\phi)$ with $\mathcal{T} = \tau_0\Theta$, where Θ is defined in Eq. (2.25). Using $\mathcal{T}\hat{J}\mathcal{T}^{-1} = -\hat{J}$, it follows that $J_{m\sigma\to m'\sigma'}(2\pi-\phi) = -J_{m-\sigma\to m'-\sigma'}(\phi)$, i.e., we can restrict ourselves to computing the current operator matrix elements in the phase interval $\phi \in [0,\pi]$.

To evaluate the off-diagonal of the current operator, we must first determine the wavefunction of Andreev levels. The eigenvectors of $M(E,\phi)$ are given by

$$W = \begin{pmatrix} W_A & 0 \\ 0 & W_D \end{pmatrix}\begin{pmatrix} \cos\frac{\gamma_{B1}}{2}e^{-i\frac{\theta_{B1}}{2}} & 0 & -\sin\frac{\gamma_{B1}}{2}e^{-i\frac{\theta_{B1}}{2}} & 0 \\ 0 & \cos\frac{\gamma_{B2}}{2}e^{-i\frac{\theta_{B2}}{2}} & 0 & -\sin\frac{\gamma_{B2}}{2}e^{-i\frac{\theta_{B2}}{2}} \\ \sin\frac{\gamma_{B1}}{2}e^{i\frac{\theta_{B1}}{2}} & 0 & \cos\frac{\gamma_{B1}}{2}e^{i\frac{\theta_{B1}}{2}} & \\ 0 & \sin\frac{\gamma_{B2}}{2}e^{i\frac{\theta_{B2}}{2}} & 0 & \cos\frac{\gamma_{B2}}{2}e^{i\frac{\theta_{B2}}{2}} \end{pmatrix}, \tag{2.106}$$

where

$$\theta_{Bi} = \frac{\pi}{2} + \varphi_{Bi}, \qquad \gamma_{Bi} = \arctan\frac{|\tilde{B}_i|}{-\mathrm{Im}\left[\tilde{A}_i\right]}, \tag{2.107}$$

with $\tilde{B}_i = |\tilde{B}_i| e^{i\varphi_{Bi}}$. Here the different columns correspond to different values of (ρ,σ), namely the first column corresponds to the state $(-,+)$, the second column to $(-,-)$, the third column to $(+,+)$, and the fourth column to $(+,-)$. with $W_{A/D} = e^{-i\frac{\theta_{A/D}}{2}\sigma_z} e^{-i\frac{\gamma_{A/D}}{2}\sigma_y}$. For the particular case of a single potential model, the coefficient in Eq. (2.106) are given by

$$\theta_{A/D} = \delta k_F (1 \pm \tilde{x}_0) d + \varphi_s \pm \varphi_t , \tag{2.108}$$

$$\theta_{Bi} = \bar{k}_F \tilde{x}_0 d + \frac{\phi}{2} + \varphi_r + \frac{\pi}{2}\left(1 + (-1)^i\right), \tag{2.109}$$

$$\gamma_{A/D} = \arctan \frac{2\sqrt{ST}\sin(\delta\lambda\epsilon(1 \mp \tilde{x}_0)/2)}{T\sin(2\delta\lambda\epsilon) \pm S\sin(2\delta\lambda\epsilon\tilde{x}_0)}, \tag{2.110}$$

$$\gamma_{Bi} = \arctan \frac{-2(-1)^i\sqrt{R(T+S)}\sin\left(\frac{\phi + (-1)^i\omega(\epsilon)}{2} + \bar{\lambda}\epsilon\tilde{x}_0\right)}{-R\sin\left(2\bar{\lambda}\epsilon\tilde{x}_0\right) + (T+S)\sin\left(\phi + (-1)^i\omega(\epsilon)\right)}, \tag{2.111}$$

where $\omega(\epsilon)$ is given in Eq. (2.65).

Some limiting cases will be useful. At $R = S = 0$, the matrix W reduces to

$$W_0 = \begin{pmatrix} e^{-i\frac{\theta_A + \theta_{B1}}{2}} & 0 & 0 & 0 \\ 0 & -ie^{i\frac{\theta_A - \theta_{B1}}{2}} & 0 & 0 \\ 0 & 0 & e^{-i\frac{\theta_D - \theta_{B1}}{2}} & 0 \\ 0 & 0 & 0 & ie^{i\frac{\theta_D + \theta_{B1}}{2}}, \end{pmatrix}. \tag{2.112}$$

Introducing $R, S \ll 1$ perturbatively yields $W \approx W_0 w_1$ with

$$w_1 = \begin{pmatrix} 1 & i\sqrt{S}\,d_{s-} & \sqrt{R}\,d_{r-} & 0 \\ i\sqrt{S}d_{s-} & 1 & 0 & \sqrt{R}\,d_{r+} \\ -\sqrt{R}\,d_{r-} & 0 & 1 & -i\sqrt{S}\,d_{s+} \\ 0 & -\sqrt{R}\,d_{r+} & -i\sqrt{S}\,d_{s+} & 1 \end{pmatrix}, \tag{2.113}$$

with $d_{s\pm} = \frac{1}{2}\tan\gamma_{D/A}$ and $d_{r\pm} = \mp\frac{1}{2}\tan\gamma_{B2/1}$. Using $\omega \approx \delta\lambda\epsilon$ where we remind that $\delta\lambda = \lambda_1 - \lambda_2$, and $\gamma_{A/D}, \gamma_{B1/2} \ll 1$, the corresponding expressions simplify to

$$d_{s\pm} = \frac{\sin\left[\frac{\delta\lambda\epsilon}{2}(1 \pm \tilde{x}_0)\right]}{\sin(\delta\lambda\epsilon)}, \tag{2.114}$$

$$d_{r\pm} = \frac{\sin\left[\frac{\phi}{2} + (\bar{\lambda}\tilde{x}_0 \pm \frac{\delta\lambda}{2})\epsilon\right]}{\sin\left(\phi \pm \delta\lambda\epsilon\right) - R\sin\left(2\bar{\lambda}\epsilon\tilde{x}_0\right)}. \tag{2.115}$$

The eigenvector of $M(E)$ give the amplitudes of incoming electron states at the interfaces with the superconducting leads. To obtain the full wavefunction, we can construct the outgoing electron and incoming/outgoing hole amplitudes with the help of the scattering matrices:

$$\psi^e_{\text{out}} = \mathcal{S}_e(E)\psi^e_{\text{in}}, \tag{2.116}$$

$$\psi^h_{\text{in}} = \alpha(E) r_A(\phi) \mathcal{S}_e(E)\psi^e_{\text{in}}, \tag{2.117}$$

$$\psi^h_{\text{out}} = \alpha^*(E) r_A(\phi)\psi^e_{\text{in}}. \tag{2.118}$$

Then, using continuity, the wavefunctions in the nanowire and the superconductors can be computed. In the basis in which the BdG-Hamiltonian of Eq. (2.28) is given, the wavefunctions for the case of a single scattering potential at position x_0 take the following form in different regions:

- in the left superconductor

$$\frac{\Psi_n(x)}{\sqrt{N_n}} = \begin{pmatrix} \mathcal{A}_{(n)1} e^{\kappa_{1n} x} / \sqrt{v_1} \\ (\mathcal{S}_{e(n)} \mathcal{A}_{(n)})_2 e^{\kappa_{1n} x} / \sqrt{v_1} \\ (\mathcal{S}_{e(n)} \mathcal{A}_{(n)})_1 e^{\kappa_{2n} x} / \sqrt{v_2} \\ \mathcal{A}_{(n)2} e^{\kappa_{2n} x} / \sqrt{v_2} \\ \alpha_n^* \mathcal{A}_{(n)1} e^{i\phi/2 + \kappa_{1n} x} / \sqrt{v_1} \\ \alpha_n (\mathcal{S}_{e(n)} \mathcal{A}_{(n)})_2 e^{i\phi/2 + \kappa_{1n} x} / \sqrt{v_1} \\ \alpha_n (\mathcal{S}_{e(n)} \mathcal{A}_{(n)})_1 e^{i\phi/2 + \kappa_{2n} x} / \sqrt{v_2} \\ \alpha_n^* \mathcal{A}_{(n)2} e^{i\phi/2 + \kappa_{2n} x} / \sqrt{v_2} \end{pmatrix}, \tag{2.119}$$

- in the normal region of the nanowire to the left of the barrier, $0 < x < x_0$:

$$\frac{\Psi_n(x)}{\sqrt{N_n}} = \begin{pmatrix} \mathcal{A}_{(n)1} e^{i k_1^e x} / \sqrt{v_1} \\ (\mathcal{S}_{e(n)} \mathcal{A}_{(n)})_2 e^{-i k_1^e x} / \sqrt{v_1} \\ (\mathcal{S}_{e(n)} \mathcal{A}_{(n)})_1 e^{-i k_2^e x} / \sqrt{v_2} \\ \mathcal{A}_{(n)2} e^{i k_2^e x} / \sqrt{v_2} \\ \alpha_n^* \mathcal{A}_{(n)1} e^{i k_1^h x + i\phi/2} / \sqrt{v_1} \\ \alpha_n (\mathcal{S}_{e(n)} \mathcal{A}_{(n)})_2 e^{-i k_1^h x + i\phi/2} / \sqrt{v_1} \\ \alpha_n (\mathcal{S}_{e(n)} \mathcal{A}_{(n)})_1 e^{-i k_2^h x + i\phi/2} / \sqrt{v_2} \\ \alpha_n^* \mathcal{A}_{(n)2} e^{i k_2^h x + i\phi/2} / \sqrt{v_2} \end{pmatrix}, \tag{2.121}$$

- in the right superconductor

$$\frac{\Psi_n(x)}{\sqrt{N_n}} = \begin{pmatrix} (\mathcal{S}_{e(n)} \mathcal{A}_{(n)})_3 e^{-\kappa_{1n}(x-d)} / \sqrt{v_1} \\ \mathcal{A}_{(n)4} e^{-\kappa_{1n}(x-d)} / \sqrt{v_1} \\ \mathcal{A}_{(n)3} e^{-\kappa_{2n}(x-d)} / \sqrt{v_2} \\ (\mathcal{S}_{e(n)} \mathcal{A}_{(n)})_4 e^{-\kappa_{2n}(x-d)} / \sqrt{v_2} \\ \alpha_n (\mathcal{S}_{e(n)} \mathcal{A}_{(n)})_3 e^{-i\phi/2 - \kappa_{1n}(x-d)} / \sqrt{v_1} \\ \alpha_n^* \mathcal{A}_{(n)4} e^{-i\phi/2 - \kappa_{1n}(x-d)} / \sqrt{v_1} \\ \alpha_n^* \mathcal{A}_{(n)3} e^{-i\phi/2 - \kappa_{2n}(x-d)} / \sqrt{v_2} \\ \alpha_n (\mathcal{S}_{e(n)} \mathcal{A}_{(n)})_4 e^{-i\phi/2 - \kappa_{2n}(x-d)} / \sqrt{v_2} \end{pmatrix}, \tag{2.120}$$

- in the normal region of the nanowire to the right of the barrier, $x_0 < x < d$:

$$\frac{\Psi_n(x)}{\sqrt{N_n}} = \begin{pmatrix} (\mathcal{S}_{e(n)} \mathcal{A}_{(n)})_3 e^{i k_1^e (x-d)} / \sqrt{v_1} \\ \mathcal{A}_{(n)4} e^{-i k_1^e (x-d)} / \sqrt{v_1} \\ \mathcal{A}_{(n)3} e^{-i k_2^e (x-d)} / \sqrt{v_2} \\ (\mathcal{S}_{e(n)} \mathcal{A}_{(n)})_4 e^{i k_2^e (x-d)} / \sqrt{v_2} \\ \alpha_n (\mathcal{S}_{e(n)} \mathcal{A}_{(n)})_3 e^{i k_1^h (x-d) - i\phi/2} / \sqrt{v_1} \\ \alpha_n^* \mathcal{A}_{(n)4} e^{-i k_1^h (x-d) - i\phi/2} / \sqrt{v_1} \\ \alpha_n^* \mathcal{A}_{(n)3} e^{-i k_2^h (x-d) - i\phi/2} / \sqrt{v_2} \\ \alpha_n (\mathcal{S}_{e(n)} \mathcal{A}_{(n)})_4 e^{i k_2^h (x-d) - i\phi/2} / \sqrt{v_2} \end{pmatrix}, \tag{2.122}$$

with N_n the normalization coefficient of the n-th ABS and $\mathcal{A}_{(n)k}$ the component k of the eigenvector of $M(E)$ associated with the state n. We defined $\kappa_{jn} = (\Delta/(\hbar v_j))\sqrt{1-\epsilon_n^2}$. In general, the subscript n or (n) indicates that a quantity is evaluated for a state with energy ϵ_n. The normalization coefficient N_n is given by

$$N_n = \frac{\Delta}{2\hbar} \frac{\sqrt{1-\epsilon_n^2}}{1 + \sum_{j=1,2} \lambda_j \zeta_{j(n)} \sqrt{1-\epsilon_n^2}}, \tag{2.123}$$

where

$$\zeta_{1(n)} = \frac{1}{2} \left[(1+\tilde{x}_0) \left(\left|\mathcal{A}_{(n)1}\right|^2 + \left|\left(\mathcal{S}_{e(n)}\mathcal{A}_{(n)}\right)_2\right|^2 \right) + (1-\tilde{x}_0) \left(\left|\mathcal{A}_{(n)4}\right|^2 + \left|\left(\mathcal{S}_{e(n)}\mathcal{A}_{(n)}\right)_3\right|^2 \right) \right], \tag{2.124}$$

$$\zeta_{2(n)} = \frac{1}{2} \left[(1+\tilde{x}_0) \left(\left|\mathcal{A}_{(n)2}\right|^2 + \left|\left(\mathcal{S}_{e(n)}\mathcal{A}_{(n)}\right)_1\right|^2 \right) + (1-\tilde{x}_0) \left(\left|\mathcal{A}_{(n)3}\right|^2 + \left|\left(\mathcal{S}_{e(n)}\mathcal{A}_{(n)}\right)_4\right|^2 \right) \right]. \tag{2.125}$$

We can now go back to the evaluation of the off-diagonal elements of the current operator. To do so, we need to know how the phase of the superconducting order parameter drops along the nanowire. Rather than evaluating the electrostatic profile along the nanowire, we will compute the elements of the current operator for the case when the entire phase drop happens at an arbitrary point x', i.e.,

$$g(x) = \theta(x-x') - 1/2, \tag{2.126}$$

such that $\partial_x g(x) = \delta(x-x')$. The off-diagonal elements of the current operator for different phase profiles can be obtained by appropriately averaging over x'. Let us note that the phase profile does not affect the value of the diagonal elements of the current operator due to the Feynman-Hellmann theorem mentionned earlier.

Using the wavefunctions given above, the current operator elements can be written in the following form

$$J_{nn'} = e\sqrt{N_n N_{n'}} \begin{cases} \sum\limits_{k=1,2} \left[f^{+}_{nn',k} \mathcal{A}^{*}_{(n)k} \mathcal{A}_{(n')k} - f^{+}_{nn',k+1} \alpha^{*}_{n} \alpha_{n'} (\mathcal{S}_{e(n)} \mathcal{A}_{(n)})^{*}_{k} (\mathcal{S}_{e(n')} \mathcal{A}_{(n')})_{k} \right], & 0 < x' < x_0, \\ -\sum\limits_{k=3,4} \left[f^{-}_{nn',k-1} \mathcal{A}^{*}_{(n)k} \mathcal{A}_{(n')k} - f^{-}_{nn',k} \alpha^{*}_{n} \alpha_{n'} (\mathcal{S}_{e(n)} \mathcal{A}_{(n)})^{*}_{k} (\mathcal{S}_{e(n')} \mathcal{A}_{(n')})_{k} \right], & x_0 < x' < d, \end{cases} \tag{2.127}$$

where $f^{\pm}_{nn',k} = e^{i\lambda_k(\epsilon_{n'}-\epsilon_n)(1\pm\tilde{x}')/2} + \alpha_n \alpha^{*}_{n'} e^{-i\lambda_k(\epsilon_{n'}-\epsilon_n)(1\pm\tilde{x}')/2}$ with $\tilde{x}' = 2x'/d - 1$, and we defined $\lambda_3 = \lambda_1$, $\lambda_4 = \lambda_2$.

It is important to note that Eq. (2.127) can be simplified when certain components $\mathcal{A}_{(n)k}$ of the wavefunction are zero. In particular, this may lead to the absence of specific transitions. If $S = 0$, the spin up and spin down states are decoupled and all spin-flip transitions are absent. A similar decoupling into two independent blocks occurs when there is only spin-flip scattering ($T = 0$). If $R = 0$, the states with different parity of m, i.e., with positive and negative slope as a function of ϕ, are decoupled and all transitions between a doublet with m odd and a doublet with m even are absent.

Eq. (2.127) allows one to compute all the elements of the current operator for arbitrary parameters numerically. Before showing the results, let us discuss limiting cases, where analytical results are possible due to the above-mentioned simplifications.

2.4.1 Spin-flip transitions without backscattering

The expressions for the elements of the current operator simplify considerably when considering the case $R = 0$ and treating $S \ll 1$ perturbatively. As in that case, states with a different parity of m are decoupled, spin-flip transitions within a given doublet are only possible in the phase interval $\varphi_m < \phi < \varphi_{m+1}$ for m odd and $\varphi_{m-1} < \phi < \varphi_m$ for m even. For inter-doublet spin-flip transitions, the phase interval is given as $\varphi_{m'} < \phi < \varphi_{m-1}$ for m, m' odd and as $\varphi_{m'-1} < \phi < \varphi_m$ for m, m' even. Within that interval, we can compute the matrix elements $J_{m\downarrow\to m'\uparrow}$ using the eigenvectors given by Eq. (2.113). For m odd, only the components $\mathcal{A}_{(n)k}$ with $k = 3,4$ contribute, whereas, for m even only the components $\mathcal{A}_{(n)k}$ with $k = 1,2$ contribute. Furthermore, only the product $\mathcal{A}^{*}_{(m\downarrow)k}\mathcal{A}_{(m'\uparrow)k-1}$ is of order 1 whereas $\mathcal{A}^{*}_{(m\downarrow)k}\mathcal{A}_{(m'\uparrow)k}$ is of order $\sqrt{S}$. Keeping only terms up to order $\sqrt{S}$ and assuming $|\delta\lambda|\epsilon$, $\delta\epsilon \ll 1$, one obtains after a lengthy but straightforward calculation the matrix elements for spin-flip transitions between doublets m and m', where $m + m'$ even. Up to a global phase factor (see Appendix D), they take the form

$$\frac{\left|J_{m\downarrow\to m'\uparrow}\right|}{\sqrt{N_\uparrow N_\downarrow}} = \sqrt{S}\frac{e}{2}|\delta\lambda\delta\epsilon| \left| \frac{\eta(\tilde{x}_0)}{2} |\delta\lambda| \bar{\epsilon} f^{(0)}_{\pm} + (-1)^m (1 \mp \tilde{x}_0) f^{(1)}_{\pm} \right|, \tag{2.128}$$

with

$$f^{(0)}_{\pm} = \cos\left[\frac{\delta\epsilon}{2} \left(\frac{1}{\sqrt{1-\bar{\epsilon}^2}} + \bar{\lambda}(1 \pm \tilde{x}') \right) \right], \tag{2.129}$$

$$f^{(1)}_{\pm} = (1 \pm \tilde{x}') \sin\left[\frac{\delta\epsilon}{2} \left(\frac{1}{\sqrt{1-\bar{\epsilon}^2}} + \bar{\lambda}(1 \pm \tilde{x}') \right) \right], \tag{2.130}$$

and $\eta(\tilde{x}_0) = (1-\tilde{x}_0^2)(1 \mp \tilde{x}_0/3)$. Here the upper (lower) sign has to be used for $x' < x_0$ ($x' > x_0$). Furthermore $\bar{\epsilon} = (\epsilon_{m'\uparrow} + \epsilon_{m\downarrow})/2$ and $\delta\epsilon = \epsilon_{m'\uparrow} - \epsilon_{m\downarrow}$.

According to Eq. (2.128) the spin-flip current operator matrix elements vanish when the barrier is at one of the interfaces, $|\tilde{x}_0| = 1$. In fact, this feature is true beyond the specific model considered here: if scattering is only taking place at the interfaces, there are no spin-flip transitions. In this case, it can be easily seen that $s(\epsilon)$ and $t(\epsilon)$ have the same form for their energy dependence, such that, the problem becomes analogous to having only one transmission coefficient. This result is reflected in $W_{A/D}$ which becomes energy independent as for the zero-length junction, yielding vanishing spin-flip elements of the current operator. The problem can be extended to the model with two scattering potentials as discussed in Appendix C. Hence, we will focus on the model with one scattering potential with $|\tilde{x}_0| \neq 1$ where Eq. (2.128) yields a finite result that will be analyzed in more detail for the case of short and long junctions below.

2.4.1.1 Short junction

In the short junction limit, the only possible transition is the intra-doublet transition $1\downarrow \rightarrow 1\uparrow$. Using $\delta\epsilon, \bar{\lambda} \ll 1$, the current matrix element Eq. (2.128) further simplifies to

$$|J_{1\downarrow\rightarrow 1\uparrow}| = \sqrt{S}\frac{e}{4}\sqrt{N_\uparrow N_\downarrow}\,\delta\lambda^2 |\delta\epsilon\,\bar{\epsilon}| \left|\eta(\tilde{x}_0) - (1\mp\tilde{x}_0)(1\pm\tilde{x}')\right|.$$

Using Eq. (2.71) to obtain $\bar{\epsilon}, \delta\epsilon$ and $\sqrt{N_\uparrow N_\downarrow} \approx \Delta\sin\big(\phi/2\big)/2\hbar$ as well as the expression for $\eta(\tilde{x}_0)$, one finds

$$|J_{1\downarrow\rightarrow 1\uparrow}| = \sqrt{S}\frac{e\Delta}{32\hbar}|\delta\lambda|^3 \sin^2\phi\,(1\mp\tilde{x}_0)\left|\frac{1}{3}(\tilde{x}_0 - \tilde{x}') - \tilde{x}_0(1\pm\tilde{x}_0)\right|. \tag{2.131}$$

The characteristic scale for the magnitude of the current matrix element is $J_0^{(\text{short})} = \sqrt{S}e\Delta|\delta\lambda|^3/32\hbar$ where we remind that $\delta\lambda = \lambda_1 - \lambda_2$.

2.4.1.2 Long junction

In the long junction limit, several doublets with energies $\epsilon \ll 1$ exist and Eq. (2.128) can be applied in a large phase interval comprising $\pi/2$ up to the level crossings given by Eq. (2.77). Approximating Eq. (2.73) as

$$\epsilon_{m,\sigma} \approx \frac{f_m(\phi)}{2\bar{\lambda}}\left(1 - (-1)^m\sigma\frac{|\delta\lambda|}{2\bar{\lambda}}\right)$$

and $\sqrt{N_\uparrow N_\downarrow} \approx \Delta/(2\hbar\bar{\lambda})$, one finds that $\delta\epsilon \approx |\delta\lambda|\bar{\epsilon}/\bar{\lambda}$ for the intra-doublet matrix elements where we remind that $\bar{\lambda} = (\lambda_1 + \lambda_2)/2$, yielding

$$|J_{m\downarrow\rightarrow m\uparrow}| = \sqrt{S}\frac{e\Delta}{32\bar{\lambda}\hbar}\left|\frac{\delta\lambda}{\bar{\lambda}}\right|^3 f_m^2(\phi)\left|\eta(\tilde{x}_0) + (-1)^m(1\mp\tilde{x}_0)(1\pm\tilde{x}')^2\right|, \tag{2.132}$$

and the phase interval is delimited by $\varphi_m < \phi < \varphi_{m-1}$ for m odd and $\varphi_{m-1} < \phi < \varphi_m$ for m even. In the long junction regime, the characteristic scale for the magnitude of the matrix elements of the current operator is $J_0^{(\text{long})} = \sqrt{S}eE_T|\delta\lambda/\bar{\lambda}|^3/32\hbar$ with the Thouless energy $E_T = \Delta/\bar{\lambda}$. As for the short junction, the amplitude is proportional to $|\delta\lambda|^3$. Namely, it is suppressed as $|\delta\lambda/\bar{\lambda}|^3 \ll 1$. However, as expected in a long junction, the overall energy scale for the transition matrix elements is set by the Thouless energy rather than the superconducting gap.

By contrast, for the inter-doublet matrix elements, $\delta\epsilon \approx (m' - m)\pi/(2\bar{\lambda})$. In that case, the two terms in the second line of Eq. (2.128) behave differently. For $|\tilde{x}\pm 1| \ll |\delta\lambda|/\bar{\lambda}$, the first term dominates and we obtain

$$|J_{m\downarrow\rightarrow m+2n\uparrow}| \approx \sqrt{S}\frac{e\Delta}{16\bar{\lambda}\hbar}\left|\frac{\delta\lambda}{\bar{\lambda}}\right|^2 \pi|n|\eta(\tilde{x}_0)f_{m+n}(\phi), \tag{2.133}$$

whereas for other values of $\tilde{x}$, the second term dominates and the result reads

$$|J_{m\downarrow\rightarrow m+2n\uparrow}| \approx \sqrt{S}\frac{e\Delta}{4\bar{\lambda}\hbar}\left|\frac{\delta\lambda}{\bar{\lambda}}\right| \pi|n|(1\mp\tilde{x}_0)(1\pm\tilde{x}')\left|\sin\left(n\frac{\pi}{2}(1\pm\tilde{x}')\right)\right|. \tag{2.134}$$

Let us first note that these matrix elements are larger than the intra-doublet matrix elements which have an additional suppression factor due to the small energy difference $\delta\epsilon \propto \delta\lambda$. Furthermore, their magnitude strongly depends on the phase profile. Namely, it is enhanced by a factor $|\bar{\lambda}/\delta\lambda| \gg 1$ when the phase drop is not at the interfaces. [1] Figure 2.10 shows the intra-doublet matrix elements of the current operator within the first doublet in the short and long junction regime, while Fig. 2.12 shows both intra-doublet and inter-doublet spin-flip matrix elements in the long junction regime. We show the matrix elements $|J_{m\downarrow\to m'\uparrow}|$ over the entire phase interval $\phi \in [0, 2\pi]$. Using the relation $J_{m\sigma\to m'\sigma'}(2\pi-\phi) = -J_{m-\sigma\to m'-\sigma'}(\phi)$, the extended phase interval allows one to deduce the matrix elements $|J_{m\uparrow\to m'\downarrow}|$ as well. The different transitions are indicated in Fig. 2.11.

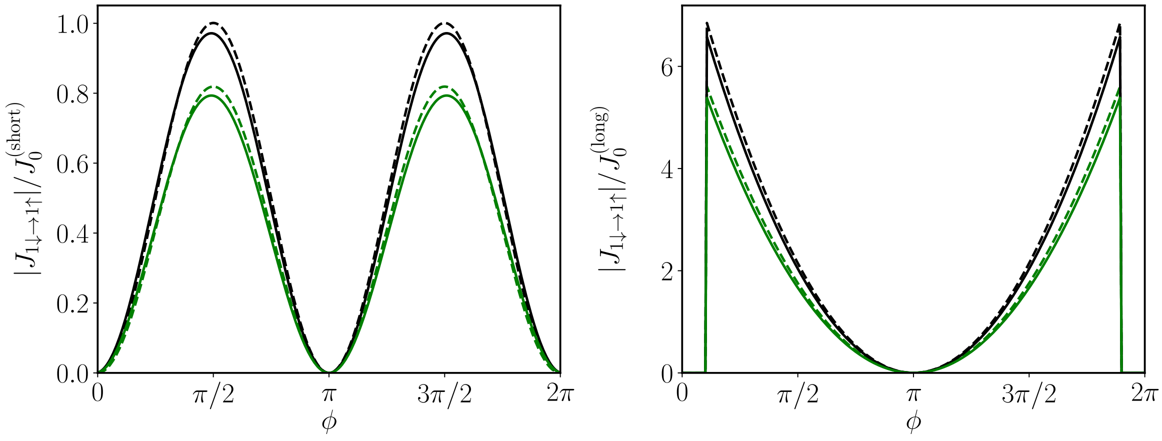

(a) (b)

Figure 2.10: Spin-flip current operator matrix elements within the lowest doublet. (a) Short junction ($\lambda_1 = 0.02$ and $\lambda_2 = 0.01$) and (b) long junction ($\lambda_1 = 20$ and $\lambda_2 = 16$). The parameters for both panels are $T = 0.99$, $S = 0.01$, and $\tilde{x}_0 = 0.3$. The current operator elements are normalized by $J_0^{(\text{short})}$ and $J_0^{(\text{long})}$ for the short and long junction, respectively. Results for a phase drop at $x' = 0$ (green) and $x' = d$ (black) are shown. Dashed lines correspond to the analytical results and full lines to the numerical results. As can be seen in panel (b), the matrix element sharply drops to zero at $\phi = \varphi_1$. In panel (a), the drop happens at a phase too close to zero to be visible.

---

[1] For $|n| > 1$, the enhancement only holds when the phase drop occurs away from the positions $n(1 \pm \tilde{x}')/2 \in \mathbb{Z}$.

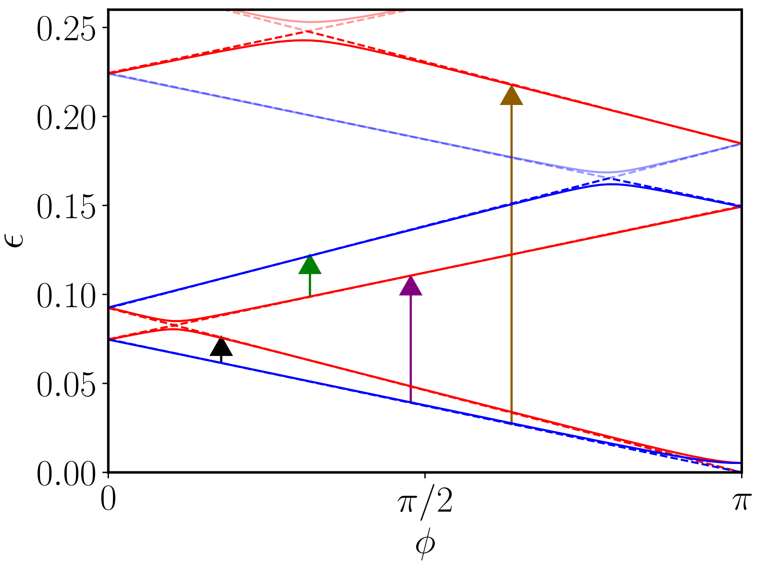

Figure 2.11: Energy spectrum at perfect transmission ($R = 0$, dashed lines) and with finite backscattering ($R = 0.01$, full lines). The colored arrows indicate the transitions for which we calculate the matrix elements of the current operator in Figs. 2.12 and 2.13. The parameters are $T = 0.99 - R$, $S = 0.01$, $\tilde{x}_0 = 0.3$, $\lambda_1 = 20$, and $\lambda_2 = 16$.

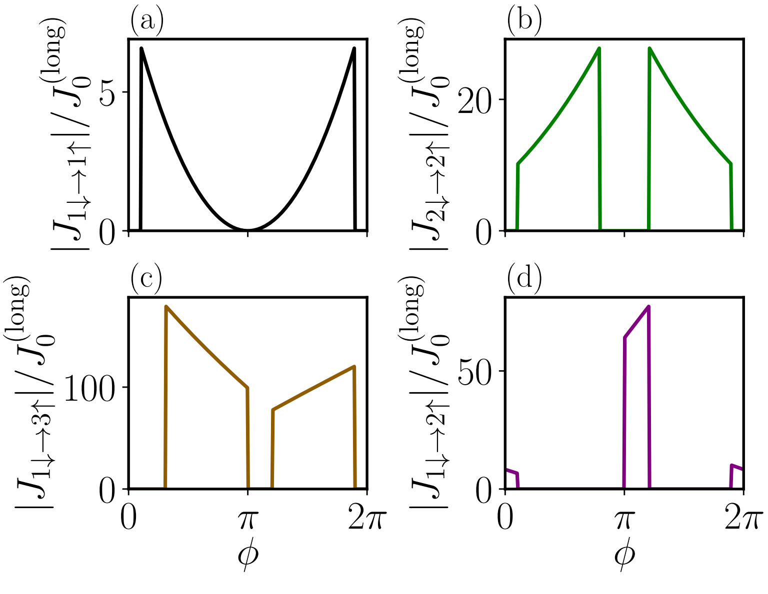

Figure 2.12: Numerical results for the matrix elements of the current operator between opposite spin states at perfect transmission associated with the spectrum shown in Fig. 2.11. Panels (a) and (b) show the intra-doublet matrix elements for the first and second doublet, respectively. Panel (c) shows the inter-doublet spin-flip matrix elements between the first and third doublet, having the same parity. Panel (d) shows the inter-doublet spin-flip matrix elements between the first and second doublet, having opposite parity. In all panels, we took $x' = d$. The abrupt drops to zero at phases φ_m are due to the various crossings between states at perfect transmission.

2.4.2 Effect of finite backscattering

Finite backscattering couples states with different parity of m and therefore renders the spin-flip current operator elements finite for all phases. This is particularly interesting in long junctions, where several doublets exist and anti-crossings take place at phases not too close to zero. To include the effect of backscattering on the current operator matrix elements in long junctions, we use the results of section 2.2.2 for the ABS at finite R. Namely, the wavefunctions corresponding to the energies given by Eq. (2.79) read

$$\psi^{>}_{m} = U_m \psi_{+m} + V_m \psi_{-m}, \tag{2.135}$$

$$\psi^{<}_{m} = - V_m \psi_{+m} + U_m \psi_{-m}, \tag{2.136}$$

where $U_m = \Gamma_m / \sqrt{\left(\sqrt{\delta\varphi_m^2 + \Gamma_m^2} - \delta\varphi_m\right)^2 + \Gamma_m^2}$ and $V_m = \sqrt{1 - U_m^2}$ with $\Gamma_m = 2\bar{\lambda}\delta_m$ and $\delta\varphi_m = \phi - \varphi_m$. Thus, U_m and V_m vary around φ_m on a typical scale set by Γ_m.

2.4.2.1 Modification of the intra- and inter-doublet spin-flip transitions in long junctions

In this section, we will focus on how the transitions we previously studied in section 2.4.1 are modified due to finite backscattering. For intra- and inter-doublet matrix elements in the limit $|1 \pm \tilde{x}'| \ll |\delta\lambda|/\bar{\lambda} \ll 1$, Eq. (2.128) simplifies to

$$|J_{m\downarrow \to m'\uparrow}| = J_0 \bar{\lambda} \left| \epsilon^2_{m\downarrow} - \epsilon^2_{m'\uparrow} \right| \tag{2.137}$$

with $J_0 = \sqrt{S} e \Delta (\delta\lambda/\bar{\lambda})^2 \eta(\tilde{x}_0)/16\hbar$.

Finite back-scattering modifies this result in the vicinity of the anti-crossings on a scale Γ_m. If the different anti-crossings are well separated in phase on that scale, we find the spin-flip matrix elements between doublets m and $m' = m + 2n$,

$$\frac{|J_{m\downarrow \to m'\uparrow}|}{J_0 \bar{\lambda}} = \begin{cases} U_{m'} V_{m-1} \left| \left(\epsilon^-_{m-1}\right)^2 - \left(\epsilon^-_{m'}\right)^2 \right| & m \text{ odd}, \\ U_{m'-1} V_m \left| \left(\epsilon^+_{m}\right)^2 - \left(\epsilon^+_{m'-1}\right)^2 \right| & m \text{ even}. \end{cases} \tag{2.138}$$

Thus, the main effect of finite backscattering is to smooth the drop to zero over a width given by Γ_m, i.e., the typical scale of variation of U_m and V_m. Figure 2.13 shows numerical results for both intra-doublet and inter-doublet matrix elements $|J_{m\downarrow \to m'\uparrow}|$ over the entire phase interval $[0, 2\pi]$.

As discussed in Sec. 2.4.1, the inter-doublet matrix elements are enhanced by a factor $\sim \bar{\lambda}/|\delta\lambda|$ for $|\tilde{x} \pm 1| \gg |\delta\lambda|/\bar{\lambda}$. The smoothing due to finite backscattering involves the same factors U_m and V_m, but starting form Eq. (2.134) instead of Eq. (2.133).

2.4.2.2 Spin-flip matrix elements between opposite parity doublets

In the absence of backscattering, spin-flip matrix elements between opposite parity doublets are possible only in a narrow phase interval around 0 and π. Including backscattering renders them finite at all phases and can be done the same way as in the previous section. For a given transition, two anti-crossings are relevant, one close to zero and another one close to π. The spin-flip matrix elements of the current operator between doublets m and $m' = m + 2n + 1$ are given as

$$\frac{|J_{m\downarrow \to m'\uparrow}|}{J_0 \bar{\lambda}} = \left| U_{m'-1} U_{m-1} \left[\left(\epsilon^+_{m-1}\right)^2 - \left(\epsilon^+_{m'-1}\right)^2 \right] + V_{m'-1} V_{m-1} \left[\left(\epsilon^-_{m-1}\right)^2 - \left(\epsilon^-_{m'-1}\right)^2 \right] \right|, \tag{2.139}$$

for m odd, and

$$\frac{|J_{m\downarrow\to m'\uparrow}|}{J_0\bar{\lambda}} = \left| U_{m'} U_m \left[(\epsilon^-_m)^2 - (\epsilon^-_{m'})^2 \right] + V_m V_{m'} \left[(\epsilon^+_m)^2 - (\epsilon^+_{m'})^2 \right] \right|, \tag{2.140}$$

for m even. Here the first line in Eq. (2.139) [in Eq. (2.140)] is significant at phases $\phi \sim \varphi_{m-1}$ (φ_m) while the second line is significant at phases $\phi \sim \varphi_{m'-1}$ $(\varphi_{m'})$ when m odd (even). As previously, the main effect of finite backscattering is to smoothen the drop to zero of the different matrix elements over a width Γ_m around each crossing. An illustration of these matrix elements is shown in panel (d) of Fig. 2.13.

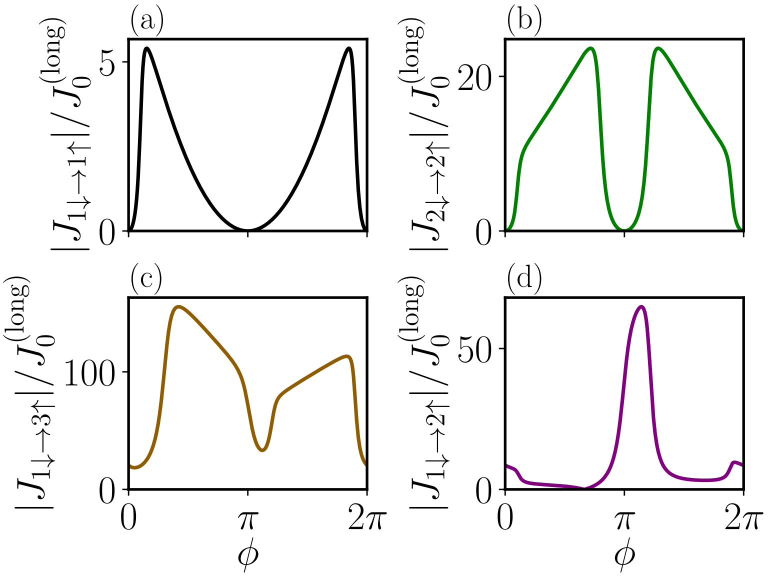

Figure 2.13: Numerical results for the matrix elements of the current operator between opposite spin states at finite backscattering ($R = 0.01$) associated with the spectrum shown in Fig. 2.11. As discussed in the main text, finite backscattering smoothens the sharp drops seen in Fig. 2.12. In panel (c), one further sees that the matrix element no longer vanishes at phases close to π. This results from the avoided crossing between positive and negative energy states at $\varphi = \pi$ in the presence of finite backscattering.

2.4.3 Spin-conserving matrix elements

Finally, we can look at the spin-conserving matrix elements of the current operator. These matrix elements do not require spin-flip scattering. We will therefore start by calculating them at $R = S = 0$. Then we will include backscattering as in section 2.4.2.

At $R = S = 0$ only one component $\mathcal{A}_{(n),k}$ with $k = 1, ..., 4$ is non zero, which simplifies Eq. (2.127) significantly. As before, at $R = 0$, only transitions between doublets with the same parity are allowed in a wide phase interval. Hence, the matrix elements between doublet m and $m' = m + 2n$ are given as

$$|J_{m\uparrow\to m'\uparrow}| \approx \frac{eE_T}{\hbar} \left| \cos\left[\frac{\pi n}{2}(1-\tilde{x}')\right] \right| \begin{cases} 1 + \mathrm{sign}(\phi - \varphi_m)|\delta\lambda|/(2\bar{\lambda}), & m \text{ odd}, \\ \\ 1 - \mathrm{sign}(\phi - \varphi_{m-1})|\delta\lambda|/(2\bar{\lambda}), & m \text{ even}. \end{cases} \tag{2.141}$$

For $\sigma = \downarrow$, one has to interchange sign$(\phi - \varphi_m)$ and sign$(\phi - \varphi_{m-1})$. For $m' = m + 2n + 1$, the same result holds, but in the complementary phase intervals where $|J_{m\uparrow\to m+2n\uparrow}| = 0$. As for the spin-flip matrix elements, the spin-conserving matrix elements sharply drop to zero at level crossings. Including backscattering smoothens these drops as discussed above for the spin-flip matrix elements.

However, there is a particular case when $m' = m + 1$. In that case, the two states involved in the transition cross at φ_m in the absence of backscattering. Backscattering mixes them and therefore enables transitions. One finds

$$|J_{m\sigma\to m+1\sigma}| = 2eE_T\,|U_m V_m|\,. \tag{2.142}$$

This leads to a peak in the amplitude of the current operator matrix element at $\phi = \varphi_m$ as shown in Fig. 2.14(a).

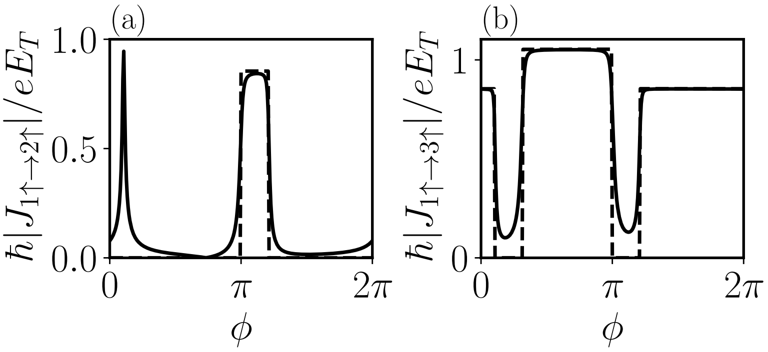

Figure 2.14: Numerical results for the spin-conserving matrix elements of the current operator. Here $S = 0$, $\tilde{x}_0 = 0.3$, $\tilde{x}' = 1$, $\lambda_1 = 20$, and $\lambda_2 = 16$. The dashed and full lines corresponds to perfect transmission $R = 0$ and finite backscattering $R = 0.001$, respectively. Panel (a) shows the matrix elements between spin-up states of the first and second doublet. The peak at $\phi = \varphi_1$ results from the mixing between the two states involved in the transition in the presence of finite backscattering. Panel (b) shows the matrix elements between spin up states of the first and third doublet.

2.4.4 Numerical results

Arbitrary length junctions and/or arbitrary values of the scattering parameters may be studied numerically using Eqs. (2.57) and (2.127). In particular, we will be interested in the case when S and T are comparable and/or when $\delta\lambda \sim \bar{\lambda}$. A sample spectrum is shown in Fig. 2.15(a) and the corresponding current operator matrix element for spin-flip transitions within the lowest doublet in Fig. 2.15(b). The phase dependence is similar to the perturbative case with maxima at the avoided crossings. For the example shown, the scale for the magnitude of the current operator matrix elements is set by $J_0^{(\text{long})} = \sqrt{S}eE_T|\delta\lambda/\bar{\lambda}|^3/32\hbar$, where $eE_T/\hbar$ is the relevant scale for the critical current of the junction. The smallness of the prefactor is due to numerical factors and does not contain a small parameter.

In Fig. 2.16, we show the dependence of the magnitude of the current operator matrix element for intra-doublet transitions within the lowest doublet $m = 1$ on various parameters. Panel (a) shows that the magnitude of the current operator matrix element is indeed maximal when S and T are comparable, whereas it vanishes when one of them is zero. Panel (b) shows the length dependence of the effect. As expected, intermediate length junctions are optimal. If the junction is too short, the effect of spin-orbit coupling is weak such that the magnitude of the spin-flip current operator matrix elements is suppressed. If the junction is too long, the overall energy scale for all the current operator matrix elements set by the

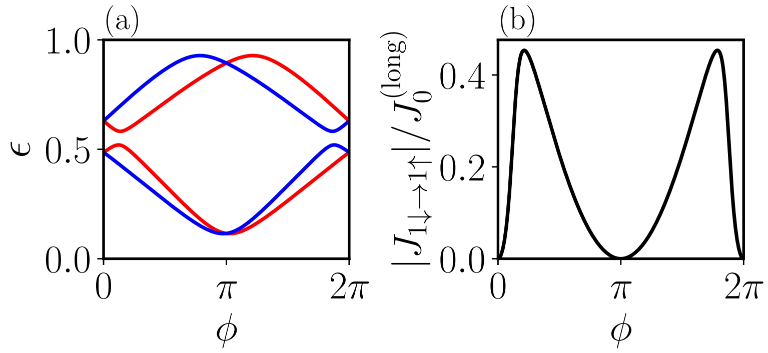

Figure 2.15: Numerical results in the non-perturbative regime: (a) spectrum and (b) current operator matrix element for spin-flip transitions within the lowest doublet. Here $S = T = 0.45$, $R = 0.1$, $\lambda_1 = 2.3$, $\lambda_2 = 1.3$, $\tilde{x}_0 = 0.3$, and $\tilde{x}' = 1$. The phase dependence is similar to the perturbative case with maxima at the avoided crossings. The scale for the magnitude of the current operator matrix elements is set by $J_0^{(\mathrm{long})} = \sqrt{S}\, e E_T |\delta\lambda/\bar{\lambda}|^3/32\hbar$.

Thouless energy is small and therefore suppresses the effect. Panel (c) shows the dependence of the magnitude of the current operator matrix element on the position of the scattering center. As mentioned earlier, spin-flip transitions are absent when scattering only occurs at the interfaces. Here we see that their amplitude is maximal when the scattering happens close to the center of the junction. Finally, panel (d) shows the variation of the current operator matrix element with the position of the phase drop. The matrix element drops to zero for a particular value of $\tilde{x}$. This can already been seen on the perturbative level, see Eqs. (2.131) and (2.132). In Fig. 2.17, we show that this generically the case for all current operator matrix elements, both spin-preserving and spin-flip.

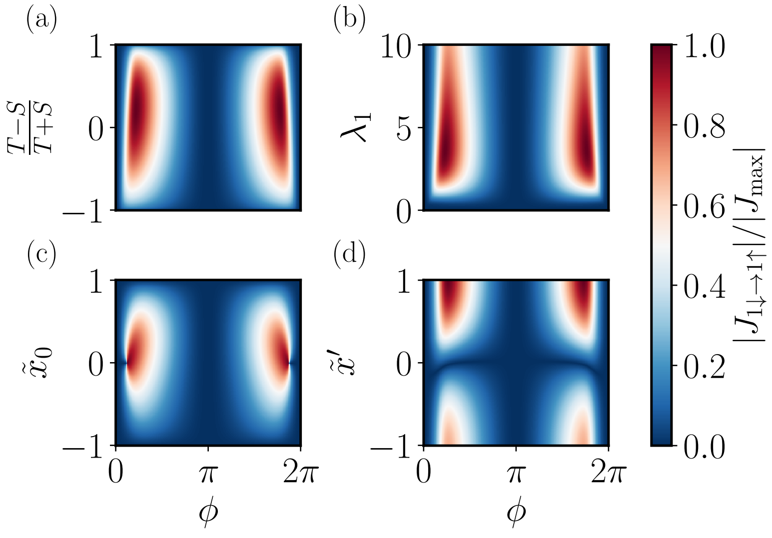

Figure 2.16: Dependence of the intra-doublet matrix elements of the current operator within the lowest doublet on different parameters. In all panels, $R = 0.1$ and $|\delta\lambda|/\bar{\lambda} = 0.556$. In panel (a)-(c), the phase drop is set at $\tilde{x}' = 1$. For panel (b)-(d), we have $T = S = 0.45$. For panels (a), (c) and (d), we set $\lambda_1 = 2.3$. For panels (a), (b) and (d), we set $\tilde{x}_0 = 0.3$.

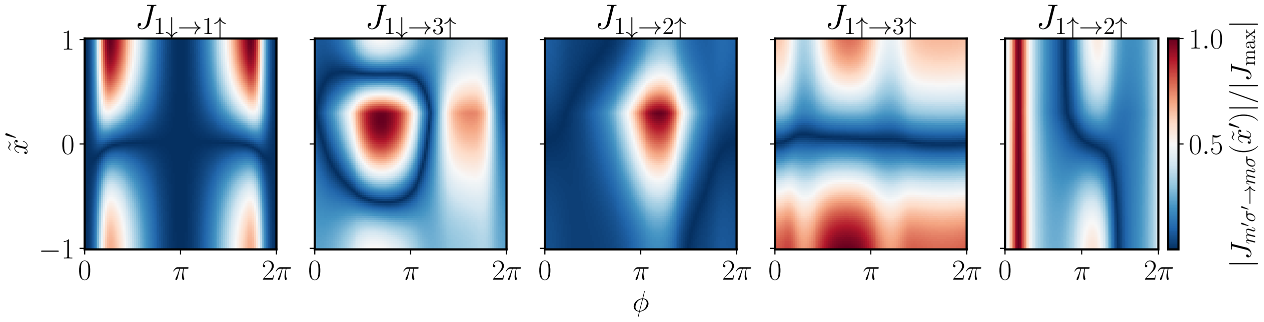

Figure 2.17: Dependence on the position of the phase drop $\tilde{x}'$ of several current operator matrix elements, covering all possible kinds of transitions. Same parameters as in Fig. 2.16 (d). We can see that both spin-preserving and spin-flip matrix elements generically vanish for particular values of $\tilde{x}$.

2.5 Conclusion

In this chapter, we have studied the spin-splitting of ABS due to SOC. In the first part, we showed how the SOC can lift the spin degeneracy of ABS in finite length junctions. We have studied the energy spectrum in detail. The model we considered involves a single scattering potential located at an arbitrary position x_0 along the normal region. We saw that considering finite spin-flip transmission can lead to a modification of the spin-splitting of ABS. Then, in the second part, we briefly presented some experimental methods that allow for the detection of ABS. We mainly focused on cQED, which are the types of experiments performed today for the detection and manipulation of ABS. Therefore, we have evaluated the relevant quantities, namely the matrix elements of the current operator, that determine which transitions are within reach in phase-driven experiments. Notably, we found that SOC with finite spin-flip transmission probability allows one to have finite matrix elements between opposite spin states within the same doublet. Our detailed study provides the specific dependence of the energy splitting and current-operator matrix elements on the phase difference, the transmission properties of the scattering potential, and its location along the nanowire. In particular, we find that the ratio between the current-operator matrix element and the energy splitting varies quadratically in the pseudo-spin band velocity asymmetry and linearly in the spin-flip transmission amplitude. The strong suppression of the current-operator matrix element does not favor the operation of the Andreev spin qubit using a flux drive if spin-orbit coupling is small. Thus, our study will contribute to identifying optimal working points, where a sufficiently strong driving may be achieved. If spin-orbit coupling is sufficiently large, the order of magnitude of the matrix element is bounded by the critical current of the junction. Thus, we do not see major challenges in operating an Andreev spin qubit in that case.

Note that recent experiments with quantum dots subject to large Coulomb repulsion allowed for stabilizing the doublet ground state in the odd sector thus removing the constraint of having a junction subject to quasiparticle poisoning, as well as resolving the spin splitting [48, 95, 111]. The next chapter will then focus on the possibility of realizing an ASQ in S-QD-S junctions.

Chapter 3

The double quantum dots junction

Contents

In chapter 2, we showed how spin-orbit coupling can lead to the lifting of the spin degeneracy of ABS. Also, we showed that thanks to spin-flip scattering processes, it is possible to couple opposite spin states within the same doublet of ABS. As such, we predict that spin-flip transition within a same doublet should be accessible in flux-driven cQED experiments, and therefore, that this transition could be used to realize an ASQ when the junction is in the odd parity sector. However, there is an issue with the system we described previously. To realize an ASQ, we must be in the odd parity sector such that the total spin of the system is non-zero. To be in this parity sector, the weak link must be subject to what is known as quasiparticle poisoning [33, 112]. This quasiparticle poisoning corresponds to an excess quasiparticle being trapped within the subgap levels. The time that this particle is trapped in an ABS is finite. It can either escape back into the continuum or recombine, ultimately bringing the weak link to its spin-zero ground state.

One way of countering this problem is to consider a junction with a quantum dot rather than a weak link. As we saw in Sec. 1.4 of chapter 1, using a quantum dot allows one to tune the ground state of the junction to be an odd-parity spin-1/2 ground state. Using this type of junction for ASQ is the solution that has been adopted in these studies [48, 95, 111]. They considered a S-QD-S junction with spin-orbit coupling, allowing spin-dependent tunneling terms between the superconducting electrodes and the resonant level of the quantum dot. In addition, their experiment showed that the spin degeneracy of ABS in such junctions can be lifted, which they explain by the presence of all other non-resonant levels in the QD that act as additional conduction channels. Using such systems and by applying a magnetic field, they were able to realize ASQs and have better control of the parity of the junction thanks to the Coulomb repulsion. Note however that, the applied magnetic field helped for the qubit manipulation and readout in [48] but was not necessary to observe the intra-doublet transition in [95]. As mentioned in the introduction of this manuscript, to manipulate the spin states of the doublet ground state, they used electric dipole spin resonance by sending a microwave pulse into a gate placed below the QD.

Here, we want to propose a simplification of their system, in which the spin degeneracy can be lifted, and potentially be an interesting platform for the realization of ASQs. The junction we will study consists of two quantum dots coupled together to form the normal region of the junction. Each of these dots is coupled to the two superconducting electrodes, with spin-dependent tunnel couplings. In this system, we therefore have two levels that can be occupied and tuned separately. Also, when one of the two dots is non-resonant then, our system becomes analogous to the one presented in [48, 95]. In this chapter, we will first show in Sec. 3.1 why it is not enough to consider a junction with a single quantum dot and spin-dependent couplings if we consider only a single resonant level. This result can be understood with an analogy to the S-N-S junction where two channels with different Fermi velocities are needed in order to lift the spin degeneracy. Then, we will consider the full system with the two quantum dots. We will show in Sec. 3.3 that adding a second quantum dot to the system results in the lifting of the spin degeneracy in the odd parity sector. Finally, as for the S-N-S junction, we will be looking at the current operator in order to determine which transitions are allowed in the system with the considered couplings. Specifically, in Sec. 3.4.3 we will determine the minimum requirements in order to have finite matrix elements between opposite spin states such that in this kind of junctions, an ASQ could be realized in phase-driven experiments. Our results indicate that these elements can be non-zero when considering a finite coupling between the two dots and spin-dependent tunnel couplings between the superconducting leads and the dots. This is again analogous to the S-N-S junction studied in Chap. 2 where the spin-flip transmission probability was necessary to couple opposite spin states. This corresponds here to the combination of the inter-dot coupling and spin-dependent tunnel coupling.

3.1 Josephson junction with a single quantum dot and SOC

We will start this chapter by showing why it is insufficient to consider a Josephson junction with a single quantum dot to lift the spin degeneracy, even if the couplings between the dot and the leads are spin-dependent. We consider tunnel couplings, independent of $\boldsymbol{k}$ as in Sec. 1.4, which respect TRS, such that we can write them under the form

$$\check{t} = t_0 + i\boldsymbol{t}\cdot\boldsymbol{\sigma}, \tag{3.1}$$

with $t_{0,x,y,z}$ reals. A schematic of the system is shown in Fig. 3.1.

In the following, we use the notation $\bar{\sigma} = -\sigma$ and $t^{(a)}_{\alpha\beta}$ where α, β are spin indices and $a = L, R$ stands for left or right electrode such that

$$t_{\uparrow\uparrow} = t^*_{\downarrow\downarrow} = t_0 + i t_z, \tag{3.2}$$

$$t_{\uparrow\downarrow} = -t^*_{\downarrow\uparrow} = i(t_x - i t_y). \tag{3.3}$$

As in Sec. 1.4, we use the single impurity Anderson model (SIAM) given in Eq. (1.167) to describe our system. We recall that the Hamiltonian is given as

$$H = \sum_{a=L,R} \left(H_a + H_{T,a}\right) + H_D, \tag{3.4}$$

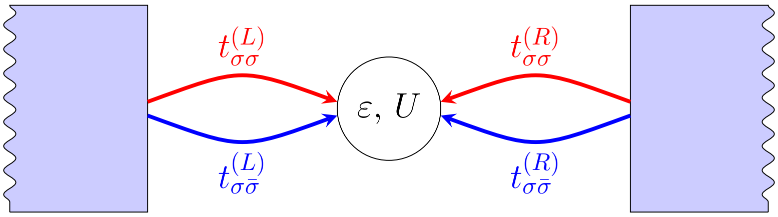

Figure 3.1: Schematic of the S-QD-S with spin-dependent tunnel couplings between the superconducting leads and the quantum dot where we used the notation $\bar{\sigma} = -\sigma$. The on-site energy of the dot is ε and with a Coulomb repulsion of strength U. The spin-conserving couplings are represented in red and the spin-flip ones in blue.

with

$$H_a = \sum_{\boldsymbol{k}\sigma,a} \xi_{\boldsymbol{k},a} c^\dagger_{\boldsymbol{k}\sigma,a} c_{\boldsymbol{k}\sigma,a} + \sum_{\boldsymbol{k},a} \left(\Delta e^{i\varphi_a} c^\dagger_{\boldsymbol{k}\uparrow,a} c_{-\boldsymbol{k}\downarrow,a} + \text{h.c.} \right), \tag{3.5}$$

$$H_{T,a} = \sum_{\boldsymbol{k}} \sum_{\alpha,\beta} \left(t^{(a)}_{\alpha\beta} d^\dagger_\alpha c_{\boldsymbol{k}\beta,a} + \text{h.c.} \right), \tag{3.6}$$

$$H_D = \sum_\sigma \varepsilon d^\dagger_\sigma d_\sigma + U d^\dagger_\uparrow d_\uparrow d^\dagger_\downarrow d_\downarrow. \tag{3.7}$$

The first Hamiltonian describes the superconducting electrode a, such that $c^\dagger_{\boldsymbol{k}\sigma,a}$ and $c_{\boldsymbol{k}\sigma,a}$ correspond to the creation and annihilation operators for an electron of spin σ and momentum $\boldsymbol{k}$ in this electrode. H_D describes the quantum dot with on-site energy ε and Coulomb potential U. The operators $d^\dagger_\sigma$ and d_σ thus stand for the creation and annihilation of an electron with spin σ in the dot. Finally, $H_{T,a}$ is the tunneling Hamiltonian between the dot and lead a with tunneling amplitude $t^{(a)}_{\alpha\beta}$. However, do note that for even parity states, the inter-dot interaction just leads to an energy shift of the different states, but the exchange interaction shifts the energy of states with an electron with parallel spin on each dot.

As in Chap. 1, we place ourselves in the atomic limit, such that we can describe the system with an effective low energy Hamiltonian. We first perform a Schrieffer-Wolff transformation $U = e^S$ on the SIAM Hamiltonian with

$$S = \sum_{a=L,R} \sum_{|\Phi_H\rangle|\Phi_L\rangle} |\Phi_H\rangle \frac{\langle \Phi_H| H_{T,a} |\Phi_L\rangle}{\langle \Phi_H| H |\Phi_H\rangle - \langle \Phi_L| H |\Phi_L\rangle} \langle \Phi_L| - \text{h.c.}, \tag{3.8}$$

Where $|\Phi_H\rangle$ denotes high energy states, i.e., states which contain at least one quasiparticle in the superconducting leads a, while $|\Phi_L\rangle$ denotes the low energy without any quasiparticle in the superconducting leads. The effective low energy Hamiltonian is obtained by projecting the "transformed" Hamiltonian into the low energy sector

$$H_{\text{eff}} = H_D + \frac{1}{2} P_L \left[S, \sum_{a=L,R} H_{T,a} \right] P_L, \tag{3.9}$$

with $P_L = \sum_{\Phi_L} |\Phi_L\rangle \langle \Phi_L|$ is the projector onto the low energy sector.

Before developing the second term, we rewrite the superconducting and tunneling Hamiltonian using the Bogoliubov-de Gennes transformation $c_{\boldsymbol{k}\sigma,a} = e^{i\varphi_a/2}\left(u_{\boldsymbol{k}}\gamma_{\boldsymbol{k}\sigma,a} - \sigma v_{\boldsymbol{k}}\gamma^\dagger_{-\boldsymbol{k}\bar{\sigma},a}\right)$ yielding

$$H_a = \sum_{\boldsymbol{k},\sigma} E_{k,a}\gamma^\dagger_{\boldsymbol{k}\sigma,a}\gamma_{\boldsymbol{k}\sigma,a}, \tag{3.10}$$

$$H_{T,a} = \sum_{\boldsymbol{k}}\sum_{\alpha,\beta}\left[\gamma^\dagger_{\boldsymbol{k}\beta,a}\left((t^{(a)}_{\alpha\beta})^* u_{\boldsymbol{k}} e^{-i\varphi_a/2} d_\alpha - \beta\, t^{(a)}_{\bar{\alpha}\bar{\beta}} v_{\boldsymbol{k}} e^{i\varphi_a/2} d^\dagger_{\bar{\alpha}}\right) + \text{h.c.}\right], \tag{3.11}$$

with $E_{\boldsymbol{k},a} = \sqrt{\xi^2_{\boldsymbol{k},a} + \Delta^2}$ the eigenvalues of the superconducting Hamiltonians. We can now develop Eq. (3.9) at the lowest order in $E_{\boldsymbol{k},i}$

$$H_{\text{eff}} = H_D - \sum_{a=L,R}\sum_{\boldsymbol{k}}\sum_{\alpha,\beta,\delta}\left[t^{(a)}_{\beta\delta} u_{\boldsymbol{k}} e^{i\frac{\varphi_a}{2}} d^\dagger_\beta - \delta (t^{(a)}_{\bar{\beta}\bar{\delta}})^* v_k e^{-i\frac{\varphi_a}{2}} d_{\bar{\beta}}\right]\frac{1}{E_{\boldsymbol{k},a}}\left[(t^{(a)}_{\alpha\delta})^* u_{\boldsymbol{k}} e^{-i\frac{\varphi_a}{2}} d_\alpha - \delta\, t^{(a)}_{\bar{\alpha}\bar{\delta}} v_k e^{i\frac{\varphi_a}{2}} d^\dagger_{\bar{\alpha}}\right]. \tag{3.12}$$

Now, using Eqs. (3.2) and (3.3), and $(d^{(\dagger)}_\alpha)^2 = 0$, we can write

$$H_{\text{eff}} = H_D - \sum_{a=L,R}\sum_{\boldsymbol{k}}\left[\sum_{\alpha,\beta,\delta}\frac{u^2_{\boldsymbol{k}} - v^2_{\boldsymbol{k}}}{E_{\boldsymbol{k},a}} t^{(a)}_{\delta\beta}(t^{(a)}_{\bar{\alpha}\beta})^* d^\dagger_{\delta} d_\alpha + 2\frac{u_{\boldsymbol{k}} v_{\boldsymbol{k}}}{E_{\boldsymbol{k},a}}\left(|t^{(a)}_0|^2 + |\boldsymbol{t}^{(a)}|^2\right)\left(d^\dagger_\uparrow d^\dagger_\downarrow e^{i\varphi_a} + \text{h.c.}\right)\right]. \tag{3.13}$$

As one can see, we find a Hamiltonian with the same structure as Eq. (1.187). The first term remains odd in momentum, so it vanishes when summed over $\boldsymbol{k}$. For the second term, the only combination is the one that was already present in Eq. (1.187). In the end, we obtain an effective low energy Hamiltonian which can be written once again as

$$H_{\text{eff}} = \sum_\sigma \varepsilon d^\dagger_\sigma d_\sigma + U d^\dagger_\uparrow d_\uparrow d^\dagger_\downarrow d_\downarrow + \left(\Gamma_\phi d^\dagger_\uparrow d^\dagger_\downarrow e^{i\frac{\varphi_R + \varphi_L}{2}} + \text{h.c.}\right), \tag{3.14}$$

with

$$\Gamma_\phi = \Gamma\cos\frac{\phi}{2} + i\delta\Gamma\sin\frac{\phi}{2}, \tag{3.15}$$

$$\Gamma = \Gamma_R + \Gamma_L, \quad \delta\Gamma = \Gamma_R - \Gamma_L, \tag{3.16}$$

$$\Gamma_a = \pi\nu_S\left(|t^{(a)}_0|^2 + |\boldsymbol{t}^{(a)}|^2\right), \tag{3.17}$$

$$\phi = \varphi_R - \varphi_L. \tag{3.18}$$

The only difference with the case without spin-dependent coupling is the hybridization Γ_ϕ between the dot and the superconducting leads which now contains the spin-dependent part of the tunnel couplings due to finite SOC. Since the Hamiltonian is the same as Eq. (1.189) and there are no spin-dependent terms, the energy spectrum will still present the spin degeneracy, even with spin-dependent tunnel coupling. This was a predictable result as pointed out in the introduction of this chapter. An analogy can be made with the S-N-S junction studied in Chap. 2 where two channels with different Fermi velocities were required in order to lift the spin degeneracy of ABS. To lift this spin degeneracy, it is necessary to either consider additional conduction channel for particles provided by the other non-resonant levels of the quantum dot as done in [48, 95], or, as we will do, add another channel by putting an additional quantum dot in the Josephson junction such that the normal region will now consist of two quantum dots connected to the superconducting leads.

3.2 Josephson junction with two quantum dots as the normal region

As we showed in the previous section, considering only one quantum dot with a single resonant level coupled with spin-dependent tunnel coupling to superconducting electrodes is not enough to lift the spin degeneracy of the eigenstates of the full system. To solve this problem, let's consider a Josephson junction whose normal region now consists of two quantum dots. Double quantum dots Josephson junctions have already been extensively studied in the literature [113–118]. As pointed out earlier in Sec. 1.4 of chapter 1, in S-QD-S junctions, the Kondo effect and superconductivity compete between each other. In superconductor - double quantum dots - superconductor (S-DQD-S) junctions, it is of course still true. However, in addition, the coupling between the two dots can be the source of spin exchange interaction in the system yielding a richer phase diagram than that of the single dot junction [113, 119, 120]. Another possibility present in S-DQD-S junctions is to have a triplet ground state in the even parity sector when each dot is occupied by one electron. In particular, in this configuration, the transition between singlet and triplet states has been addressed theoretically [118, 121, 122] and experimentally [123].

This extra quantum dot gives an extra conduction channel for electrons to flow when it is coupled to the superconducting leads. When one of the two dots is non-resonant, then this junction becomes analogous to the one studied in [48, 95]. The benefit of our approach is that each dot can be tuned separately, allowing for a better control of the system parameters such as the Coulomb repulsion strength or the tunnel coupling with the superconducting electrodes. In this section, we will start by deriving the Hamiltonian, which we will use to describe the system. We will continue by briefly studying the main feature of the energy spectrum of the S-DQD-S junction without SOC in the couplings in Sec. 3.2.1. Then, in Sec. 3.3, we will study the effect of SOC on the energy spectrum in the odd parity sector in order to determine the required ingredients to lift the spin degeneracy. Finally, we'll conclude with a study of the non-diagonal matrix elements of the current operator in the odd sector in Sec. 3.4, with the aim of determining the parameters that allow transitions between opposite spin states.

First, let's assume that each dot is coupled to the superconducting electrodes and that there is also a non-zero coupling between these two dots. We'll consider that all of these couplings respect TRS, such that we can write them as

$$\check{t} = t_0 + i\boldsymbol{t}\cdot\boldsymbol{\sigma}, \qquad \check{\kappa} = \kappa_0 + i\boldsymbol{\kappa}\cdot\boldsymbol{\sigma}, \tag{3.19}$$

where t-couplings describe the tunnel couplings between the dots and the leads, whereas the κ-coupling describes the coupling between the two quantum dots. A schematic of the junction is shown in Fig. 3.2. We use the same notation as in the previous section for the coupling terms in order to simplify the equations, i.e.,

$$t_{\uparrow\uparrow} = t^*_{\downarrow\downarrow} = t_0 + i t_z, \quad t_{\uparrow\downarrow} = -t^*_{\downarrow\uparrow} = i(t_x - i t_y), \tag{3.20}$$

$$\kappa_{\uparrow\uparrow} = \kappa^*_{\downarrow\downarrow} = \kappa_0 + i\kappa_z, \quad \kappa_{\uparrow\downarrow} = -\kappa^*_{\downarrow\uparrow} = i(\kappa_x - i\kappa_y), \tag{3.21}$$

such that in the following we denote the coupling terms as $t_{\alpha\beta}$ and $\kappa_{\alpha\beta}$ where α, β are spin indices. We model the system with the following Hamiltonian

$$H = \sum_{a=L,R}\left(H_a + \sum_{j=1,2} H_{T,aj}\right) + \sum_{j=1,2} H_{D,j} + H_{D-D}, \tag{3.22}$$

with as usual H_a being the Hamiltonians describing the superconducting leads given in Eq. (3.5). $H_{T,aj}$ is the tunneling Hamiltonian between lead a and dot j, $H_{D,j}$ is the Hamiltonian which describes the dot j, and, finally, H_{D-D} is the Hamiltonian which describes the coupling between the two dots. These Hamil-

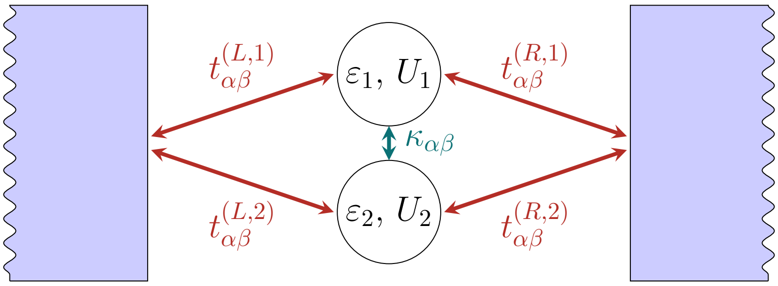

Figure 3.2: Schematic of the double quantum dots Josephson junction. Each dot is coupled to the superconducting leads via spin-dependent tunneling coupling $t^{(i,j)}_{\alpha\beta}$. Furthermore, the quantum dots are coupled together through $\kappa_{\alpha\beta}$ which is also spin-dependent. The on-site energy for each dot is ε_j with Coulomb repulsion of strength U_j. Note that we did not consider finite inter-dot interaction between the two dots as discussed in the main text.

tonians are given as

$$H_{T,aj} = \sum_{\boldsymbol{k}}\sum_{\alpha\beta}\left(t^{(a,j)}_{\alpha\beta} d^\dagger_{j\alpha} c_{\boldsymbol{k}\sigma,a} + \text{h.c.}\right), \tag{3.23}$$

$$H_{D,j} = \sum_{\sigma} \varepsilon_j d^\dagger_{j\sigma} d_{j\sigma} + U_j n_{j\uparrow} n_{j\downarrow}, \tag{3.24}$$

$$H_{D-D} = \sum_{\alpha\beta}\left(\kappa_{\alpha\beta} d^\dagger_{1\alpha} d_{2\beta} + \text{h.c.}\right), \tag{3.25}$$

with $n_{j\sigma} = d^\dagger_{j\sigma} d_{j\sigma}$. As usual, c operators are for electrons in the superconducting leads, and, d operators are for electrons in the quantum dots. Additional terms could have been considered in our Hamiltonian. In particular, we did not consider any inter-dot interaction of the form $U_{12}N_1N_2$, where N_j is the total number of electrons on dot j and Hund spin-spin exchange term of the form $J_H \boldsymbol{S}_1 \cdot \boldsymbol{S}_2$ where $\boldsymbol{S}_j$ denotes the total spin on dot j as we are interested in odd parity states, where an odd number of electrons are occupying the dots. In this case, we either have one or three electrons on the dots such that the spin-spin exchange interaction yields zero for these states, and the inter-dot interaction leads to a shift of the three particle states energy. Including this term in the Hamiltonian for the dots allows one to easily see this claim. In this case, the Hamiltonian for the dots reads

$$\begin{aligned} H_{\text{dots}} = &\sum_{\sigma}\left(\varepsilon_j + \sigma J_H + \frac{U_j}{2}\right) d^\dagger_{j\sigma} d_{j\sigma} + \sum_{j=1,2} \frac{\tilde{U}_j}{2}\left(\sum_{\sigma} d^\dagger_{j\sigma} d_{j\sigma} - 1\right)^2 \\ &+ \frac{J_H}{2}\left(\sum_{j=1,2}\sum_{\sigma} \sigma d^\dagger_{j\sigma} d_{j\sigma} - 1\right)^2 + \frac{U_{12}}{2}\left(\sum_{j=1,2}\sum_{\sigma} d^\dagger_{j\sigma} d_{j\sigma} - 1\right)^2 - \frac{1}{2}(J_H + \tilde{U}_1 + \tilde{U}_2 + U_{12}), \end{aligned} \tag{3.26}$$

with $\tilde{U}_j = U_j + J_H - U_{12}$. It can be easily seen from this Hamiltonian that in the odd parity sector, the only change is a global energy shift $2U_{12}$ of the three particle states. As these terms do not give a particular contribution in the odd sector, we will take $U_{12} = J_H = 0$ from now on. However, do note that in the even sector, the inter-dot interaction yields an energy shift for the different states, and the exchange interaction yields a different contribution for the two triplet states in which each dot is occupied by one electron with parallel spins.

Our strategy to describe this junction is the same as in Sec. 1.4 and Sec. 3.1. We will consider the superconducting atomic limit $\Delta \to \infty$. Therefore, we will use the Schrieffer-Wolff transformation, then project the Hamiltonian onto the low energy sector spanned by the quantum dots states. We will not present the details of the derivation, since it is very similar to the case with only one quantum dot. Also, from now on, we will take $\varphi_R = -\varphi_L = \phi/2$ which is always possible using an appropriate gauge transformation. The obtained low energy effective Hamiltonian is given as

$$\begin{aligned} H_{\text{eff}} = & \sum_{j=1,2} H_{D,j} + H_{D-D} \\ & + \sum_{j=1,2} \left(\Gamma_{j\phi} d^\dagger_{j\uparrow} d^\dagger_{j\downarrow} + \text{h.c.} \right) + \sum_{\alpha\beta} \left(\tau_{\alpha\beta,\phi} d^\dagger_{1\alpha} d^\dagger_{2\beta} + \text{h.c.} \right), \end{aligned} \tag{3.27}$$

with,

$$\Gamma_{j\phi} = \Gamma_j \cos\frac{\phi}{2} + i\delta\Gamma_j \sin\frac{\phi}{2}, \tag{3.28}$$

$$\Gamma_j = \Gamma_{R,j} + \Gamma_{L,j}, \quad \delta\Gamma_j = \Gamma_{R,j} - \Gamma_{L,j}, \tag{3.29}$$

$$\Gamma_{a,j} = \pi\nu_S \left(|t_0^{(aj)}|^2 + |\boldsymbol{t}^{(aj)}|^2 \right), \tag{3.30}$$

and

$$\tau_{\uparrow\downarrow,\phi} = \left[\tau_{\uparrow\downarrow} \cos\left(\frac{\phi + \delta\varphi_{\uparrow\downarrow}}{2} \right) + i\delta\tau_{\uparrow\downarrow} \sin\left(\frac{\phi + \delta\varphi_{\uparrow\downarrow}}{2} \right) \right] e^{i\bar{\varphi}_{\uparrow\downarrow}}, \tag{3.31}$$

$$\tau_{\downarrow\uparrow,\phi} = - \left[\tau_{\uparrow\downarrow} \cos\left(\frac{\phi - \delta\varphi_{\uparrow\downarrow}}{2} \right) + i\delta\tau_{\uparrow\downarrow} \sin\left(\frac{\phi - \delta\varphi_{\uparrow\downarrow}}{2} \right) \right] e^{-i\bar{\varphi}_{\uparrow\downarrow}}, \tag{3.32}$$

$$\tau_{\uparrow\uparrow,\phi} = \left[\tau_{\uparrow\uparrow} \cos\left(\frac{\phi + \delta\varphi_{\uparrow\uparrow}}{2} \right) + i\delta\tau_{\uparrow\uparrow} \sin\left(\frac{\phi + \delta\varphi_{\uparrow\uparrow}}{2} \right) \right] e^{i\bar{\varphi}_{\uparrow\uparrow}}, \tag{3.33}$$

$$\tau_{\downarrow\downarrow,\phi} = \left[\tau_{\uparrow\uparrow} \cos\left(\frac{\phi - \delta\varphi_{\uparrow\uparrow}}{2} \right) + i\delta\tau_{\uparrow\uparrow} \sin\left(\frac{\phi - \delta\varphi_{\uparrow\uparrow}}{2} \right) \right] e^{-i\bar{\varphi}_{\uparrow\uparrow}}, \tag{3.34}$$

where we used

$$\tau_{\alpha\beta} = \tau^{(R)}_{\alpha\beta} + \tau^{(L)}_{\alpha\beta}, \quad \delta\tau_{\alpha\beta} = \tau^{(R)}_{\alpha\beta} - \tau^{(L)}_{\alpha\beta}, \tag{3.35}$$

$$\tau^{(a)}_{\alpha\beta} = \pi\nu_S \left| t^{(a1)}_{\alpha\uparrow} t^{(a2)}_{\beta\downarrow} - t^{(a1)}_{\alpha\downarrow} t^{(a2)}_{\beta\uparrow} \right|, \tag{3.36}$$

$$\bar{\varphi}_{\alpha\beta} = \left(\varphi^{(R)}_{\alpha\beta} + \varphi^{(L)}_{\alpha\beta} \right)/2, \quad \delta\varphi_{\alpha\beta} = \varphi^{(R)}_{\alpha\beta} - \varphi^{(L)}_{\alpha\beta}, \tag{3.37}$$

$$\varphi^{(a)}_{\alpha\beta} = \arg\left(t^{(a1)}_{\alpha\uparrow} t^{(a2)}_{\beta\downarrow} - t^{(a1)}_{\alpha\downarrow} t^{(a2)}_{\beta\uparrow} \right). \tag{3.38}$$

One can further notice that

$$\Gamma_{j\phi}(\phi) = \Gamma^*_{j\phi}(-\phi), \tag{3.39}$$

$$\tau_{\downarrow\uparrow,\phi}(\phi) = -\tau^*_{\uparrow\downarrow,\phi}(-\phi), \tag{3.40}$$

$$\tau_{\downarrow\downarrow,\phi}(\phi) = \tau^*_{\uparrow\uparrow,\phi}(-\phi). \tag{3.41}$$

Before we go any further, let's talk a bit about this Hamiltonian. The first line of Eq. (3.27) describes each dot and the coupling $\check{\kappa}$ between them, which corresponds to what we would have without the coupling to the superconducting leads. Note that at the lowest order in $1/E_{\boldsymbol{k}}$ when deriving Eq. (3.27), there is no additional inter-dot coupling as this term vanishes when summing over $\boldsymbol{k}$. However, it can become non-zero when considering $\boldsymbol{k}$ dependent tunnel couplings, i.e., when considering that the two dots are not connected at the same point of the reservoir on the Fermi length scale. Now, we can discuss the terms arising from the coupling with electrodes. We placed ourselves in the superconducting atomic limit, such that Δ is the dominant energy of the system. As a consequence, the dots are only coupled to the Cooper pair of the leads and not the continuum. Hence, we recover a hybridization term $\Gamma_{j\phi}$

which describes the transfer of a Cooper pair from the leads to one of the quantum dots as in the single quantum dot junction. The only difference is that here, the Cooper pair can either tunnel through one or the other dot. The last term of our Hamiltonian $\tau_{\alpha\beta,\phi}$ also describes the coupling between Cooper pairs and quantum dots. But whereas $\Gamma_{j\phi}$ describes the tunneling of a Cooper pair to the dot j, here, the Cooper pair is being split between the two dots. This is known as crossed Andreev reflection [124, 125].

The only terms that we can expect to lift the spin degeneracy are the $\tau_{\alpha\beta,\phi}$ and $\kappa_{\alpha\beta}$ (see Eq. (3.25)) as they are the only spin-dependent terms in the Hamiltonian. For the $\kappa_{\alpha\beta}$ terms, they are not sufficient by themselves as $\check{\kappa}$ respects TRS (see Eq. (3.19)). Their combination with Andreev reflection terms is required as they provide a ϕ-dependence that breaks TRS.

We can see that each of the terms $\tau_{\alpha\beta,\phi}$ presents a phase shift $\pm\delta\varphi_{\alpha\beta}$ with respect to ϕ. We can expect that this phase shift may play a role in the lifting of the spin degeneracy. To illustrate this, we can do an analogy with the junction we studied in Chap. 2. In the previous Josephson nanowire, the spin degeneracy was lifted thanks to a phase difference resulting from the spin-dependent Fermi velocities. Here, this phase difference is provided by the crossed Andreev reflection terms $\tau_{\alpha\beta,\phi}$ such that, a transfer of Cooper pair from one superconducting electrode to the other involving this mechanism will lead to a phase shift depending on the spins of the particles. We can see in Eq. (3.38) that without SOC, i.e. $\boldsymbol{t}=0$, the phases $\varphi^{(a)}_{\alpha\beta}=0$ such that the phase shifts we talked about vanish.

$\tau_{\alpha\beta,\phi}$ and $\Gamma_{j\phi}$ are proportional to $\pi\nu_S$ and depends on $t^{aj}_{\sigma\sigma'}$ thus, we will give t_0 and $\boldsymbol{t}$ in unit of $1/\sqrt{\pi\nu_S}$ in the following.

As parity is conserved due to the coupling with the superconducting leads, the Hamiltonian of Eq. (3.27) can be decomposed into two independent Hamiltonians which describe the even sector where an even number of particles are occupying the dots, and, an odd sector with an odd number of particles occupying the dots. The even sector contains the following singlet and triplet states

$$\begin{aligned}
\text{singlet}: \quad & |0\rangle, \quad |\uparrow_1\downarrow_1\rangle = d^\dagger_{1\uparrow}d^\dagger_{1\downarrow}|0\rangle, \quad |\uparrow_2\downarrow_2\rangle = d^\dagger_{2\uparrow}d^\dagger_{2\downarrow}|0\rangle, \\
& \frac{|\uparrow_1\downarrow_2\rangle-|\downarrow_1\uparrow_2\rangle}{\sqrt{2}} = \frac{d^\dagger_{1\uparrow}d^\dagger_{2\downarrow}-d^\dagger_{1\downarrow}d^\dagger_{2\uparrow}}{\sqrt{2}}|0\rangle, \quad |\uparrow_1\downarrow_1\uparrow_2\downarrow_2\rangle = d^\dagger_{1\uparrow}d^\dagger_{1\downarrow}d^\dagger_{2\uparrow}d^\dagger_{2\downarrow}|0\rangle, \\
\text{triplet}: \quad & |\uparrow_1\uparrow_2\rangle = d^\dagger_{1\uparrow}d^\dagger_{2\uparrow}|0\rangle, \quad |\downarrow_1\downarrow_2\rangle = d^\dagger_{1\downarrow}d^\dagger_{2\downarrow}|0\rangle, \quad \frac{|\uparrow_1\downarrow_2\rangle+|\downarrow_1\uparrow_2\rangle}{\sqrt{2}} = \frac{d^\dagger_{1\uparrow}d^\dagger_{2\downarrow}+d^\dagger_{1\downarrow}d^\dagger_{2\uparrow}}{\sqrt{2}}|0\rangle,
\end{aligned}$$

which, in the basis $\Psi_{\text{even}}=\begin{pmatrix}|0\rangle & |\uparrow_1\downarrow_1\rangle & |\uparrow_2\downarrow_2\rangle & |\uparrow_1\downarrow_1\uparrow_2\downarrow_2\rangle & \frac{|\uparrow_1\downarrow_2\rangle-|\downarrow_1\uparrow_2\rangle}{\sqrt{2}} & |\uparrow_1\uparrow_2\rangle & |\downarrow_1\downarrow_2\rangle & \frac{|\uparrow_1\downarrow_2\rangle+|\downarrow_1\uparrow_2\rangle}{\sqrt{2}}\end{pmatrix}^T$, are described by the Hamiltonian

$$\mathscr{H}_{\text{even}}=\begin{pmatrix}
0 & \Gamma^*_{1\phi} & \Gamma^*_{2\phi} & 0 & \frac{\tau^*_{\uparrow\downarrow,\phi}-\tau^*_{\downarrow\uparrow,\phi}}{\sqrt{2}} & \tau^*_{\uparrow\uparrow,\phi} & \tau^*_{\downarrow\downarrow,\phi} & \frac{\tau^*_{\uparrow\downarrow,\phi}+\tau^*_{\downarrow\uparrow,\phi}}{\sqrt{2}} \\
\Gamma_{1\phi} & 2\varepsilon_1+U_1 & 0 & \Gamma^*_{2\phi} & \frac{\kappa_{\downarrow\downarrow}+\kappa_{\uparrow\uparrow}}{\sqrt{2}} & \kappa_{\downarrow\uparrow} & -\kappa_{\uparrow\downarrow} & \frac{\kappa_{\downarrow\downarrow}-\kappa_{\uparrow\uparrow}}{\sqrt{2}} \\
\Gamma_{2\phi} & 0 & 2\varepsilon_2+U_2 & \Gamma^*_{1\phi} & \frac{\kappa^*_{\downarrow\downarrow}+\kappa^*_{\uparrow\uparrow}}{\sqrt{2}} & -\kappa^*_{\uparrow\downarrow} & \kappa^*_{\downarrow\uparrow} & -\frac{\kappa^*_{\downarrow\downarrow}-\kappa^*_{\uparrow\uparrow}}{\sqrt{2}} \\
0 & \Gamma_{2\phi} & \Gamma_{1\phi} & 2(\varepsilon_1+\varepsilon_2)+U_1+U_2 & \frac{\tau_{\downarrow\uparrow,\phi}-\tau_{\uparrow\downarrow,\phi}}{\sqrt{2}} & -\tau_{\downarrow\downarrow,\phi} & -\tau_{\uparrow\uparrow,\phi} & \frac{\tau_{\downarrow\uparrow,\phi}+\tau_{\uparrow\downarrow,\phi}}{\sqrt{2}} \\
\frac{\tau_{\uparrow\downarrow,\phi}-\tau_{\downarrow\uparrow,\phi}}{\sqrt{2}} & \frac{\kappa^*_{\downarrow\downarrow}+\kappa^*_{\uparrow\uparrow}}{\sqrt{2}} & \frac{\kappa_{\downarrow\downarrow}+\kappa_{\uparrow\uparrow}}{\sqrt{2}} & \frac{\tau^*_{\downarrow\uparrow,\phi}-\tau^*_{\uparrow\downarrow,\phi}}{\sqrt{2}} & \varepsilon_1+\varepsilon_2 & 0 & 0 & 0 \\
\tau_{\uparrow\uparrow,\phi} & \kappa^*_{\downarrow\uparrow} & -\kappa_{\uparrow\downarrow} & -\tau^*_{\downarrow\downarrow,\phi} & 0 & \varepsilon_1+\varepsilon_2 & 0 & 0 \\
\tau_{\downarrow\downarrow,\phi} & -\kappa^*_{\uparrow\downarrow} & \kappa_{\downarrow\uparrow} & -\tau^*_{\uparrow\uparrow,\phi} & 0 & 0 & \varepsilon_1+\varepsilon_2 & 0 \\
\frac{\tau_{\uparrow\downarrow,\phi}+\tau_{\downarrow\uparrow,\phi}}{\sqrt{2}} & \frac{\kappa^*_{\downarrow\downarrow}-\kappa^*_{\uparrow\uparrow}}{\sqrt{2}} & -\frac{\kappa_{\downarrow\downarrow}-\kappa_{\uparrow\uparrow}}{\sqrt{2}} & \frac{\tau^*_{\downarrow\uparrow,\phi}+\tau^*_{\uparrow\downarrow,\phi}}{\sqrt{2}} & 0 & 0 & 0 & \varepsilon_1+\varepsilon_2
\end{pmatrix}. \tag{3.42}$$

The changes in sign for the $\kappa_{\alpha\beta}$ and $\tau_{\alpha\beta}$ terms come from the anti-commutation rules for fermionic operators $d_{j\sigma}^{(\dagger)}$. An important thing to notice here, is that when there is no SOC in the different couplings, we have $\kappa_{\sigma\bar{\sigma}} = \tau_{\sigma\sigma,\phi} = 0$ and $\tau_{\uparrow\downarrow,\phi} = -\tau_{\downarrow\uparrow,\phi}$ such that the triplet states become completely decoupled from the singlet states. As can be seen, the triplet states are not coupled between them. They are also decoupled from the singlet state $(|\uparrow_1\downarrow_2\rangle - |\downarrow_1\uparrow_2\rangle)/\sqrt{2}$ which results in a diagonal block in Eq. (3.42)

On the other hand, the odd sector contains the following doublet states, i.e., states with an effective spin of 1/2,

$$\begin{aligned}
\text{doublet}: \quad & |\uparrow_1\rangle = d_{1\uparrow}^\dagger |0\rangle, \quad |\downarrow_1\rangle = d_{1\downarrow}^\dagger |0\rangle, \quad |\uparrow_2\rangle = d_{2\uparrow}^\dagger |0\rangle, \quad |\downarrow_2\rangle = d_{2\downarrow}^\dagger |0\rangle, \\
& |\uparrow_1\downarrow_1\uparrow_2\rangle = d_{1\uparrow}^\dagger d_{1\downarrow}^\dagger d_{2\downarrow}^\dagger |0\rangle, \qquad |\uparrow_1\downarrow_1\downarrow_2\rangle = d_{1\uparrow}^\dagger d_{1\downarrow}^\dagger d_{2\downarrow}^\dagger |0\rangle, \\
& |\uparrow_1\uparrow_2\downarrow_2\rangle = d_{1\uparrow}^\dagger d_{2\uparrow}^\dagger d_{2\downarrow}^\dagger |0\rangle, \qquad |\downarrow_1\uparrow_2\downarrow_2\rangle = d_{1\downarrow}^\dagger d_{2\uparrow}^\dagger d_{2\downarrow}^\dagger |0\rangle,
\end{aligned}$$

which, in the basis $\Psi_{\text{odd}} = \begin{pmatrix} |\uparrow_1\rangle & |\downarrow_1\rangle & |\uparrow_2\rangle & |\downarrow_2\rangle & |\uparrow_1\downarrow_1\uparrow_2\rangle & |\uparrow_1\downarrow_1\downarrow_2\rangle & |\uparrow_1\uparrow_2\downarrow_2\rangle & |\downarrow_1\uparrow_2\downarrow_2\rangle \end{pmatrix}^T$, are described by the Hamiltonian

$$\mathscr{H}_{\text{odd}} = \begin{pmatrix}
\varepsilon_1 & 0 & \kappa_{\uparrow\uparrow} & \kappa_{\uparrow\downarrow} & \tau^*_{\downarrow\uparrow,\phi} & \tau^*_{\downarrow\downarrow,\phi} & \Gamma^*_{2\phi} & 0 \\
0 & \varepsilon_1 & \kappa_{\downarrow\uparrow} & \kappa_{\downarrow\downarrow} & -\tau^*_{\uparrow\uparrow,\phi} & -\tau^*_{\uparrow\downarrow,\phi} & 0 & \Gamma^*_{2\phi} \\
\kappa^*_{\uparrow\uparrow} & \kappa^*_{\downarrow\uparrow} & \varepsilon_2 & 0 & \Gamma^*_{1\phi} & 0 & -\tau^*_{\uparrow\downarrow,\phi} & -\tau^*_{\downarrow\downarrow,\phi} \\
\kappa^*_{\uparrow\downarrow} & \kappa^*_{\downarrow\downarrow} & 0 & \varepsilon_2 & 0 & \Gamma^*_{1\phi} & \tau^*_{\uparrow\uparrow,\phi} & \tau^*_{\downarrow\uparrow,\phi} \\
\tau_{\downarrow\uparrow,\phi} & -\tau_{\uparrow\uparrow,\phi} & \Gamma_{1\phi} & 0 & 2\varepsilon_1+\varepsilon_2+U_1 & 0 & -\kappa_{\downarrow\downarrow} & \kappa_{\uparrow\downarrow} \\
\tau_{\downarrow\downarrow,\phi} & -\tau_{\uparrow\downarrow,\phi} & 0 & \Gamma_{1\phi} & 0 & 2\varepsilon_1+\varepsilon_2+U_1 & \kappa_{\downarrow\uparrow} & -\kappa_{\uparrow\uparrow} \\
\Gamma_{2\phi} & 0 & -\tau_{\uparrow\downarrow,\phi} & \tau_{\uparrow\uparrow,\phi} & -\kappa^*_{\downarrow\downarrow} & \kappa^*_{\downarrow\uparrow} & 2\varepsilon_2+\varepsilon_1+U_2 & 0 \\
0 & \Gamma_{2\phi} & -\tau_{\downarrow\downarrow,\phi} & \tau_{\downarrow\uparrow,\phi} & \kappa^*_{\uparrow\downarrow} & -\kappa^*_{\uparrow\uparrow} & 0 & 2\varepsilon_2+\varepsilon_1+U_2
\end{pmatrix}. \tag{3.43}$$

Here again, the changes in sign in front of the $\kappa_{\alpha\beta}$ and $\tau_{\alpha\beta}$ terms come from the anti-commutation rules for fermionic operators $d_{j\sigma}^{(\dagger)}$. We can see that, as opposed to the S-QD-S junction studied in Sec. 1.4, here the doublet states can present a ϕ dependence as states with one electron and states with three electrons are coupled through the terms involving the transfer of Cooper pairs [126]. Without SOC, we have $\kappa_{\sigma\bar{\sigma}} = \tau_{\sigma\sigma,\phi} = 0$ so that the spin states decouple. Thus, Eq. (3.43) can be separated into two identical and independent blocks for each spin, and $\tau_{\uparrow\downarrow,\phi} = -\tau_{\downarrow\uparrow,\phi}$ in this case (see Eq. (3.45)).

In the following, we will study the energy spectrum of the system without SOC, which we will obtain numerically in Sec. 3.2.1. We will describe the main features of this spectrum for different configurations of the system and compare them to the energy spectrum of the single dot junction. Since we are mainly interested in the odd parity sector, in which we want to break the spin degeneracy, we will try to find the suitable range of parameters to have a spin doublet ground state.

3.2.1 Energy spectrum without SOC

We will start by discussing the energy spectrum of this system when there is no SOC in the couplings. In this case, the Hamiltonian in Eq. (3.42) can be separated into a block describing the singlet states and another one for the triplet states, while the Hamiltonian in Eq. (3.43) can be separated into two independent spin sectors. We denote H_T the Hamiltonian describing the triplet states which we write in the basis $\Psi_T = \begin{pmatrix} |\uparrow_1\uparrow_2\rangle & |\downarrow_1\downarrow_2\rangle & \frac{|\uparrow_1\downarrow_2\rangle + |\downarrow_1\uparrow_2\rangle}{\sqrt{2}} \end{pmatrix}^T$, H_S for the singlet states in the basis $\Psi_S = \begin{pmatrix} |0\rangle & |\uparrow_1\downarrow_1\rangle & |\uparrow_2\downarrow_2\rangle & |\uparrow_1\downarrow_1\uparrow_2\downarrow_2\rangle & \frac{|\uparrow_1\downarrow_2\rangle - |\downarrow_1\uparrow_2\rangle}{\sqrt{2}} \end{pmatrix}^T$ and, H_σ describes the states of spin σ and is written in the basis $\Psi_\sigma = \big(|\sigma_1\rangle \quad |\sigma_2\rangle \quad |\sigma_1 \uparrow_2\downarrow_2\rangle \quad |\uparrow_1\downarrow_1 \sigma_2\rangle\big)^T$. Without SOC, we have $\tau_{\uparrow\downarrow,\phi} = -\tau_{\downarrow\uparrow,\phi}$, so we will use the notation $\tau_\phi = \tau_{\uparrow\downarrow,\phi} = -\tau_{\downarrow\uparrow,\phi}$ for simplicity. These Hamiltonians are given as

$$H_T = (\varepsilon_1 + \varepsilon_2)\mathbb{1}_3, \tag{3.44}$$

$$H_\sigma = \begin{pmatrix} \varepsilon_1 & \kappa_0 & -\tau_\phi^* & \Gamma_{2\phi}^* \\ \kappa_0 & \varepsilon_2 & \Gamma_{1\phi}^* & -\tau_\phi^* \\ -\tau_\phi & \Gamma_{1\phi} & 2\varepsilon_1 + \varepsilon_2 + U_1 & -\kappa_0 \\ \Gamma_{2\phi} & -\tau_\phi & -\kappa_0 & 2\varepsilon_2 + \varepsilon_1 + U_2 \end{pmatrix}, \tag{3.45}$$

$$H_S = \begin{pmatrix} 0 & \Gamma_{1\phi}^* & \Gamma_{2\phi}^* & 0 & \sqrt{2}\tau_\phi^* \\ \Gamma_{1\phi} & 2\varepsilon_1 + U_1 & 0 & \Gamma_{2\phi}^* & \sqrt{2}\kappa_0 \\ \Gamma_{2\phi} & 0 & 2\varepsilon_2 + U_2 & \Gamma_{1\phi}^* & \sqrt{2}\kappa_0 \\ 0 & \Gamma_{2\phi} & \Gamma_{1\phi} & 2(\varepsilon_1+\varepsilon_2) + U_1 + U_2 & -\sqrt{2}\tau_\phi \\ \sqrt{2}\tau_\phi & \sqrt{2}\kappa_0 & \sqrt{2}\kappa_0 & -\sqrt{2}\tau_\phi^* & \varepsilon_1 + \varepsilon_2 \end{pmatrix}, \tag{3.46}$$

We will discuss the main features of the energy spectrum for different shapes of the junction. Namely, we will look at the two dots being in parallel ($\check{\kappa} = 0$ and $t_0^{(aj)} \neq 0$), in series ($\kappa_0 \neq 0$, $t_0^{(L1,R2)}$ or $t_0^{(R1,L2)}$ non-zero with $t_0^{(R1,L2)} = 0$ or $t_0^{(L1,R2)} = 0$ respectively) and with a finite value for all different couplings as depicted in Fig. 3.2, i.e., κ_0 and $t_0^{(aj)}$ non-zero. We obtained the energy spectrum for all configurations by numerically diagonalizing the Hamiltonians of Eqs. (3.42) and (3.43). The resulting spectrum is shown in Fig. 3.3 for symmetric and asymmetric tunnel coupling (same/different tunnel couplings between the dots and the right and left superconducting electrodes), respectively. In this figure, the parallel configuration is shown in the first column, the series configuration in the middle one and, finally, the configuration with all couplings in the third column.

Let's first discuss the symmetric case. In contrast to the single quantum dot junction, here the energy spectrum is much richer. Notably, doublet states in green dashed lines exhibit dispersion with the superconducting phase difference ϕ, originating from the coupling between the one and three particles states. Without spin-orbit coupling, triplet states, shown in red lines, remain decoupled from other states and show no phase dependence. Finally, we can notice a qualitative difference in phase dependence for the configuration where the two dots are in series, i.e., in the middle column of Fig. 3.3. Compared to the parallel configuration a π-phase shift can be observed between the lowest / highest energy levels and the second lowest / highest energy levels. This particularity in the phase dependence can also be seen for the doublet states. However, when all the couplings are finite, this particularity does not survive in the symmetric case.

In the asymmetric case, the main difference that can be observed in panel (b) of Fig. 3.3 is for the configuration with all couplings being finite (right column). For this configuration, a mix between the phase difference of the dots in parallel and the dot in series can be observed for phases close to π. In this way, it is possible to get closer to the phase dependence of one configuration or the other as a function of the relative values of the various couplings.

We will not give more details on the general energy spectrum. Instead, we will now try to find a suitable range of parameters to favor an odd parity ground state. More precisely, we want to find the parameters such that in the weak tunnel couplings limit, the ground state of the system is a state with a single electron on the dots. Since we cannot derive analytically the eigenvalues of the Hamiltonians of Eqs. (3.42) and (3.43) in the general case, we can first look at a stability diagram of the two dots without

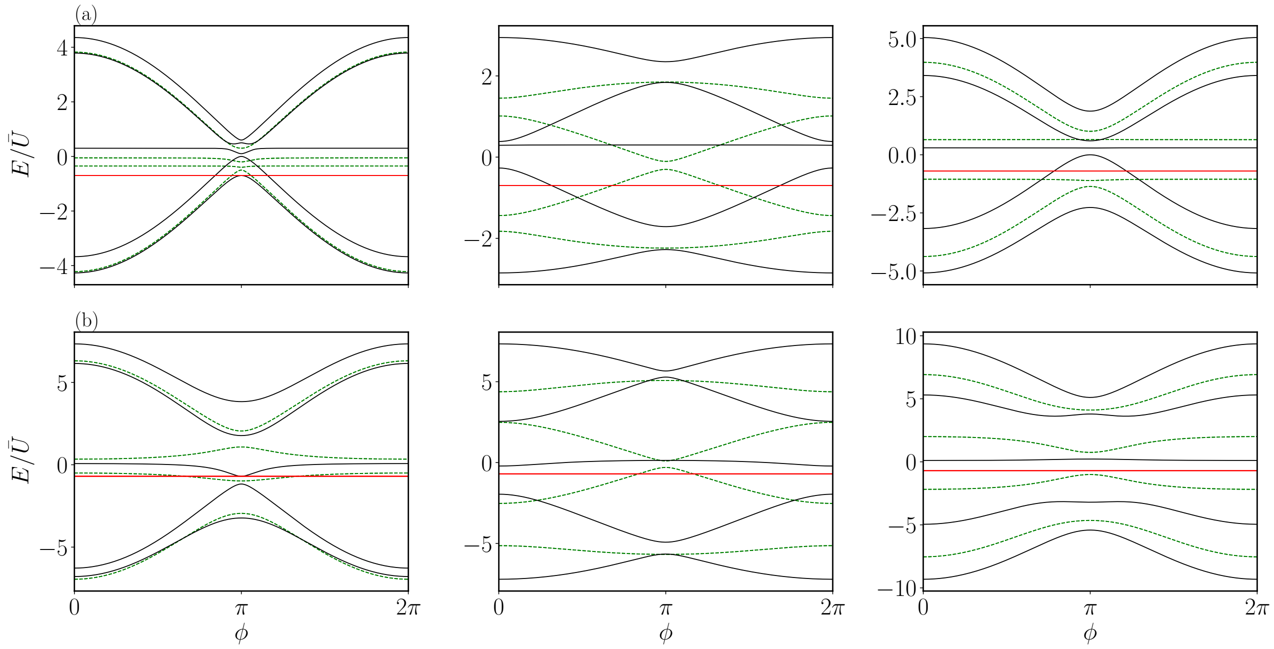

Figure 3.3: Energy spectrum of the S-DQD-S junction obtained numerically and normalized by $\bar{U} = (U_1 + U_2)/2$. For each plot, we chose $\varepsilon_1/\bar{U} = -0.5$, $\varepsilon_2/\bar{U} = -0.2$, and, $\delta U/\bar{U} = 0.5$ with $\delta U = U_1 - U_2$. Red lines correspond to triplet states, green dashed lines to doublet states and, in black are the singlet states. The first/second row is for the symmetric/asymmetric tunnel couplings to the leads. The parallel configuration is shown in the first column, the series configuration in the middle one and, the configuration with all couplings in the third column. For the symmetric coupling (panel (a)), we have for the parallel configuration $\Gamma_1/\bar{U} = \Gamma_2/\bar{U} = 2$, and $\delta\Gamma_1/\bar{U} = \delta\Gamma_2/\bar{U} = \kappa_0/\bar{U} = 0$. For the series configuration, $\Gamma_1/\bar{U} = \Gamma_2/\bar{U} = \kappa_0/\bar{U} = 1$, and $\delta\Gamma_1/\bar{U} = -\delta\Gamma_2/\bar{U} = -1$. And, for the configuration with all couplings, we set $\Gamma_1/\bar{U} = \Gamma_2/\bar{U} = 2$, $\kappa_0/\bar{U} = 1$ and $\delta\Gamma_1/\bar{U} = \delta\Gamma_2/\bar{U} = 0$. For the asymmetric tunnel couplings (panel (b)), the parameters are $\Gamma_1/\bar{U} = 2$, $\Gamma_2/\bar{U} = 5$, $\delta\Gamma_1/\bar{U} = -1$, $\delta\Gamma_2/\bar{U} = 2.5$ for the parallel configuration. For the dots in series, we have $\Gamma_1/\bar{U} = -\delta\Gamma_1/\bar{U} = 1.5$, $\Gamma_2/\bar{U} = \Gamma_2/\bar{U} = 3.75$ and $\kappa_0/\bar{U} = 2.5$. Finally, for the configuration with all couplings, we have $\Gamma_1/\bar{U} = 2$, $\Gamma_2/\bar{U} = 5$, $\delta\Gamma_1/\bar{U} = -1$, $\delta\Gamma_2/\bar{U} = 2.5$ and $\kappa_0/\bar{U} = 2.5$. The parameters have been chosen such that all the couplings are of the same order of magnitude.

the superconducting leads depicted in Fig. 3.4. [1] According to this simple diagram, to have a single electron occupying the dots when there is no inter-dot interaction, we need to have a negative on-site energy for one of the two dots within the range $-U_j < \varepsilon_j < 0$, while the other on-site energy needs to be positive.

From the study of the ground state parity made in Chap. 1, we also know that the couplings between a dot and the superconducting leads play a role in the parity of the ground state. However, Eq. (1.200) shows that if Coulomb repulsion is strong enough compared to other energies of the system, i.e., on-site energy and hybridization between the dot and the leads, a doublet ground state will be favored. Here, the situation is a bit different as we now have two dots coupled to the leads, and the two dots can be coupled to each other. Thankfully, strong Coulomb repulsion, i.e., $\Gamma_{j\phi}, \tau_{\alpha\beta,\phi} \ll \bar{U} = (U_1 + U_2)/2$, as for the S-QD-S junction, helps moderate the effect of the couplings with the leads on the parity of the ground state. The

---

[1] In the case of symmetric couplings between the left and right leads, several simplifications can be made. When the couplings are symmetric, we have $\tau_{\sigma\sigma,\phi} = 0$ and $\tau_{\uparrow\downarrow,\phi} = -\tau_{\downarrow\uparrow,\phi}$. These simplifications allow one to rewrite Eq. (3.43) as two 4x4 independent matrices which take the same form as Eq. (3.45).

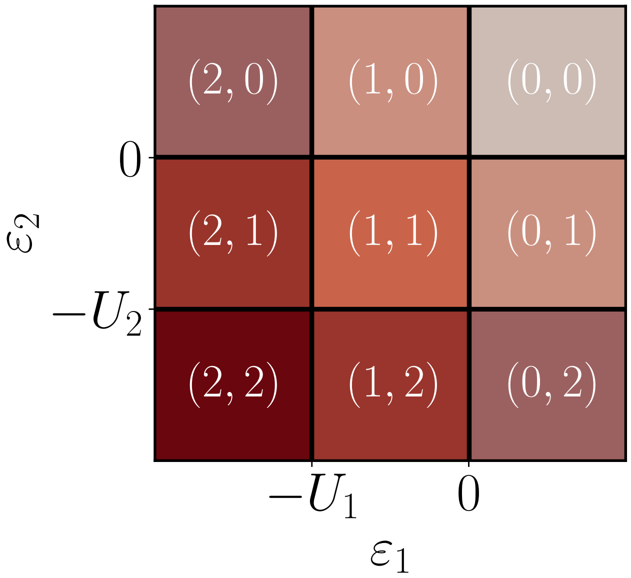

Figure 3.4: Stability diagram of the two dots without any couplings. The number of electrons on each dot is indicated in parentheses, where the first element corresponds to the number of electrons in dot 1 and the second element gives the number of electrons in dot 2.

last parameters that can affect the parity of the ground state are the on-site energy of each dot and the coupling between them. For the on-site energies, we already know from the stability diagram in Fig. 3.4 that we need to have opposite sign on-site energies. However, due to the couplings with the leads, the difference between these on-site energies will also play a role. Finally, the inter-dot coupling, as we will see in the next section, is responsible for shifting the energy of the dots such that it plays a similar role as the on-site energy difference. The effect of those parameters on the parity of the ground states is shown in Fig. 3.5.

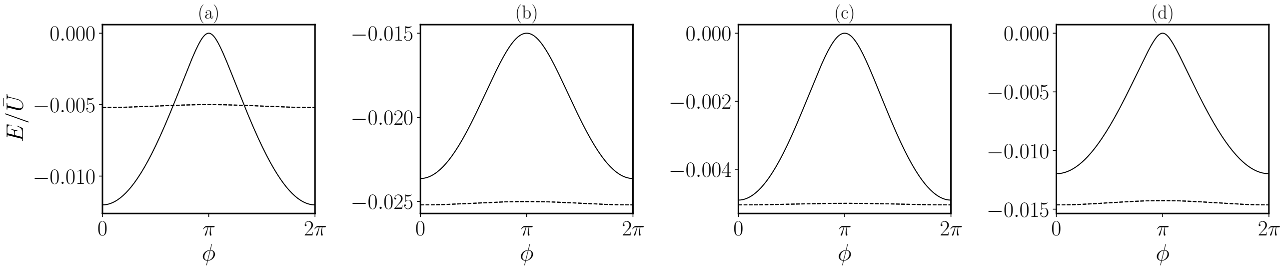

Figure 3.5: Effect of the on-site energy difference, tunnel couplings and inter-dot coupling on the ground state parity of the junction. Panel (a) shows a reference energy spectrum with the two lowest energy states being shown. The level in dashed lines is the doublet state and the other one is the singlet state. For this panel, the parameters are $\varepsilon_1/\bar{U} = -5\times10^{-3}$, $\varepsilon_2/\bar{U} = 10^{-2}$, $t_0/\bar{U} = 5\times10^{-3}$ and $\kappa_0/\bar{U} = 0$. In panels (b)-(d), we change only one parameter from panel (a) in order to show the effect of the different parameters. In the panel (b) is shown the effect of on-site energy difference where we took $\varepsilon_1/\bar{U} = -2.5\times10^{-2}$. For the panel (c), we show the effect of the tunnel couplings where $t_0/\bar{U} = 3.5\times10^{-3}$. Finally, in the panel (d), we put $\kappa_0/\bar{U} = 1.5\times10^{-2}$.

For the moment, we have qualitatively described the energy spectrum of the S-DQD-S junction. Also, we discussed the parameters that can affect the parity of the ground state. Thus, in the next section, we will delve more deeply into the study of the energy spectrum in the odd parity sector. We will focus on the minimal ingredients required to lift the spin degeneracy by adding SOC in the different couplings of the system.

3.3 Lifting the spin degeneracy

As previously said, in this section, we will study the energy spectrum in the odd sector. Namely, we will focus on sets of parameters that allow to have an odd parity ground state. In particular, we will show how SOC in the inter-dot coupling $\check{\kappa}$ or in the tunnel coupling $\check{t}$ can lead to a spin-splitting of the quantum dots states. We recall that the Hamiltonian $\mathscr{H}_{\text{odd}}$ describing the odd sector is given by Eq. (3.43) which is written in the basis $\Psi_{\text{odd}} = \big(|{\uparrow_1}\rangle \quad |{\downarrow_1}\rangle \quad |{\uparrow_2}\rangle \quad |{\downarrow_2}\rangle \quad |{\uparrow_1\downarrow_1\uparrow_2}\rangle \quad |{\uparrow_1\downarrow_1\downarrow_2}\rangle \quad |{\uparrow_1\uparrow_2\downarrow_2}\rangle \quad |{\downarrow_1\uparrow_2\downarrow_2}\rangle\big)^T$. We can divide this Hamiltonian into several blocks. The first one is the upper left block, which describes states with one electron on a given dot. We can write it as

$$H_1 = \bar{\varepsilon}\rho_0\sigma_0 + \frac{\delta\varepsilon}{2}\rho_z\sigma_0 + \kappa_0\rho_x\sigma_0 - \rho_y\boldsymbol{\kappa}\cdot\sigma, \tag{3.47}$$

where we used the notations $\bar{\varepsilon} = (\varepsilon_1 + \varepsilon_2)/2$ and $\delta\varepsilon = \varepsilon_1 - \varepsilon_2$. $\sigma_{x,y,z}$ and $\rho_{x,y,z}$ are Pauli matrices acting in the spin space and dot space respectively. The second block is the one describing the states with three electrons, which can be written as

$$H_3 = (3\bar{\varepsilon} + \bar{U})\rho_0\sigma_0 + \frac{\delta\varepsilon + \delta U}{2}\rho_z\sigma_0 - \kappa_0\rho_x\sigma_0 - \rho_y\boldsymbol{\kappa}\cdot\sigma, \tag{3.48}$$

with $\bar{U} = (U_1 + U_2)/2$ and $\delta U = U_1 - U_2$. At large U, this separation allows one to define a low and a high energy sector corresponding to the sector with one electron and three electrons on the dots, respectively. The last Hamiltonian we need is the one that contains the off-diagonal block. We denote this Hamiltonian as $H_{\mathcal{V}}$ which is given as

$$H_{\mathcal{V}} = \begin{pmatrix} 0 & \mathcal{V}^\dagger \\ \mathcal{V} & 0 \end{pmatrix}, \tag{3.49}$$

$$\mathcal{V} = \left[\tau_0\rho_0 + \frac{\Gamma_{1\phi} + \Gamma_{2\phi}}{2}\rho_x + i\frac{\Gamma_{1\phi} - \Gamma_{2\phi}}{2}\rho_y\right]\sigma_0 + \rho_z\boldsymbol{\tau}\cdot\boldsymbol{\sigma}, \tag{3.50}$$

with

$$\tau_0 = \frac{\tau_{\downarrow\uparrow,\phi} - \tau_{\uparrow\downarrow,\phi}}{2} = -\left[\tau^{(R)}_{\uparrow\downarrow}\cos\varphi^{(R)}_{\uparrow\downarrow} + \tau^{(L)}_{\uparrow\downarrow}\cos\varphi^{(L)}_{\uparrow\downarrow}\right]\cos\frac{\phi}{2} + i\left[\tau^{(L)}_{\uparrow\downarrow}\cos\varphi^{(L)}_{\uparrow\downarrow} - \tau^{(R)}_{\uparrow\downarrow}\cos\varphi^{(R)}_{\uparrow\downarrow}\right]\sin\frac{\phi}{2}, \tag{3.51}$$

$$\tau_x = \frac{\tau_{\downarrow\downarrow,\phi} - \tau_{\uparrow\uparrow,\phi}}{2} = \left[\tau^{(R)}_{\uparrow\uparrow}\sin\varphi^{(R)}_{\uparrow\uparrow} - \tau^{(L)}_{\uparrow\uparrow}\sin\varphi^{(L)}_{\uparrow\uparrow}\right]\sin\frac{\phi}{2} - i\left[\tau^{(R)}_{\uparrow\uparrow}\cos\varphi^{(R)}_{\uparrow\uparrow} + \tau^{(L)}_{\uparrow\uparrow}\cos\varphi^{(L)}_{\uparrow\uparrow}\right]\cos\frac{\phi}{2}, \tag{3.52}$$

$$\tau_y = -i\frac{\tau_{\downarrow\downarrow,\phi} + \tau_{\uparrow\uparrow,\phi}}{2} = \left[\tau^{(R)}_{\uparrow\uparrow}\cos\varphi^{(R)}_{\uparrow\uparrow} - \tau^{(L)}_{\uparrow\uparrow}\cos\varphi^{(L)}_{\uparrow\uparrow}\right]\sin\frac{\phi}{2} - i\left[\tau^{(R)}_{\uparrow\uparrow}\cos\varphi^{(R)}_{\uparrow\uparrow} + \tau^{(L)}_{\uparrow\uparrow}\cos\varphi^{(L)}_{\uparrow\uparrow}\right]\cos\frac{\phi}{2}, \tag{3.53}$$

$$\tau_z = \frac{\tau_{\downarrow\uparrow,\phi} + \tau_{\uparrow\downarrow,\phi}}{2} = \left[\tau^{(L)}_{\uparrow\downarrow}\sin\varphi^{(L)}_{\uparrow\downarrow} - \tau^{(R)}_{\uparrow\downarrow}\sin\varphi^{(R)}_{\uparrow\downarrow}\right]\sin\frac{\phi}{2} + i\left[\tau^{(R)}_{\uparrow\downarrow}\sin\varphi^{(R)}_{\uparrow\downarrow} + \tau^{(L)}_{\uparrow\downarrow}\sin\varphi^{(L)}_{\uparrow\downarrow}\right]\cos\frac{\phi}{2}, \tag{3.54}$$

where one can notice that the real part of τ_0 and imaginary part of $\boldsymbol{\tau}$ are proportional to $\cos\phi/2$ while their imaginary / real parts are proportional to $\sin\phi/2$. From these relations, it is easy to see that $\tau_0^*(\phi) = \tau_0(-\phi)$ and $\boldsymbol{\tau}^*(\phi) = -\boldsymbol{\tau}(-\phi)$. Hence, we can easily verify that under TRS, we have $\Theta\mathscr{H}_{\text{odd}}(\phi)\Theta^{-1} = \mathscr{H}_{\text{odd}}(-\phi)$ with $\Theta = i\sigma_y\rho_0\Sigma_0\mathcal{C}$ where σ_y acts in the spin space, ρ_0 in dot space and Σ_0 is the Pauli matrix acting in the $1-3$ particles space.

To simplify the problem, we will assume that the Coulomb repulsion is very strong such that U is the dominant energy, i.e., ε_j, $\kappa_{\alpha\beta}$, $\Gamma_{i\phi}$, $\tau_{\alpha\beta,\phi} \ll U_j$. This way, we will use the Schrieffer-Wolff transformation to obtain an effective Hamiltonian to describe the states with only one electron. In addition, in the following, we will also assume that $\delta U \ll \bar{U}$ in the following such that the energy scale of the problem is set by $\bar{U}$ allowing us to treat other energies as perturbations. But, first, we need to diagonalize H_1 and H_3. This is easily done thanks to TRS. The two rotation matrices that diagonalize these two blocks are

$$R_1 = e^{-i\frac{\theta_\kappa}{2}\rho_0\sigma_z} e^{-i\frac{\gamma_\kappa}{2}\rho_0\sigma_y} e^{-i\frac{\alpha_\kappa}{2}\rho_z\sigma_z} e^{-i\frac{\beta_1}{2}\rho_y\sigma_0}, \tag{3.55}$$

$$R_3 = e^{-i\frac{\theta_\kappa}{2}\rho_0\sigma_z} e^{-i\frac{\gamma_\kappa}{2}\rho_0\sigma_y} e^{i\frac{\alpha_\kappa}{2}\rho_z\sigma_z} e^{-i\frac{\beta_3}{2}\rho_y\sigma_0}, \tag{3.56}$$

where R_1 is the rotation matrix for H_1, R_3 for H_3 and

$$\theta_\kappa = \arctan\frac{\kappa_y}{\kappa_x}, \quad \gamma_\kappa = \arctan\frac{\sqrt{\kappa_x^2+\kappa_y^2}}{\kappa_z}, \quad \alpha_\kappa = \arctan\frac{-|\boldsymbol{\kappa}|}{\kappa_0}, \tag{3.57}$$

$$\beta_1 = \arctan\frac{2\sqrt{\kappa_0^2+|\boldsymbol{\kappa}|^2}}{\delta\varepsilon}, \quad \beta_3 = \arctan\frac{-2\sqrt{\kappa_0^2+|\boldsymbol{\kappa}|^2}}{\delta\varepsilon+\delta U}. \tag{3.58}$$

Applying these rotations leads to

$$\tilde{H}_1 = R_1^\dagger H_1 R_1 = \bar{\varepsilon}\rho_0\sigma_0 + \sqrt{\frac{\delta\varepsilon^2}{4}+\kappa_0^2+|\boldsymbol{\kappa}|^2}\,\rho_z\sigma_0, \tag{3.59}$$

$$\tilde{H}_3 = R_3^\dagger H_3 R_3 = (3\bar{\varepsilon}+\bar{U})\rho_0\sigma_0 + \sqrt{\left(\frac{\delta\varepsilon+\delta U}{2}\right)^2+\kappa_0^2+|\boldsymbol{\kappa}|^2}\,\rho_z\sigma_0. \tag{3.60}$$

We can see in the above equations that the inter-dot coupling $\check{\kappa}$ cannot lift the spin degeneracy by itself due to TRS. Its effect is simply to shift the energy levels of the two dots.

In addition, we define $\tilde{H}_\mathcal{V} = \mathrm{diag}(R_1^\dagger, R_3^\dagger)\cdot H_\mathcal{V}\cdot\mathrm{diag}(R_1, R_3)$ and $\tilde{\mathcal{V}} = R_3^\dagger \mathcal{V} R_1$. In general, we will denote with a "$\sim$" symbol the quantities when we have projected Eq. (3.43) into the eigenbasis of H_1 and H_3 with R_1 and R_3.

We can now apply the Schrieffer-Wolff transformation e^S to $\mathscr{H}_\text{odd}$, where S is defined as

$$S = \sum_{|\Phi_3\rangle|\Phi_1\rangle} |\Phi_3\rangle \frac{\langle\Phi_3|\tilde{H}_\mathcal{V}|\Phi_1\rangle}{\langle\Phi_3|\tilde{H}_3|\Phi_3\rangle - \langle\Phi_1|\tilde{H}_1|\Phi_1\rangle} \langle\Phi_1| - \text{h.c.}, \tag{3.61}$$

and $\left|\Phi_{1,3}\right\rangle$ denotes the states of $\tilde{H}_{1,3}$ respectively. The resulting Hamiltonian is given as

$$\begin{aligned} H_{1,\text{eff}} &= \tilde{H}_1 - \frac{1}{2}\sum_{|\Phi_3\rangle|\Phi_1\rangle\left|\Phi_1'\right\rangle} |\Phi_1\rangle \left[\frac{\langle\Phi_1|\tilde{H}_\mathcal{V}|\Phi_3\rangle\langle\Phi_3|\tilde{H}_\mathcal{V}\left|\Phi_1'\right\rangle}{\langle\Phi_3|\tilde{H}_3|\Phi_3\rangle - \langle\Phi_1|\tilde{H}_1|\Phi_1\rangle} + \frac{\langle\Phi_1|\tilde{H}_\mathcal{V}|\Phi_3\rangle\langle\Phi_3|\tilde{H}_\mathcal{V}\left|\Phi_1'\right\rangle}{\langle\Phi_3|\tilde{H}_3|\Phi_3\rangle - \left\langle\Phi_1'\right|\tilde{H}_1\left|\Phi_1'\right\rangle}\right] \left\langle\Phi_1'\right|, \\ &\equiv \tilde{H}_1 - \tilde{H}_{\mathcal{V},\text{eff}}. \end{aligned} \tag{3.62}$$

This Hamiltonian allows one to describe the one particle states where $\tilde{H}_{\mathcal{V},\text{eff}}$ takes into account the coupling between the one and three particle states. Namely, when a Cooper pair tunnels to the dots, corresponding to the terms $\langle\Phi_3|\tilde{H}_\mathcal{V}\left|\Phi_1'\right\rangle$, we have a virtual high energy state with three electrons occupying the dots. Then, this Cooper pair tunnels back into one of the superconducting leads, which is described by $\langle\Phi_1|\tilde{H}_\mathcal{V}|\Phi_3\rangle$, leaving the junction in a low energy state. These processes are represented in Fig. 3.6 for a junction without inter-dot coupling.

In the denominator of $\tilde{H}_{\mathcal{V},\text{eff}}$, we keep $\tilde{H}_1$ since it contains terms that can be of the same order of magnitude as those in $\tilde{H}_3$ besides $\bar{U}$ such as the terms proportional to ε_j, δU and $\kappa_{\alpha\beta}$. We keep these terms because, as we will see later, it can be necessary to go to first order in $(\alpha\bar{\varepsilon}+\beta\delta\varepsilon+\delta\kappa_{\alpha\beta}+\gamma\delta U)/\bar{U}$ where $\alpha,\beta,\delta,\gamma$ are adimensional coefficients resulting from $\langle\Phi_3|\,\tilde{H}_3\,|\Phi_3\rangle-\langle\Phi_1|\,\tilde{H}_1\,|\Phi_1\rangle$.

Our goal here is to determine the ingredients we need to lift the spin degeneracy. Using again the analogy with the S-N-S junction of Chap. 2, we know that we need to have at least two channels and a phase shift between opposite spin states. The two channels are provided by the dots when they are both connected to the superconducting leads. For the phase shift, we saw in Sec. 3.2 that it can be provided by the crossed Andreev reflection terms $\tau_{\alpha\beta,\phi}$ when the tunnel couplings have a finite spin dependence $\boldsymbol{t}\neq 0$. The other mechanism that can provide this phase shift is the inter-dot coupling if the latter also has a finite spin dependence $\boldsymbol{\kappa}\neq 0$, and if the two dots are connected to the leads. Therefore, in the following, we will study two simple cases. For both of them, we will consider that there is no spin-flip such that $t_{x,y}=\kappa_{x,y}=0$. This simplifies a lot the problem as it leaves the two spin sectors uncoupled. In the first case, we will consider the parallel configuration, i.e., without inter-dot coupling $\check{\kappa}=0$ and SOC in the tunnel couplings such that $\check{t}=t_0+i t_z\sigma_z$. In the second case, we will consider the configuration when all the couplings are present (tunnel and inter-dot), with SOC in the inter-dot coupling such that $\check{\kappa}=\kappa_0+i\kappa_z\sigma_z$ and no SOC in the tunnel couplings $\check{t}=t_0$. With these two cases, we will be able to show that the spin degeneracy can be lifted if at least one of the couplings has a finite spin dependence.

3.3.1 Effect of SOC in the couplings

As mentioned before, in this section, we will study the effect of SOC in the couplings of the system (tunnel or inter-dot couplings) without spin-flip transmission probability $t_{x,y}=\kappa_{x,y}=0$. We will start with the case without inter-dot coupling (parallel configuration) and then, study the case with SOC in the inter-dot coupling (configuration where all the couplings are present).

3.3.1.1 Effect of SOC in the tunnel couplings $\check{t}$

Let's start with the study of the energy spectrum without inter-dot coupling $\check{\kappa}=0$, i.e., the parallel configuration. Here, we will characterize the spin-splitting of states within a same doublet when the tunnel couplings have a finite spin dependence of the form $\check{t}=t_0+i t_z\sigma_z$. The Hamiltonians for the one and three particle states take the simple form

$$H_1=\bar{\varepsilon}\rho_0+\frac{\delta\varepsilon}{2}\rho_z, \tag{3.63}$$

$$H_3=(3\bar{\varepsilon}+\bar{U})\rho_0+\frac{\delta\varepsilon+\delta U}{2}\rho_z, \tag{3.64}$$

Without spin-flip $\tau_{\uparrow\uparrow}=\tau_{\downarrow\downarrow}=0$, $\mathcal{V}$ simplifies to

$$\mathcal{V}=\left[\frac{\tau_{\downarrow\uparrow,\phi}-\tau_{\uparrow\downarrow,\phi}}{2}\rho_0+\frac{\Gamma_{1\phi}+\Gamma_{2\phi}}{2}\rho_x+i\frac{\Gamma_{1\phi}-\Gamma_{2\phi}}{2}\rho_y\right]\sigma_0+\frac{\tau_{\downarrow\uparrow,\phi}+\tau_{\uparrow\downarrow,\phi}}{2}\rho_z\sigma_z. \tag{3.65}$$

From these Hamiltonians, we can get $H_{\mathcal{V},\text{eff}}$. Without spin-flip in the coupling, the two spin sectors remain decoupled and we can look at each block separately which are given as

$$H_{\mathcal{V},\text{eff},\sigma}=\frac{1}{2}\begin{pmatrix} 2\left(\frac{|\tau_{\bar{\sigma}\sigma,\phi}|^2}{2\bar{\varepsilon}+\bar{U}+\delta U/2}+\frac{|\Gamma_{2\phi}|^2}{2\bar{\varepsilon}+\bar{U}-\delta\varepsilon-\delta U/2}\right) & \kappa^*_{\text{eff},\sigma} \\ \kappa_{\text{eff},\sigma} & 2\left(\frac{|\tau_{\sigma\bar{\sigma},\phi}|^2}{2\bar{\varepsilon}+\bar{U}-\delta U/2}+\frac{|\Gamma_{1\phi}|^2}{2\bar{\varepsilon}+\bar{U}+\delta\varepsilon-\delta U/2}\right)\end{pmatrix}, \tag{3.66}$$

where

$$\kappa_{\mathrm{eff},\sigma} = \sigma \left[\Gamma_{1\phi}^{*} \tau_{\bar{\sigma}\sigma,\phi} \left(\frac{1}{2\bar{\varepsilon} + \bar{U} + \delta U/2} + \frac{1}{2\bar{\varepsilon} + \bar{U} + \delta\varepsilon + \delta U/2} \right) \right. \\ \left. - \tau_{\sigma\bar{\sigma},\phi}^{*} \Gamma_{2\phi} \left(\frac{1}{2\bar{\varepsilon} + \bar{U} - \delta U/2} + \frac{1}{2\bar{\varepsilon} + \bar{U} - \delta\varepsilon - \delta U/2} \right) \right]. \tag{3.67}$$

As we discussed in the previous section, the Hamiltonian $H_{1,\mathrm{eff}}$ from Eq. (3.62) describes a state with one electron in one of the two dots. Cooper pairs can tunnel from one of the superconducting electrodes to the dots and bring the system into a three particles state so that the system is in a virtual high energy state. These Coopers then tunnel back into one of the electrodes leaving the system in a one particle state. Without inter-dot coupling, Cooper pairs can either tunnel into the same dot or they can be split between the two dots as depicted in Fig. 3.6. Thanks to this coupling to the three particle states sector, an effective coupling between the two dots which we denote $\kappa_{\mathrm{eff},\sigma}$ in Eq. (3.66) is possible. The eigenvalues of Eq. (3.66) can easily be obtained. We write them as

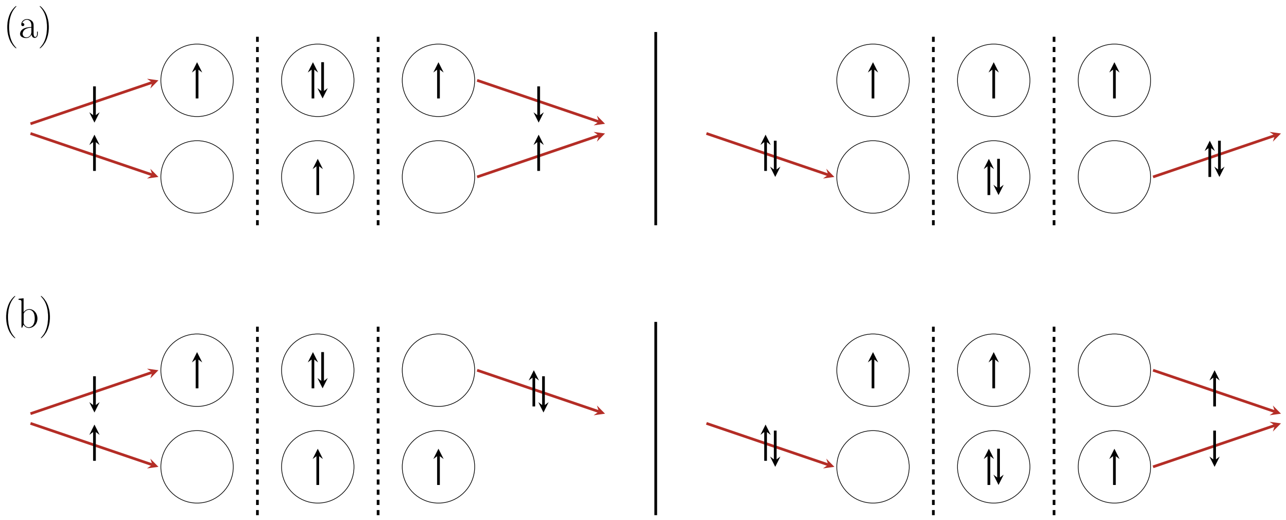

Figure 3.6: Illustration depicting the physics governed by $H_{1,\mathrm{eff}}$ in a system without inter-dot coupling ($\check{\kappa} = 0$). In panel (a), the process involves either splitting or tunneling of the Cooper pair into the unoccupied dot, followed by its exit in the same manner. In panel (b), the sequential events of Cooper pair tunneling into both dots and the co-tunneling of the two electrons occupying the same quantum dot or vice versa allow an effective transfer of an electron from one dot to the other.

$$\varepsilon_{\sigma,\pm} = \bar{\varepsilon} - \frac{(H_{\mathcal{V},\mathrm{eff},\sigma})_{11} + (H_{\mathcal{V},\mathrm{eff},\sigma})_{22}}{2} \pm \sqrt{\frac{1}{4}\left(\delta\varepsilon + \left((H_{\mathcal{V},\mathrm{eff},\sigma})_{11} - (H_{\mathcal{V},\mathrm{eff},\sigma})_{22}\right)\right)^2 + \left|(H_{\mathcal{V},\mathrm{eff},\sigma})_{21}\right|^2}, \tag{3.68}$$

In the limit $|\delta\varepsilon| \gg |(H_{\mathcal{V},\mathrm{eff},\sigma})_{ij}|$, i.e. $|\delta\varepsilon| \gg (\pi\nu_S|\check{t}|^2)^2/\bar{U}$, we obtain the following spin-splitting

$$\bar{U}\delta\varepsilon_{\pm} = \mp s(|\tau_{\downarrow\uparrow,\phi}|^2 - |\tau_{\uparrow\downarrow,\phi}|^2) = \pm s(\tau_{\uparrow\downarrow}^2 - \delta\tau_{\uparrow\downarrow}^2)\sin\delta\varphi_{\uparrow\downarrow}\sin\phi, \tag{3.69}$$

with $s = \mathrm{sign}(\delta\varepsilon)$ and $\delta\varepsilon_{\pm} = \varepsilon_{\uparrow\pm} - \varepsilon_{\downarrow\pm}$. Foremost, we can see that the resulting spin-splitting has a $\sin\phi$ dependence and is opposite for the two doublets. The SOC strength is encoded in $\delta\varphi_{\uparrow\downarrow}$. An interesting point is that from Eq. (3.69), we can see that SOC allows one to lift the spin degeneracy except when $\delta\varphi_{\uparrow\downarrow}$ is a multiple of π. This is the case when there is a symmetry between the couplings, i.e., when $\check{t}^{(a1)} = \check{t}^{(a2)}$. Hence, as long as the tunnel couplings are different, there is a finite splitting between the spin states of a same doublet. We can also see that the splitting vanishes when $\tau_{\uparrow\downarrow} = \delta\tau_{\uparrow\downarrow}$ which simply

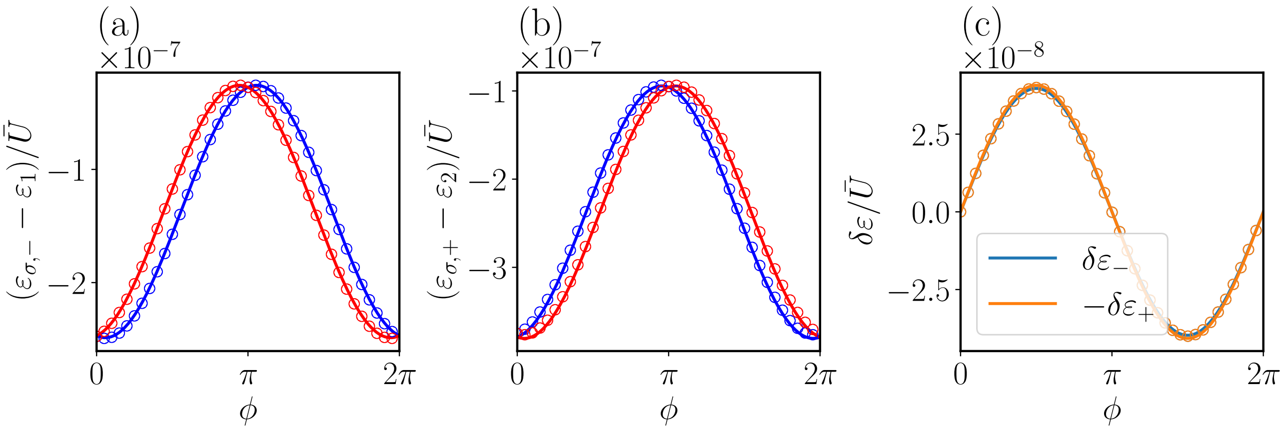

Figure 3.7: Energy spectrum of the lowest energy states for the S-DQD-S studied in Sec. 3.3.1.1 for the regime $|\delta\varepsilon| \gg |(H_{\mathcal{V},\mathrm{eff},\sigma})_{ij}|$. Full lines correspond to the numerical diagonalization of Eq. (3.43) while dotted lines correspond to the analytical results obtained in Sec. 3.3.1.1 at first order in $1/\bar{U}$. For each panel, we set $\delta U/\bar{U} = 2.5 \times 10^{-2}$, $\varepsilon_1/\bar{U} = -1 \times 10^{-2}$ and $\varepsilon_2/\bar{U} = 5 \times 10^{-3}$. For the tunnel couplings, we have $t_0^{R1} = t_0^{R2} = t_0^{L2} = t_z^{R1} = t_z^{L2} = \bar{U}/2 \times 10^{-3}$ and $t_0^{L1} = t_z^{L1} = t_z^{R2} = \bar{U} \times 10^{-3}$. We have normalized the energies by $\bar{U}$ as it sets the energy scale. The scale on each plot is set by the smallness of the tunnel couplings and $\bar{U}$ as the dispersion with the phase is proportional to $(\pi\nu_S t^2)^2/\bar{U}$ according to Eq. (3.68) and is here of the order of $\sim 10^{-7}$. The panel (a) shows the energy of the lowest energy doublet $\varepsilon_{-\sigma}$. The panel (b) shows the same but for the higher-energy doublet $\varepsilon_{+\sigma}$. Finally, panel (c) shows the energy splitting between states within a same doublet. We have a $\sin\phi$ spin splitting for the two doublets of states which are nearly identical as predicted by Eq. (3.69). The smallness of the parameters has been chosen such that a doublet ground state is favored.

indicates that there is no splitting when one of the two superconducting leads is not connected to the dots, which is expected as in this case, the spectrum becomes independent of the phase difference. The phase dispersion and spin-splitting for each doublet is shown in Fig. 3.7.

We can also look at the limit $\delta\varepsilon = 0$. This regime can be achieved via the use of electrostatic gates to tune the on-site energy of each dot. From Fig. 3.4, we already know that in this case, it should not stabilize a doublet ground state, but we can still look at the required ingredients to lift the spin degeneracy. Developing Eq. (3.68) to the second order in $1/\bar{U}$ leads to

$$\delta\varepsilon_\pm = \frac{\delta U}{2\bar{U}^2}\left(|\tau_{\uparrow\downarrow,\phi}|^2 - |\tau_{\downarrow\uparrow,\phi}|^2\right)\left[1 \pm \frac{|\Gamma_{1\phi}|^2 + |\Gamma_{2\phi}|^2 + |\tau_{\uparrow\downarrow,\phi}|^2 + |\tau_{\downarrow\uparrow,\phi}|^2}{\sqrt{\left(|\tau_{\downarrow\uparrow,\phi}|^2 + |\Gamma_{2\phi}|^2 - |\tau_{\uparrow\downarrow,\phi}|^2 - |\Gamma_{1\phi}|^2\right)^2 + 4\left|\Gamma_{1\phi}^*\tau_{\downarrow\uparrow,\phi} - \Gamma_{2\phi}\tau_{\uparrow\downarrow,\phi}^*\right|^2}}\right]. \tag{3.70}$$

First, a factor $\delta U/\bar{U}$ now reduces the splitting. The factor $(|\tau_{\uparrow\downarrow,\phi}|^2 - |\tau_{\downarrow\uparrow,\phi}|^2)$ of Eq. (3.70) is the same as the one in Eq. (3.69) and gives a $\sin\phi$ splitting. However, the phase dependence of the second term in parentheses can be more complicated. In addition, the two terms in parentheses of Eq. (3.70) can be of the same order of magnitude. Hence, the resulting splitting for one of the doublets can be significantly smaller than for the other one due to the ± sign in front of the second term in parentheses. As for the limit $|\delta\varepsilon| \gg |(H_{\mathcal{V},\mathrm{eff},\sigma})_{ij}|$, the factor $(|\tau_{\uparrow\downarrow,\phi}|^2 - |\tau_{\downarrow\uparrow,\phi}|^2)$ implies that we need to have an asymmetry between the tunnel couplings to have a finite spin-splitting. The resulting dispersion with the phase difference and spin-splitting is shown in Fig. 3.8

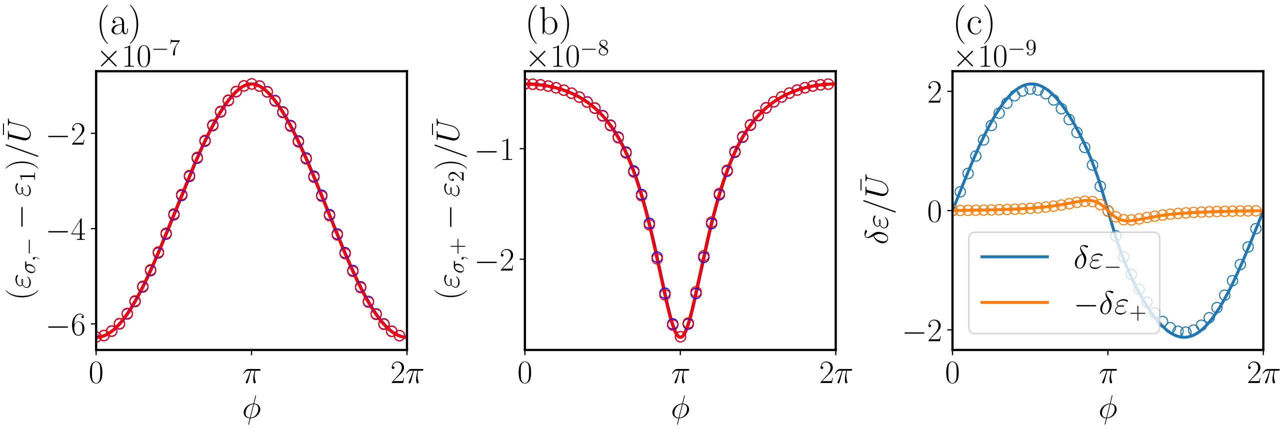

Figure 3.8: Same Figure as Fig. 3.7 but for the regime $\delta\varepsilon = 0$. Full lines correspond to the numerical diagonalization of Eq. (3.43) while dotted lines correspond to the analytical results obtained in Sec. 3.3.1.1 at second order in $1/\bar{U}$. For each plot, we here have $\delta U/\bar{U} = 5\times10^{-2}$, $\varepsilon_1/\bar{U} = \varepsilon_2/\bar{U} = -1\times10^{-2}$. The tunnel couplings are the same as in Fig. 3.7. As expected from Eq. (3.70), the splitting of one of the two doublets is significantly lower than the other and differ from a $\sin\phi$.

According to Eq. (3.70), if the two dots are identical $\delta\varepsilon = \delta U = 0$ then, there is no spin-splitting. The question is whether this result is more general than what the effective Hamiltonian of Eq. (3.66) yields. This can be easily done by looking back at the initial Hamiltonians of Eqs. (3.63)-(3.65). When the two dots are identical, H_1 and H_3 become proportional to identity. In this case, the Hamiltonian $\mathscr{H}_{\mathrm{odd}}$ of Eq. (3.43) can be easily diagonalized and yields the same eigenvalues for the two spin sectors.

Interestingly, we can see with the two limits we have studied that, in order to lift the spin degeneracy, it is necessary to have non-identical dots. Namely, their on-site energy ε and/or Coulomb repulsion strength U must be different. In addition, there must be an asymmetry in the tunnel couplings with the leads to have a finite spin-splitting. Away from the two limits we describe, the spin-splitting can become different from the $\sin\phi$ we obtained, but keep the two-fold degeneracy for ϕ multiple of π which effectively preserves TRS. in Fig. 3.9, we show a typical energy spectrum obtained numerically for this scenario.

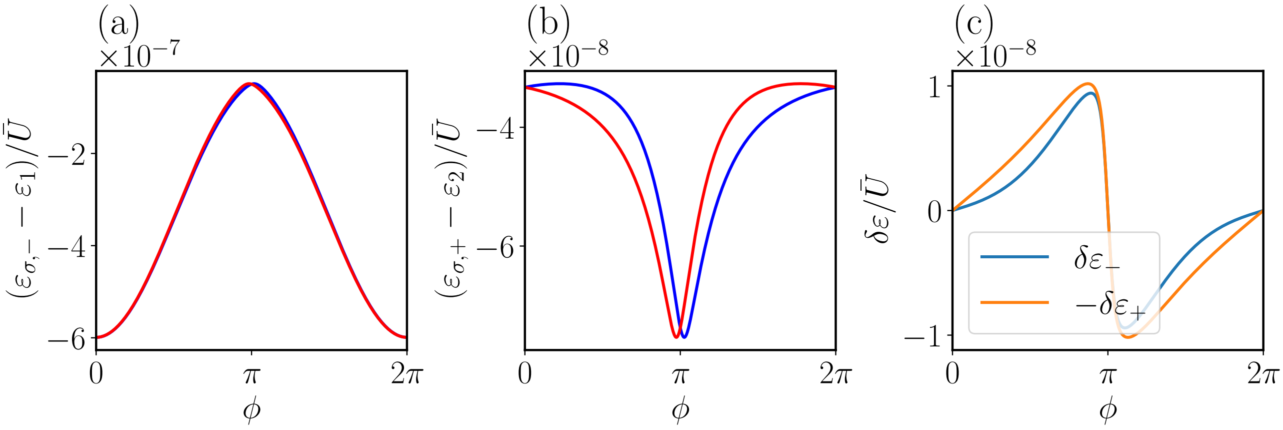

Figure 3.9: Same Figure as Fig. 3.7 but for the regime $|\delta\varepsilon| \sim |(H_{\mathcal{V},\mathrm{eff},\sigma})_{ij}|$. The parameters are $\delta U/\bar{U} = 5\times10^{-2}$, $\varepsilon_1/\bar{U} = -1\times10^{-2}$ and $|\delta\varepsilon|/\bar{U} = 5\times10^{-8}$. We used the same tunnel couplings as in Fig. 3.7.

3.3.1.2 Effect of SOC in the inter-dot coupling $\check{\kappa}$

We now turn to the evaluation of the energy spectrum in the scenario where we have SOC in the inter-dot coupling $\check{\kappa} = \kappa_0 + i\kappa_z\sigma_z$ and finite spin-independent tunnel couplings $\check{t} = t_0$. The Hamiltonians describing the one and three particles states are in this case

$$H_1 = \bar{\varepsilon}\rho_0\sigma_0 + \frac{\delta\varepsilon}{2}\rho_z\sigma_0 + \kappa_0\rho_x\sigma_0 - \kappa_z\rho_y\sigma_z, \tag{3.71}$$

$$H_3 = (3\bar{\varepsilon} + \bar{U})\rho_0\sigma_0 + \frac{\delta\varepsilon + \delta U}{2}\rho_z\sigma_0 - \kappa_0\rho_x\sigma_0 - \kappa_z\rho_y\sigma_z, \tag{3.72}$$

while $\mathcal{V}$ is given as

$$\mathcal{V} = -\tau_\phi\rho_0 + \frac{\Gamma_{1\phi} + \Gamma_{2\phi}}{2}\rho_x + i\frac{\Gamma_{1\phi} - \Gamma_{2\phi}}{2}\rho_y, \tag{3.73}$$

where

$$\tau_\phi = \tau\cos\frac{\phi}{2} + i\delta\tau\sin\frac{\phi}{2}, \tag{3.74}$$

$$\tau = \tau_R + \tau_L, \qquad \delta\tau = \tau_R - \tau_L, \tag{3.75}$$

$$\tau_a = \pi\nu_S\left|t_0^{(a1)}t_0^{(a2)}\right| \tag{3.76}$$

Projecting Eq. (3.43) into the eigenspace of H_1 and H_3 yields

$$\tilde{H}_1 = \bar{\varepsilon}\rho_0 + \sqrt{\frac{\delta\varepsilon^2}{4} + \kappa_0^2 + \kappa_z^2}\,\rho_z \equiv \bar{\varepsilon}\rho_0 + \frac{\widetilde{\delta\varepsilon}_{(1)}}{2}\rho_z, \tag{3.77}$$

$$\tilde{H}_3 = (3\bar{\varepsilon} + \bar{U})\rho_0 + \sqrt{\left(\frac{\delta\varepsilon + \delta U}{2}\right) + \kappa_0^2 + \kappa_z^2}\,\rho_z \equiv (3\bar{\varepsilon} + \bar{U})\rho_0 + \frac{\widetilde{\delta\varepsilon}_{(3)}}{2}\rho_z. \tag{3.78}$$

while $\mathcal{V}$ becomes

$$\tilde{\mathcal{V}} = \left[\mathcal{V}_{00}\rho_0 + \mathcal{V}_{z0}\rho_z + \mathcal{V}_{x0}\rho_x + \mathcal{V}_{y0}\rho_y\right]\sigma_0 + \left[\mathcal{V}_{zz}\rho_z + \mathcal{V}_{xz}\rho_x\right]\sigma_z, \tag{3.79}$$

with

$$\mathcal{V}_{z0} = \frac{1}{2}\left(\Gamma_{1\phi} + \Gamma_{2\phi}\right)\sin\left(\frac{\beta_1 + \beta_3}{2}\right), \tag{3.80}$$

$$\mathcal{V}_{zz} = i\tau_\phi\sin\alpha_\kappa\cos\left(\frac{\beta_1 + \beta_3}{2}\right), \tag{3.81}$$

$$\mathcal{V}_{x0} = \frac{1}{2}\left(\Gamma_{1\phi} + \Gamma_{2\phi}\right)\cos\left(\frac{\beta_1 + \beta_3}{2}\right), \tag{3.82}$$

$$\mathcal{V}_{xz} = -i\tau_\phi\sin\alpha_\kappa\sin\left(\frac{\beta_1 + \beta_3}{2}\right), \tag{3.83}$$

$$\mathcal{V}_{00} = \frac{1}{2}\left(\Gamma_{1\phi} - \Gamma_{2\phi}\right)\sin\left(\frac{\beta_1 - \beta_3}{2}\right) - \tau_\phi\cos\alpha_\kappa\cos\left(\frac{\beta_1 - \beta_3}{2}\right), \tag{3.84}$$

$$\mathcal{V}_{y0} = i\left[\tau_\phi\cos\alpha_\kappa\sin\left(\frac{\beta_1 - \beta_3}{2}\right) + \frac{1}{2}\left(\Gamma_{1\phi} - \Gamma_{2\phi}\right)\cos\left(\frac{\beta_1 - \beta_3}{2}\right)\right]. \tag{3.85}$$

As mentioned at the beginning of Sec. 3.3, the inter-dot coupling by itself, even with SOC, does not directly lift the spin degeneracy of the one and three particle states. However, it induces a spin structure in $\tilde{H}_{\mathcal{V}}$. Hence, we can expect that the spin degeneracy will be lifted thanks to this coupling. The effective

Hamiltonian describing the one particle states thus describes a similar physic as in the previous section. The main difference here is that the electrons are delocalized between the two dots due to the finite value of $\check{\kappa}$. The derivation of the eigenvalues of $H_{1,\mathrm{eff}}$ is the same as the one we did for the scenario with SOC in $\check{t}$ (see Eq. (3.68)). So we will jump directly to the resulting spin-splitting. In the limit $\widetilde{\delta\varepsilon}_{(1)} \gg |(\tilde{H}_{\mathcal{V},\mathrm{eff},\sigma})_{ij}|$ that favors a doublet ground state, we obtain at the lowest order in $1/\bar{U}$ the following splitting

$$\delta\varepsilon_\pm = \pm\frac{1}{\bar{U}}\left[\tau\left(\delta\Gamma_1 - \delta\Gamma_2\right) - \delta\tau\left(\Gamma_1 - \Gamma_2\right)\right]\sin\beta_1 \sin\alpha_\kappa \sin\phi. \tag{3.86}$$

Here again, we observe a $\sin\phi$ spin-splitting. The splitting is maximal when β_1 and α_κ are equal to $\pi/2$, which is the case when $\delta\varepsilon = \delta U = 0$ for β_1, and when $\kappa_0 = 0$ for α_κ. Unlike the previous scenario, here, it is not necessary to have a finite non-spin-dependent part of the coupling, in this case κ_0. In addition, the splitting vanishes when $\tau = \delta\tau = 0$, which corresponds to the configuration where the dots are in series or simply means that the dots are not coupled to the superconducting leads. Also, there is no splitting when $\Gamma_1 - \Gamma_2 = \delta\Gamma_1 - \delta\Gamma_2 = 0$, which is verified when $\Gamma_{i,1} = \Gamma_{i,2}$. With $\check{\kappa} \neq 0$, we can't be in the limit $\widetilde{\delta\varepsilon}_{(1)} = 2\sqrt{\frac{\delta\varepsilon^2}{4} + \kappa_0^2 + \kappa_z^2} = 0$, therefore, we won't cover this limit here. The energy spectrum for the lowest energy states is shown in Fig. 3.10

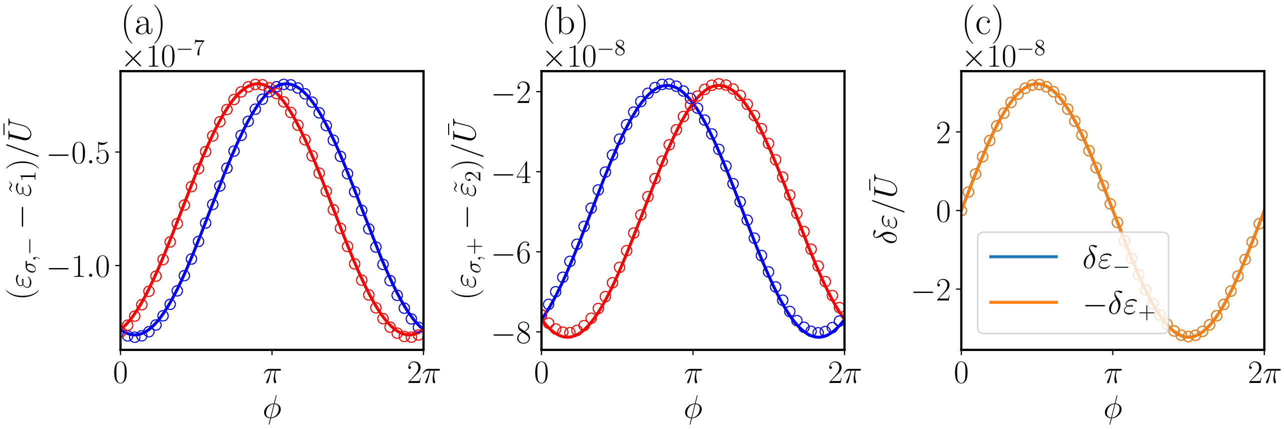

Figure 3.10: Energy spectrum of the lowest energy states for the S-DQD-S junction with SOC in the inter-dot coupling in the regime $\widetilde{\delta\varepsilon}_{(1)} \gg |(\tilde{H}_{\mathcal{V},\mathrm{eff},\sigma})_{ij}|$. Full lines are for the numerical results and dotted lines are for the analytical result of Eq. (3.68) at first order in $1/\bar{U}$. For each plot, we set $\delta U = 0$, $\varepsilon_1/\bar{U} = -1\times 10^{-2}$, $\varepsilon_2/\bar{U} = 5\times 10^{-3}$, $\kappa_0/\bar{U} = 2.5\times 10^{-3}$ and $\kappa_z/\bar{U} = 5\times 10^{-3}$. For the tunnel couplings, we have $t_0^{L1} = t_0^{R2} = \bar{U}/2\times 10^{-3}$, $t_0^{R1} = t_0^{L1} = \bar{U}\times 10^{-3}$. As in Fig. 3.7, the panel (a) shows the energy of the lowest doublet $\varepsilon_{-\sigma}$ shifted by ε_1 and normalized by $\bar{U}$. The panel (b) is the same but for the higher-energy doublet $\varepsilon_{+\sigma}$. Finally, the panel (c) shows the energy splitting between states within a same doublet. As predicted by Eq. (3.86), we obtain a $\sin\phi$ spin splitting for the two doublets of states that are nearly identical in this regime.

Finally, as can be seen in Fig. 3.11, in the limit $\widetilde{\delta\varepsilon} \sim |(H_{\mathcal{V},\mathrm{eff},\sigma})_{ij}|$ the spin-splitting differs from the simple $\sin\phi$ splitting we obtained as in Fig. 3.7.

We have now described the energy spectrum in the odd parity sector. Using an effective Hamiltonian describing the one particle states, we have shown how SOC can lead to a spin-split energy spectrum. To do so, we have studied the simple scenario of a junction with spin-dependent tunnel coupling between the two dots and the superconducting and no inter-dot coupling. And, we studied a junction with spin-dependent inter-dot coupling and finite tunnel coupling between the dots and the leads without SOC. Our results indicate that to lift the spin degeneracy, the following ingredients are required

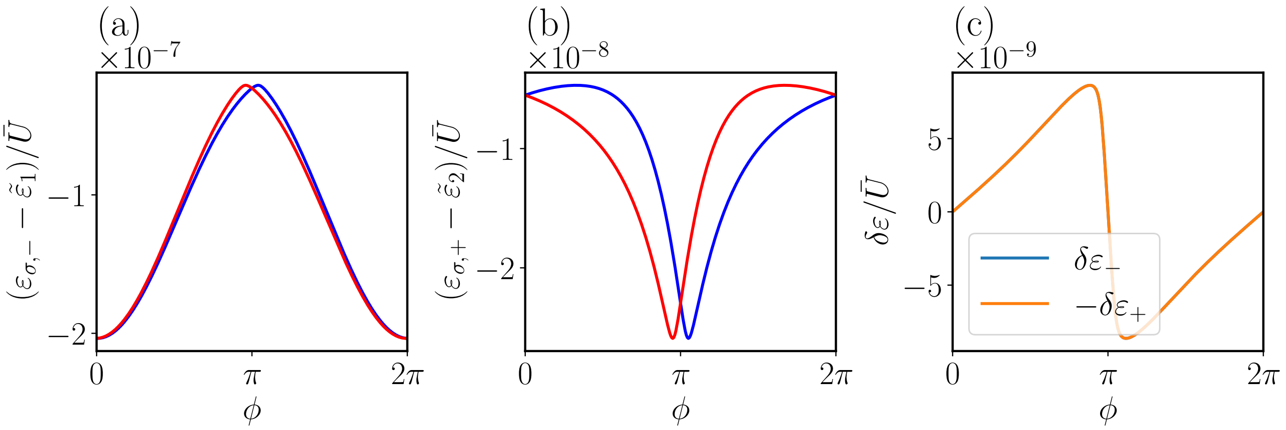

Figure 3.11: Same figure as Fig. 3.10 but for the regime $\widetilde{\delta\varepsilon}_{(1)} \sim |(\tilde{H}_{\mathcal{V},\text{eff},\sigma})_{ij}|$. For each plot, we set $\delta U = 0$, $\varepsilon_1/\bar{U} = -1\times10^{-2}$, $\varepsilon_2 = \varepsilon_1$, $\kappa_0/\bar{U} = 2.5\times10^{-9}$ and $\kappa_z/\bar{U} = 0.5\times10^{-8}$. The tunnel couplings are the same as in Fig. 3.10. As opposed to the splitting obtained in Fig. 3.9, here the two doublets show a quasi-identical spin-splitting.

- SOC in the tunnel or inter-dot couplings.
- Each dot needs to be connected to both leads.
- Non-identical dots, i.e. finite on-site energy difference $\delta\varepsilon \neq 0$, Coulomb repulsion strength difference $\delta U \neq 0$ or introduced via the inter-dot coupling $\check{\kappa}$.
- Asymmetry between the left and right tunnel couplings between the dots and the leads (no inter-dot coupling), or different tunnel couplings for each dot (with inter-dot coupling).

In the next section, we will study the current operator. As in Chap. 2, we will study the off-diagonal matrix element of this operator. Our main goal here will be to determine what is needed to obtain finite off-diagonal matrix elements between opposite spin states. We will also characterize, with numerical results, the dependence of these elements on the parameters of the system.

3.4 Current operator

As said previously, in this section we will evaluate the matrix elements of the current operator. Our objective will be to highlight the minimal set of ingredients to obtain finite matrix elements between opposite spin states. In particular, we want to obtain these requirements for the matrix element for states within the same doublet. To fulfill this objective, we will start by deriving the current operator in the superconducting atomic limit $\Delta \to \infty$ which we used to obtain the Hamiltonians describing the even and odd parity sector. Then, as we did for the energy spectrum, we will only study the odd parity sector and consider strong Coulomb repulsion to describe only the one particle states. From the effective model which describes the latter, we will show that in order to have finite matrix elements between opposite spin states, spin-flip in the tunnel couplings, finite inter-dot coupling and different Coulomb repulsion on the two dots are required. Finally, we will use numerical results to characterize the different matrix elements of the current operator and give perspectives to obtain analytical results to evaluate these matrix elements.

3.4.1 Current operator in the superconducting atomic limit

Let's start by deriving the current operator in the superconducting atomic limit $\Delta \to \infty$. As we will see below, in this limit the current operator is the derivative of the effective Hamiltonian H_{eff} defined in Eq. (3.27) with respect to the phase difference ϕ. To show this, we first need to know how the current operator is defined in the general case. This operator should describe the flow of particles in the junction. Therefore, we can define it from the variations of the number of particles in the superconducting leads. The current operator describing the variation of the number of particles in one of the leads can thus be written as

$$J_{L/R} = e\dot{N}_{L/R}, \qquad N_a = \sum_{\boldsymbol{k}\sigma} c^{\dagger}_{\boldsymbol{k}\sigma,a} c_{\boldsymbol{k}\sigma,a}, \tag{3.87}$$

where $\dot{N}_a = \mathrm{d}N_a/\mathrm{d}t$. Using Heisenberg equation of motion, we can simply write

$$\begin{aligned} J_a =& i\frac{e}{\hbar}[H, N_a] \\ =& \frac{ie}{\hbar}\sum_{\boldsymbol{k}}\sum_{j=1,2}\sum_{\alpha\beta}\left(t^{(aj)}_{\alpha\beta} d^{\dagger}_{j\alpha} c_{\boldsymbol{k}\beta,a} - \text{h.c.}\right). \end{aligned} \tag{3.88}$$

Note that we could have obtained this result from a different derivation. In fact, by performing an appropriate gauge transformation such that

$$c_{\boldsymbol{k},\sigma,a} \to c_{\boldsymbol{k},\sigma,a} e^{i\varphi_a/2}, \tag{3.89}$$

then, the superconducting Hamiltonians for both electrodes contain only real terms. However, the tunneling Hamiltonian which couples the electrodes to the dots becomes

$$H_{T,a} = \sum_{\boldsymbol{k}}\sum_{j=1,2}\sum_{\alpha\beta}\left(t^{(aj)}_{\alpha\beta} e^{i\varphi_a/2} d^{\dagger}_{\alpha} c_{\boldsymbol{k},\beta,a} + \text{h.c.}\right). \tag{3.90}$$

It results that Eq. (3.88) can thus be obtained by taking the derivative of H with respect to φ_a, i.e., $J_a = \frac{2e}{\hbar}\partial_{\varphi_a} H_{T,a}$.

From this definition, we want to obtain a current operator that describes the flow of electrons from the left lead to the right lead. More precisely, when an electron leaves the left lead, and an electron enters the right lead so that $\dot{N}_R = -\dot{N}_L$, this operator should describe the transfer of one charge across the junction. Also, when the number of electrons in each lead increases by one charge $\dot{N}_R = \dot{N}_L$, then we should not have any current in the junction. Therefore, the current operator we obtain is given as [127]

$$J_{L\to R} = \frac{J_R - J_L}{2}, \tag{3.91}$$

Using the derivation for J_a, we obtain

$$J_{L\to R} = e\frac{\dot{N}_R - \dot{N}_L}{2} = \frac{e}{\hbar}\left(\frac{\partial H_{T,R}}{\partial \varphi_R} - \frac{\partial H_{T,L}}{\partial \varphi_L}\right) = \frac{2e}{\hbar}\frac{\partial H}{\partial \phi}, \tag{3.92}$$

The fact that only the tunnel Hamiltonian H_T appears in the current operator is not surprising as the only possible way to transfer electrons from one lead to the other is by their tunneling to the quantum dots. Also, the fact that we recover the usual current-phase relation by performing the appropriate gauge transformation is not surprising as well, given that we are describing a Josephson junction.

To obtain the current operator in the atomic limit, the procedure is the same as for the Hamiltonian. We will first perform a Schrieffer-Wolff transformation on $J_{L\to R}$ then project onto the low energy sector. This reads

$$J_{\text{eff},a} = \sum_{|\Phi_L\rangle|\Phi'_D\rangle} |\Phi_L\rangle\langle\Phi_L|(J_a + [S, J_a])\left|\Phi'_D\right\rangle\left\langle\Phi'_D\right|, \tag{3.93}$$

where S is given in Eq. (3.8) and $|\Phi_L\rangle$, $\left|\Phi'_D\right\rangle$ denotes the states of the dots.

From our previous results, we can easily see that, at first order in $1/E_{\boldsymbol{k},a}$ with $E_{\boldsymbol{k},a} = \sqrt{\xi_{\boldsymbol{k},a} + \Delta^2}$, the effective current operator obtained is none other than the derivative of the effective Hamiltonian H_{eff} defined in Eq. (3.27) with respect to the phase such that we can write

$$J_{\text{eff},a} = \frac{2e}{\hbar}\frac{\partial H_{\text{eff}}}{\partial\varphi_a}. \tag{3.94}$$

It results that the current operator describing the flow of electrons from the left to the right electrodes of Eq. (3.91) can, in the superconducting atomic limit, be written as

$$J_{\text{eff}} = \frac{2e}{\hbar}\frac{\partial H_{\text{eff}}}{\partial\phi}, \tag{3.95}$$

where we have dropped the subscript $L \to R$ for readability.

In the following, it is this current operator that we will use as a basis for our numerical results.

3.4.2 Effective current operator in the odd parity sector

From here, we will focus on the matrix elements of the current operator in the odd parity sector. In $\mathscr{H}_{\text{odd}}$ only the off-diagonal blocks described by $H_{\mathcal{V}}$ depends on the phase difference ϕ such that $\partial_\phi\mathscr{H}_{\text{odd}} = \partial_\phi H_{\mathcal{V}}$.

As for the energy spectrum, we will consider a strong Coulomb repulsion so that U is the dominant energy. Therefore, we want to evaluate the matrix elements of the current operator in the low energy sector constituted by the one particle states. We can, once again, use a Schrieffer-Wolff transformation onto J_{odd} then project onto the basis spanned by the one particle states. We denote the resulting current operator as $J_{1,\text{eff}}$ which is given as

$$J_{1,\text{eff}} = -\frac{2e}{\hbar}\sum_{|\Phi_3\rangle|\Phi_1\rangle\left|\Phi'_1\right\rangle} |\Phi_1\rangle\left[\frac{\langle\Phi_1|\tilde{H}_{\mathcal{V}}|\Phi_3\rangle\langle\Phi_3|\partial_\phi\tilde{H}_{\mathcal{V}}\left|\Phi'_1\right\rangle}{\langle\Phi_3|\tilde{H}_3|\Phi_3\rangle - \langle\Phi_1|\tilde{H}_1|\Phi_1\rangle} + \frac{\langle\Phi_1|\partial_\phi\tilde{H}_{\mathcal{V}}|\Phi_3\rangle\langle\Phi_3|\tilde{H}_{\mathcal{V}}\left|\Phi'_1\right\rangle}{\langle\Phi_3|\tilde{H}_3|\Phi_3\rangle - \left\langle\Phi'_1\right|\tilde{H}_1\left|\Phi'_1\right\rangle}\right]\left\langle\Phi'_1\right|, \tag{3.96}$$

where $|\Phi_3\rangle$ denotes the states of $\tilde{H}_3$ and $|\Phi_1\rangle$, $\left|\Phi'_1\right\rangle$ the states of $\tilde{H}_1$.

From this equation, we can already see that at first order in $1/\bar{U}$, we will obtain $J_{1,\text{eff}} = 2e\partial_\phi H_{1,\text{eff}}/\hbar$. However, as we saw for the energy spectrum, it may be necessary to go to higher orders in $1/\bar{U}$ to properly describe the physics contained in $\mathscr{H}_{\text{odd}}$. Therefore, we will leave Eq. (3.96) as it is for now, and develop this equation at given orders when necessary.

3.4.3 Minimal ingredients for finite elements between opposite spin states

We can now study the matrix elements of $J_{1,\text{eff}}$ in more detail. We can already see that the two scenarios we covered in the previous section on the energy spectrum don't allow us to obtain finite matrix elements between opposite spin states. In those scenarios, we considered finite SOC in the couplings between the dots and the leads or in the coupling between the two dots. However, in both cases, the two spin-sectors remained decoupled because we did not include spin-flip transmission probability in the couplings. So, we can simply start by studying these two scenarios again, but this time including finite spin-flip transmission probabilities. More precisely, for the scenario studied in Sec. 3.3.1.1, we will this time consider $\check{t} = t_0 + i\boldsymbol{t}\cdot\boldsymbol{\sigma}$ and, for the scenario of Sec. 3.3.1.2 we will consider $\check{\kappa} = \kappa_0 + i\boldsymbol{\kappa}\cdot\boldsymbol{\sigma}$. Unfortunately, as we shall demonstrate, even in these cases this is not enough to have finite matrix elements between opposite spin states. In fact, as we will show below, a minimal model with spin-flip in the tunnel couplings, finite inter-dot coupling and a finite difference between the Coulomb repulsion strengths is required to have finite matrix elements between opposite spin states.

3.4.3.1 Spin-flip in the inter-dot coupling

Let's start with the case of Sec. 3.3.1.2 and include spin-flip in the inter-dot coupling $\check{\kappa} = \kappa_0 + i\boldsymbol{\kappa}\cdot\boldsymbol{\sigma}$. In this case, it is quite trivial to see that the spin states remain decoupled. We recall that the diagonalized Hamiltonians for the one and three particle states are given in Eqs. (3.47) and (3.48). Those two Hamiltonians have been diagonalized by the rotation matrices R_1 and R_3 respectively which are given in Eqs. (3.55) and (3.56). Without SOC in the tunnel couplings, the Hamiltonian $H_{\mathcal{V}}$ which couples the one and three particles states does not present any spin-structure and therefore, commute with $\rho_0\sigma_i$ with $i = x, y, z$. Therefore, the matrix $e^{-i\frac{\theta_\kappa}{2}\rho_0\sigma_z}e^{-i\frac{\gamma_\kappa}{2}\rho_0\sigma_y}$ in $R_{1/3}$ will commute with $H_{\mathcal{V}}$ and, the problem turns out to be exactly the same as if we had considered only $\check{\kappa} = \kappa_0 + i\kappa_z\sigma_z$ as in Sec. 3.3.1.2. Hence, the spin sectors remain decoupled such that it is not possible to have finite matrix elements of the current operator between opposite spin states.

3.4.3.2 Spin-flip in the parallel configuration

Let's now study the parallel configuration of Sec. 3.3.1.1 when we add spin-flip such that $\check{t} = t_0 + i\boldsymbol{t}\cdot\boldsymbol{\sigma}$. As we will see, for this scenario it is possible to find an appropriate unitary transformation independent of the superconducting phase difference ϕ, which diagonalizes the block of $\mathcal{V}$ and results in a redefinition of the spin but leaves the spin sector uncoupled. The Hamiltonians describing the one and three particles states are given in Eqs. (3.63) and (3.64). The Hamiltonian $H_{\mathcal{V}}$ which couples the one and three particle states is given by Eq. (3.49). We can write $\mathcal{V}$ in the form

$$\mathcal{V} = \begin{pmatrix} \mathcal{T}_1 & \Gamma'_1 \\ \Gamma'_2 & \mathcal{T}_2 \end{pmatrix}. \tag{3.97}$$

The off-diagonal blocks contain the terms coming from Andreev reflection and are given as $\Gamma'_j = \Gamma_{j\phi}\mathbb{1}_2$. The diagonal blocks $\mathcal{T}_{1,2}$ contain the $\tau_{\alpha\beta,\phi}$ terms and encode the spin structure of $\mathcal{V}$. These blocks can be written as $\mathcal{T}_{1,2} = \tau_0\mathbb{1}_2 \pm \boldsymbol{\tau}\cdot\boldsymbol{\sigma}$ where τ_0 and $\boldsymbol{\tau}$ are given in Eqs. (3.51)-(3.54). One can observe that they verify the relation $\mathcal{T}_1^\dagger = \eta\mathcal{T}_2\eta^{-1}$ with $\eta = i\sigma_y\mathcal{C}$. From the defintion of $\tau_{\alpha\beta,\phi}$, we can see in Eqs. (3.51)-(3.54) that the real part of τ_0 and the imaginary part of τ_i with $i = x, y, z$ are proportional to $\cos\phi/2$ while, their imaginary / real parts are proportional to $\sin\phi/2$.

We now have everything we need. The only blocks of $\mathcal{V}$ that are not diagonal in spin space are the blocks $\mathcal{T}_{1/2}$. These two blocks contain only complex terms and are not hermitian, so we cannot diagonalize them with a single unitary transformation. But, we can use the relation $\mathcal{T}_1^\dagger = \eta\mathcal{T}_2\eta^{-1}$ and diagonalize the matrices $\mathcal{T}_{1/2}^\dagger\mathcal{T}_{1/2}$ which are 2×2 hermitian matrices. Since these matrices are hermitian, we can diagonalize them by rotations around $\sigma_{x,y,z}$ which commute with η. Hence, as we now show, diagonalizing $\mathcal{T}_{1/2}^\dagger\mathcal{T}_{1/2}$ is equivalent to diagonalize $\mathcal{T}_1$ and $\mathcal{T}_2$ at the same time. These matrices are given as

$$\mathcal{T}_{1/2}^\dagger\mathcal{T}_{1/2} = \left(|\tau_0|^2 + |\boldsymbol{\tau}|^2\right)\sigma_0 \pm 2\sum_i \mathrm{Re}\left[\tau_0^*\boldsymbol{\tau}\right]\cdot\boldsymbol{\sigma} - 2\sum_{i<j}\sum_k \mathrm{Im}\left[\epsilon_{ijk}\tau_i^*\tau_j\right]\sigma_k, \tag{3.98}$$

where the sums over i or j go over x, y, z and ϵ_{ijk} is the Levi-Civita symbol.

Expanding the products of τ terms leads to a global $\sin\phi$ phase dependence for the terms proportional to σ_i with $i = x, y, z$. Thus, the rotation matrices that diagonalize these matrices won't depend on the superconducting phase difference ϕ. These rotation matrices are given as

$$W_k = e^{-i\frac{\theta_{\tau,k}}{2}\sigma_z} e^{-i\frac{\gamma_{\tau,k}}{2}\sigma_y}, \tag{3.99}$$

with $k = 1, 2$ and

$$\theta_{\tau,k} = \arctan\frac{\mathrm{Re}\left[\tau_0^*\tau_y\right] - (-1)^k\,\mathrm{Im}\left[\tau_x^*\tau_z\right]}{\mathrm{Re}\left[\tau_0^*\tau_x\right] + (-1)^k\,\mathrm{Im}\left[\tau_y^*\tau_z\right]}, \tag{3.100}$$

$$\gamma_{\tau,k} = \arctan\frac{(-1)^{k+1}\sqrt{\sum_{i=x,y}\left(\mathrm{Re}\left[\tau_0^*\tau_i\right] - \sum_{j=x,y}\mathrm{Im}\left[\epsilon_{j3i}\tau_j^*\tau_z\right]\right)^2}}{\mathrm{Re}\left[\tau_0^*\tau_z\right] + (-1)^k\,\mathrm{Im}\left[\tau_x^*\tau_y\right]}. \tag{3.101}$$

After being diagonalized, one can show that $\mathcal{T}_1^\dagger\mathcal{T}_1$ and $\mathcal{T}_2^\dagger\mathcal{T}_2$ can be written in the form

$$\begin{aligned} W_k^\dagger\mathcal{T}_k^\dagger\mathcal{T}_k W_k = &\left(|\tau_0|^2 + |\boldsymbol{\tau}|^2\right)\sigma_0 \\ &- (-1)^k 2\sqrt{\left(\mathrm{Re}\left[\tau_0^*\tau_z\right] + (-1)^k\,\mathrm{Im}\left[\tau_x^*\tau_y\right]\right)^2 + \sum_{i=x,y}\left(\mathrm{Re}\left[\tau_0^*\tau_i\right] - \sum_{j=x,y}\mathrm{Im}\left[\epsilon_{j3i}\tau_j^*\tau_z\right]\right)^2}\,\sigma_z. \end{aligned} \tag{3.102}$$

Using the relation $\mathcal{T}_1^\dagger = T\mathcal{T}_2 T^{-1}$ and $\eta\boldsymbol{\sigma}\eta^{-1} = -\boldsymbol{\sigma}$, we can easily see that

$$\mathcal{T}_{1/2}\mathcal{T}_{1/2}^\dagger = \left(|\tau_0|^2 + |\boldsymbol{\tau}|^2\right)\sigma_0 \pm 2\sum_i \mathrm{Re}\left[\tau_0^*\boldsymbol{\tau}\right]\cdot\boldsymbol{\sigma} + 2\sum_{i<j}\sum_k \mathrm{Im}\left[\epsilon_{ijk}\tau_i^*\tau_j\right]\sigma_k. \tag{3.103}$$

One can see that for $\mathcal{T}_1\mathcal{T}_1^\dagger$ the terms proportional to σ_i with $i = x, y, z$ have an opposite sign compared to $\mathcal{T}_2^\dagger\mathcal{T}_2$. The same applies to $\mathcal{T}_2\mathcal{T}_2^\dagger$ and $\mathcal{T}_1^\dagger\mathcal{T}_1$. Hence, the rotation W_2 diagonalizes $\mathcal{T}_1\mathcal{T}_1^\dagger$ while W_1 diagonalizes $\mathcal{T}_2\mathcal{T}_2^\dagger$.

The rotation matrices that diagonalize individually $\mathcal{T}_1$ and $\mathcal{T}_2$ can be found with the result we just derived. To do so, we can first remark that

$$\left(W_1^\dagger\mathcal{T}_1^\dagger\mathcal{T}_1 W_1 - W_2^\dagger\mathcal{T}_1\mathcal{T}_1^\dagger W_2\right) = 0, \tag{3.104}$$

$$\left(W_2^\dagger\mathcal{T}_2^\dagger\mathcal{T}_2 W_2 - W_1^\dagger\mathcal{T}_2\mathcal{T}_2^\dagger W_1\right) = 0. \tag{3.105}$$

It turns out that these two relationships appear in the evaluation of the commutators $\left[W_1^\dagger\mathcal{T}_1^\dagger\mathcal{T}_1 W_1,\, W_2^\dagger\mathcal{T}_1 W_1\right]$ and $\left[W_2^\dagger\mathcal{T}_2^\dagger\mathcal{T}_2 W_2,\, W_1^\dagger\mathcal{T}_2 W_2\right]$. They are given as

$$\left[W_1^\dagger\mathcal{T}_1^\dagger\mathcal{T}_1 W_1,\, W_2^\dagger\mathcal{T}_1 W_1\right] = \left(W_1^\dagger\mathcal{T}_1^\dagger\mathcal{T}_1 W_1 - W_2^\dagger\mathcal{T}_1\mathcal{T}_1^\dagger W_2\right) W_2^\dagger\mathcal{T}_1 W_1 = 0, \tag{3.106}$$

$$\left[W_2^\dagger\mathcal{T}_2^\dagger\mathcal{T}_2 W_2,\, W_1^\dagger\mathcal{T}_2 W_2\right] = \left(W_2^\dagger\mathcal{T}_2^\dagger\mathcal{T}_2 W_2 - W_1^\dagger\mathcal{T}_2\mathcal{T}_2^\dagger W_1\right) W_1^\dagger\mathcal{T}_2 W_2 = 0, \tag{3.107}$$

where we used the relation $W_k^\dagger W_k = \mathbb{1}$. These commutators being zero, it implies that $W_2^\dagger\mathcal{T}_1 W_1$ and $W_1^\dagger\mathcal{T}_1 W_2$ have only terms proportional to σ_0 and σ_z, meaning that these two matrices are diagonal.

What we have shown here is that, with an appropriate unitarity transformation that is independent of the superconducting phase difference ϕ, it is possible to diagonalize $\mathcal{T}_j$ which results in a redefinition of the spin of our states but leaves the two spin sector uncoupled. Hence, even in this case where we have spin-flip transmission in the tunnel couplings between the dots and the leads, it is not enough to have finite matrix elements of the current operator between opposite spin states. This results, as for the previous scenario with $\check{\kappa} = \kappa_0 + i\boldsymbol{\kappa}\cdot\boldsymbol{\sigma}$ is valid at all orders in $1/\bar{U}$.

3.4.3.3 Minimal model for finite matrix elements between opposite spin states

In fact, to have finite matrix elements of the current operator between opposite spin states, it is necessary to have a ϕ dependent unitary transformation such that it is not possible to diagonalize all the blocks of $\tilde{\mathcal{V}}$ at the same time. A minimal model for which it is possible to have finite matrix elements between opposite spin states involves at least spin-dependent tunnel couplings $\check{t} = t_0 + i\boldsymbol{t}\cdot\boldsymbol{\sigma}$, a finite inter-dot coupling of the form $\check{\kappa} = \kappa_0$ and, a finite difference $\delta U \neq 0$ between the Coulomb repulsion strengths of the two dots. The last two conditions come from the diagonalization of the Hamiltonians describing states with one and three electrons on the dots. The rotation matrices that diagonalize these Hamiltonians are in this case

$$R_{1/3} = \exp\left[-i\frac{\beta_{1/3}}{2}\rho_y\sigma_0\right], \tag{3.108}$$

with

$$\beta_1 = \arctan\frac{2\kappa_0}{\delta\varepsilon}, \tag{3.109}$$

$$\beta_3 = \arctan\frac{-2\kappa_0}{\delta\varepsilon + \delta U}. \tag{3.110}$$

The dependence in ρ_y in $R_{1/3}$ allows one to couple the different blocks $\mathcal{T}_{1/2}$ and $\Gamma'_{1/2}$ of $\mathcal{V}$. However, in the particular case of $\delta U = 0$, then, $\beta_3 = -\beta_1$ and one can show that this will lead to a $\tilde{\mathcal{V}}$ with spin-dependent diagonal blocks and spin-independent off-diagonal blocks, analogous to the study we've done in the previous section. In this case, another ϕ-independent unitary transformation diagonalizing the diagonal block of $\tilde{\mathcal{V}}$ leaving the spin sectors decoupled can be found. This result can even be extended to a more complex inter-dot coupling which is spin-dependent of the form $\check{\kappa} = \kappa_0 + i\boldsymbol{\kappa}\cdot\sigma$. As can be seen in Eq. (3.57) and Eq. (3.58), it is mandatory to have $\delta U \neq 0$. This condition implies that developing Eq. (3.96) at first order in $1/\bar{U}$ is not sufficient in order to have finite matrix elements between opposite spin in the effective model.

We will not go further into details in this section. Instead, in the next section we will look at the characteristics of the matrix elements of the current operator, in particular, we will study the matrix elements between states within the same doublet. To do so, we will use numerical results obtained from the diagonalization of Eq. (3.43) to determine the typical ϕ dependence of these matrix elements and which parameters fix their amplitude.

3.4.4 Numerical results

We will now qualitatively characterize the matrix elements of the current operator. Especially, we want to find the dependence of the matrix element between states of the lowest energy doublets on the parameters of the system such as the superconducting phase difference ϕ, or, the Coulomb repulsion strength $\bar{U}$. We will use numerical results obtained by projecting J_{eff} which we defined in Eq. (3.95) into the eigenbasis of Eq. (3.43) which we have diagonalized numerically, such that the only approximation made here is the superconducting atomic limit $\Delta \to \infty$.

Figure 3.12 shows a typical energy spectrum and the matrix elements of the current operator between states of the lowest energy doublet. These curves are obtained for a regime in which this doublet of states constitutes the ground states of the junction. We considered a junction with strong Coulomb repulsion strength $\varepsilon_j, \check{\kappa}, \check{t}\,\delta U \ll \bar{U}$. The inter-dot coupling does not present SOC and is set to $\kappa_0/\bar{U} = 10^{-2}$. The on-site energies are set to $\varepsilon_1/\bar{U} = -1 \times 10^{-2}$ and $\varepsilon_2/\bar{U} = 5 \times 10^{-3}$ with different Coulomb repulsion strength given by $\delta U/\bar{U} = 5 \times 10^{-2}$. Finally, we consider spin-dependent tunnel couplings between the dots and the superconducting leads such that $\check{t} = t_0 + i\boldsymbol{t}\cdot\boldsymbol{\sigma}$. The values for the couplings are resumed in Tab. 3.1. A typical $\sin\phi$ splitting can be seen in the energy spectrum, characteristic of the regime $\sqrt{(\delta\varepsilon/2)^2 + \kappa_0^2} \gg |(\tilde{H}_{\mathcal{V},\mathrm{eff}})_{ij}|$. We normalized the matrix element of the current operator $|J_{\varepsilon_{-\downarrow}\to\varepsilon_{-\uparrow}}|$ by $J_0 = e\bar{U}/\hbar$. The latter shows a phase dependence resembling a $\sin^2\phi$ can be seen. According to the parameters we took, the maximum amplitude seems to be limited by the cube of the Coulomb repulsion strength. To characterize more precisely the dependence of $|J_{\varepsilon_{-\downarrow}\to\varepsilon_{-\uparrow}}|$ on parameters other than the phase ϕ, we looked at the maximum amplitude of $|J_{\varepsilon_{-\downarrow}\to\varepsilon_{-\uparrow}}|/J_0$ with $J_0 = e\bar{U}/\hbar$ versus the Coulomb repulsion strength $\bar{U}$, the difference between the Coulomb repulsion strength δU and the inter-dot coupling κ_0 in Fig. 3.13. In this figure, a dependence on $\bar{U}^4$ is highlighted in panel (a) with a fit in open dots given by $\alpha\delta U/\bar{U}^4$, where α depends on the values of other parameters such as $\check{t}$ and κ_0. Here, $\alpha = 0.09$. This fit also indicates a linear dependence on δU, corroborating what can be seen on panel (b). Finally, for the dependence with κ_0, the maximum amplitude first increases with κ_0 until it reaches a maximum. This dependence can be understood from the definition of β_1 and β_3 which are used to diagonalize the Hamiltonians describing one and three particle states. They are given by Eqs. (3.109) and (3.110). As κ_0 increases, we tend to have $\beta_3 \to -\beta_1$, and as we discussed in the previous section, in this case we cannot have finite matrix elements of the current operator between opposite spin states. Finally, Fig. 3.14 shows different matrix elements of the current operator. However, note that the parameters used for this figure do not allow one to have a doublet ground state and were chosen for visibility. The parameters are $\delta U/\bar{U} = 5\times 10^{-2}$,

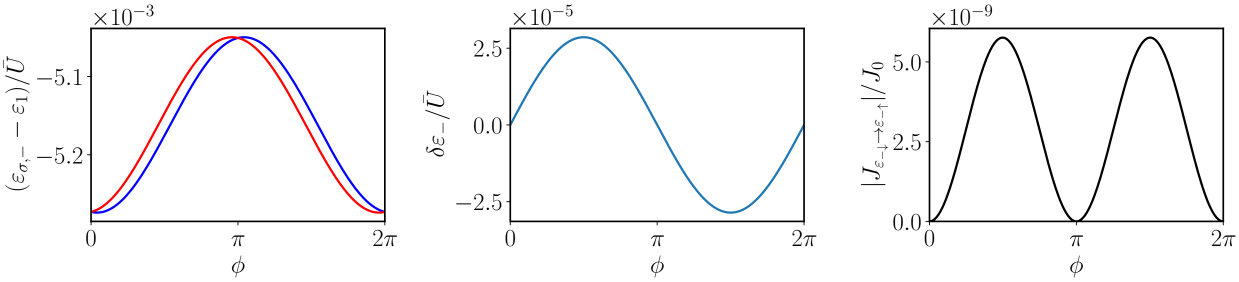

Figure 3.12: Energy spectrum (left) and off-diagonal matrix element of the current operator (right) for the lowest energy doublet ε_-. The parameters are $\varepsilon_1/\bar{U} = -1 \times 10^{-2}$, $\varepsilon_2/\bar{U} = 5 \times 10^{-3}$, $\delta U/\bar{U} = 5 \times 10^{-2}$ and $\kappa_0/\bar{U} = 10^{-2}$. The values of the tunnel couplings are given in Tab. 3.1. A $\sin\phi$ splitting can be seen in the energy spectrum in the middle panel, characteristic of the regime $\sqrt{(\delta\varepsilon/2)^2 + \kappa_0^2} \gg |(\tilde{H}_{\mathcal{V},\mathrm{eff}})_{ij}|$. The matrix element of the current operator is normalized by $J_0 = e\bar{U}/\hbar$, and its amplitude seems to be limited by $\bar{U}^3$. The latter shows a phase dependence resembling a $\sin^2\phi$.

	$t_0/\bar{U}$	$t_x/\bar{U}$	$t_y/\bar{U}$	$t_z/\bar{U}$
$\check{t}_{L1}$	5×10^{-3}	10^{-3}	1.5×10^{-3}	10^{-3}
$\check{t}_{R1}$	10^{-2}	5×10^{-4}	5×10^{-4}	5×10^{-4}
$\check{t}_{L2}$	10^{-3}	10^{-3}	1.5×10^{-3}	10^{-3}
$\check{t}_{R2}$	5×10^{-4}	10^{-3}	2.5×10^{-3}	5×10^{-4}

Table 3.1: Values of the tunnel couplings used for Fig. 3.12

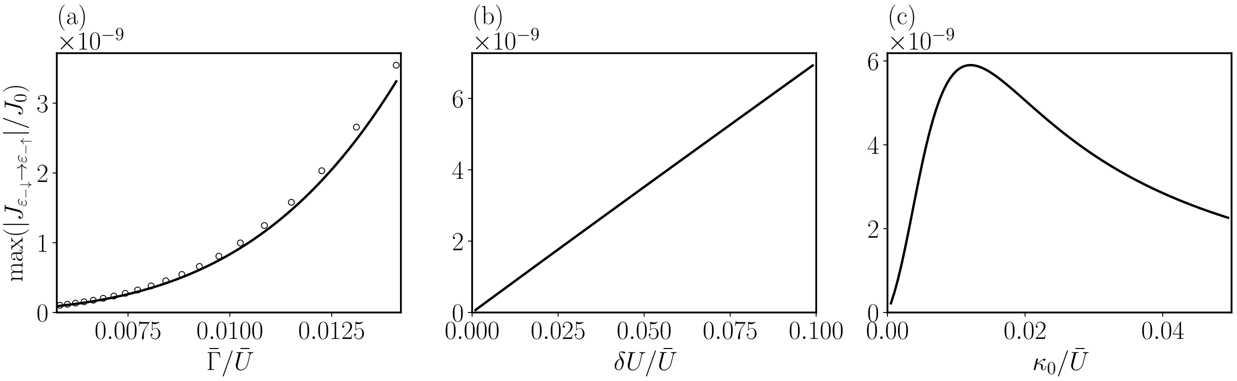

Figure 3.13: Maximum amplitude of $J_{\varepsilon_{-\downarrow}\to\varepsilon_{-\uparrow}}$ versus $\bar{\Gamma}/\bar{U}$ with fixed $\bar{\Gamma}=(\Gamma_1+\Gamma_2)/2$ (panel (a)), $\delta U/\bar{U}$ with $\bar{U}$ fixed (panel (b)) and, $\kappa_0/\bar{U}$ with $\bar{U}$ fixed (panel (c)). With panels (a) and (b), we can see a linear dependence on δU and a cubic dependence of $|J_{\varepsilon_{-,\downarrow}\to\varepsilon_{-,\uparrow}}|$ on $1/\bar{U}$. When being fixed, the parameters are $\delta U/\bar{U}=5\times10^{-2}$, $\kappa_0/\bar{U}=10^{-2}$ and $\bar{\Gamma}/\bar{U}=1.43\times10^{-2}$. The tunnel couplings are given in Tab. 3.1. We used this result to fit the curve of panel (a) with $\alpha\delta U/\bar{U}^4$ where α depends on the values of other parameters such as $\check{t}$ and κ_0, and is here set to $\alpha=0.09$. The dependence on κ_0 shows a global maximum which is explained in the main text.

$\varepsilon_1/\bar{U}=-7.5\times10^{-3}$ and $\varepsilon_2/\bar{U}=-2.5\times10^{-3}$. $\kappa_0/\bar{U}$ is set to $\kappa_0/\bar{U}=1\times10^{-3}$ while the tunnel couplings are given in Tab. 3.2. The main point in this figure is that the matrix element between states of the same spin (in purple) has a qualitatively higher amplitude than the ones between opposite spin states (black and green). Also, compared to the phase dependence of the intra-doublet element, the phase dependence of $J_{\varepsilon_{-\downarrow}\to\varepsilon_{+\uparrow}}$ and $J_{\varepsilon_{-\downarrow}\to\varepsilon_{+\downarrow}}$ looks more complicated.

	$t_0/\bar{U}$	$t_x/\bar{U}$	$t_y/\bar{U}$	$t_z/\bar{U}$
$\check{t}_{L1}$	1×10^{-3}	6×10^{-3}	2×10^{-3}	7×10^{-3}
$\check{t}_{R1}$	9×10^{-3}	4×10^{-3}	2×10^{-3}	3×10^{-3}
$\check{t}_{L2}$	2×10^{-3}	3×10^{-3}	5×10^{-3}	1×10^{-3}
$\check{t}_{R2}$	7×10^{-3}	3×10^{-3}	7×10^{-3}	4×10^{-3}

Table 3.2: Values of the tunnel couplings used for Fig. 3.14

All of these results indicate that in order to characterize more precisely the matrix elements of the current operator with analytical results, it is necessary to develop Eq. (3.96) to the third order in $1/\bar{U}$. This means that one needs to go to a higher order when performing the Schrieffer-Wolff transformation. However, the linear dependence with δU shows that developing Eq. (3.96) to the third order in $1/\bar{U}$ may be sufficient, as the spin-flip matrix element goes to zero when $\delta U=0$. In order to further simplify the problem, an effective model describing only the lowest energy doublet could be considered.

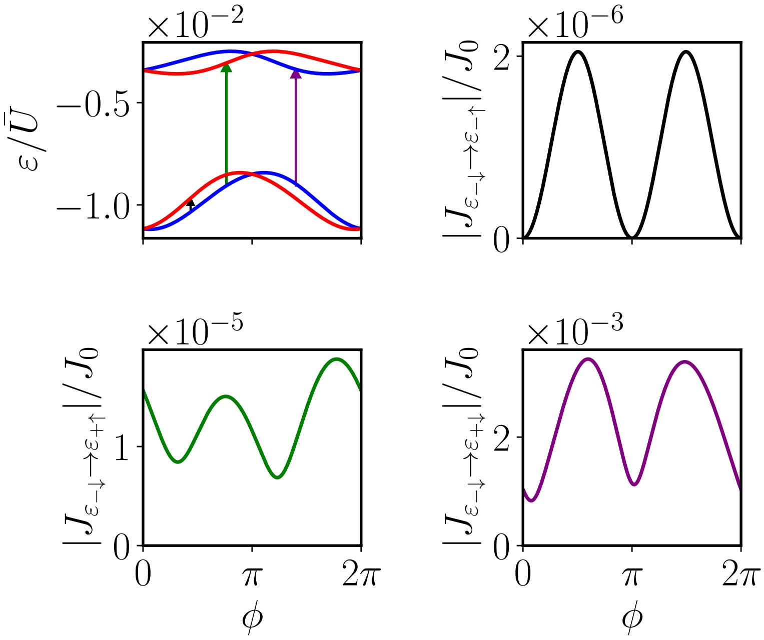

Figure 3.14: Energy spectrum for the single particle states and some matrix elements of the current operator associated with the arrows depicted in the energy spectrum. The spin-conserving transition shows a qualitatively greater amplitude than the spin-flip ones. Additionally, the phase dependence of $|J_{\varepsilon_{-\downarrow}\to\varepsilon_{+\uparrow}}|$ and $|J_{\varepsilon_{-\downarrow}\to\varepsilon_{+\downarrow}}|$ looks more complicated than for the intra-doublet transition.

3.5 Conclusion

In this chapter, we have studied a Josephson junction in which the normal region is constituted by two quantum dots. We showed that in this kind of Josephson junction, the spin degeneracy can be lifted thanks to SOC in the tunnel couplings between the quantum dots and the superconducting leads, and/or, in the inter-dot coupling. Using an effective model describing the one particle states, we have characterized the resulting spin-splitting in parameter regimes in which a doublet ground state with one electron occupying the dots is favored. In particular, we showed that when the on-site energy difference between the two dots is sufficiently high, this splitting shows a $\sin\phi$ dependence. Finally, we found the minimal required ingredients to have finite matrix elements of the current operator between opposite spin states. Thanks to numerical results, we showed that the intra-doublet elements present a $\sin^2\phi$ for parameters that allow one to have a doublet ground state. Its maximum amplitude seems to be limited by the cube of the Coulomb repulsion strength and requires to have at least, a finite inter-dot coupling, spin-dependent tunnel couplings with spin-flip transmission and a difference between the Coulomb repulsion strengths of the two dots. These results indicate that analytical results could be obtained by developing Eq. (3.96) to the third order in $1/\bar{U}$. Also, a simpler effective model describing only the lowest energy doublet could be considered.

Conclusion and perspectives

The work presented in this thesis focused on the theoretical study of Andreev bound states in Josephson junctions with spin-orbit coupling. This research was motivated by the opportunity to realize an Andreev spin qubit using the spin of Andreev bound states. A key result of this thesis is that the concomittance of spin-split ABS, and spin-flip scattering processes due to the presence of a generic scatterer or electrostatic gates, allows for non-vanishing current operator matrix elements between ABS of opposite spin. This result indicates that the direct manipulation of a phase-driven Andreev spin qubit should be possible. Two types of Josephson junctions which could be promising platforms for the realization of such qubits were studied in this thesis in chapter 2 and chapter 3.

Chapter 2 focuses on the study of a superconductor-normal-superconductor junction, in which the normal region consists of a nanowire with Rashba SOC. We first show how spin-orbit coupling allows lifting the spin degeneracy of ABS. A finite spin-splitting can be obtained when at least three ingredients are present. The first one is an asymmetry of the velocities in opposite pseudo-spin bands in the nanowire, which is possible thanks to the concomitance of SOC and a finite transverse width of the nanowire. The second ingredient is a finite length of the nanowire. Finally, a finite superconducting phase difference that differs from the effective time-reversal invariant values 0 and π is needed. When these requirements are fulfilled, the spin-splitting is only limited by the minimum of the superconducting gap in the superconducting leads for short junctions and the inverse of the dwell time in the normal region for long junctions. In this chapter, we consider a scattering center located along the nanowire, responsible for inducing spin-flip transmission probability. Unless the system possesses additional symmetries, such scattering is generally present. We first study the effect of SOC and spin-flip transmission probabilities on the energy spectrum of ABS. We then turn to the evaluation of the matrix elements of the current operator. We show that generic scattering potentials, such as the one we consider, yield non-vanishing matrix elements for all possible transitions, including the intra-doublet spin-flip transitions, in the absence of a magnetic field. The amplitude of the matrix element for intra-doublet spin-flip transitions is controlled by the spin-splitting of the spectrum and the presence of spin-flip scattering in the junction. Our findings indicate that the strong driving of the ASQ can be reached in a Josephson junction made with a nanowire of intermediate length (on the scale of the superconducting coherence length), provided that spin-orbit coupling (characterized by the relative asymmetry of the Fermi velocities in each of the pseudo-spin bands intercepting the Fermi level) is strong.

In the nanowire-based Josephson junctions that we investigated, we ignored the effect of Coulomb interaction. Thereby, the Andreev spin qubit resides above the even ground state, and it requires a quasiparticle to “poison” the junction [33, 112] in order to be realized. Recent experiments with quantum dots subject to large Coulomb repulsion allowed stabilizing the doublet ground state in the odd sector, as well as resolving the spin splitting [48, 95, 111].

Hence, in our second project presented in Chapter 3, we study a superconductor-double quantum dots-superconductor junction. In this chapter, we first show why one quantum dot with a single level is insufficient to lift the spin degeneracy. Introducing a second quantum dot in the normal region allows for having an additional channel for electrons to flow, thus resembling the model presented in [95]. However, our system presents the advantage of offering more control over on-site energy and Coulomb repulsion for each dot. By using an effective model, we are able to determine and characterize the minimal set of ingredients to lift the spin degeneracy in the superconducting atomic limit $\Delta \to \infty$. Our study reveals that a finite spin-splitting can be obtained when the tunnel or inter-dot couplings are spin-dependent and preserve TRS. Such couplings can for instance be obtained with quantum dots realized with InAs nanowires and electrostatic gates. The resulting spin-splitting is reduced by the Coulomb repulsion strength and requires non-identical tunnel couplings between the left and right leads and the two dots. As for our study of the Josephson junction with the Rashba nanowire, we then proceed to the study of the current operator matrix elements. We are able to show that finite matrix elements between opposite spin states are possible within the framework of a minimal model. This model involves a finite coupling between the two dots, spin-dependent tunnel couplings between the leads and the dots, and a finite Coulomb repulsion strength difference between the two dots. Thanks to numerical results, we are able to characterize the dependence of the intra-doublet spin-flip elements on the system parameters. In a regime of parameters that favor a doublet ground state with one electron occupying one of the two dots, our results indicate a typical $\sin^2 \phi$ phase dependence. The amplitude of these matrix elements seems to be limited by the inverse of the cube of the Coulomb repulsion strength and shows a linear dependence with the Coulomb repulsion strength difference between the two dots when the latter is small compared to the mean of the two.

In the future, some questions need to be addressed. One of them is on what factor the phase profile along the junction we discussed in Chap. 2 depends on when the system is driven. Answering this question would involve the evaluation of the AC profile of the drive along the junction. One might expect this phase profile to be mostly influenced by the electrostatic profile of the weak link such that for instance the phase drop would occur at the normal - superconductor interfaces, the scattering center or a mix of both. Experimental work on the S-DQD-S junction depicted in Chap. 3 is also needed to show the viability of this platform for the realization of ASQ. For the nanowire Josephson junction, a better understanding of the poisoning mechanism is required as it limits the maximum time during which the qubit can be manipulated. Answering these questions will help to find the best platform for the realization of such qubits. Additionally, the coupling of multiple Andreev spin qubits as well as with other kinds of qubits will have to be studied. Also, the experimental realization of these qubits shows a coherence time of only a few nanoseconds and seems to be limited by the spinful nuclear bath of the indium arsenide used for the normal region. As pointed out in [48], the use of nuclear-spin-free semiconductors like Silicon-28 or isotopically purified germanium could be envisaged as alternative platforms for the realizations of ASQ. Hence, this point should be improved in the future.

The systems studied in this thesis could also be of interest for other realizations besides Andreev spin qubits. In particular, with the addition of an external magnetic field, for instance, it would become possible to obtain a spin-polarized ground state allowing for the possibility to realize a φ_0-Josephson junction. These junctions present the property to show a finite supercurrent at zero superconducting phase difference [39, 128, 129]. Spin-split ABS energy levels present a finite slope with the phase at zero phase difference. And, the current flowing in the junction is given by the derivative of the energy of the occupied ABS with respect to the phase. Thus, a spin-polarized ground state will lead to a non-zero supercurrent at zero superconducting phase difference. These systems could also be of interest for the study of the superconducting diode effect, an effect characterized by different magnitudes of the critical supercurrents flowing in opposite directions [129–131]. Such junctions can be realized when both time reversal and inversion symmetry are broken [132]. In analogy with the role of a semiconducting diode, which is one of the building blocks of our actual digital technologies, superconducting diodes may form building blocks for dissipationless digital technologies. In the same spirit, the so-called Andreev molecules could be studied [133, 134]. The latter can occur when two weak links of a Josephson junction are within a coherence length from each other. If that's the case then, their ABS will become coupled such that the current flowing in one weak link would be dependent on the phase difference of the other, allowing to realize φ_0-Josephon junctions. For instance, one could imagine using this interaction between the two weak links to couple two ASQ [111]. Finally, with sufficiently large magnetic fields, it would become possible to enter into the topological regime and explore the physics of Majorana bound states [34–36, 135]. These particular bound states which occur at zero energy would be robust against local noise or perturbations due to their topological protection making them an excellent candidate for the realization of low-error qubits.

APPENDIX **A**

Time reversal symmetry

Most systems are asymmetric when we reverse the direction of time, such that we can distinguish whether the time of a movie is running forward or backward. However, when dissipation is removed, the laws of mechanics are time reversal invariant. In this appendix, we will mainly follow the PhD thesis of Jens Hjörleifur Bárðarson [136]. In 1930, while studying the Schrödinger equation, H. A. Kramers discovered a mapping Θ. This mapping when appled to a solution $\left|\psi\right\rangle$ with energy E produces another solution $\Theta\left|\psi\right\rangle$ with the same energy [137]. In cases involving an odd number of spin 1/2 particles, these solutions are orthogonal, introducing a degeneracy in the spectrum known as Kramers degeneracy. Wigner showed that the transformation discovered by Kramers is time reversal, and the degeneracy reflects the existence of time reversal symmetry [138]. Besides causing the Kramers degeneracy of energy eigenvalues, the presence of time reversal also enforces a symmetry on the Hamiltonians and scattering matrices.

According to a theorem of Wigner [139], symmetries can be represented by two types of operators. The first ones are unitary and linear operators. The symmetries described by these operators lead to the conservation of quantities. For instance, translational symmetry conserves momentum, and rotational symmetry conserves angular momentum. The other types of operators are antiunitary and antilinear operators. The symmetries they are describing generally do not conserve quantities. Their effect is thus more nuanced as evidenced by the Kramers degeneracy due to time reversal symmetry. However, these symmetries are equally crucial as the unitary ones.

We will begin by a short review on antiunitary operators, followed by an explanation and derivation of the time reversal symmetry operator and its consequences for scattering matrices.

A.1 Antiunitary operators

Let's start by discussing the properties of antilinear and antiunitary operators. An operator Θ is said to be antilinear if for any states $\left|\phi\right\rangle$, $\left|\psi\right\rangle$ and for any complex numbers α and β, it satisfies the following relation

$$\Theta\left(\alpha\left|\phi\right\rangle+\beta\left|\psi\right\rangle\right)=\alpha^{*}\Theta\left|\phi\right\rangle+\beta^{*}\Theta\left|\psi\right\rangle. \tag{A.1}$$

Furthermore, if this operator satisfies the relation

$$\left|\left\langle\phi\middle|\psi\right\rangle\right|=\left|\left\langle\Theta\phi\middle|\Theta\psi\right\rangle\right|, \tag{A.2}$$

then, this operator is an antiunitary operator. This property can be written as

$$\left\langle\Theta\phi\middle|\Theta\psi\right\rangle=\left\langle\phi\middle|\psi\right\rangle^{*}. \tag{A.3}$$

The simplest operator that verifies these conditions is the complex conjugation operator $\mathcal{C}$ and it satisfies

$$\mathcal{C}\,|n\rangle = |n\rangle\,, \qquad \mathcal{C}^2 = 1, \tag{A.4}$$

where $|n\rangle$ is a state in an orthogonal basis which we denote as $\{|n\rangle\}$. The action of this operator on a state $\left|\psi\right\rangle = \sum_n c_n\,|n\rangle$ can thus be written as

$$\mathcal{C}\left|\psi\right\rangle = \sum_n c_n^*\,|n\rangle\,. \tag{A.5}$$

Another property is that a product of an antiunitary and unitary operator is again antiunitary while the product of two antiunitary operators is unitary. Therefore, any antiunitary operator Θ can be written as a product of a unitary operator U and the complex conjugation operator $\mathcal{C}$.

A.2 Time reversal symmetry operator

With this mathematical background, we can turn our attention to the study of the time reversal operator. As it will be shown here, this operator needs to be antiunitary. The effect that it should have on the physics of the system is that it needs to reverse the momentum of a particle while it keeps its position unchanged. We can describe the evolution of state $\left|\psi(t)\right\rangle$ to the state $\left|\psi(t')\right\rangle$ with the time evolution operator $U(t,t') = \exp[-iH(t'-t)/\hbar]$. If we apply the time reversal operator on the state $\left|\psi(t_0)\right\rangle$, it should reverse its motion such that, if the system is time reversal symmetric, then

$$U(t_0, t_0+\delta t_0)\Theta\left|\psi\right\rangle = \Theta U(t_0, t_0-\delta t_0)\left|\psi\right\rangle, \tag{A.6}$$

which can be understood as follows. If the system is time reversal symmetric, it is equivalent to first reversing the motion then evolving forward in time or to first evolving backward in time and then reversing the motion. In particular, if δt is small, we can write

$$(1 - iH\delta t/\hbar)\Theta = \Theta(1 + iH\delta t/\hbar). \tag{A.7}$$

If Θ is taken to be a linear operator such that $\Theta H = -H\Theta$, it would mean that, for any energy eigenvalue E, it would exist a state with an energy eigenvalue $-E$ which is a nonsensical result and implies that H is not bounded from below. A basic example is free electrons. The latter has a strictly positive energy spectrum. Therefore, we have to take Θ as an antiunitary operator verifying $[\Theta, H] = 0$.

A.2.1 Spinless system

For a spinless system, the complex conjugation operator $\mathcal{C}$ fulfills all the requirements that we have for the time reversal operator Θ with respect to the position basis $\{|x\rangle\}$. We can see this on a general state vector $\left|\psi\right\rangle$:

$$\mathcal{C}\hat{x}\left|\psi\right\rangle = \mathcal{C}\int \mathrm{d}x\,\hat{x}\psi(x)|x\rangle = \int \mathrm{d}x\,\hat{x}\psi^*(x)|x\rangle = \hat{x}\mathcal{C}\left|\psi\right\rangle, \tag{A.8}$$

$$\mathcal{C}\hat{p}\left|\psi\right\rangle = \mathcal{C}\int \mathrm{d}x\left(-i\hbar\frac{\partial}{\partial x}\right)\psi(x)|x\rangle = \int \mathrm{d}x\left(i\hbar\frac{\partial}{\partial x}\psi^*(x)\right)|x\rangle = -\hat{p}\mathcal{C}\left|\psi\right\rangle. \tag{A.9}$$

These relations are valid for any $\left|\psi\right\rangle$. Thus, the operators need to satisfy

$$\mathcal{C}\hat{x}\mathcal{C}^{-1} = \hat{x}, \tag{A.10}$$

$$\mathcal{C}\hat{p}\mathcal{C}^{-1} = -\hat{p}, \tag{A.11}$$

which is exactly what we want for the time reversal operator, thus $\Theta = \mathcal{C}$.

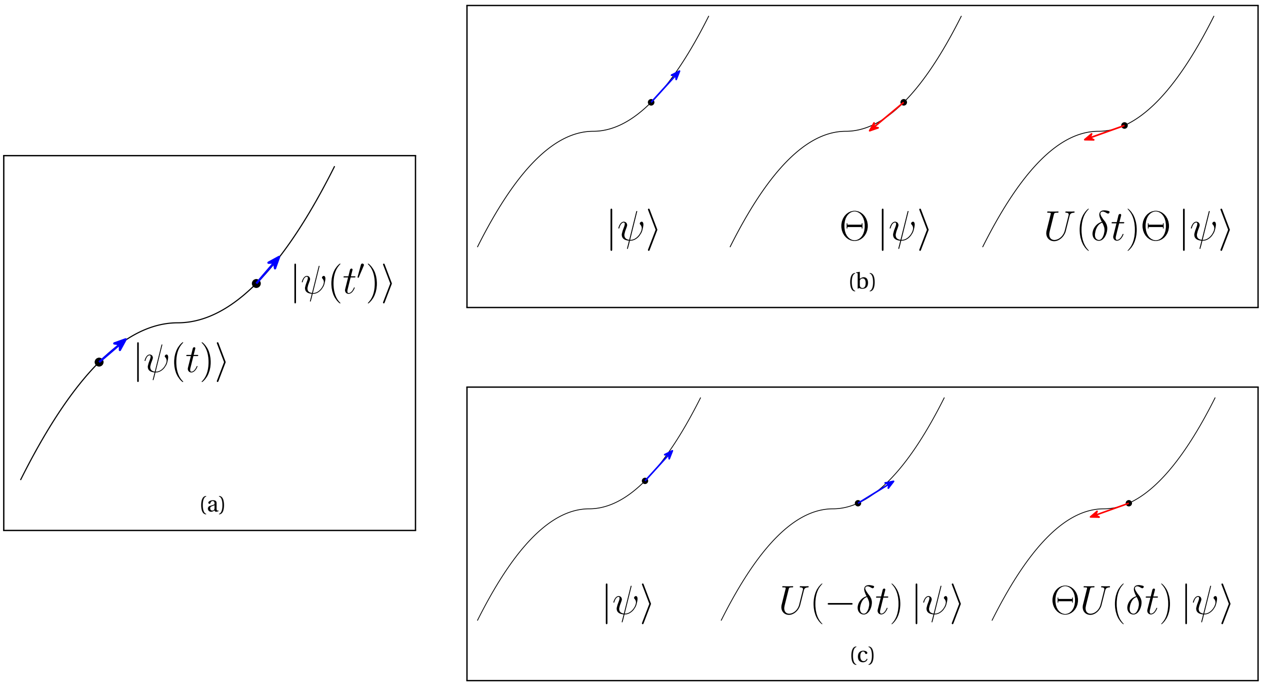

Figure 1.1: Representation of the time evolution of a state $|\psi\rangle$ in panel (a). In a time reversal symmetric system, reversing the motion and evolving forward in time as represented in panel (b) is equivalent to evolving backward in time and then reversing the motion as represented in panel (c). This figure has been taken from [136].

A.2.2 Spin $1/2$ system

In general, the time reversal operator needs to reverse all the momenta. However, we can see that the time reversal operator that we defined for a spinless case does not work for spin $1/2$ particles. In particular, its action on the Pauli matrices which describe the spin of particles is,

$$\mathcal{C}\sigma_x\mathcal{C}^{-1} = \sigma_x, \tag{A.12}$$

$$\mathcal{C}\sigma_y\mathcal{C}^{-1} = -\sigma_y, \tag{A.13}$$

$$\mathcal{C}\sigma_z\mathcal{C}^{-1} = \sigma_z, \tag{A.14}$$

and we need to have an operator such that $\Theta\boldsymbol{\sigma}\Theta^{-1} = -\boldsymbol{\sigma}$ as we want it to reverse momentum and spin. Thus, we want to write the time reversal operator as $\Theta = U\mathcal{C}$ with $U \neq \mathbb{1}$ because complex conjugation is not enough by itself. However, we can see that $\mathcal{C}$ is sufficient to reverse σ_y. Therefore, we want an operator U which commutes with σ_y and anticommutes with σ_x and σ_z. It turns out that this is one of the properties of σ_y. Hence, we can define

$$\Theta = i\sigma_y\mathcal{C}, \tag{A.15}$$

where we have put an accompanying phase i such that the unitary operator is real. This reasoning can be extended to particles of any spin. By denoting the matrices in the three directions for these particles as $S_{x,y,z}$ that are proportional to the Pauli matrices, we need to construct an operator that must anticommute with $S_{x,z}$ and commute with S_y. This corresponds to a rotation of π around the y axis, which can be written as

$$\Theta = e^{i\pi S_y/\hbar}\mathcal{C}. \tag{A.16}$$

From this relation, one can easily recover Eq. (A.15) by taking $S_y = \frac{\hbar}{2}\sigma_y$ so that

$$\Theta = e^{i\frac{\pi}{2}\sigma_y}\mathcal{C} = i\sigma_y\mathcal{C}. \tag{A.17}$$

One property of the operator defined in Eq. (A.15) is that its square value depends on the spin of the particle such that

$$\Theta^2 = \begin{cases} 1 & \text{for integer spin particles,} \\ -1 & \text{for spin-half particles.} \end{cases} \tag{A.18}$$

A.2.3 Consequences of time reversal symmetry (TRS) on scattering matrix

The scattering matrix links the amplitude of ingoing and outgoing states in the following way,

$$\psi_{\text{out}} = \mathcal{S}\psi_{\text{in}}. \tag{A.19}$$

The scattering matrix $\mathcal{S}$ being unitary, we can also write

$$\psi_{\text{in}} = \mathcal{S}^{\dagger}\psi_{\text{out}}. \tag{A.20}$$

Now, if we consider that the system we study is time reversal symmetric, it means that the time reversed states described by the scattering matrix are also solutions of the Hamiltonian and should be described by the same scattering matrix. Thus, we can write

$$\Theta\psi_{\text{in}} = \mathcal{S}\Theta\psi_{\text{out}}. \tag{A.21}$$

By using the property of the scattering matrix $\mathcal{S}$ and of Θ, we can write

$$\psi_{\text{in}} = \Theta^{-1}\mathcal{S}\Theta\psi_{\text{out}} = \mathcal{S}^{\dagger}\psi_{\text{out}}. \tag{A.22}$$

Thus, we can see that if the system is time reversal symmetric, the scattering matrix $\mathcal{S}$ must verify the condition

$$\mathcal{S} = \Theta\mathcal{S}^{\dagger}\Theta^{-1}. \tag{A.23}$$

So that $\mathcal{S} = \mathcal{S}^T$ for spinless particles and $\mathcal{S} = \sigma_y\mathcal{S}^T\sigma_y$ for spinfull particles.

Appendix B

Diagonalization of $M(E,\phi)$

To find the solutions of Eq. (1.133) for the Rashba nanowire Josephson junction studied in Chap. 2, we will diagonalize the matrix $M(E,\phi)$ in this appendix. We can write this matrix as

$$M(E,\phi) = e^{i\xi(E)-i\xi(-E)} \begin{pmatrix} A & -B^{\dagger} \\ B & D \end{pmatrix}, \tag{B.1}$$

where

$$A = \mathcal{R}^{\dagger}(-E)\mathcal{R}(E) + \mathcal{T}^{\dagger}(-E)\mathcal{T}(E)e^{-i\phi}, \tag{B.2}$$

$$D = \mathcal{R}(-E)\mathcal{R}^{\dagger}(E) + \mathcal{T}(-E)\mathcal{T}^{\dagger}(E)e^{i\phi}, \tag{B.3}$$

$$B = \mathcal{R}(-E)\mathcal{T}(E) - \mathcal{T}(-E)\mathcal{R}(E)e^{i\phi}, \tag{B.4}$$

and

$$\mathcal{R}(E) = r(E)\mathbb{1}_2, \qquad \mathcal{T}(E) = \begin{pmatrix} t(E) & s^*(E) \\ s(E) & -t^*(E) \end{pmatrix}. \tag{B.5}$$

As one can see, putting no backscattering simplifies a lot the problem as the block B goes to zero. In this case, the problem reduces to the diagonalization of the 2×2 matrices corresponding to the blocks A and D. Thus, we will start by diagonalizing these blocks, and then, we will care about the block B. Let's start with block A. It can be written in the form

$$\begin{aligned} A &= \begin{pmatrix} \alpha_A + \beta_A e^{-i\phi} & -\delta_A^* e^{-i\phi} \\ \delta_A e^{-i\phi} & \alpha_A + \beta_A^* e^{-i\phi} \end{pmatrix} \\ &= \alpha_A \sigma_0 + \left\{ \mathrm{Re}\left[\beta_A\right]\sigma_0 + i\left(\mathrm{Im}\left[\beta_A\right]\sigma_z + \mathrm{Im}[\delta_A]\sigma_x - \mathrm{Re}[\delta_A]\sigma_y\right)\right\} e^{-i\phi}, \end{aligned} \tag{B.6}$$

with

$$\alpha_A = r^*(-E)r(E), \qquad \beta_A = t^*(-E)t(E) + s^*(-E)s(E), \qquad \delta_A = s(-E)t(E) - t(-E)s(E). \tag{B.7}$$

This matrix can be easily diagonalized by the following rotation

$$W_A = e^{-i\frac{\theta_A}{2}\sigma_z} e^{-i\frac{\gamma_A}{2}\sigma_y} = \begin{pmatrix} \cos\frac{\gamma_A}{2} e^{-i\frac{\theta_A}{2}} & -\sin\frac{\gamma_A}{2} e^{-i\frac{\theta_A}{2}} \\ \sin\frac{\gamma_A}{2} e^{i\frac{\theta_A}{2}} & \cos\frac{\gamma_A}{2} e^{i\frac{\theta_A}{2}}, \end{pmatrix} \tag{B.8}$$

where

$$\gamma_A = \arctan\frac{|\delta_A|}{\mathrm{Im}\left[\beta_A\right]}, \qquad \theta_A = \arctan\frac{-\mathrm{Re}[\delta_A]}{\mathrm{Im}[\delta_A]} = \varphi_A - \frac{\pi}{2}, \tag{B.9}$$

with $\delta_A = |\delta_A|\, e^{i\varphi_A}$. We will denote this matrix in the rotated basis as $\tilde{A}$ which reads

$$\tilde{A} = \alpha_A\sigma_0 + \mathrm{Re}\left[\beta_A\right] e^{-i\phi}\sigma_0 + i\sqrt{\mathrm{Im}\left[\beta_A\right]^2 + |\delta_A|^2} e^{-i\phi}\sigma_z. \tag{B.10}$$

We can now do the same for the block D. We write this block under the form

$$D = \alpha_D\sigma_0 + \left\{\mathrm{Re}\left[\beta_D\right]\sigma_0 - i\left(-\mathrm{Im}\left[\beta_D\right]\sigma_z - \mathrm{Im}[\delta_D]\sigma_x + \mathrm{Re}[\delta_D]\sigma_y\right)\right\} e^{i\phi}, \tag{B.11}$$

with

$$\alpha_D = r(-E)r^*(E), \qquad \beta_D = t(-E)t^*(E) + s^*(-E)s(E), \qquad \delta_D = s(-E)t^*(E) - t^*(-E)s(E). \tag{B.12}$$

We choose to write the signs differently as compared to Eq. (B.6) such that in the rotated basis, $\tilde{A}$ and $\tilde{D}$ have opposite sign imaginary part and same sign real parts. As we will show below, this will allow us to write $\tilde{D} = \tilde{A}^\dagger$. The block D can be diagonalized with the rotation $W_D = e^{-i\frac{\theta_D}{2}\sigma_z} e^{-i\frac{\gamma_D}{2}\sigma_y}$ where

$$\gamma_D = \arctan\frac{|\delta_D|}{-\mathrm{Im}\left\{\beta_D\right\}}, \qquad \theta_D = \varphi_D + \frac{\pi}{2}. \tag{B.13}$$

Using the same notation convention, we obtain

$$\tilde{D} = \alpha_D\sigma_0 + \mathrm{Re}\left[\beta_D\right] e^{i\phi}\sigma_0 - i\sqrt{\mathrm{Im}\left[\beta_D\right]^2 + |\delta_D|^2} e^{i\phi}\sigma_z. \tag{B.14}$$

Note that, due to the square roots in Eq. (B.10) and Eq. (B.14) which result from the rotation of the blocks, there is an ambiguity in the spin definition. In particular, in the limit $= |t|^2 = 1$, the square root simplifies to $|\mathrm{Im}\left[\beta_{A/D}\right]|$, which changes the way we label spin when $\mathrm{Im}\left[\beta_{A/D}\right] < 0$.

Now that we've diagonalized these two blocks, we can take a closer look at the various terms they contain. First, we can begin by noting the following relationships

$$\alpha_A = \alpha_D^*, \qquad \mathrm{Re}\left[\beta_A\right] = \mathrm{Re}\left[\beta_D\right]. \tag{B.15}$$

For the terms under the square root, after some math, they both can be cast in the form

$$\left(|t(E)|^2 + |s(E)|^2\right)\left(|t(-E)|^2 + |s(-E)|^2\right) + (\mathrm{Re}[t^*(-E)t(E)] + \mathrm{Re}[s^*(-E)s(E)])^2. \tag{B.16}$$

To simplify the notations, we introduce

$$\tau(E) = \sqrt{\left(|t(E)|^2 + |s(E)|^2\right)\left(|t(-E)|^2 + |s(-E)|^2\right)}, \tag{B.17}$$

$$\omega(E) = \mathrm{sign}(E)\arccos\left(\frac{\mathrm{Re}[t^*(-E)t(E) + s^*(-E)s(E)]}{\tau(E)}\right), \tag{B.18}$$

such that we can write

$$A = D^* = r^*(-E)r(E) + \tau(E)e^{-i\phi}e^{i\omega(E)\sigma_z}. \tag{B.19}$$

We can now look at the block B. Using the unitarity of $M(E,\phi)$, we obtain

$$D^\dagger B - BA = 0. \tag{B.20}$$

Thus, in the rotated basis where

$$\tilde{M}(E,\phi)=\begin{pmatrix} W_A^\dagger & 0 \\ 0 & W_D^\dagger \end{pmatrix} M(E,\phi) \begin{pmatrix} W_A & 0 \\ 0 & W_D \end{pmatrix}, \tag{B.21}$$

it implies that $\tilde{A}$ must commute with $\tilde{B}$ where $\tilde{B} = W_D^\dagger B W_A$, meaning that in this basis, $\tilde{B}$ must be diagonal, i.e.,

$$\tilde{B} = \begin{pmatrix} \tilde{B}_1 & 0 \\ 0 & \tilde{B}_2 \end{pmatrix}. \tag{B.22}$$

In fact, one can show after a lengthy calculation that $W_D \mathcal{T}(\pm E) W_A^\dagger$ is diagonal and can be written in the form

$$W_D \mathcal{T}(\pm E) W_A^\dagger = \sqrt{|t(\pm E)|^2 + |s(\pm E)|^2}\, e^{i\theta_{\mathcal{T}(\pm E)}\sigma_z} \sigma_z, \tag{B.23}$$

such that $\omega(E) = \theta_{\mathcal{T}}(E) - \theta_{\mathcal{T}}(-E)$.

As a consequence, the diagonalization of the blocks A and D allows decomposing $M(E,\phi)$ into two 2×2 independent blocks, which can be readily diagonalized and yield eigenvalues in the form

$$\exp\left[2i\rho\chi_\sigma(E,\phi) + i\xi(E) - i\xi(-E)\right], \tag{B.24}$$

with $\sigma, \rho = \pm 1$ and,

$$\chi_\sigma(E,\phi) = \arccos\sqrt{\frac{1+\tau(E)\cos\big(\phi - \sigma\omega(E)\big) + \mathrm{Re}[r^*(-E)r(E)]}{2}}. \tag{B.25}$$

The eigenvectors are given by

$$W = \begin{pmatrix} W_A & 0 \\ 0 & W_D \end{pmatrix} \begin{pmatrix} \cos\frac{\gamma_{B1}}{2} e^{-i\frac{\theta_{B1}}{2}} & 0 & -\sin\frac{\gamma_{B1}}{2} e^{-i\frac{\theta_{B1}}{2}} & 0 \\ 0 & \cos\frac{\gamma_{B2}}{2} e^{-i\frac{\theta_{B2}}{2}} & 0 & -\sin\frac{\gamma_{B2}}{2} e^{-i\frac{\theta_{B2}}{2}} \\ \sin\frac{\gamma_{B1}}{2} e^{i\frac{\theta_{B1}}{2}} & 0 & \cos\frac{\gamma_{B1}}{2} e^{i\frac{\theta_{B1}}{2}} & \\ 0 & \sin\frac{\gamma_{B2}}{2} e^{i\frac{\theta_{B2}}{2}} & 0 & \cos\frac{\gamma_{B2}}{2} e^{i\frac{\theta_{B2}}{2}} \end{pmatrix}, \tag{B.26}$$

where

$$\theta_{Bi} = \frac{\pi}{2} + \varphi_{Bi}, \qquad \gamma_{Bi} = \arctan\frac{|\tilde{B}_i|}{-\mathrm{Im}\left[\tilde{A}_i\right]}, \tag{B.27}$$

with $\tilde{B}_i = |\tilde{B}_i| e^{i\varphi_{Bi}}$. Here the different columns correspond to different values of (ρ,σ), namely the first column corresponds to the state $(-,+)$, the second column to $(-,-)$, the third column to $(+,+)$, and the fourth column to $(+,-)$. Note that this result is independent of the scattering model, the only requirement is that it respect TRS.

APPENDIX C

Particular case of the two delta potentials barriers

Here, we will briefly describe the specificities of the model with a delta potential at each nanowire-superconductor interface. Let's start by discussing the energy spectrum of ABS for this model. Using the scattering and transfer matrix formalisms presented in Sec. 1.2.2, we obtain the following scattering coefficients

$$
\begin{aligned}
r(E) &= \frac{i}{|K(E)|}\left[r_L e^{-i\theta_R - i\bar{k}d} - r_R e^{i\theta_L + i\bar{k}d}\right], && \text{(C.1)}\\
t(E) &= \frac{i}{|K(E)|}\left[t_L t_R e^{\frac{1}{2}i\delta k d} + s_L S_R^{*} e^{-\frac{1}{2}i\delta k d}\right], && \text{(C.2)}\\
s(E) &= \frac{i}{|K(E)|}\left[t_L s_R e^{\frac{1}{2}i\delta k d} - s_L t_R^{*} e^{-\frac{1}{2}i\delta k d}\right], && \text{(C.3)}\\
\xi(E) &= \theta_L + \theta_R + \bar{k}d - \zeta(E) - \pi/2, && \text{(C.4)}\\
\zeta(E) &= \arctan\left(-\frac{\sqrt{R_L R_R}\sin\left(\varphi_{\text{tot}} + 2\bar{\lambda}\epsilon\right)}{1 - \sqrt{R_L R_R}\cos\left(\varphi_{\text{tot}} + 2\bar{\lambda}\epsilon\right)}\right), && \text{(C.5)}\\
|K(E)|^2 &= (1 - \sqrt{R_L R_R})^2 + 4R_L R_R \sin^2(\varphi_{\text{tot}} + \bar{\lambda}\epsilon), && \text{(C.6)}\\
2\varphi_{\text{tot}} &= \theta_L + \theta_R + \varphi_{r_R} - \varphi_{r_L} + (k_{F1} + k_{F2})d, && \text{(C.7)}
\end{aligned}
$$

where $\theta_{R/L}$ are the global phases of the scattering matrix at each interface, and, $\varphi_{r_{R/L}}$ are the phases of the reflection coefficient of each scattering matrix. As can be seen, the spin-conserving and spin-flip transmission coefficient present the same form of energy dependence, such that it leads to $\omega(\epsilon) = \delta\lambda\epsilon$. The resulting energy spectrum is very similar to the one obtained with the one scattering potential model. However, as we saw previously in Sec. 1.3.3.3, a model with two identical scattering potentials can lead to resonance for specific values of φ_{tot}. The resonance condition is $|K(E)| = |K(-E)|$ which is verified for $\varphi_{\text{tot}} = n\pi$ and $\varphi_{\text{tot}} = (2n+1)\pi/2$ with $n \in \mathbb{Z}$. Hence, for $\varphi_{\text{tot}} = n\pi$, the gap at $\phi = \pi$ for the doublet $m = 1$ is closed as well as the gap at φ_m between doublet m and $m+1$ for m even. For $\varphi_{\text{tot}} = (2n+1)\pi/2$, it is the gap at φ_m between doublet m and $m+1$ for m odd that are closed. An energy spectrum showing the different resonant conditions is shown in Fig. 3.1.

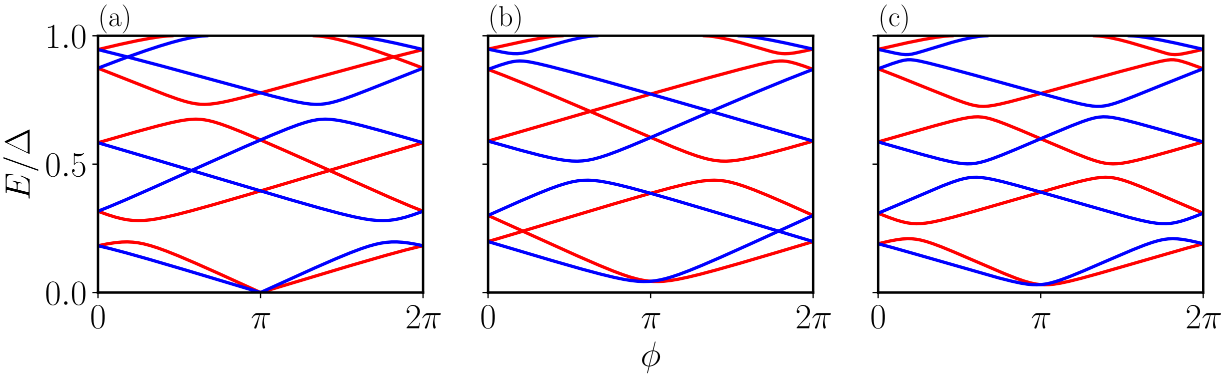

Figure 3.1: Energy spectrum of spin-split ABS obtained with the model with two scattering potentials for $\lambda_1 = 7$ and $\lambda_2 = 4.2$. In all panels, we set $T_R = T_L = S_R = S_L = 0.49$, such that the resonance condition can be satisfied depending on the value of φ_{tot}. In panel (a), we have $\varphi_{\text{tot}} = 0$, while in panel (b), we have $\varphi_{\text{tot}} = \pi/2$. In these two cases, the resonance condition is satisfied leading to crossings between different states. Finally, in panel (c), we have $\varphi_{\text{tot}} = \pi/4$, therefore the resonance condition is not satisfied and we don't have any crossings apart from the two-fold degeneracy at $\phi = n\pi$ within a doublet due to TRS.

In this model, $s(E)$ and $t(E)$ have the same energy dependency and as a consequence the matrices W_A and W_D given in Appendix. B are energy independent:

$$\cos\gamma_{A/D} = \frac{T_{L/R} - S_{L/R}}{T_{L/R} + S_{L/R}}, \tag{C.8}$$

$$\sin\gamma_{A/D} = \frac{2\sqrt{T_{L/R}S_{L/R}}}{T_{L/R} + S_{L/R}}, \tag{C.9}$$

while

$$\theta_A = \varphi_{t_L} + \varphi_{s_L}, \quad \theta_D = \varphi_{s_R} - \varphi_{t_R}. \tag{C.10}$$

As for the single scatterer model, this yields zero spin-flip matrix elements when plugged into Eq. (2.127).

APPENDIX D

Global phase of the current operator matrix elements

In this appendix, we show that the global phase of the matrix elements of the current operator obtained from Eq. (2.127) does not depend on $\tilde{x}'$.

The matrix W given in Eq. (2.106) containing the eigenvectors can be cast in the form $W = D_\varphi(\varphi_2) r_A(-\phi/2)\tilde{W}$, where

$$\tilde{W} = \begin{pmatrix} \cos\frac{\gamma_A}{2}\cos\frac{\gamma_{B1}}{2} & i\sin\frac{\gamma_A}{2}\cos\frac{\gamma_{B2}}{2} & -\cos\frac{\gamma_A}{2}\sin\frac{\gamma_{B1}}{2} & -i\sin\frac{\gamma_A}{2}\sin\frac{\gamma_{B2}}{2} \\ \sin\frac{\gamma_A}{2}\cos\frac{\gamma_{B1}}{2} & -i\cos\frac{\gamma_A}{2}\cos\frac{\gamma_{B2}}{2} & -\sin\frac{\gamma_A}{2}\sin\frac{\gamma_{B1}}{2} & i\cos\frac{\gamma_A}{2}\sin\frac{\gamma_{B2}}{2} \\ \cos\frac{\gamma_D}{2}\sin\frac{\gamma_{B1}}{2} & -i\sin\frac{\gamma_D}{2}\sin\frac{\gamma_{B2}}{2} & \cos\frac{\gamma_D}{2}\cos\frac{\gamma_{B1}}{2} & -i\sin\frac{\gamma_D}{2}\cos\frac{\gamma_{B2}}{2} \\ \sin\frac{\gamma_D}{2}\sin\frac{\gamma_{B1}}{2} & i\cos\frac{\gamma_D}{2}\sin\frac{\gamma_{B2}}{2} & \sin\frac{\gamma_D}{2}\cos\frac{\gamma_{B1}}{2} & i\cos\frac{\gamma_D}{2}\cos\frac{\gamma_{B2}}{2} \end{pmatrix}, \tag{D.1}$$

and $D_\varphi(\varphi_2)$ is a diagonal-matrix containing energy-independent phases,

$$D_\varphi(\varphi_2) = \exp\left[-\frac{i}{2}\left(\varphi_1\sigma_z + \varphi_2\tau_z + \varphi_3\sigma_z\tau_z\right)\right] \tag{D.2}$$

with $\varphi_1 = \delta k_F d/2 + \varphi_s$, $\varphi_2 = \bar{k}_F d\tilde{x}_0 + \varphi_r$ and $\varphi_3 = \delta k_F d\tilde{x}_0/2 + \varphi_t$. Thus, the phase of $\mathcal{A}_{(n)k}$ does not depend on the energy such that $\mathcal{A}^*_{(n)k}\mathcal{A}_{(n')k}$ is real.

Furthermore, we may use that the matrix

$$S_e(E) = e^{i\theta + i\bar{k}(E)d}\begin{pmatrix} re^{i\bar{k}(E)d\tilde{x}_0} & 0 & -t^*e^{-i\frac{\delta k(E)}{2}d} & -s^*e^{-i\frac{\delta k(E)}{2}d\tilde{x}_0} \\ 0 & re^{i\bar{k}(E)d\tilde{x}_0} & -se^{i\frac{\delta k(E)}{2}d\tilde{x}_0} & te^{i\frac{\delta k(E)}{2}d} \\ te^{i\frac{\delta k(E)}{2}d} & s^*e^{-i\frac{\delta k(E)}{2}d\tilde{x}_0} & r^*e^{-i\bar{k}(E)d\tilde{x}_0} & 0 \\ se^{i\frac{\delta k(E)}{2}d\tilde{x}_0} & -t^*e^{-i\frac{\delta k(E)}{2}d} & 0 & r^*e^{-i\bar{k}(E)d\tilde{x}_0} \end{pmatrix} \tag{D.3}$$

can be written in the form $S_e(E) = e^{i(\theta + \bar{k}_F d)} D_\varphi(-\varphi_2)\tilde{S}_e(E)D^\dagger_\varphi(\varphi_2)$, where $\tilde{S}_e(-E) = \tilde{S}^*_e(E)$. This allows us to rewrite the matrix M in the form

$$M = D_\varphi(\varphi_2) r_A(-\phi)\tilde{S}^T_e(E) r_A(\phi)\tilde{S}_e(E) D^\dagger_\varphi(\varphi_2). \tag{D.4}$$

With this, we can then cast the equation $\alpha^2 MW = W$ in the form $m\tilde{W} = m^*\tilde{W}$ with the matrix

$$m = \alpha r_A(\phi/2)\tilde{S}_e(E) r_A(-\phi/2). \tag{D.5}$$

Since the columns $\tilde{\mathcal{A}}$ of $\tilde{W}$ are either purely real or purely imaginary, this shows that $m\tilde{\mathcal{A}}$ is either purely real or purely imaginary. As a consequence the global phase of $(\alpha S_{(n)}\mathcal{A}_{(n)})_k = (e^{i(\theta+\bar{k}_F d)} r_A(-\phi/2) D_\varphi(-\varphi_2))_{kk}(m_{(n)}\tilde{A}_{(n)})_k$ does not dependent on energy and $(\alpha S_{(n)}\mathcal{A}_{(n)})^*_k(\alpha S_{(n')}\mathcal{A}_{(n')})_k$ is real.

With this we conclude that the phase of the current matrix operator elements is determined by the phase of $f^{\pm}_{nn',k} = e^{i\lambda_k(\epsilon_{n'}-\epsilon_n)(1\pm\tilde{x}')/2} + \alpha_n\alpha^*_{n'} e^{-i\lambda_k(\epsilon_{n'}-\epsilon_n)(1\pm\tilde{x}')/2}$, which is given as

$$\theta_{nn'} = (\arccos\epsilon_{n'} - \arccos\epsilon_n)/2. \tag{D.6}$$

As observed in Fig. 2.16, the current operator matrix elements may vanish for particular values of $\tilde{x}$. In Fig. 2.17, we show that this is generally the case for all current operator matrix elements, both spin-preserving and spin-flip.

Bibliography

1. Arute, F. *et al.* Quantum supremacy using a programmable superconducting processor. *Nature* **574,** 505–510 (Oct. 2019).
2. Josephson, B. D. Possible new effects in superconductive tunnelling. *Physics Letters* **1,** 251–253 (July 1962).
3. McCumber, D. E. Effect of ac Impedance on dc Voltage-Current Characteristics of Superconductor Weak-Link Junctions. *Journal of Applied Physics* **39,** 3113–3118 (Nov. 2003).
4. Martinis, J. M., Devoret, M. H. & Clarke, J. Energy-Level Quantization in the Zero-Voltage State of a Current-Biased Josephson Junction. *Physical Review Letters* **55,** 1543–1546 (Oct. 1985).
5. Devoret, M. H. & Schoelkopf, R. J. Superconducting Circuits for Quantum Information: An Outlook. *Science* **339,** 1169–1174 (Mar. 2013).
6. Koch, J. *et al.* Charge-insensitive qubit design derived from the Cooper pair box. *Physical Review A* **76,** 042319 (Oct. 2007).
7. Hanson, R., Kouwenhoven, L. P., Petta, J. R., Tarucha, S. & Vandersypen, L. M. K. Spins in few-electron quantum dots. *Reviews of Modern Physics* **79,** 1217–1265 (Oct. 2007).
8. Nadj-Perge, S., Frolov, S. M., Bakkers, E. P. a. M. & Kouwenhoven, L. P. Spin–orbit qubit in a semiconductor nanowire. *Nature* **468,** 1084–1087 (Dec. 2010).
9. Nowack, K. C., Koppens, F. H. L., Nazarov, Y. V. & Vandersypen, L. M. K. Coherent Control of a Single Electron Spin with Electric Fields. *Science* **318,** 1430–1433 (Nov. 2007).
10. Golovach, V. N., Borhani, M. & Loss, D. Electric-dipole-induced spin resonance in quantum dots. *Physical Review B* **74,** 165319 (Oct. 2006).
11. Tyryshkin, A. M. *et al.* Electron spin coherence exceeding seconds in high-purity silicon. *Nature Materials* **11** (Feb. 2012).
12. Bar-Gill, N., Pham, L. M., Jarmola, A., Budker, D. & Walsworth, R. L. Solid-state electronic spin coherence time approaching one second. *Nature Communications* **4,** 1743 (Apr. 2013).
13. Hanson, R. *et al.* Zeeman Energy and Spin Relaxation in a One-Electron Quantum Dot. *Physical Review Letters* **91,** 196802 (Nov. 2003).
14. Koppens, F. H. L., Nowack, K. C. & Vandersypen, L. M. K. Spin Echo of a Single Electron Spin in a Quantum Dot. *Physical Review Letters* **100,** 236802 (June 2008).

15. Petta, J. R. *et al.* Coherent Manipulation of Coupled Electron Spins in Semiconductor Quantum Dots. *Science* **309,** 2180–2184 (Sept. 2005).
16. Hanson, R. & Awschalom, D. D. Coherent manipulation of single spins in semiconductors. *Nature* **453,** 1043–1049 (June 2008).
17. Yamamoto, T., Pashkin, Y. A., Astafiev, O., Nakamura, Y. & Tsai, J. S. Demonstration of conditional gate operation using superconducting charge qubits. *Nature* **425,** 941–944 (Oct. 2003).
18. Pashkin, Y. A. *et al.* Quantum oscillations in two coupled charge qubits. *Nature* **421,** 823–826 (Feb. 2003).
19. Steffen, M. *et al.* Measurement of the Entanglement of Two Superconducting Qubits via State Tomography. *Science* **313,** 1423–1425 (Sept. 2006).
20. Martinis, J. M. *et al.* Decoherence in Josephson Qubits from Dielectric Loss. *Physical Review Letters* **95,** 210503 (Nov. 2005).
21. Likharev, K. K. Superconducting weak links. *Reviews of Modern Physics* **51,** 101–159 (Jan. 1979).
22. Golubov, A. A., Kupriyanov, M. Y. & Il'ichev, E. The current-phase relation in Josephson junctions. *Reviews of Modern Physics* **76,** 411–469 (Apr. 2004).
23. Andreev, A. F. Electron Spectrum of the Intermediate State of Superconductors. *Soviet Journal of Experimental and Theoretical Physics* **22,** 455 (Feb. 1966).
24. Kulik, I. O. Macroscopic Quantization and the Proximity Effect in S-N-S Junctions. *Soviet Journal of Experimental and Theoretical Physics* **30,** 944 (Jan. 1969).
25. Beenakker, C. W. J. & van Houten, H. Josephson current through a superconducting quantum point contact shorter than the coherence length. *Physical Review Letters* **66,** 3056–3059 (June 1991).
26. Furusaki, A. & Tsukada, M. Dc Josephson effect and Andreev reflection. *Solid State Communications* **78,** 299–302 (Apr. 1991).
27. Bretheau, L., Girit, Ç. Ö., Pothier, H., Esteve, D. & Urbina, C. Exciting Andreev pairs in a superconducting atomic contact. *Nature* **499,** 312–315 (July 2013).
28. Bretheau, L., Girit, Ç. Ö., Urbina, C., Esteve, D. & Pothier, H. Supercurrent Spectroscopy of Andreev States. *Physical Review X* **3,** 041034 (Dec. 2013).
29. Pillet, J.-D. *et al.* Andreev bound states in supercurrent-carrying carbon nanotubes revealed. *Nature Physics* **6,** 965–969 (Dec. 2010).
30. Lee, E. J. H. *et al.* Spin-resolved Andreev levels and parity crossings in hybrid superconductor–semiconductor nanostructures. *Nature Nanotechnology* **9,** 79–84 (Jan. 2014).
31. Hays, M. *et al.* Direct Microwave Measurement of Andreev-Bound-State Dynamics in a Semiconductor-Nanowire Josephson Junction. *Physical Review Letters* **121,** 047001 (July 2018).
32. Blais, A., Huang, R.-S., Wallraff, A., Girvin, S. M. & Schoelkopf, R. J. Cavity quantum electrodynamics for superconducting electrical circuits: An architecture for quantum computation. *Physical Review A* **69,** 062320 (June 2004).
33. Zgirski, M. *et al.* Evidence for Long-Lived Quasiparticles Trapped in Superconducting Point Contacts. *Physical Review Letters* **106,** 257003 (June 2011).
34. Fu, L. & Kane, C. L. Superconducting Proximity Effect and Majorana Fermions at the Surface of a Topological Insulator. *Physical Review Letters* **100,** 096407 (Mar. 2008).

35. Mourik, V. *et al.* Signatures of Majorana Fermions in Hybrid Superconductor-Semiconductor Nanowire Devices. *Science* **336,** 1003–1007 (May 2012).
36. Deng, M.-T. *et al.* Nonlocality of Majorana modes in hybrid nanowires. *Physical Review B* **98,** 085125 (Aug. 2018).
37. Chtchelkatchev, N. M. & Nazarov, Y. V. Andreev Quantum Dots for Spin Manipulation. *Physical Review Letters* **90,** 226806 (June 2003).
38. Cheng, M. & Lutchyn, R. M. Josephson current through a superconductor/semiconductor-nanowire/superconductor junction: Effects of strong spin-orbit coupling and Zeeman splitting. *Physical Review B* **86,** 134522 (Oct. 2012).
39. Yokoyama, T., Eto, M. & Nazarov, Y. V. Anomalous Josephson effect induced by spin-orbit interaction and Zeeman effect in semiconductor nanowires. *Physical Review B* **89,** 195407 (May 2014).
40. Béri, B., Bardarson, J. H. & Beenakker, C. W. J. Splitting of Andreev levels in a Josephson junction by spin-orbit coupling. *Physical Review B* **77,** 045311 (Jan. 2008).
41. Padurariu, C. & Nazarov, Y. V. Theoretical proposal for superconducting spin qubits. *Physical Review B* **81,** 144519 (Apr. 2010).
42. Park, S. & Yeyati, A. L. Andreev spin qubits in multichannel Rashba nanowires. *Physical Review B* **96,** 125416 (Sept. 2017).
43. Tosi, L. *et al.* Spin-Orbit Splitting of Andreev States Revealed by Microwave Spectroscopy. *Physical Review X* **9,** 011010 (Jan. 2019).
44. Hays, M. *et al.* Continuous monitoring of a trapped superconducting spin. *Nature Physics* **16,** 1103–1107 (Nov. 2020).
45. Metzger, C. *et al.* Circuit-QED with phase-biased Josephson weak links. *Physical Review Research* **3,** 013036 (Jan. 2021).
46. Fauvel, Y., Meyer, J. S. & Houzet, M. Opportunities for the direct manipulation of a phase-driven Andreev spin qubit. *Phys. Rev. B* **109,** 184515 (18 2024).
47. Hays, M. *et al.* Coherent manipulation of an Andreev spin qubit. *Science* **373,** 430–433 (July 2021).
48. Pita-Vidal, M. *et al.* Direct manipulation of a superconducting spin qubit strongly coupled to a transmon qubit. *Nature Physics* **19,** 1110–1115 (Aug. 2023).
49. Palacios-Laloy, A. *Superconducting qubit in a resonator : test of the Legget-Garg inequality and single-shot readout* PhD thesis (Université Pierre et Marie Curie - Paris VI, Sept. 2010).
50. Metzger, C. *Spin and charge effects in Andreev Bound States* PhD thesis (Mar. 2022).
51. Hays, M. *Realizing an Andreev Spin Qubit* PhD thesis (Jan. 2022).
52. Bardeen, J., Cooper, L. N. & Schrieffer, J. R. Microscopic Theory of Superconductivity. *Physical Review* **106,** 162–164 (Apr. 1957).
53. Tinkham, M. *Introduction to Superconductivity* (Jan. 2004).
54. Asano, Y. *Andreev Reflection in Superconducting Junctions* (Springer, Singapore, 2021).
55. Timm, C. *Theory of Superconductivity* 2017.
56. Cooper, L. N. Bound Electron Pairs in a Degenerate Fermi Gas. *Physical Review* **104,** 1189–1190 (Nov. 1956).

57. Fröhlich, H. Theory of the Superconducting State. I. The Ground State at the Absolute Zero of Temperature. *Physical Review* **79,** 845–856 (Sept. 1950).
58. Maxwell, E. Isotope Effect in the Superconductivity of Mercury. *Physical Review* **78,** 477–477 (May 1950).
59. Reynolds, C. A., Serin, B., Wright, W. H. & Nesbitt, L. B. Superconductivity of Isotopes of Mercury. *Physical Review* **78,** 487–487 (May 1950).
60. Gennes, P. G. D. *Superconductivity Of Metals And Alloys* (Boca Raton, May 2019).
61. Bogoliubov, N. N. A new method in the theory of superconductivity. III. *Journal of Experimental and Theoretical Physics* (1958).
62. Bogoliubov, N. N. A new method in the theory of superconductivity. I. *Journal of Experimental and Theoretical Physics* (1958).
63. Markoš, P. & Soukoulis, C. M. *Wave Propagation: From Electrons to Photonic Crystals and Left-handed Materials* (2008).
64. Breit, G. & Wigner, E. Capture of Slow Neutrons. *Physical Review* **49,** 519–531 (Apr. 1936).
65. Josephson, B. Supercurrents through barriers. *Advances in Physics* **14,** 419–451 (1965).
66. Andreev, A. F. The Thermal Conductivity of the Intermediate State in Superconductors. *Soviet Journal of Experimental and Theoretical Physics* **19,** 1228 (Nov. 1964).
67. Yokoyama, T. & Nazarov, Y. V. Singularities in the Andreev spectrum of a multiterminal Josephson junction. *Phys. Rev. B* **92,** 155437 (15 2015).
68. Bagwell, P. F. Suppression of the Josephson current through a narrow, mesoscopic, semiconductor channel by a single impurity. *Physical Review B* **46,** 12573–12586 (Nov. 1992).
69. Samuelsson, P., Lantz, J., Shumeiko, V. S. & Wendin, G. Nonequilibrium Josephson effect in mesoscopic ballistic multiterminal SNS junctions. *Physical Review B* **62,** 1319–1337 (July 2000).
70. Kopnin, N. B., Mel'nikov, A. S. & Vinokur, V. M. Resonance Energy and Charge Pumping through Quantum SINIS Contacts. *Physical Review Letters* **96,** 146802 (Apr. 2006).
71. Kopnin, N. B. & Voutilainen, J. Nonequilibrium charge transport in quantum SINIS structures. *Physical Review B* **75,** 174509 (May 2007).
72. Beenakker, C. W. J. & van Houten, H. Resonant Josephson Current Through a Quantum Dot. *Springer Series in Electronics and Photonics* (eds Koch, H. & Lübbig, H.) 175–179 (1992).
73. Aleiner, I., Brouwer, P. & Glazman, L. Quantum effects in Coulomb blockade. *Physics Reports* **358,** 309–440 (2002).
74. Beenakker, C. W. J. Theory of Coulomb-blockade oscillations in the conductance of a quantum dot. *Phys. Rev. B* **44,** 1646–1656 (1991).
75. Grabert, H. & Devoret, M. H. *Single Charge Tunneling. Coulomb Blockade Phenomena In Nanostructures* (Springer, 1992).
76. Stampfer, C. *et al.* Tunable Coulomb blockade in nanostructured graphene. *Applied Physics Letters* **92,** 012102 (Jan. 2008).
77. Kondo, J. Resistance Minimum in Dilute Magnetic Alloys. *Progress of Theoretical Physics* **32,** 37–49 (July 1964).

78. Cronenwett, S. M., Oosterkamp, T. H. & Kouwenhoven, L. P. A Tunable Kondo Effect in Quantum Dots. *Science* **281,** 540–544 (1998).
79. Anderson, P. W. Localized Magnetic States in Metals. *Physical Review* **124,** 41–53 (Oct. 1961).
80. Cleuziou, J.-P., Wernsdorfer, W., Bouchiat, V., Ondarçuhu, T. & Monthioux, M. Carbon nanotube superconducting quantum interference device. *Nature Nanotechnology* **1,** 53–59 (Oct. 2006).
81. Jorgensen, H. I., Novotny, T., Grove-Rasmussen, K., Flensberg, K. & Lindelof, P. E. Critical Current 0-π Transition in Designed Josephson Quantum Dot Junctions. *Nano Letters* **7,** 2441–2445 (2007).
82. Vecino, E., Martín-Rodero, A. & Yeyati, A. L. Josephson current through a correlated quantum level: Andreev states and $\ensuremath{\pi}$ junction behavior. *Physical Review B* **68,** 035105 (July 2003).
83. Glazman, L. I. & Matveev, K. A. Resonant Josephson current through Kondo impurities in a tunnel barrier. *Soviet Journal of Experimental and Theoretical Physics Letters* **49.** ADS Bibcode: 1989JETPL..49..659G, 659 (May 1989).
84. Bauer, J., Oguri, A. & Hewson, A. C. Spectral properties of locally correlated electrons in a Bardeen–Cooper–Schrieffer superconductor. *Journal of Physics: Condensed Matter* **19,** 486211 (Nov. 2007).
85. Karrasch, C., Oguri, A. & Meden, V. Josephson current through a single Anderson impurity coupled to BCS leads. *Physical Review B* **77,** 024517 (Jan. 2008).
86. Choi, M.-S., Lee, M., Kang, K. & Belzig, W. Kondo effect and Josephson current through a quantum dot between two superconductors. *Physical Review B* **70,** 020502 (July 2004).
87. Tanaka, Y., Oguri, A. & Hewson, A. C. Kondo effect in asymmetric Josephson couplings through a quantum dot. *New Journal of Physics* **9,** 115 (May 2007).
88. Siano, F. & Egger, R. Josephson Current through a Nanoscale Magnetic Quantum Dot. *Physical Review Letters* **93,** 047002 (July 2004).
89. Anderson, P. W. Localized Magnetic States in Metals. *Phys. Rev.* **124,** 41–53 (1 1961).
90. Schrieffer, J. R. & Wolff, P. A. Relation between the Anderson and Kondo Hamiltonians. *Physical Review* **149,** 491–492 (Sept. 1966).
91. Meng, T. *Andreev boun states in Josephson quantum dot devices* PhD thesis (Mar. 2009).
92. Meng, T., Florens, S. & Simon, P. Self-consistent description of Andreev bound states in Josephson quantum dot devices. *Phys. Rev. B* **79,** 224521 (22 2009).
93. Bezuglyi, E. V., Rozhavsky, A. S., Vagner, I. D. & Wyder, P. Combined effect of Zeeman splitting and spin-orbit interaction on the Josephson current in a superconductor–two-dimensional electron gas–superconductor structure. *Physical Review B* **66,** 052508 (Aug. 2002).
94. Krive, I. V., Gorelik, L. Y., Shekhter, R. I. & Jonson, M. Chiral symmetry breaking and the Josephson current in a ballistic superconductor–quantum wire–superconductor junction. *Low Temperature Physics* **30,** 398–404 (May 2004).
95. Bargerbos, A. *et al.* Spectroscopy of Spin-Split Andreev Levels in a Quantum Dot with Superconducting Leads. *Phys. Rev. Lett.* **131,** 097001 (9 2023).
96. Thomas, L. H. *The Motion of the Spinning Electron* 1926.
97. Dresselhaus, G. Spin-Orbit Coupling Effects in Zinc Blende Structures. *Phys. Rev.* **100,** 580–586 (2 1955).

98. Moroz, A. V. & Barnes, C. H. W. Effect of the spin-orbit interaction on the band structure and conductance of quasi-one-dimensional systems. *Physical Review B* **60,** 14272–14285 (Nov. 1999).

99. Delplace, P., Li, J. & Büttiker, M. Magnetic-Field-Induced Localization in 2D Topological Insulators. *Physical Review Letters* **109,** 246803 (Dec. 2012).

100. Dimitrova, O. V. & Feigel'man, M. V. Two-dimensional S-N-S junction with Rashba spin-orbit coupling. *JETP* (2006).

101. Le Sueur, H., Joyez, P., Pothier, H., Urbina, C. & Esteve, D. Phase Controlled Superconducting Proximity Effect Probed by Tunneling Spectroscopy. *Physical Review Letters* **100,** 197002 (May 2008).

102. Bretheau, L. *et al.* Tunnelling spectroscopy of Andreev states in graphene. *Nature Physics* **13,** 756–760 (Aug. 2017).

103. Chang, W., Manucharyan, V. E., Jespersen, T. S., Nygård, J. & Marcus, C. M. Tunneling Spectroscopy of Quasiparticle Bound States in a Spinful Josephson Junction. *Physical Review Letters* **110,** 217005 (May 2013).

104. Pillet, J.-D., Joyez, P., Žitko, R. & Goffman, M. F. Tunneling spectroscopy of a single quantum dot coupled to a superconductor: From Kondo ridge to Andreev bound states. *Physical Review B* **88,** 045101 (July 2013).

105. Wallraff, A. *et al.* Strong coupling of a single photon to a superconducting qubit using circuit quantum electrodynamics. *Nature* **431,** 162–167 (Sept. 2004).

106. Park, S. *et al.* From Adiabatic to Dispersive Readout of Quantum Circuits. *Physical Review Letters* **125,** 077701 (Aug. 2020).

107. Vool, U. & Devoret, M. Introduction to quantum electromagnetic circuits. en. *International Journal of Circuit Theory and Applications* **45,** 897–934 (2017).

108. Park, S. *et al.* From Adiabatic to Dispersive Readout of Quantum Circuits - Sup. Mat. *Physical Review Letters* **125,** 077701 (Aug. 2020).

109. Jaynes, E. & Cummings, F. Comparison of quantum and semiclassical radiation theories with application to the beam maser. *Proceedings of the IEEE* **51,** 89–109 (1963).

110. D.F. Walls, G. J. M. *Quantum Optics - Chap. 10* (1994).

111. Pita-Vidal, M. *et al. Strong tunable coupling between two distant superconducting spin qubits* 2023. arXiv: `2307.15654 [quant-ph]`.

112. Aumentado, J., Keller, M. W., Martinis, J. M. & Devoret, M. H. Nonequilibrium Quasiparticles and 2e Periodicity in Single-Cooper-Pair Transistors. *Physical Review Letters* **92,** 066802 (Feb. 2004).

113. Bergeret, F. S., Yeyati, A. L. & Martín-Rodero, A. Interplay between Josephson effect and magnetic interactions in double quantum dots. *Physical Review B* **74,** 132505 (Oct. 2006).

114. Deacon, R. S. *et al.* Cooper pair splitting in parallel quantum dot Josephson junctions. en. *Nature Communications* **6,** 7446 (July 2015).

115. Estrada Saldaña, J. *et al.* Supercurrent in a Double Quantum Dot. *Physical Review Letters* **121,** 257701 (Dec. 2018).

116. Kumar, B., Verma, S. & Ajay. Phase and Thermal-Driven Transport Across T-Shaped Double Quantum Dot Josephson Junction. en. *Journal of Superconductivity and Novel Magnetism* **36,** 831–841 (Mar. 2023).

117. Ortega-Taberner, C., Jauho, A.-P. & Paaske, J. Anomalous Josephson current through a driven double quantum dot. en. *Physical Review B* **107,** 115165 (Mar. 2023).

118. Choi, M.-S., Bruder, C. & Loss, D. Spin-dependent Josephson current through double quantum dots and measurement of entangled electron states. *Physical Review B* **62,** 13569–13572 (Nov. 2000).

119. Žitko, R., Lee, M., López, R., Aguado, R. & Choi, M.-S. Josephson Current in Strongly Correlated Double Quantum Dots. *Physical Review Letters* **105,** 116803 (Sept. 2010).

120. López, R., Choi, M.-S. & Aguado, R. Josephson current through a Kondo molecule. *Physical Review B* **75,** 045132 (Jan. 2007).

121. Droste, S., Andergassen, S. & Splettstoesser, J. Josephson current through interacting double quantum dots with spin–orbit coupling. en. *Journal of Physics: Condensed Matter* **24,** 415301 (Sept. 2012).

122. Probst, B., Domínguez, F., Schroer, A., Yeyati, A. L. & Recher, P. Signatures of nonlocal Cooper-pair transport and of a singlet-triplet transition in the critical current of a double-quantum-dot Josephson junction. *Physical Review B* **94,** 155445 (Oct. 2016).

123. Bouman, D. *et al.* Triplet-blockaded Josephson supercurrent in double quantum dots. *Phys. Rev. B* **102,** 220505 (22 2020).

124. Byers, J. M. & Flatté, M. E. Probing Spatial Correlations with Nanoscale Two-Contact Tunneling. *Phys. Rev. Lett.* **74,** 306–309 (2 1995).

125. Deutscher, G. & Feinberg, D. Coupling superconducting-ferromagnetic point contacts by Andreev reflections. *Applied Physics Letters* **76,** 487–489 (Jan. 2000).

126. Zonda, M. *et al.* Generalized atomic limit of a double quantum dot coupled to superconducting leads. *Phys. Rev. B* **107,** 115407 (11 2023).

127. Kurilovich, P. D., Kurilovich, V. D., Fatemi, V., Devoret, M. H. & Glazman, L. I. Microwave response of an Andreev bound state. *Physical Review B* **104,** 174517 (Nov. 2021).

128. Zazunov, A., Egger, R., Jonckheere, T. & Martin, T. Anomalous Josephson Current through a Spin-Orbit Coupled Quantum Dot. *Physical Review Letters* **103,** 147004 (Oct. 2009).

129. Zhang, B. *et al.* *Evidence of* ϕ_0*-Josephson junction from skewed diffraction patterns in Sn-InSb nanowires* 2024. arXiv: `2212.00199 [cond-mat.mes-hall]`.

130. Chen, C.-Z. *et al.* Asymmetric Josephson effect in inversion symmetry breaking topological materials. *Physical Review B* **98,** 075430 (Aug. 2018).

131. Minutillo, M., Giuliano, D., Lucignano, P., Tagliacozzo, A. & Campagnano, G. Anomalous Josephson effect in S/SO/F/S heterostructures. *Physical Review B* **98,** 144510 (Oct. 2018).

132. Szombati, D. B. *et al.* Josephson -junction in nanowire quantum dots. *Nature Physics* **12,** 568–572 (June 2016).

133. Su, Z. *et al.* Andreev molecules in semiconductor nanowire double quantum dots. en. *Nature Communications* **8,** 585 (Sept. 2017).

134. Pillet, J.-D., Benzoni, V., Griesmar, J., Smirr, J.-L. & Girit, C. O. Nonlocal Josephson Effect in Andreev Molecules. *Nano Letters* **19,** 7138–7143 (Oct. 2019).

135. Prada, E. *et al.* From Andreev to Majorana bound states in hybrid superconductor–semiconductor nanowires. en. *Nature Reviews Physics* **2,** 575–594 (Oct. 2020).

136. Bardarson, J. H. *Effects of Spin-Orbit Coupling on Quantum Transport* PhD thesis (Jan. 2008).

137. Kramers, H. A. *Koninkl. Ned. Akad. Wetenschap. Proc. Ser. B* **33,** 959 (1930).

138. Wigner, E. Ueber die Operation der Zeitumkehr in der Quantenmechanik. *Nachrichten von der Gesellschaft der Wissenschaften zu Göttingen, Mathematisch-Physikalische Klasse* **1932,** 546–559 (1932).

139. Wigner, E. P. *Group Theory and its Applications to the QuantumMechanics of Atomic Spectra* 1959.